TWO SEARCHES FOR SIGNALS OF DARK MATTER WITH THE ATLAS DETECTOR IN 139 FB^{-1} OF LHC $\sqrt{\mathrm{S}} = 13\,\mathrm{TEV}$ PROTON-PROTON COLLISION DATA

by

GALEN RHODES GLEDHILL

A DISSERTATION

Presented to the Department of Physics
and the Division of Graduate Studies of the University of Oregon
in partial fulfillment of the requirements
for the degree of
Doctor of Philosophy

December 2022

DISSERTATION APPROVAL PAGE

Student: Galen Rhodes Gledhill

Title: Two Searches for Signals of Dark Matter with the ATLAS Detector in 139 fb^{-1} of LHC $\sqrt{s} = 13\,\mathrm{TeV}$ Proton-Proton Collision Data

This dissertation has been accepted and approved in partial fulfillment of the requirements for the Doctor of Philosophy degree in the Institute for Fundamental Science by:

Laura Jeanty	Chair
Stephanie Majewski	Advisor
Graham Kribs	Core Member
David Johnson	Institutional Representative

and

Krista Chronister	Vice Provost of Graduate Studies

Original approval signatures are on file with the University of Oregon Division of Graduate Studies.

Degree awarded December 2022

DISSERTATION ABSTRACT

Galen Rhodes Gledhill

Doctor of Philosophy

Department of Physics

December 2022

Title: Two Searches for Signals of Dark Matter with the ATLAS Detector in 139 fb^{-1} of LHC $\sqrt{\mathrm{s}} = 13\,\mathrm{TeV}$ Proton-Proton Collision Data

This dissertation presents two searches for signals of dark matter in an integrated luminosity of $139\,\mathrm{fb}^{-1}$ of proton-proton collision data collected at a center of mass energy of $\sqrt{s} = 13\,\mathrm{TeV}$ with the ATLAS detector at the Large Hadron Collider (LHC). The search for direct pair production of the supersymmetric partner to the top quark (the stop) in the all-hadronic $t\bar{t}$ plus missing transverse momentum final state yields no significant excess over the expected Standard Model background and was able to exclude stop masses up to 1.25 TeV for dark matter candidate masses below 200 GeV. The search for dark mesons decaying into top and bottom quarks is sensitive to a proposed strongly coupled dark sector which contains a viable dark matter candidate scalar baryon. This analysis considers the all-hadronic channel of a final state of all top and bottom quarks ($tttb$ or $tbtb$) with no additional missing transverse momentum. No previous LHC searches have considered this dark meson model and we expect to set new limits on dark pion masses of up to 500 GeV.

This dissertation contains previously published and unpublished coauthored material.

CURRICULUM VITAE

NAME OF AUTHOR: Galen Rhodes Gledhill

GRADUATE AND UNDERGRADUATE SCHOOLS ATTENDED:

University of Oregon, Eugene, Oregon, USA
Portland State University Honors College, Portland, Oregon, USA

DEGREES AWARDED:

Doctor of Philosophy, Physics, 2022, University of Oregon
Master of Science, Physics, 2015, University of Oregon
Bachelor of Arts, Physics, 2014, Portland State University Honors College

PROFESSIONAL EXPERIENCE:

Sergeant, United States Marine Corps, 2006-2010
Scientist, Thermo Fisher Scientific, 2014-current

SELECTED PUBLICATIONS:

Budnik et al. Nanoscale 3D tomography by in-flight fluorescence spectroscopy of atoms sputtered by a focused ion beam. *Nano Letters* 22(20):8287, 2022.

ATLAS Collaboration. Search for a scalar partner of the top quark in the all-hadronic $t\bar{t}$ plus missing transverse momentum final state at $\sqrt{s} = 13$ TeV with the ATLAS detector. *European Physics Journal C* 80(8):737, 2020.

PATENTS:

US Patent 10923318, Optical alignment correction using convolutional neural network evaluation of a beam image, February 16, 2021.

US Patent 10896802, Combined SEM-CL and FIB-IOE microscopy, January 19, 2021.

US Patent 10692694, Method and apparatus for enhancing SE detection in mirror-based light imaging charged particle microscopes, June 23, 2020.

ACKNOWLEDGEMENTS

I can only thank a small number of the many teachers, mentors and friends who have supported me during graduate school. I'm extremely grateful to my advisor Stephanie Majewski for her insight and guidance. I also thank my committee members Graham Kribs and Laura Jeanty for their assistance in reaching this point.

I'm grateful to the members of the ATLAS groups I worked with during my PhD program. From the dark meson analysis, I particularly valued working with Jochen Heinrich, Olga Gudnadottir, and Tim Mathew. From the direct stop analysis, I thank Johan Bonilla and Walter Hopkins for our many productive conversations. The JetEtMiss group has been welcoming and supportive and I thank Jennifer Roloff, TJ Khoo, Sarah Williams and Peter Loch.

My PSU Honors College professors Katheleen Merrow and Lawrence Wheeler deserve special thanks for their dedication to teaching and contribution to my academic development. Many faculty and students at the University of Oregon physics department deserve thanks for the valuable assistance they have provided. I gratefully acknowledge Nima Dinyari, Anne McGinley, and Ben McMorran for their support. I am also grateful to my Thermo Fisher Advanced Technology colleagues and especially Mostafa Maazous.

Finally, I thank my family for their steadfast support throughout my studies.

TABLE OF CONTENTS

Chapter Page

Chapter Page

LIST OF FIGURES

Figure Page

Figure Page

Figure Page

Figure Page

LIST OF TABLES

Table Page

CHAPTER I

INTRODUCTION

The Standard Model of particle physics provides a precise description of almost all laboratory scale fundamental interactions. At cosmological scales, we can describe the evolution of the universe from a hot big bang to the present-day observed structure. But astrophysical models and observations describe a universe in which over 80 % of the matter content is non-luminous [1, 2, 3, 4] and likely constituted by particles unaccounted for in the Standard Model. Uncovering the nature of dark matter will require observing and measuring the interactions of dark matter with Standard Model particles. In this thesis I describe two searches for beyond the Standard Model physics with the ATLAS detector at the Large Hadron Collider (LHC) which aim to discover or exclude possible dark matter models.

LHC searches for dark matter have evaluated a wide range of effective, simplified, and complete models. The searches in this thesis use the complete models of supersymmetry [5] and the dark meson [6] sector of Stealth Dark Matter [7] to interpret their results. Dark matter stability is guaranteed in these models from new symmetries. Supersymmetry models can contain a neutralino lightest supersymmetric particle (LSP) which is prevented from decaying to Standard Model or beyond the Standard Model states by the R-parity symmetry. This dark matter candidate is neutral and stable and could be produced at the LHC through the decay of the stop squark (the supersymmetric partner to the top quark). Supersymmetry also provides a solution to the hierarchy problem by canceling the Higgs mass loop correction terms with quadratic sensitivity to the high energy cut off (Λ_{UV}) of the Standard Model. Bound states of new strongly coupled sectors [8, 9] can generate viable dark matter candidate particles while avoiding detection from previous search strategies. Stealth

Dark Matter proposes a composite baryonic scalar of a strongly coupled theory with constituent fermions that transform as vector-like representations of the electroweak group. Stability is guaranteed from an accidental $U(1)_{\text{dark baryon}}$ symmetry which emerges from the model. The dark mesons bound states could be produced at the LHC and would provide a signal for this otherwise dark sector. An overview of the Standard Model and beyond the Standard Model phenomenology relevant for these models is presented in Chapter II.

Typical production cross sections for the beyond the Standard Model signals considered in this thesis are less than 0.01 pb at $\sqrt{s} = 13\,\text{TeV}$, around 10^{13} times lower than the total proton-proton inelastic cross section. The ATLAS experiment at the LHC provides unprecedented center of mass energy and detector resolution combined with the collected integrated luminosity necessary to perform these searches. Chapter III describes the experimental methods used in this thesis including an overview of the ATLAS experiment at the LHC. The hadronic final state reconstruction methods used in Chapters IV and V are described in detail.

The analysis described in Chapter IV is a search for evidence of the direct pair production of stops. Stops decay to neutralinos and top quarks ($\tilde{t} \rightarrow t + \tilde{\chi}_1^0$) resulting in an all-hadronic experimental signature of two top quarks and missing transverse momentum ($t\bar{t}$ + $E_{\mathrm{T}}^{\mathrm{miss}}$). This analysis has four signal regions targeting various topologies and kinematics for these decay products. My primary contribution to this analysis was estimation of the dominant Standard Model background, Z + jets, and validation of this background estimate. This search [10] detected no significant excess over the predicted Standard Model background and was able to exclude stop masses up to 1.25 TeV for neutralino ($\tilde{\chi}_1^0$) masses below 200 GeV. In combination with the other direct stop production searches [11, 12, 13] we have excluded much of the parameter space motivated by the hierarchy problem.

The analysis described in Chapter V is the first search for the dark meson sector of Stealth Dark Matter. Dark matter detection and collider experiments can have low sensitivity to this “stealth" model resulting in weak exclusion limits from reinterpretation of previous searches and precision measurements. Dark mesons are pair produced and then decay to top and bottom quarks with no intrinsic missing transverse momentum. The dominant decays of dark mesons for this all-hadronic search are *tbtb* and *tttb* with hadronic top quark decays. This results in an experimental signature of up to ten jets with four jets arising from *b*-hadrons. This search is in editorial review and the signal regions are blinded at the time of this writing. Although observed limits are not included in this chapter, the sensitivity for discovery or exclusion is shown based on the defined regions. My primary contribution to this search was the development of the signal regions and background estimation for these regions, including a data-driven estimate of the dominant background arising from multiple jets. The all-hadronic channel of this search is expected to exclude dark pion masses up to 500 GeV for 2 TeV dark rho mesons.

The two analysis described in this thesis use full ATLAS Run 2 data of 139 fb^{-1} corresponding to around 10^{16} inelastic proton-proton collisions. LHC Run 3 is now in progress and is projected to produce 250 fb^{-1} of proton-proton collisions at $\sqrt{s} =$ 13.6 TeV by its conclusion in 2025. [14] The High-Luminosity LHC (HL-LHC) [15] will increase collision rate and center of mass energy to allow collection of $3000 - 4000$ fb^{-1} of proton-proton collisions at $\sqrt{s} = 14\,\text{TeV}$. Chapter VI summarizes the results of this thesis and provide sensitivity projections at increased energy and integrated luminosity. Future searches for direct stop production and dark mesons will make use of higher center of mass energies, increased luminosity and improved analysis strategies to further contribute to our understanding of dark matter.

CHAPTER II

STANDARD MODEL PHENOMENOLOGY AND BEYOND

Our most comprehensive theory of fundamental interactions is the Standard Model (SM) of particle physics. This theory describes chiral fermion fields interacting under the strong, electromagnetic (EM), and weak forces. Standard Model masses are generated through coupling to the Higgs sector fields. Gravity is not included in the Standard Model and formulating a quantum theory of gravity remains an open problem in physics. All particles predicted by the Standard Model have been experimentally observed. Recent discoveries include the top quark observation by the CDF [16] and DØ [17] experiments at Fermilab in 1995 and a Higgs observation by the ATLAS [18] and CMS [19] experiments at CERN in 2012. Figure 1 provides a summary of the agreement between theory and ATLAS measurements for selected production cross sections.

Although measured interaction cross sections agree with Standard Model predictions for almost all known processes, there are important discrepancies which require beyond the Standard Model physics to explain. Over 80% of the matter in the universe has no observed Standard Model interactions and is best explained though the addition of new physics to the Standard Model. The Standard Model also does not allow neutrinos to be as massive, as observed by experiment. Massive neutrinos require extending the Standard Model with new physics but this subject is outside of the scope of this thesis. Experiments such as the recent CDF precision measurement [20] of the W boson mass show tension between experiment and Standard Model predictions.

Another challenge to the Standard Model is its conflict with the naturalness principle. The Standard Model hierarchy of scales requires an extreme fine tuning of

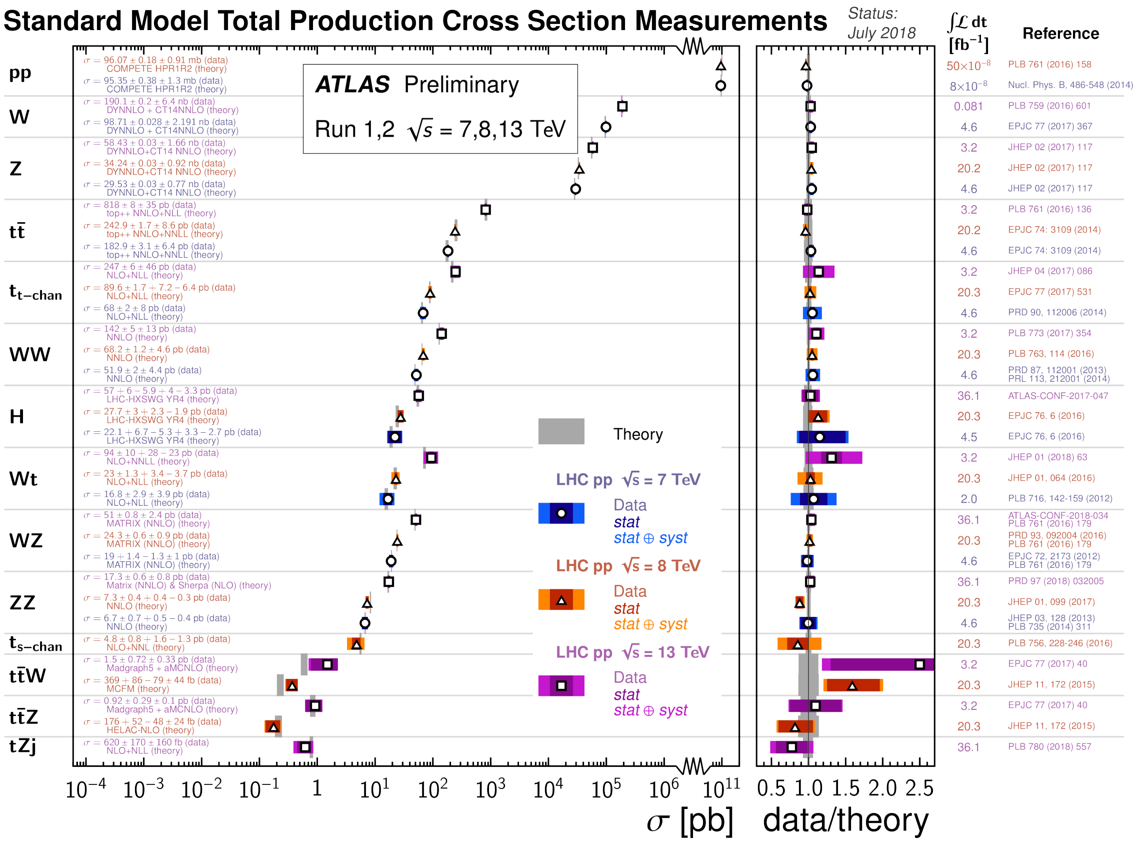

Figure 1. Summary of ATLAS cross section measurements compared to Standard Model predictions.

the Higgs bare mass to compensate for the quadratic sensitivity of Higgs mass loop corrections to the high energy cutoff sclae of the theory Λ_{UV} . If Λ_{UV} is taken to be the Planck scale around 10^{19} GeV, then this requires fine tuning by many orders of magnitude to obtain the observed Higgs mass near 125 GeV.

2.1 The Standard Model

2.1.1 Particles and Interactions

The Standard Model is a relativistic quantum field theory that describes particles as excitations of fermionic fields interacting through coupling to bosonic fields. Three generations of chiral fermions are observed with identical quantum numbers between generations except particle mass. The gauge symmetry group of the Standard Model is

$$SU(3)_C \times SU(2)_L \times U(1)_Y, \tag{2.1}$$

which reduces to $SU(3)_C \times U(1)_{EM}$ after electroweak symmetry breaking.

The strong force is carried by gluons which have interactions with quarks and self interactions as described by the $SU(3)_C$ gauge symmetry. The strong coupling of this non-Abelian symmetry is described in section 2.1.3. Electromagnetism retains a $U(1)_{EM}$ symmetry with a massless photon after symmetry breaking and has charge $Q = T_3 + Y$. Weak isospin, T_3, is a generator of $SU(2)_L$ and hypercharge, Y, is the generator of $U(1)_Y$. Table 1 shows the gauge quantum numbers of Standard Model fermions. Left handed fermions are $SU(2)$ doublets and right handed fermions are uncharged singlets under the weak interaction.

Table 1. Chiral fermion fields of the standard model and their gauge quantum numbers. The superscript i indicates fermion generation $e^i = (e^-, \mu, \tau)$, $u^i = (u, c, t)$, and $d^i = (d, s, b)$. Antiparticle fields are the charge conjugates of these fields.

Field	$SU(3)_C$	$SU(2)_{\mathrm{L}}$	$U(1)_{\mathrm{Y}}$ charge
$Q^i_L = \binom{u^i_L}{d^i_L}$	**3**	**2**	1/6
u^i_R	**3**	**1**	4/6
d^i_R	**3**	**1**	−2/6
$L^i_L = \binom{\nu^i_L}{e^i_L}$	**1**	**2**	−1/2
e^i_R	**1**	**1**	−1

The Higgs mechanism generates Standard Model particle masses and determines the weak boson masses from the weak coupling constants (g,g') and the vacuum expectation value. Fermion masses are specified by Yukawa couplings to the Higgs field which must be determined experimentally. The Standard Model fermion mass spectrum is shown in Figure 2. After spontaneous symmetry breaking, the spin-0 Higgs boson couples to all Standard Model particles.

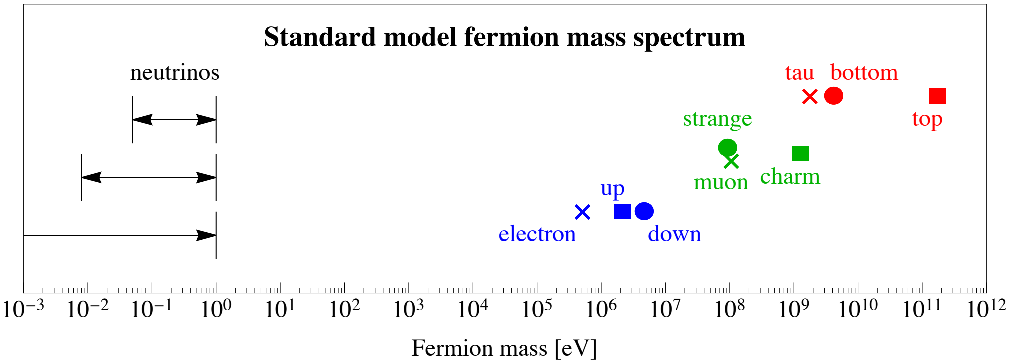

Figure 2. The observed fermion mass spectrum. The blue, green, and red markers correspond to generations I, II, and III. Figure from [21].

The complete Standard Model Lagrangian is

$$\mathcal{L} = \mathcal{L}_{gauge} + \mathcal{L}_{fermion} + \mathcal{L}_{Higgs} + \mathcal{L}_{Yukawa}, \tag{2.2}$$

where $\mathcal{L}_{gauge}$ described the gauge boson kinetic energies and self interactions and $\mathcal{L}_{fermion}$ described fermion kinetic energies and gauge interactions. The Higgs and Yukawa terms are described in the next section. Conservation of lepton (L) and baryon (B) number emerges as a global accidental symmetry

$$U(1)_B \times U(1)_e \times U(1)_\mu \times U(1)_\tau. \tag{2.3}$$

$U(1)_e \times U(1)_\mu \times U(1)_\tau$ is further broken by neutrino mass, but this is beyond the scope of this thesis. In the composite dark matter models described in section 2.3, dark baryon number can emerge as an accidental global symmetry that ensures stability of dark matter analogous to this Standard Model $U(1)_B$. The B and L symmetries are replaced with $B - L$ in the R-parity conserving supersymmetry models described in Section 2.2.

2.1.2 Electroweak Symmetry Breaking and the Higgs Mechanism

The Higgs mechanism can be incorporated into the Standard model by adding an isospin doublet of complex scalar fields ϕ with a potential

$$V(\phi) = \frac{1}{2}\mu^2 \phi^\dagger \phi + \frac{1}{4}\lambda(\phi^\dagger \phi)^2. \tag{2.4}$$

This defines the Higgs sector

$$\mathcal{L}_{Higgs} = (D_\mu \phi)^\dagger (D^\mu \phi) - V(\phi). \tag{2.5}$$

The parameters $\mu^2 < 0$ and $\lambda > 0$ result in minima at $|\phi| = \frac{\mu^2}{\lambda} = v$. Choosing a minimum gives $\phi_0 = \frac{1}{\sqrt{2}}\binom{0}{v}$. An excitation about this minimum provides the Higgs field

$$\phi = \frac{1}{\sqrt{2}} \begin{pmatrix} 0 \\ v + h(x) \end{pmatrix}. \tag{2.6}$$

The vacuum expectation value is experimentally determined to be ~ 246 GeV.

Chiral fermions cannot have mass terms of the form $m\psi\overline{\psi}$ and instead acquire mass through coupling to the Higgs field. This L_{Yukawa} term contains a contribution

$$\mathcal{L}_{Yukawa,f} = y_f \overline{\psi}_L \psi_R \phi \tag{2.7}$$

for each fermion term. After spontaneous symmetry breaking this provides a chiral mass term

$$m_f = y_f \frac{v}{\sqrt{2}} \tag{2.8}$$

and a coupling to the Higgs field proportional to m_f.

Spontaneous symmetry breaking of the Higgs doublet also provides mass terms for the electroweak gauge bosons. Requiring $SU(2)_L \times U(1)_Y$ invariance of the Higgs sector gives

$$\mathcal{L}_{Higgs} = |(\partial_\mu + igT_a W_\mu^a + ig'YB_\mu)\phi|^2 - V(\phi), \tag{2.9}$$

where g and g' are the electroweak couplings. After spontaneous symmetry breaking the electroweak W^a and B fields mix to form the weak $W^\pm$ and Z bosons. The weak bosons gain masses from coupling to v,

$$\begin{aligned} m_W &= \frac{1}{2} v g, \\ m_Z &= \frac{1}{2} v \sqrt{g^2 + g'^2}. \end{aligned} \tag{2.10}$$

The relative strength of the neutral and charged current interactions,

$$\rho = \left(\frac{m_W}{m_Z cos\theta_W}\right)^2, \tag{2.11}$$

is equal to 1.

The $O(4) \approx SU(2)_L \times SU(2)_R$ global symmetry of the Higgs multiplet (from the two complex fields in this formulation) is reduced to $SU(2)_{L+R}$ after spontaneous symmetry breaking. This accidental symmetry is broken in the Standard Model by gauging $U(1)_Y$ and by the asymmetry in Yukawa couplings between up type and down type fermions. The ρ parameter of Equation 2.11 is protected from radiative corrections by this custodial symmetry, it can be restored to an exact symmetry in the Higgs sector by taking the limit $g' \to 0$.

2.1.3 Quantum Chromodynamics

Quantum Chromodynamics (QCD) has an $SU(3)_C$ gauge symmetry group with 8 generators corresponding to eight mediating gluon fields. As a non-Abelian symmetry QCD allows gluon-gluon interactions which causes an anti-screening effect on the quark charge. QCD is strongly coupled ($\alpha_s \sim 1$) for interactions with low momentum transfer Q which prevents a perturbative treatment and results in confinement. Quarks are confined as meson (quark-antiquark) or baryon (three quark) color neutral bound states. The running of α_s causes QCD to become weaker at large and allows quarks to become asymptotically free. This is in contrast to the running of electromagnetism where α becomes smaller at large Q due to charge screening.

The analyses described in this thesis consider final states which consist of top and bottom quarks, with or without missing energy. The high mass of the top quark allows it to rapidly decay to a W boson and b quark before it can hadronize. These analyses consider all-hadronic channels where the W bosons decay to quarks. Quark final states shower and then hadronize into sprays of mesons and baryons which are detected as calorimeter energy showers as described in Chapter III. Event reconstruction of this complex final state signature is a major part of my contribution to these analyses.

2.1.4 Evidence for Dark Matter

Astrophysical observations provide strong evidence for the existence of a large amount of non-baryonic matter. This dark matter is detected through its gravitational impact on luminous matter and also has a critical role in cosmological models. Evidence for the existence of dark matter includes:

1. Galaxy rotation speeds are in excess of those expected from the observed baryonic matter distribution [3].
2. Gravitational lensing around galaxy clusters in excess of that of the luminous matter [2].
3. Anisotropies in the Cosmic Microwave Background (CMB) [1].

Attempts to explain these observations through modified gravity such as Modified Newtonian Dynamics are incompatible with observations such the Bullet Cluster [4] and do not account for the structure of the CMB. Standard Model explanations of non-luminous matter have been strongly excluded by experiments such as [22]. The hypothesis of gravitationally interacting particle dark matter is the most consistent explanation for these measurements. Weakly interacting massive particle (WIMP) dark matter with electroweak-scale masses and scattering cross sections is well motivated by cosmological models and could be experimentally accessible. Dark matter must be (very close to) electrically neutral, stable on time scales much longer than the universe lifetime, cold (non-relativistic) and have the correct relic abundance based on its interactions with the Standard Model.

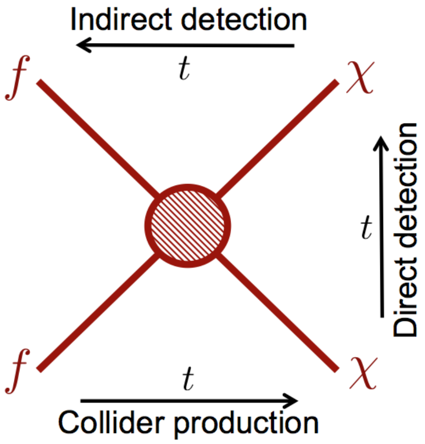

Figure 3. Collider searches look for the production of dark matter signals from Standard Model scattering while direct searches look for evidence of new particles such as WIMPs scattering from Standard Model particles. Indirect detection experiments look for Standard Model particles produced from dark matter annihilation.

Dark matter models are tested experimentally using three complementary approaches: direct detection, indirect detection, and collider production. These approaches search for dark matter using possible interactions between the Standard Model and dark matter particles as shown in Figure 3. Direct detection experiments search for signals from the dark matter flux interacting with detector active material. Indirect detection uses astrophysical measurements to look for an excess of Standard Model particles resulting from dark matter matter annihilation or decay. Collider production looks for the creation of dark matter or other particles from a new dark sector. In these experiments dark matter particle could be produced experimentally and escape the detector as missing energy. Collider searches can also look for mediators or other dark sector signals.

Dark matter direction detection experiments have constrained the WIMP interaction cross section of dark matter with nucleons as show in Figure 4. The models described in this thesis could produce dark matter signals at a large enough cross section for collider detection while evading direct detection from experimental bounds.

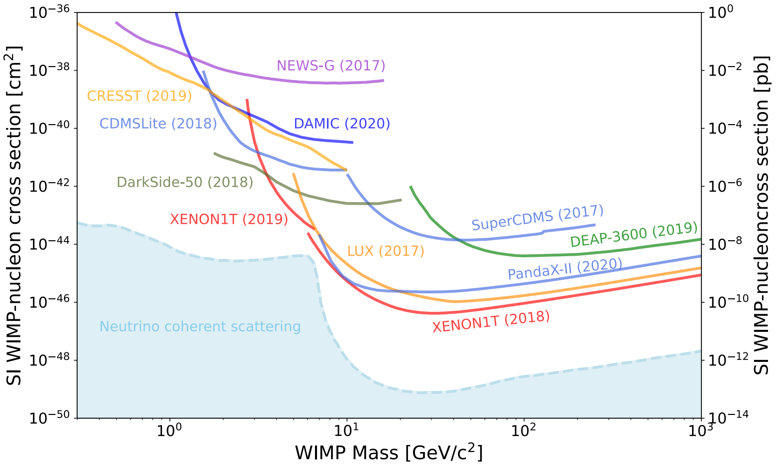

Figure 4. Upper limits on nucleon scattering for WIMP dark matter as a function of mass. Figure from [23].

2.2 Supersymmetry

Supersymmetry (SUSY) extends the Standard Model with a new fundamental symmetry between bosonic and fermionic states. Describing this symmetry by an operator Q gives the transformations

$$Q|\text{fermion}\rangle = |\text{boson}\rangle, \tag{2.12}$$

$$Q|\text{boson}\rangle = |\text{fermion}\rangle. \tag{2.13}$$

For each fermion (boson) there is a superpartner boson (fermion) in the same gauge representation. This operator carries spin $\frac{1}{2}$ which allows this symmetry to extend the space-time symmetry group of the Standard Model[1]. Exact supersymmetry requires particles and their superpartners to have identical mass in addition to identical charges under the gauge symmetries. To allow for mass differences between particle and their superpartners, supersymmetry must be broken. Without this symmetry breaking superpartner particles would already have been observed.

The Minimal Supersymmetric Standard Model (MSSM) extends the Standard Model with the minimal number of new particles and interactions consistent with experimental observations and a supersymmetric theory. This section follows the description of the MSSM given in [5]. Fermions and their superpartness form chiral supermultiplets as shown in Table 2. The superpartners of particles are *sparticles* and fermion partners are *squarks* and *sleptons*. The superpartners of the left and right handed top quarks, $\tilde{t}_L$, $\tilde{t}_R$, mix to form mass eigenstates $\tilde{t}_1$, $\tilde{t}_2$. The 1 subscript indicates the lightest sparticles of the mass eigenstates. This sparticle is referred to as the stop and labeled $\tilde{t}$ in this thesis. Multiple Higgses with spin-$\frac{1}{2}$ *Higgsino* partners are required for the MSSM and also form chiral supermultiplets.

---

[1] Adding additional space-time symmetries to the Standard Model is otherwise prohibited [24].

Gauge bosons and their *gaugino* superpartners form vector supermultiplets as shown in Table 3. The two neutral Higgsinos and two neutral gauginos mix to form neutralino mass eigenstates. The lightest neutralino is the $\widetilde{\chi}^0_1$ sparticle.

Table 2. The chiral supermultiplets of the MSSM. Table from [5].

Names		spin 0	spin 1/2	$SU(3)_C$, $SU(2)_L$, $U(1)_Y$
squarks, quarks	Q	$(\widetilde{u}_L\ \ \widetilde{d}_L)$	$(u_L\ \ d_L)$	$(\ \mathbf{3},\ \mathbf{2}\ ,\ \frac{1}{6})$
(×3 families)	$\overline{u}$	$\widetilde{u}^*_R$	$u^\dagger_R$	$(\ \overline{\mathbf{3}},\ \mathbf{1},\ -\frac{2}{3})$
	$\overline{d}$	$\widetilde{d}^*_R$	$d^\dagger_R$	$(\ \overline{\mathbf{3}},\ \mathbf{1},\ \frac{1}{3})$
sleptons, leptons	L	$(\widetilde{\nu}\ \ \widetilde{e}_L)$	$(\nu\ \ e_L)$	$(\ \mathbf{1},\ \mathbf{2}\ ,\ -\frac{1}{2})$
(×3 families)	$\overline{e}$	$\widetilde{e}^*_R$	$e^\dagger_R$	$(\ \mathbf{1},\ \mathbf{1},\ 1)$
Higgs, higgsinos	H_u	$(H^+_u\ \ H^0_u)$	$(\widetilde{H}^+_u\ \ \widetilde{H}^0_u)$	$(\ \mathbf{1},\ \mathbf{2}\ ,\ +\frac{1}{2})$
	H_d	$(H^0_d\ \ H^-_d)$	$(\widetilde{H}^0_d\ \ \widetilde{H}^-_d)$	$(\ \mathbf{1},\ \mathbf{2}\ ,\ -\frac{1}{2})$

Table 3. The vector supermultiplets of the MSSM. Table from [5].

Names	spin 1/2	spin 1	$SU(3)_C$, $SU(2)_L$, $U(1)_Y$
gluino, gluon	$\widetilde{g}$	g	$(\ \mathbf{8},\ \mathbf{1}\ ,\ 0)$
winos, W bosons	$\widetilde{W}^\pm\ \ \widetilde{W}^0$	$W^\pm\ \ W^0$	$(\ \mathbf{1},\ \mathbf{3}\ ,\ 0)$
bino, B boson	$\widetilde{B}^0$	B^0	$(\ \mathbf{1},\ \mathbf{1}\ ,\ 0)$

A supersymmetric theory can exactly solve the gauge hierarchy problem by canceling out the quadratically divergent terms through the introduction of compensating loops. Higgs mass loop corrections include terms for all particles that couple to the Higgs. For fermion loops this is given by

$$\Delta m_H^2 = -\frac{|\lambda_f|^2}{8\pi^2}\Lambda_{UV}^2 + \dots \tag{2.14}$$

and for scalars the corrections have the opposite sign. The exact cancellation of these terms is provided by the compensating loops shown in Figure 5.

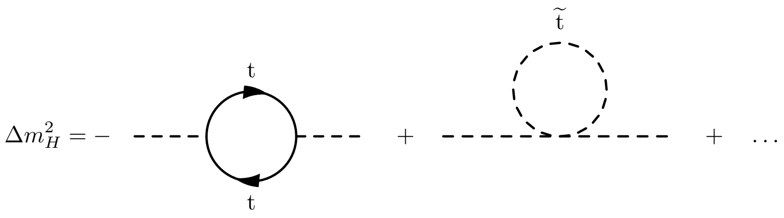

Figure 5. Higgs mass loop corrections from the top quark and its superpartner.

Supersymmetry is spontaneously broken in MSSM with an L_{soft} term added to the supersymetric Lagrangian to break the mass degeneracy,

$$\mathcal{L} = \mathcal{L}_{SUSY} + \mathcal{L}_{soft}. \tag{2.15}$$

This “soft" supersymmetry breaking allows the for cancellation of the quadratic sensitivity of the Higgs mass correction to Λ_{UV}, but large mass differences between superpartners still requires some fine tuning to correct. With this term, the ultraviolet sensitivity of the Higgs mass loop corrections becomes logarithmic

$$\Delta m_H^2 = m_{soft}^2 (\frac{\lambda}{16\pi^2} log(\Lambda_{UV}/m_{soft} + \ldots). \tag{2.16}$$

m_{soft} is the largest mass scale in the $\mathcal{L}_{soft}$ term, λ is an effective coupling, and the ellipsis indicates terms which depend on Λ_{UV} by powers of logerithms at most. In the limit $m_{soft} \to 0$ the exact cancellation of unbroken SUSY is restored. The m_{soft} mass determines the mass splitting of particles and their superpartness and naturalness would require this term to not greatly exceed the top quark mass.

The MSSM introduces many free parameters into the model as masses, phases, and mixing angles. The phenomenological MSSM (pMSSM) introduces phenomenological constraints such as R-parity, the neutralino is the Lightest Supersymmetric Particle, no new CP-violation and no new flavor changing neural currents. This reduces the number of parameters of the model from 105 to 19.

For many supersymmetric models the lepton and baryon number conservation of the Standard Model is generalized to R-parity. R-parity,

$$P_R = (-1)^{3(B-L)+2s}, \tag{2.17}$$

is even for Standard Model particles and odd for sparticles. R-parity conserving supersymmetry models, such as the ones considered in this thesis, require sparticles to be produced in pairs with their decay products eventually reaching a stable Lightest Supersymmetric Particle. In the pMSSM, this particle is the lightest neutralino ($\tilde{\chi}_1^0$) and is neutral, stable and with correct abundance to be a dark matter candidate particle.

Chapter IV describes a search for direct pair production of stops with an all-hadronic final state. Stops are produced through gluon-gluon fusion in LHC proton-proton collisions and then each decay to top plus neutralino final states $\tilde{t} \rightarrow t + \tilde{\chi}_1^0$ in this model. The leading stop decay diagram for the signal regions that this thesis focuses on are shown in Figure 6. In this final state the event signature is a top quark pair and missing transverse energy ($t\bar{t} + E_{\mathrm{T}}^{\mathrm{miss}}$).

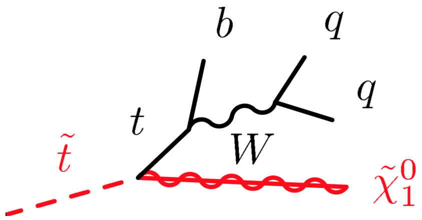

Figure 6. A Feynman diagram of a stop decay to a top and neutralino. In the all-hadronic channel the W boson decays to two quarks.

2.3 The dark meson sector of Stealth Dark Matter

Bound states of new strongly coupled sectors [8] [9] can generate viable dark matter candidate particles while avoiding detection from previous search strategies. Stealth Dark Matter [7] proposes a composite baryonic scalar of an $SU(N_D)$ strongly coupled theory with constituent fermions that transform as vector-like representations of the electroweak group. Stability is guaranteed from an accidental $U(1)_{\text{dark baryon}}$ symmetry which emerges form the model. Assuming the dark fermion interactions obey a global $SU(2)$ custodial symmetry the lightest dark baryon is electrically neutral and removes interactions such as the neutral weak current and charge radius interactions. Dark matter detection and collider experiments can have low sensitivity to this “stealth" model resulting in weak exclusion limits from reinterpretation of previous searches and precision measurements.

The dark meson sector of Stealth Dark Matter developed in [6] describes the phenomenology of composite states which could be produced at the LHC. The vector-like mass of the dark fermions prevent these models from being constrained by electroweak or Higgs coupling measurement. Previous LHC beyond the standard model searches typically require large missing energy, target single-production or are optimized for high mass resonances but have weak sensitivity to the mass regime relevant for dark mesons.

The new dark sector contains mesons and baryons analogous to those of QCD but with a confinement scale near or above the electroweak scale. The phenomenology includes at least one triplet each of pseudoscalar $(\pi_D^{\pm}, \pi_D^0)$ and vector $(\rho_D^{\pm}, \rho_D^0)$ mesons. Dark fermions are charged under the electroweak and the $SU(N_D)$ dark color symmetries. Interactions fo the dark fermions with the Higgs sector breaks the dark sector global symmetry and allows dark mesons to decay into Standard Model states. The dark meson Lagrangian,

$$\mathcal{L}_{dark\ sector} = \mathcal{L}_{kinetic} + \mathcal{L}_{mass} + \mathcal{L}_{\pi_D,\rho_D} + \mathcal{L}_{kinetic\ mixing} + \mathcal{L}_{decay}, \tag{2.18}$$

includes kinetic and mass terms for the dark pion and dark rho, dark pion to dark rho coupling, kinetic mixing of the dark rho with electroweak gauge bosons, and dark pion decay to Standard Model particles. In this dark sector the Higgs custodial symmetry is preserved and is identified with the $SU(2)$ dark flavor symmetry.

Signal points in the dark meson parameter space are parameterized by the dark pion mass, m_{π_D}, and ratio of the dark pion and dark rho masses,

$$\eta = m_{\pi_D}/m_{\rho_D}. \tag{2.19}$$

For models with $\eta < 0.5$, the decay $\rho_D^{\pm} \to \pi_D^{\pm}\pi_D^{\mp,0}$ has a branching fraction of nearly 1.0, while for models with $\eta > 0.5$ this decay is kinematically forbidden and the ρ_D thus decays to pairs of Standard Model fermions.

The primary portal from the Standard Model to the dark sector is provided by kinetic mixing of electroweak gauge bosons with dark rho mesons.

$$\mathcal{L}_{kinetic\ mixing} = -\frac{\epsilon}{2}\rho^a_{D,\mu\nu}F^{a\mu\nu}. \tag{2.20}$$

Two mixing models are possible depending on whether $SU(2)_L$ or just the $U(1)_Y$ symmetry is gauged after spontaneous symmetry breaking. These models are referred to as $SU(2)_L$ and $SU(2)_R$ because the dark sector respects the full $SU(2)_{L+R}$ global symmetry. In the $SU(2)_L$ model, the dark rhos can mix with the full W boson triplet ($F^{a\mu\nu} = W^{a\mu\nu}$) while in the $SU(2)_R$ model only mixing with the hypercharge gauge boson B ($F^{\mu\nu} = B^{\mu\nu}$) is possible. The major phenomenological impact is that the $SU(2)_R$ model has a reduced production cross section and cannot produce charged ρ_D mesons.

The coupling between dark rhos and dark pions,

$$\mathcal{L}_{\rho_D,\pi_D} = -g_{\rho_D\pi_D\pi_D}f^{abc}\rho^a_\mu\pi^b_D D^\mu\pi^c_D, \tag{2.21}$$

is analogous to the $g_{\rho\pi\pi}$ coupling of QCD. The strength of this coupling is estimated by naive dimensional analysis to be

$$g_{\rho_D\pi_D\pi_D} \approx \frac{4\pi}{\sqrt{N_D}}. \tag{2.22}$$

In the Stealth Dark Matter model, the number of dark colors, N_D, is fixed at 4. The phenomenological consequences of a larger N_D are minor as long as this value is not excessively large. In addition to resonant pair production through the dark rho, dark pions can be produced through Drell-Yan production. Resonant production dominates dark pion production accounts for almost the entire parameter space of the dark mesons model of interest to this work. Figure 7 shows Feynman diagrams illustrating these mechanisms.

Dark pion decays to Standard Model fermions are described by a decay term,

$$\begin{aligned}\mathcal{L}_{decay} = \frac{\sqrt{2}}{v_\pi}\Big[&\pi_D^+\overline{\psi}_u(m_dP_R - m_uP_L)\psi_d + \\ &\pi_D^-\overline{\psi}_d(m_dP_L - m_uP_R)\psi_u + \\ &\frac{i}{\sqrt{2}}\pi_D^0(m_u\overline{\psi}_u\gamma_5\psi_u - m_d\overline{\psi}_d\gamma_5\psi_d)\Big],\end{aligned} \tag{2.23}$$

where ϕ_u, ϕ_d are Standard Model fermions and $1/v_\pi$ sets the scale of the operators. Models with decays to Standard Model bosons (gaugephilic) are possible but not considered in this thesis. Dark pions decay promptly and provide an all Standard Model detector signature with no intrinsic missing transverse momentum.

Chapter V describes an all-hadronic search for dark pions pair produced at the LHC. The signal models considered are described in additional detail in this chapter. This search targets a kinematic region where dark pion decays to top and bottom quarks are dominant.

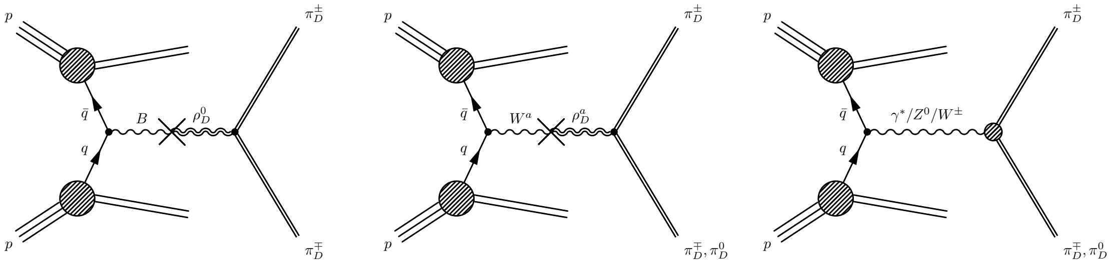

Figure 7. Dark pion production mechanisms. The dominant production mechanism is through kinetic mixing of a dark rho with the B (left) or W (middle) fields. Drell-Yan pair production of dark pions is also possible as shown on the right.

CHAPTER III

ATLAS AND THE LHC

The analyses described in this thesis use the full LHC Run 2 data set of proton-proton collisions collected at $\sqrt{s} = 13$ TeV with the ATLAS detector. Run 2 data collection took place from 2015 to 2018, in this period 156 fb^{-1} were delivered to ATLAS out of which 139 fb^{-1} were declared good for physics. The direct stop search described in Chapter IV extends a previous search from 36.2 fb^{-1} to 139 fb^{-1} and makes additional improvements to the analysis strategy. The dark meson search described in Chapter V is the first search for its final state and also uses full Run 2 data. Run 3 started in 2022 with collisions at $\sqrt{s} = 13.6$ TeV and integrated luminosity as high as 250 fb^{-1} is targeted [14]. Run 3 projections for a future dark meson analysis are described in Chapter VI.

This chapter describes the LHC beamline, the ATLAS detector, and the reconstruction of detector signals as physics objects for analyses. Specific object definitions and discriminating variables are described in the analysis chapters of thesis.

3.1 The Large Hadron Collider

The Large Hadron Collider (LHC) [25] is a super-conducting hadron collider located at the CERN facility near Geneva, Switzerland. The two counter-rotating beams of proton (and heavy ion in some cases) bunches are accelerated to 6.5 TeV and collided at the four interaction points illustrated in Figure 8. Two general purpose, ATLAS and CMS, and two more specialized experiments, LHCb and ALICE, are located at these points. Collisions occur at the interaction points up to every 25 ns during operation with each LHC bunch containing around 10^{11} protons.

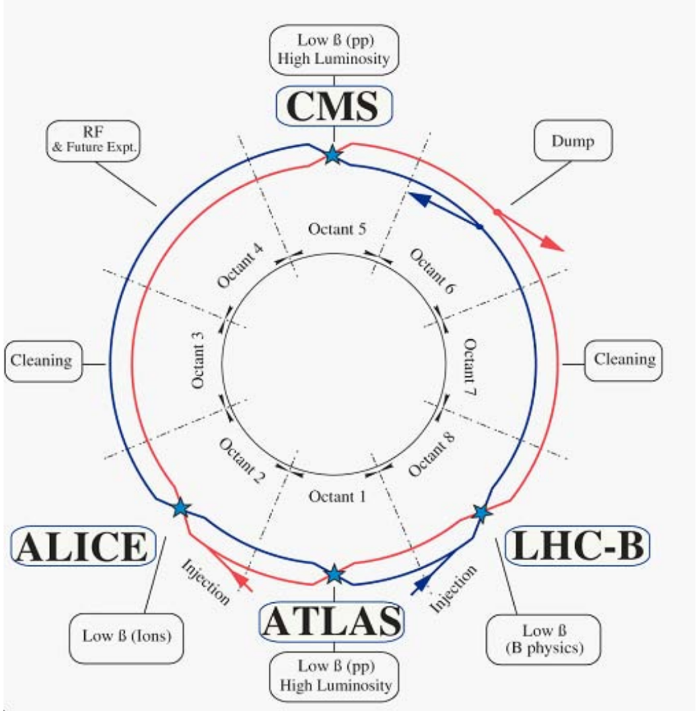

Figure 8. The four LHC interaction points and their experiments. The betatron factor β is a measure of beam size. Figure from [25].

The LHC is installed in the 26.7 kmLarge Electron Positron (LEP) collider tunnel. This tunnel was repurposed for the LHC and was originally designed with eight curved and eight linear segments for e^+e^- acceleration in the linear segments. The LHC beamline is kept at ultra high vacuum through the combination of a cryogenic getter coating and ion getter pumps.

LHC protons are accelerated through multiple stages [26] to reach a collision energy of $\sqrt{s} = 6.5$ TeV. Figure 9 shows the CERN LHC acceleration complex and experiments. First, the protons are ionized and extracted from hydrogen gas using a Duoplasmatron source and then accelerated to 50 MeV using the Linac2 injector chain. Next the protons reach the 157 m diameter Proton Synchrotron Booster (PSB) where they are accelerated to 1.4 GeV prior to their transfer the 628 m diameter Proton Synchrotron (PS). The PS accelerates the protons to 25 GeV and additionally

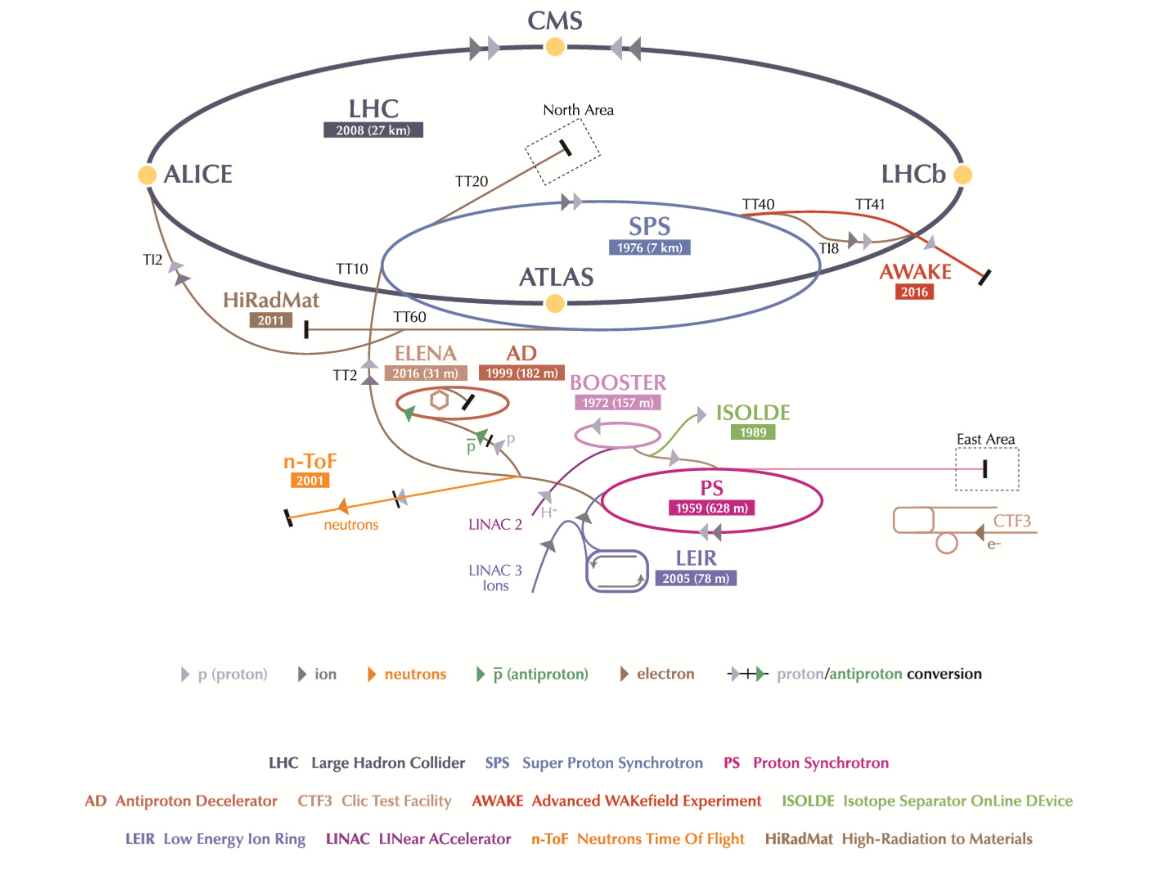

Figure 9. LHC protons are accelerated through multiple stages to reach a collision energy of 6.5 TeV [26].

bunches them into the beam structure used for LHC collisions. Last, the 7 km Super Proton Synchrotron (SPS) accelerates these bunches up to 450 GeV, splits them into two beams, and delivers these to the LHC injection points. The SPS takes around 4 minutes to fill the LHC ring with 12 cycles of SPS fills. Once a fill is complete the 450 GeV protons bunches are accelerated up to their final energy. The LHC buckets are grouped into bunch trains with an optimized pattern of filled and empty buckets with around 3600 bunches per beam.

The LHC uses RF cavities for beam acceleration, dipole magnets to bend the beam along the ring, quadrupole magnets for confining/focusing, and higher order multipoles for beam shaping. The superconducting RF cavities are frequency matched to the rotating bunches in order to slow down the fastest protons in the bunch and speed up the slowest. During acceleration the RF cavity frequency is increased to take the bunches from 450 GeV to 6.5 TeV.

LHC dipole magnets shown in Figure 10 supply opposite polarity fields to the two beam pipes to allow same sign protons beams to circulate in opposite directions. This novel design allows the beam pipes to share mechanical structure to fit within the LEP tunnel. These 8-9 T magnets deflect the 6.5 TeV proton beams along the LHC bending sections. To achieve this field strength the 15 m superconducting magnets use NbTi Rutherford wires cooled to 1.9 K with liquid He.

At the interaction points, the counter-rotating beams are focused to overlap and produce collisions at a rate determined by the total scattering cross section times the instantaneous luminosity,

$$\frac{dN_{event}}{dt} = \sigma\mathcal{L}. \tag{3.1}$$

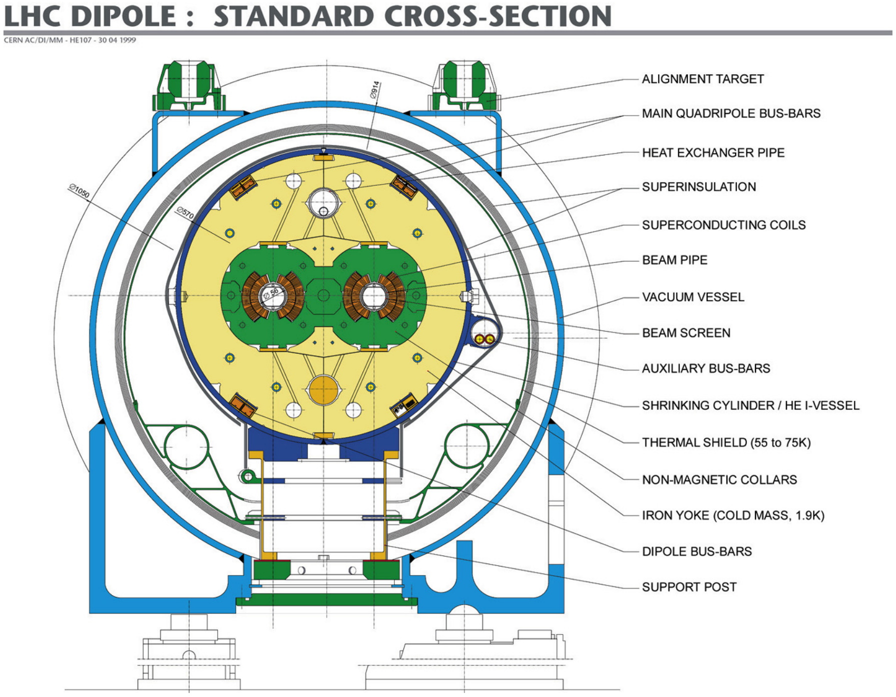

Figure 10. LHC dipoles provide same direction bending for counter rotating proton beams. Figure from [25].

The total production cross section for $p{-}p$ collisions at $\sqrt{s} = 13$ TeV is around 78 mb. With the Gaussian beam shape approximation the luminosity can be specified as

$$\mathcal{L} = \frac{N^2 N_b f}{4\pi\sigma_x\sigma_y} S. \tag{3.2}$$

$\mathcal{L}$ depends on the number of particle per bunch N, the number of bunches N_b, the bunch frequency f, a geometric factor S, and the bunch sizes σ_x, σ_y.

The design luminosity of the LHC is $\mathcal{L} = 10^{34}$ cm^{-2} s^{-1} and a peak luminosity of $2{\times}10^{34}$ cm^{-2} s^{-1} was reached in Run 2. High instantaneous luminosity allows increased data collection for rare processes, but also increases pileup and requires more restrictive triggering to meet the data recording limit.

ATLAS luminosity varies depending on machine conditions and is measured to provide integrated luminosity and a systematic uncertainty on this measurement for periods of data taking. During Run 2 ATLAS recorded $147\,\mathrm{fb}^{-1}$ and $139\,\mathrm{fb}^{-1}$ were declared good for physics. These events belong to luminosity blocks which meet the standard data quality requirements corresponding to the "all-good" good run list (GRL). Figure 11 shows the total integrated luminosity delivered to ATLAS and declared good for physics.

ATLAS uses multiple detectors and algorithms to measure luminosity [27] with the primary measurement provided by the LUCID-2 detector [28]. This detector uses thin quartz windows on photo-multiplier tubes as a Cherenkov medium for detection of hits and integrated signal. LHC luminosity decays over a physics run, primarily due to particle collisions, resulting in a variable collision rate for data taking. To reduce collision rates at the start of a fill, the LHC luminosity is intentionally lowered by adjusting machine parameters using a leveling strategy as shown in Figure 11 (right).

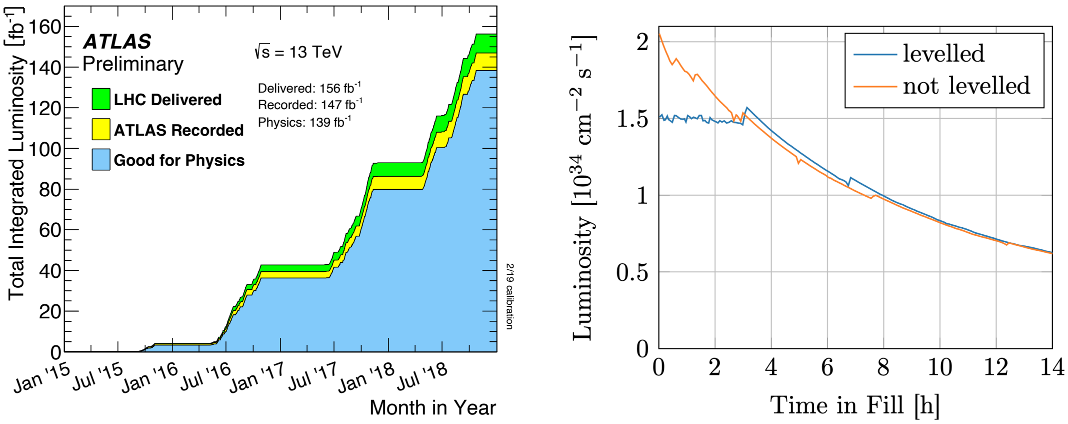

Figure 11. The LHC delivered 156 fb^{-1} and ATLAS declared 139 fb^{-1} good for physics during Run 2 (left) [29]. Leveling is used to lower ATLAS luminosity at the start of LHC fills (right). [30]

Typical LHC bunch crossings have many hard proton-proton interactions which cause a large background of jets for the low cross section processes of interest. This number of interactions per bunch crossing, μ, scales with instantaneous luminosity and creates a background of jets called pileup. This background must be accounted for when reconstructing physics objects. Pileup profiles vary by run year as shown in Figure 12 with an average μ value of 33.7 for Run 2. Studies of discriminating variable stability to pileup are included in Appendix A.

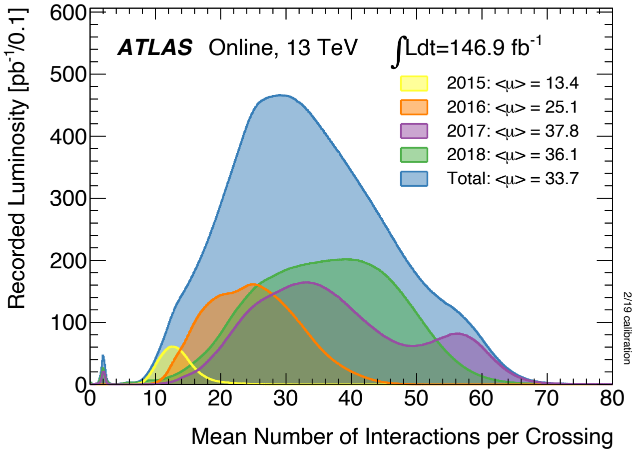

Figure 12. The mean number of interactions per crossing during Run 2. [31]

3.2 The ATLAS detector

ATLAS is a general-purpose detector designed to detect and measure scattering products from LHC collisions. ATLAS has a cylindrical geometry with mirror symmetry in $\hat{z}$ direction and multiple detector subsystems embedded in magnets, the cryostat, cables, and support superstructure as shown in figure 13. The closest detector to the interaction point is the the Inner Detector (ID) which tracks charged particles with minimal absorption. Surrounding the inner detector are multiple

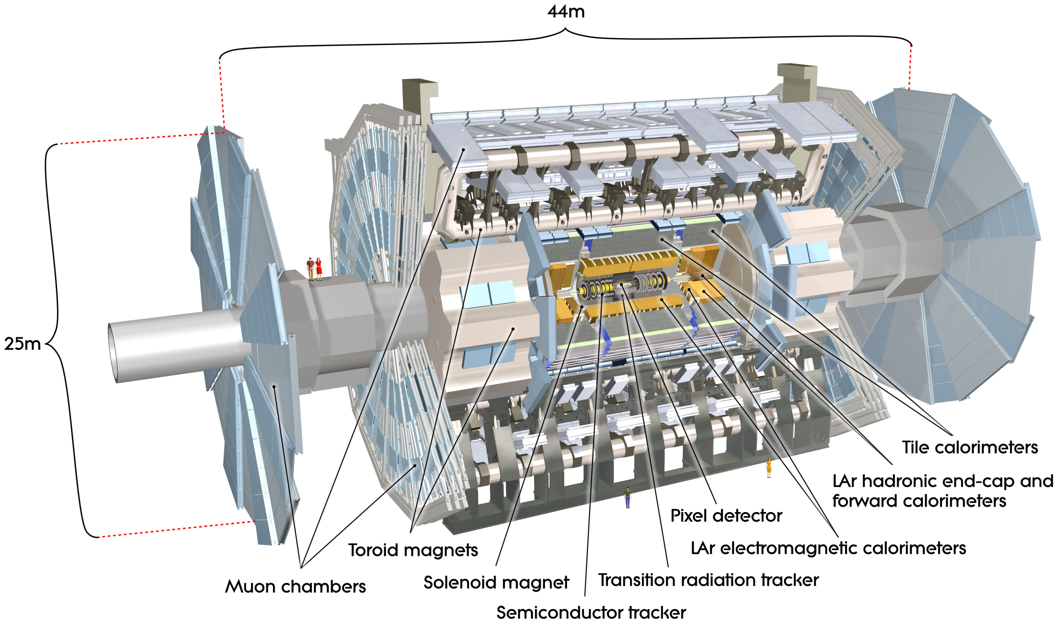

Figure 13. Illustration of the ATLAS detector and subsystems. Figure from [32].

calorimeters systems which absorb and measure all Standard Model particles except muons and neutrinos. ATLAS has a Hermetic solid angle coverage of nearly 4π to allow invisible particles to be inferred through momentum imbalance measurements. The major ATLAS design requirement for detector resolution are summarized in Table 4

Table 4. Resolution requirements of the ATLAS detector. The units for E and p_T are GeV. Table from [32].

Detector component	Required resolution	η coverage	
		Measurement	Trigger
Tracking	$\sigma_{p_T}/p_T = 0.05\%\ p_T \oplus 1\%$	± 2.5	
EM calorimetry	$\sigma_E/E = 10\%\ /\sqrt{E} \oplus 0.7\%$	± 3.2	± 2.5
Hadronic calorimetry	$\sigma_E/E = 50\%/\sqrt{E} \oplus 3\%$ $\sigma_E/E = 100\%/\sqrt{E} \oplus 10\%$	± 3.2 $3.1 < \lvert\eta\rvert < 4.9$	± 3.2 $3.1 < \lvert\eta\rvert < 4.9$
Muon spectrometer	$\sigma_{p_T}/p_T = 10\%$ at $p_T = 1$ TeV	± 2.7	± 2.4

ATLAS uses right-handed Cartesian coordinates system with the origin at the interaction point, $\hat{y}$ pointed up, $\hat{x}$ pointed toward the center of the LHC and $\hat{z}$ pointed along the beam line. This corresponds to spherical polar coordinates with ϕ in the transverse (x-y) plane and θ specifying the angle from the z-axis. To describe collision products and detector coverage this system is transformed into pseudorapidity polar coordinates in which the spherical polar angle θ is replaced with η = - ln(tan(θ/2)). Transverse coordinates such as transverse momentum ($\mathrm{p_T}$) and transverse missing energy ($E_{\mathrm{T}}^{\mathrm{miss}}$) refer to the x-y plane. Pseudorapidity approximates rapidity for particles with $\mathrm{p_T}$ large compared to their mass. The Lorentz boost invariance of rapidity differences allows angles in η-ϕ to be compared for any longitudinal event boost. Distances in η-ϕ space are used a distance metric for physics objects with $\Delta R = \sqrt{\Delta\phi^2 + \Delta\eta^2}$.

ATLAS uses a combination of solenoid and toroidal superconducting magnet systems to provide a strong bending field throughout the detector. The four magnet systems are illustrated in Figure 14. The barrel thin superconducting solenoid magnet surrounds the ID and provides a magnetic field of up to 2 T with minimal material placed in front of the LAr calorimeter. The Barrel and Endcap toroidal magnets provide a field of up 3.5 T covering $|\eta| < 2.7$. These air-core toroidal magnets are located between the outer calorimeters and the muon chambers.

3.2.1 Particle Tracking with the Inner Detector

The Inner Detector (ID) [33] is the closest detector to the interaction point, it extends to $|z| = 3.512$ m, a radius of 1.15 m, and covers $|\eta| < 2.5$. Figure 15 shows the ID subdector systems and η coverage. This detector records charged particle hits

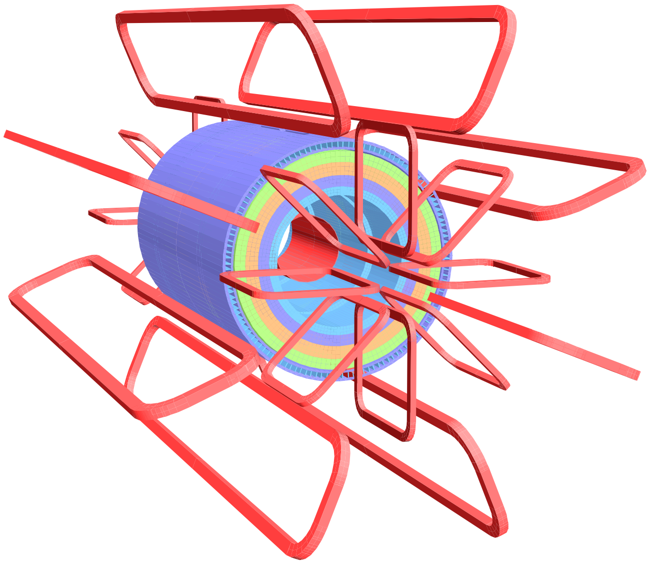

Figure 14. The ATLAS magnet systems (red) provide 2 T in the barrel solenoid and up to 3.5 T in the barrel toroid and endcap toroid regions. Figure from [32].

using the Pixel, Semiconductor Tracker (SCT) and Transition Radiation Tracker (TRT) detectors for the purpose of reconstructing particle trajectories in the ID. High spatial resolution is provided by the Pixel and SCT detectors while the TRT provide additional hits at lower granularity. The ID is immersed in field of 2 T from the barrel solenoid to bend charged particles trajectories with a radius proportional to $\mathrm{p_T^{-1}}$.

The Pixel detector surrounds the ATLAS Interaction Point and provides high spatial resolution particle tracking. This detector consists of silicon wafer elements, each with a grid of semiconductor sensor pixels of 50 µm × 400-600 µm which detect the passage of charged particles through electron-hole pair production. In the barrel region, these sensors are stacked with overlapping edges into four layers. The sensors are tilted with a turbine layout for overlapping coverage in ϕ as shown in Figure 16. In the endcap regions of the Pixel detector there are 3 disk layers to provide coverage out to $|\eta| < 2.5$.

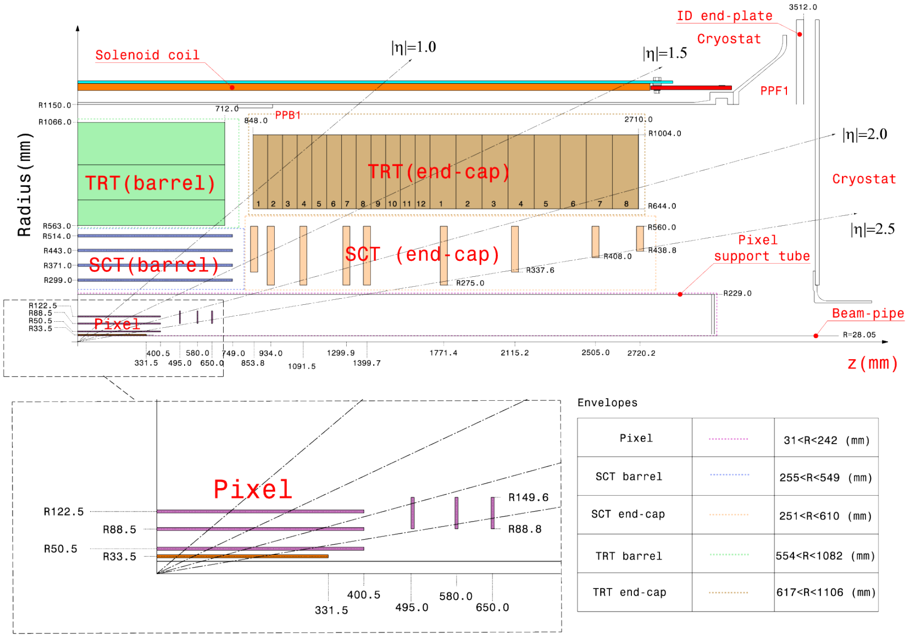

Envelopes

Pixel	⋯	31<R<242 (mm)
SCT barrel	⋯	255<R<549 (mm)
SCT end-cap	⋯	251<R<610 (mm)
TRT barrel	⋯	554<R<1082 (mm)
TRT end-cap	⋯	617<R<1106 (mm)

Figure 15. The ATLAS inner detector with Pixel detector detail. Figure from [34].

The Insertable B Layer (IBL) [35] was installed during Long Shutdown 1 before Run 2. This upgrade replaced the ID beam pipe and added a new detector layer at 33 mm radius with 50 × 250 µm pixels. The new layer improves displaced vertex discrimination for B-meson identification and pile-up rejection. Identification of displaced vertices through tracing tracks from detector hits to their originating vertex is critical to identification of bottom and charm decays as well as the suppression of background pile-up collisions.

Surrounding the Pixel detector, the SCT uses silicon sensors arranged in a microstrip geometry to cover a large area. The microstrip detectors are mounted in pairs with a 40 mrad stereo angle between them to allow track resolution in $\hat{z}$. The SCT has four cylindrical layers in the barrel region and 9 disks in each end cap region to cover $|\eta| < 2.5$. The resolution of this detector is 16 µm in $R\phi$ and 580 µm in z.

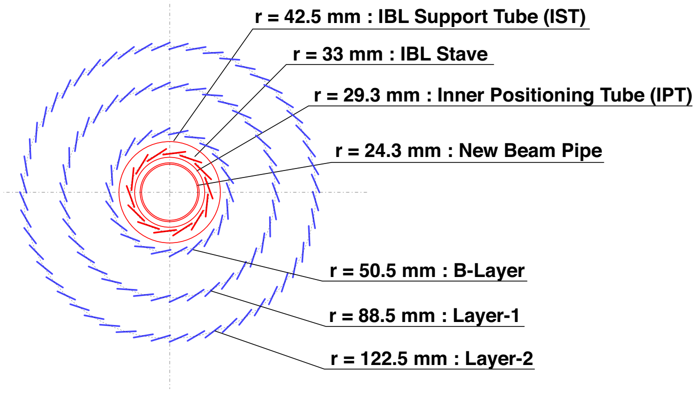

Figure 16. Overlapping coverage is provided by the tilted Pixel detector sensors. The IBL layer was added for Run 2. Figure from [36].

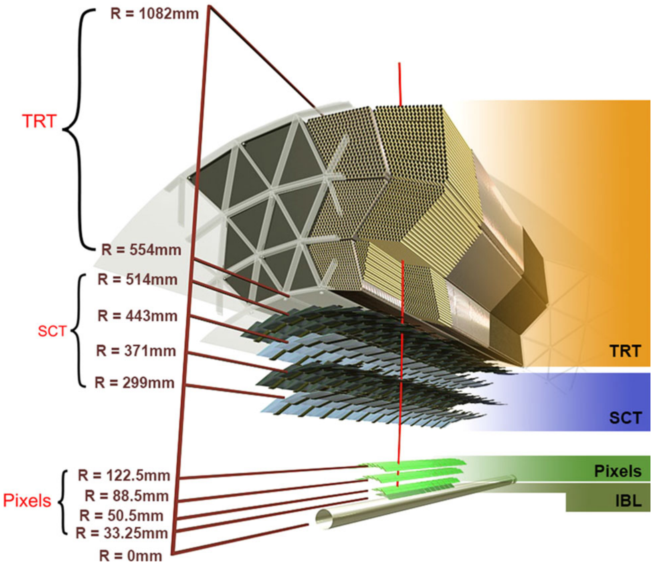

Figure 17. The TRT detector surrounds the SCT detector in the barrel region. [37]

The TRT [38] uses of layers of straw (proportional drift) tubes for particle identification and tracking. This detector is the outermost layer of the ID covering $|\eta| < 2$. The TRT consists of 4 mm diameter Kapton tubes with a gold-plated tungsten wire running through them and filled with an Argon based gas mixture. Ionization from charged particles traversing the tubes is amplified and shaped to create a hit signal. As the charged particles pass through fiber or foil interfaces located between the straws they emit KeV scale transition radiation which provides discriminations of particle mass. The TRT provides around 36 hits to complement the high resolution of the other detectors.

3.2.2 ATLAS Calorimetry

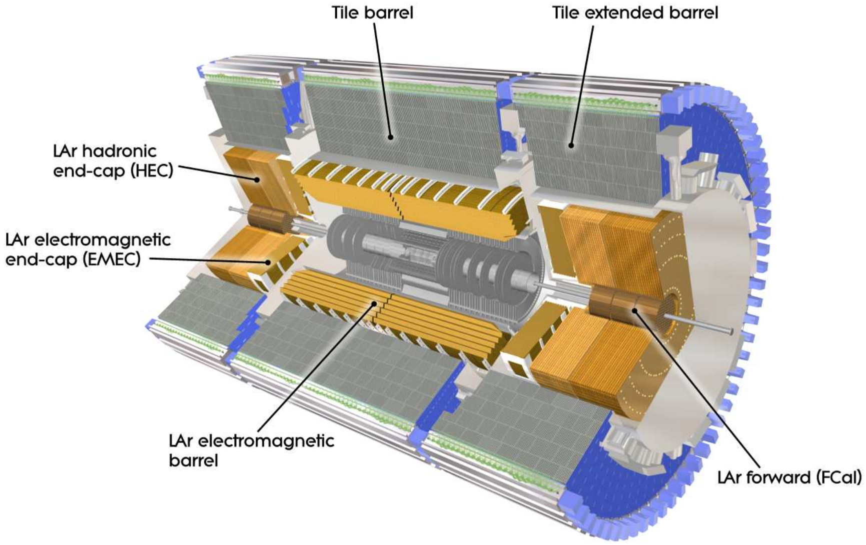

Figure 18. The major ATLAS calorimeter systems. Figure from [32].

The major ATLAS calorimeters systems are Liquid Argon (LAr) barrel, LAr ElectroMagnetic End Cap (LAr EMEC), LAr Forward Calorimeter (FCal), Tile barrel and Tile extended calorimeters. Figure 18 shows the arrangement of these systems with barrel calorimeters surround the ID and the forward and end cap detectors forward of the ID. These calorimeter systems provides particle identification for elections and photons and are the primary detectors for hadrons. The combined calorimeter systems provide 7 sampling layers in barrel and 8 in the end cap regions with around 188,000 readout channels.

Liquid Argon (LAr) and scintillating tile (Tile) are sampling calorimeters which alternate absorbing with sensing layers. The absorbing layers scatter the incident particle to create a shower of decay products which are detected through ionization of the active media. Calorimeter energy resolution,

$$\frac{\sigma}{E} = \frac{a}{\sqrt{E}} \oplus \frac{b}{E} \oplus c, \tag{3.3}$$

depends on stochastic effects during showering (a), electronic noise (b) and other detector effects (c). ATLAS was designed with a barrel region jet energy resolution requirement of

$$\frac{\sigma}{E} = \frac{50\%}{\sqrt{E}} \oplus 3\%, \tag{3.4}$$

for E in GeV.

3.2.3 The Liquid Argon calorimeter

Four LAr [40] calorimeters surround the inner detector. LAr EM Barrel covers $|\eta| < 1.475$, EM End Cap $1.375 < |\eta| < 3.3$, Hadronic End Cap $1.5 < |\eta| < 3.2$ and FCal $3.1 < |\eta| < 4.9$. The EM barrel and End Cap detectors uses lead absorber sheets arranged in an accordion geometry as shown in Figure 19 with liquid

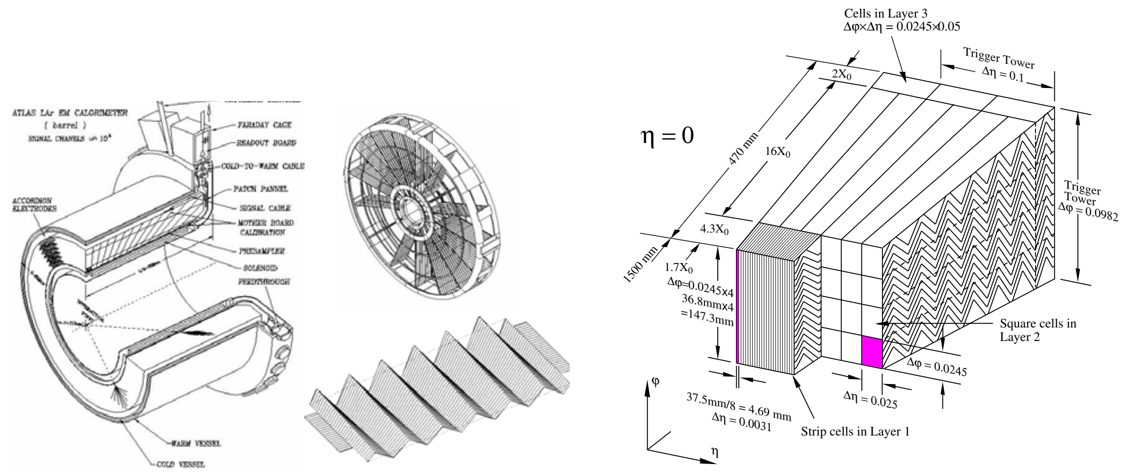

Figure 19. The LAr barrel and end cap using lead absorber sheets arranged in an accordion structure (left). The LAr tower geometry in the barrel region (right). Figures from [39].

argon filling the gaps between layers. EM showers consist of cascades of alternating bremsstrahlung and pair production processes. The EM calorimeters extend out to greater at least 24 radiation lengths[1] to fully capture EM showers. Ionizing particles produce charge avalanches as they travel through the liquid argon which are read out by the electronics.

Ion drift time in the liquid argon results in a delayed pulse signal which is longer than the LHC collision rate of 25 ns. A pulse shaping strategy is used to suppress out of time pileup caused by residual signals from previous bunch crossings. The bipolar pulse shaping is performed by an analog circuit to provides a sharply peaked signal with an integral of 0 as shown in Figure 20. The average of out of time pileup LAr signals is small due to this shaping. An Optimal Filter algorithm is used to calculate the amplitude and phase relative to the bunch crossing with the assumption of a known pulse shape [39]. The measured time resolution for the LAr EMB is shown in Figure 21.

---

[1] A radiation length X_0 is distance is takes an electron to lose all but 1/e of its energy.

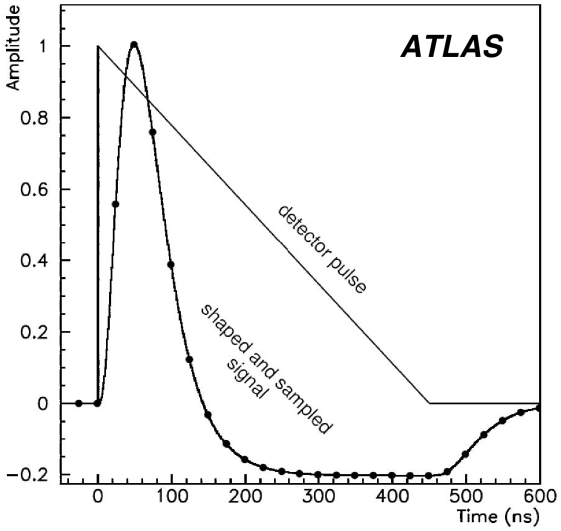

Figure 20. LAr uses pulse shaping to minimize the impact of out of time pile up. [39]

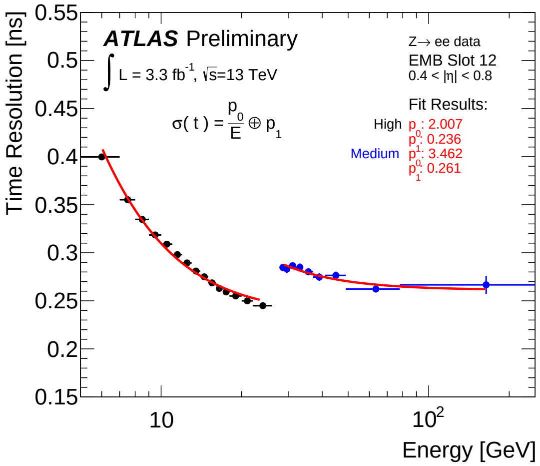

Figure 21. Time resolution as a function of energy for High and Medium gain in Electromagnetic Barrel (EMB) Slot 12 ($0.4 < |\eta| < 0.8$). The coefficients p0, p1 multiply the noise term and constant term respectively. A calculated correlated contribution of $\tilde{2}00$ ps to the constant term of the time resolution can be attributed to the beamspread. Figure from [41].

The EM Barrel calorimeter cells are arranged in three layers with a pseudo-projective geometry in η-ϕ. Cells have increased granularity in the innermost layers with 0.003×0.1 for the first layer. The second layer has a granularity of 0.025×0.025 and the third layer has a granularity of 0.050×0.025.

The EM End Cap calorimeter consists of two concentric wheels covering $1.375 < |\eta| < 3.2$. EMEC cells are similar to EMB cell but with a geometry as shown in Figure 19 (left) and a reduced granularity that varies with η and cell layer. Additional presampler layers are located between the cryostat cold wall and the calorimeter in the barrel and end cap regions to measure the energy of deposited by particles before they reach the calorimeter.

The Forward and Hadronic End Cap calorimeters also use liquid argon as the active medium. The HEC consists of two wheels of parallel copper plates and covers $1.5 < \eta < 3.2$. HEC granularity ranges from $\eta \times \phi = 0.1 \times 0.1$ to 0.2×0.2. The forward calorimeters cover $3.1 < |\eta| < 4.9$ consisting of three layers with copper (EM) and tungsten (hadronic) absorber layers with liquid argon tubes running through them. These tubes are oriented parallel to the beamline as shown in Figure 22. This tube geometry is used for additional radiation hardness in the high flux forward region.

3.2.4 The Tile Calorimeter

Hadronic objects which punch through the LAr colorimeter are absorbed by the Tile calorimeter. The Tile calorimeter [42] consists of the barrel ($|\eta| < 0.8$) and two extended barrel ($0.8 < |\eta| < 1.7$) sections which surround the LAr Calorimeters. The

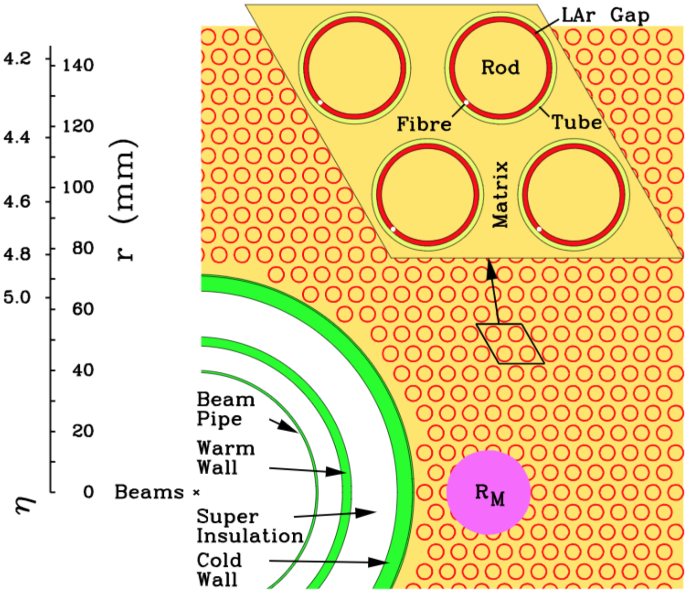

Figure 22. The Tile Calorimeter scintillating tiles and readout. Figure from [39].

Tile calorimeter extends from a radius of 2.28 m to 4.25 m with three layers of cells as shown in Figure 23. There are 64 tile modules, with a ϕ coverage of $\pi/32$ rad.

This calorimeter uses alternating layers of scintillating plastic and steel absorber tiles to measure hadronic showers. Hadronic showers consist of nuclear interaction processes and are longer and wider than EM showers. The ATLAS calorimeters extend out to more than 10 hadronic interaction lengths for almost the full η coverage as shown in Figure 24.

Scintillator tiles transmit light to Photo Multiplier Tubes (PMTs) with wavelength shifting fibers. The PMTs group tiles together into calorimeter cells. This detector has a pseudo-projective geometry with groups of tiles covering $\eta \times \phi$ from 0.1×0.1 to 0.2×0.1. Two additional detectors, the Plug Tile calorimeter and Gap Scintillator are placed in the gap between the barrel and extended barrel tile calorimeters.

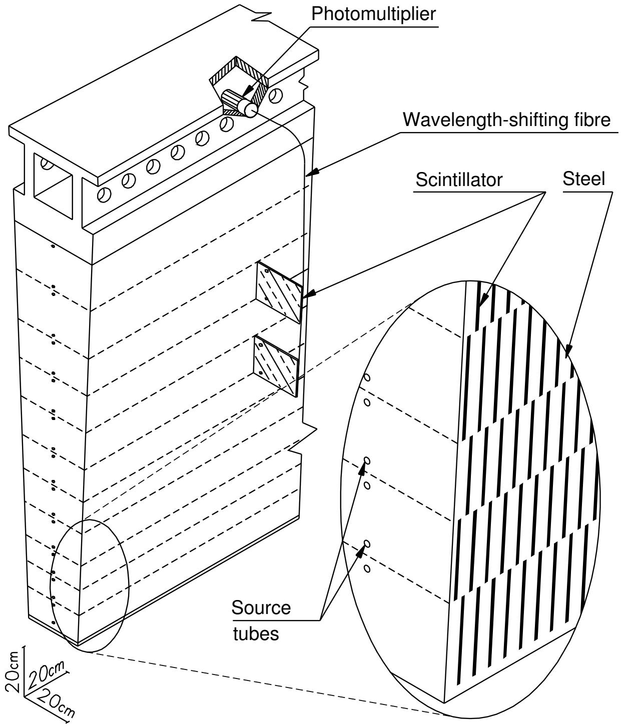

Figure 23. The Tile Calorimeter scintillating tiles and readout. Figure from [32].

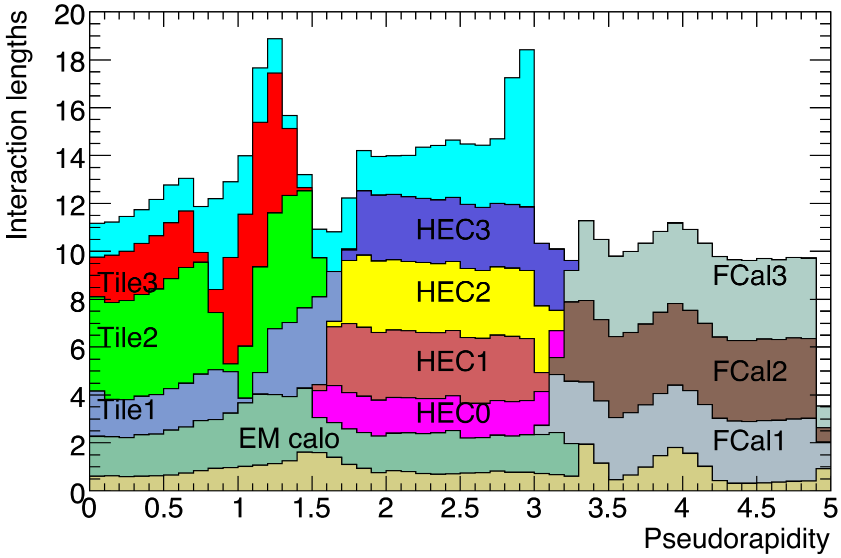

Figure 24. Hadronic interaction lengths for the ATLAS calorimeters. Figure from [32].

3.2.5 The Muon Spectrometer

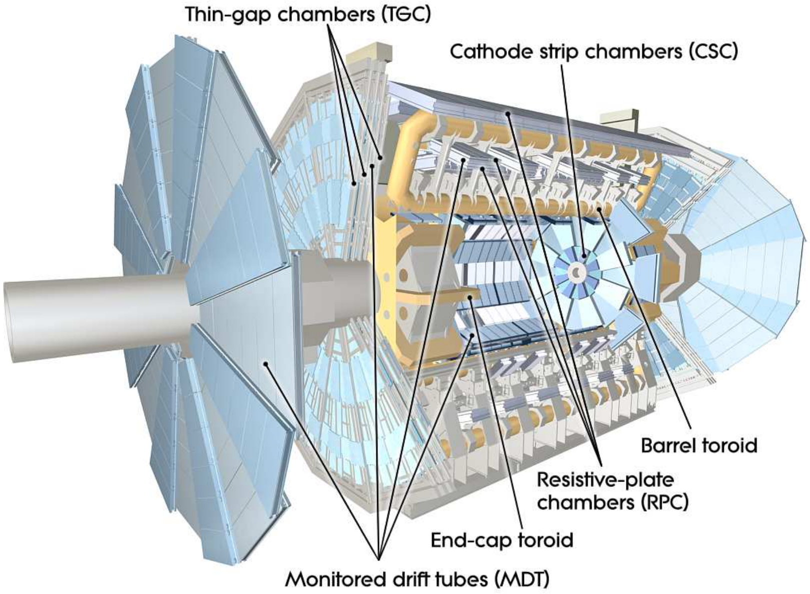

Figure 25. The ATLAS muon spectrometer chambers. Figure from [43].

The outermost ATLAS sub-detector is the Muon Spectrometer (MS) which measures muon momentum out to $|\eta| < 2.7$. This spectrometer uses the four types of chambers shown in Figure 25 for muon triggering and momentum measurement. The η coverage of each chamber subsystem is shown in Figure 26. Monitored Drift Tube (MDT) chambers provide precision tracking for the full MS η range. The ATLAS MDTs consist of 30 mm diameter aluminum tubes with anode wires running through their center and filled with argon-based gas. The individual tubes are precisely positioned and provide mechanical isolation of the measurement. Cathode Strip Cambers are used at high $|\eta|$ for robust operation at high occupancy. The CSCs are multi-wire proportional chambers with a segmented cathode strip readout. The

MS uses high precision mechanical assembly and optical alignment to meet its particle tracking resolution requirements.

Muon triggering is provided by Resistive Plate Chambers (RPC) in the barrel and Thin Gap Chambers (TGC) in the endcap regions up to $|\eta| < 2.4$. RPCs consist of pairs of resistive plates at 9.8 kV with a 2 mm gap and filled with tetrafluorethane. Readout strips in x and y provide track resolution. The TPGs are multi-wire proportional chambers similar to the CSCs. In addition to muon triggering, RPCs and TPCs can supplement the other chambers for tracking in offline reconstruction.

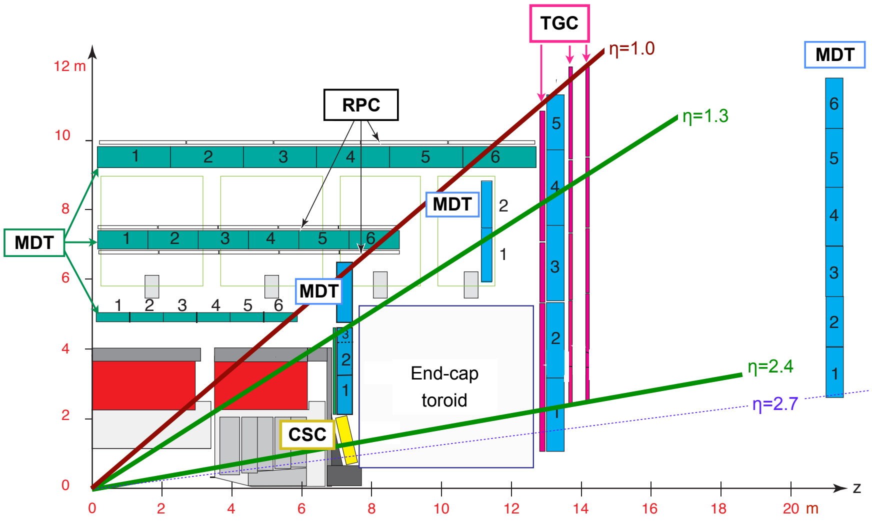

Figure 26. The η coverage of the Muon Spectrometer subsystems. Figure from[44].

3.2.6 Event Triggering and Data Acquisition

ATLAS uses a two level trigger system [45] to determine which events to record to tape for permanent storage. ATLAS triggers reduce the number of events recorded from the machine rate of 40 MHz to around 1 kHz for the main physics stream. Events are selected when they meet some trigger criteria specified by the trigger menu. The total event rate recorded is limited by disk space and computing power so different possible triggers must be prioritized. Triggers with a high event yield are prescaled by randomly keeping some fraction of events and then applying a scale factor to recorded data yields.

The first level, L1, uses the hardware triggers L1Calo, L1Muon, and additional subsystems to select events. These selections reduce the event rate from the 40 MHz collision rate to the 100 kHz L1 rate. The L1Calo system uses LAr calorimeter information to identify and measure electrons, photons, and jets using coarse granularity and fast algorithms. LAr cells are grouped into towers of $\eta \times \phi = 0.1 \times 0.1 - 0.2 \times 0.1$ for jet finding. L1Muon triggers on muons for $|\eta| < 2.4$ with the muon detector systems.

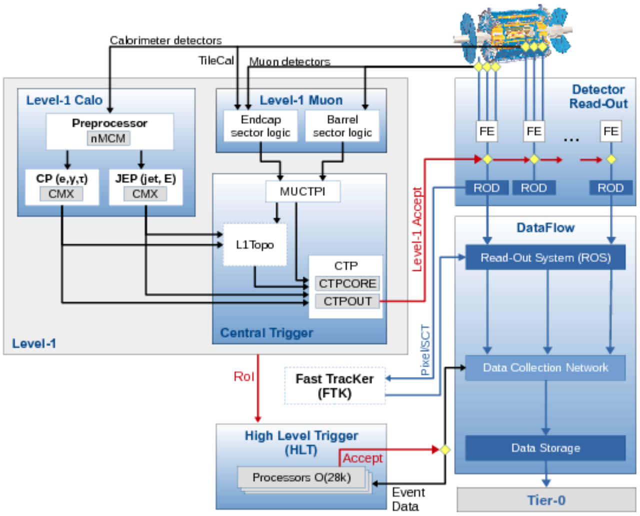

Figure 27. Data flow in the ATLAS trigger system. L1 identifies events and with a ROI for HLT. Events accepted by the HLT are written to permanent storage. [46]

Reconstructed objects from these triggers are sent to the L1 central processor where a selection is applied based on the trigger menu. Passing events and an associated Region of Interest (RoI) are sent to the software level trigger The High-Level Trigger (HLT) is implemented in software on a local processor farm using commodity hardware. The HLT distributes events to nodes for reconstruction in parallel using a high performance version of the Athena ATLAS reconstruction software. This software level reconstruction makes uses of additional detector systems, higher granularity detector readouts, and more sophisticated algorithms to apply a final trigger decision based on the trigger menu. Figure 27 shows the data flow in the ATLAS trigger system. The $\mathrm{H_T}$ trigger used in the dark meson search is described in Chapter IV and the $E_{\mathrm{T}}^{\mathrm{miss}}$ and lepton triggers used by the direct stop search are described in Chapter V.

3.3 Particle reconstruction

ATLAS detector signals are reconstructed as physics objects (representations of particle like objects) and other discriminating variables. Electrons, photons and muons are reconstructed as 4-vectors with properties such as reconstruction quality. Hadronic objects are observed as an energy spray deposited in calorimeter cells which is then reconstructed as a jet. Jets are particle like objects which relates detector signals to hadronic final states. Analysis discriminating variables are computed from these physics objects and are described in the analysis chapters.

3.3.1 e^- and γ Reconstruction

Electrons are reconstructed [48] using a combination of inner detector tracks and calorimeter shower energy deposits. As an electron travels through the Inner Detector

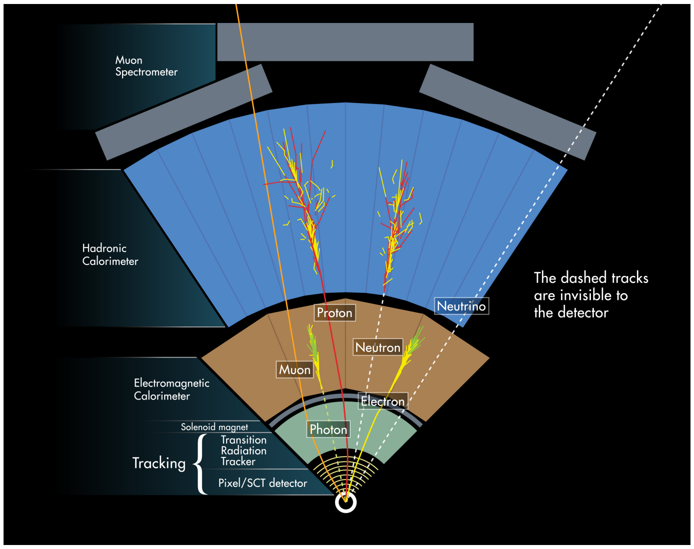

Figure 28. The particle interactions of the major ATLAS detector systems. [47]

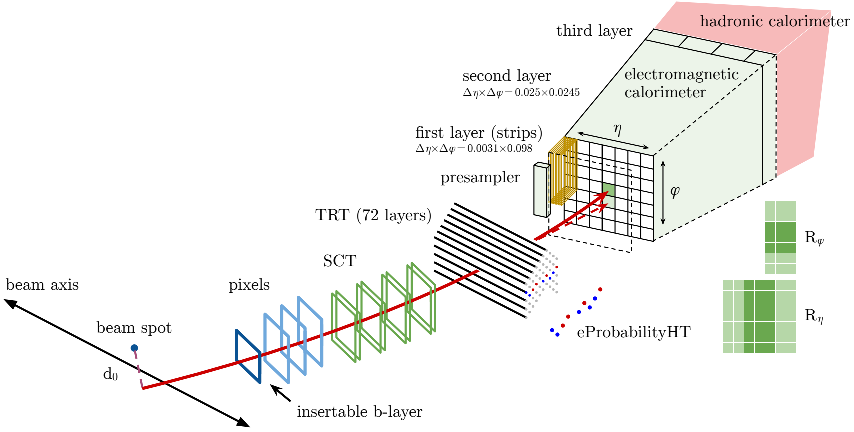

Figure 29. Electron reconstruction uses a combination of ID detector hits and calorimeter shower energy deposits. [48]

it leaves hits which allow the trajectory to be reconstructed. This trajectory is matched to energy deposits in the electromagnetic calorimeter and assigned an electron likelihood value based on a multivariate algorithm which includes shower shape and track matching. Figure 29 illustrates the reconstruction of an electron from these signals.

Different working points can be used to select electrons at a chosen confidence level. Typical working points are MEDIUM or TIGHT for signal leptons and LOOSE for exclusion of events with electrons in a 0-lepton region. The particular working points used in this thesis are described in the analysis chapters. Signal electrons are also required to pass isolation and overlap removal requirement as described in these sections.

Photons create showers in the EM calorimeter but leave no tracks in the Inner Detector. For both all-hadronic analyses described in this thesis photons are not reconstructed and are neither selected nor vetoed.

3.3.2 Tau Lepton Veto

τ-leptons are not reconstructed in either of the searches described in this thesis. The direct stop search uses a custom hadronic tau veto for signal regions A and B in order to reject high $E_{\mathrm{T}}^{\mathrm{miss}}$ events where the $E_{\mathrm{T}}^{\mathrm{miss}}$ is aligned with the tau in ϕ. Hadronic tau jets are identified by their number of tracks and alignment with the event $E_{\mathrm{T}}^{\mathrm{miss}}$. Hadronic taus decay to a neutrino and 1 or 3 tracks depending on the number of charged pions produced. Hadronic tau candidates are defined as any non b-tagged calorimeter jet within the tracker acceptance ($\eta < 2.5$) associated to four tracks or less. Only the candidate which is best aligned with the $E_{\mathrm{T}}^{\mathrm{miss}}$ is considered in each event and has to satisfy $\Delta\phi(E_{\mathrm{T}}^{\mathrm{miss}}\,\mathrm{jet}) < \pi/5$ to be considered.

3.3.3 Hadronic Object Reconstruction

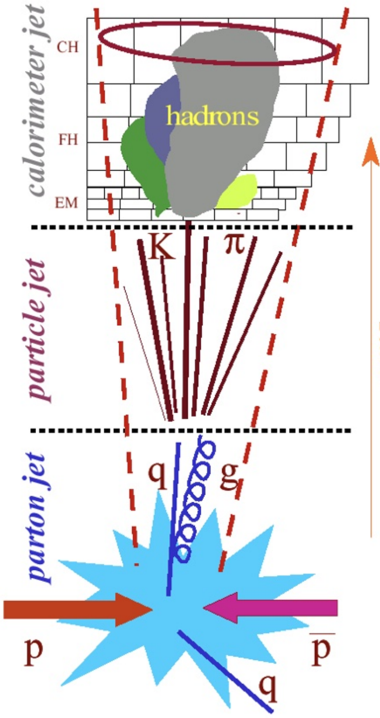

Figure 30. Parton jet reconstruction from calorimeter energy deposits. Figure from [49].

Final state partons hadronize into sprays of particle that leave a primary detector signature of calorimeter cell energy deposits. Figure 30 illustrates the formation of calorimeter energy deposites from parton final states. Jet reconstruction uses these energy deposits to determine originating particle kinematic using two steps of clustering and several steps of noise suppression, cleaning and calibration. This reclustering can reconstruct the final partons or an originating parent particle. Additional information can be associated to a jet such as flavor tagging of constituents or sub-jet moments. Other collections of four-momenta such as particle tracks or MC truth level particles can be clustered with the same jet algorithm to form jet objects. For a review of jet reclustering methods for hadron colliders see [50].

This first step in hadronic object reconstruction is clustering the 3D calorimeter energy cell deposits into 2D projections of topologically connected cell signals (topo-clusters). Topo-clustering provides a signal of particle shower energy while filtering electronic noise and pile-up. Topo-clusters are formed using a seeding-growing-thresholding algorithm with parameters 4-2-0. For each cell a signal significance estimate is determined using.

$$\zeta_{cell}^{EM} = \frac{E_{cell}^{EM}}{\sigma_{cell}^{EM}}. \tag{3.5}$$

Where σ_{cell}^{EM} is the RMS of a cells energy under background conditions. Cells with $|\zeta_{cell}^{EM}| > 4$ are used as topo-cluster seeds which are then iteratively extended to include neighboring cells with $|\zeta_{cell}^{EM}| > 2$ and finally extended with all neighboring cells with $|\zeta_{cell}^{EM}| > 0$. See [51] for a full description of ATLAS topo-clustering.

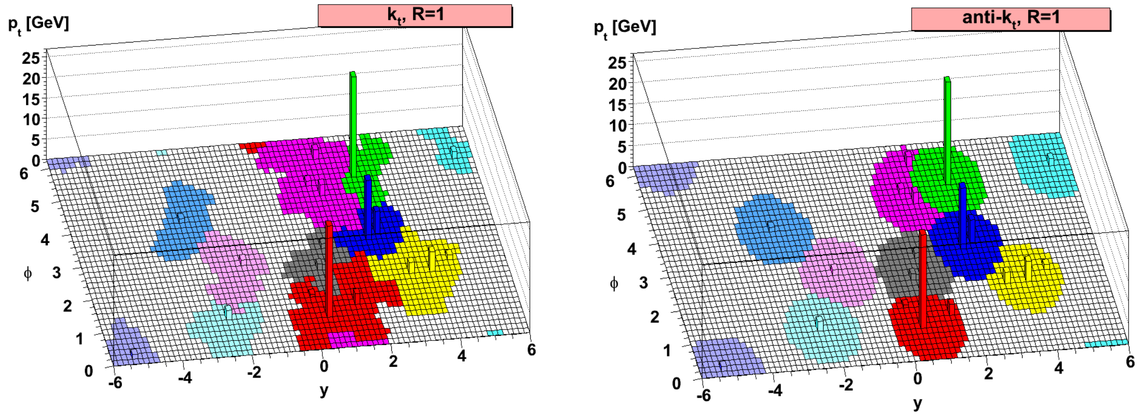

Figure 31. Jet clustering with the k_T and anti-k_T algorithms. Figure from [52].

Next, a jet clustering algorithm takes the collection of topo-cluster 4-vectors and combines close inputs according a some distance metric R to form jets. The anti-k_T algorithm is the primary ATLAS jet reconstruction algorithm because it is IR and collinear safe, efficiently computed, and provides a convenient measure of detector area for calibration against pileup. Isolated anti-$\mathrm{k_T}$ jets are circular with pileup that scales with jet area. Two examples of jet clustering are shown in Figure 31. $\mathrm{k_T}$ jet clustering retains IR and collinear safety but clusters soft objects into hard objects such that the record of iterative 4-vector clustering can be reversed to reconstruct the decay of massive objects into subjets. IR safety is the requirement that a reclustering algorithm be robust against the emission of a soft jets and collinear safety is the requirement that a reclustering algorithm be robust against jet splitting as shown in Figure 32.

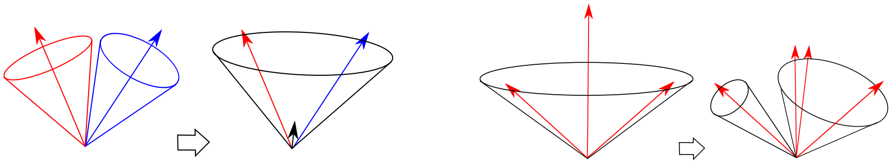

Figure 32. Examples of jet clustering which violates infra-red and collinear (IRC) safety. An IRC safe jet collection will not change with the additional of a soft jet (left) or the collinear splitting of a jet (right).

The key parameter for jet clustering with anti-$\mathrm{k_T}$ is the radius parameter R. R determines the maximum Euclidean distance in η-ϕ space for which jets can be clustered. If a hard jet has no nearby hard neighbors within $2R$, all the soft jets within R will be clustered into it to form a perfectly conical jet of radius R. Larger R parameters allow the algorithm to cluster jet inputs at greater distance and the optimal R parameter depends on the kinematics of the objects to be reconstructed.

R=0.4 anti-$\mathrm{k_T}$ EMTopo jets are used in the direct stop analyses and R=0.4 anti-$\mathrm{k_T}$ EMPFlow jets are used in the dark meson search as the primary jet collections. EMTopo jets are constructed from EM scale topoclusters alone while PFlow [53] jets combines the EM scale topoclusters with charged hadron tracking from the ID for improved low p_T energy resolution and pile-up exclusion.

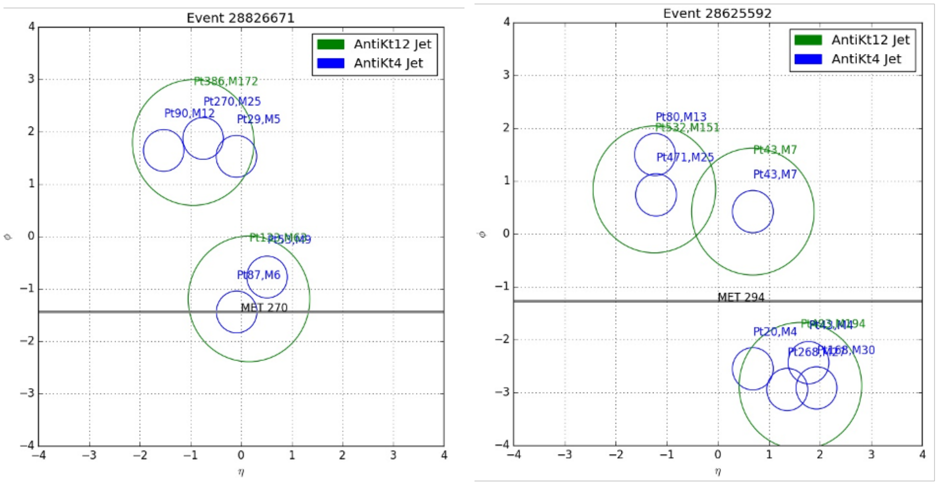

Figure 33. Event display plots of jets and $E_{\mathrm{T}}^{\mathrm{miss}}$ for two Monte Carlo simulated $t\bar{t}$ events. The blue circles indicate R=0.4 jets and the green circles indicate R=1.2 anti-k_T reclustered jets. The plot on the top right shows an event where the decay products of the subleading top were too separated for the R=1.2 reclustering parameter to reconstruct the full top quark.

Calibrated jet collections can be re-clustered with larger R parameters to form large-R jets as shown in Figure 33 Reclustered large-R jets allow the reconstruction of high mass objects without requiring additional calibration. In this thesis this large-R jet reclustering is uses to reconstruct top quarks and dark pions with R=1.2 anti-k_T reclustering as shown in Figure 34. R parameter optimization studies for the dark meson search are presented in Appendix A.

3.3.4 Jet Calibration and Cleaning

The jets used in this thesis are calibrated with several stages of corrections applied to their energy and direction as shown in Figure 35. Jet energies must be scaled suing the Jet Energy Scale (JES) to correct for calorimeter measurements of hadronic showers.

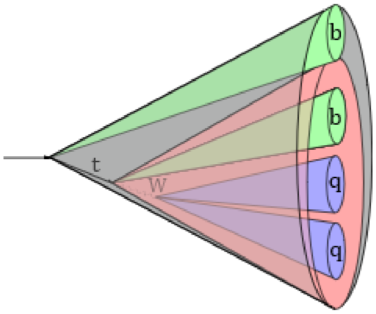

Figure 34. Diagram of an all-hadronic dark pion decay. Jet reclustering is used to reconstruct the dark pion from its decay products.

Clustering of topo-clusters results in jets measured at the EM scale, corresponding to the energy deposited by an electromagnetic interacting particle. The ATLAS jet calibration procedure is:

1. The direction of the jet is corrected so that it originates at the event's primary vertex.
2. A pileup term is subtracted from the jet energy based on it's area, the pileup energy density, the mean number of events, and number of primary vertices (N_{PV}).
3. An MC derived calibration is applied to the jet energies. In this calibration particle level and reconstruction level jet energies are compared in order to account for detector measurement effects.
4. The GSC applies an additional correction based on the jet shape and composition using a numerical inversion scheme.
5. Residual in-situ calibration corrects MC jet response to data by comparing data to MC using well-measured reference jets.

Pile up jets with $|\eta < 2.5|$ are suppressed with a Jet Vertex Tagger (JVT) algorithm [55]. The JVT computes a multivariate discriminant based on the

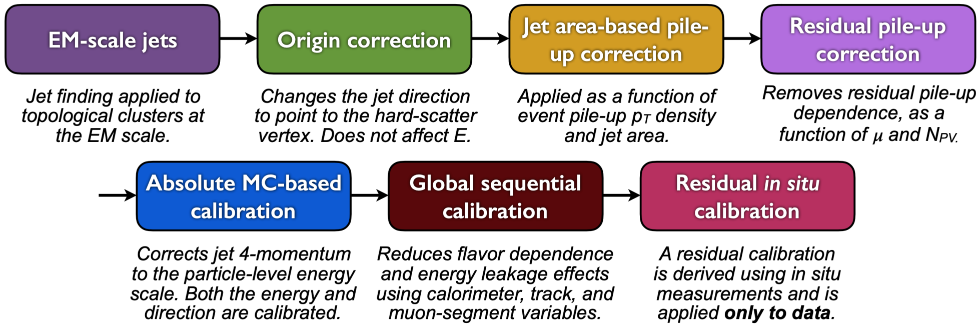

Figure 35. The ATLAS jet calibration sequence. [54]

association of jet tracks to the primary and other vertices. For $|2.5 < \eta < 2.8|$ the vertexing is unavailable and the forward JVT algorithm (fJVT) is instead applied [56]. The fJVT rejects forward jets which are back-to-back with central pileup jets. Tight working points are used in this thesis for both algorithms.

Additional jet cleaning is applied to remove jets from background processes such as beam induced background, cosmic-ray showers, and calorimeter noise. ATLAS jet quality working points are described in [54]. The Loose bad-jet rejection working point is applied with an efficiency of 99.5% (99.9%) for jets with $p_T > 20(100)$ GeV.

3.3.5 Jet Flavor Tagging

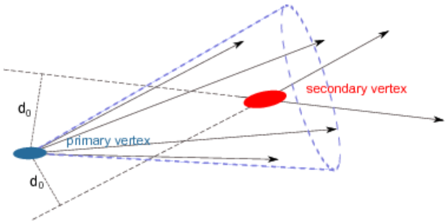

Figure 36. A displaced vertex with a distance of closest approach d_0. Figure from [57].

B mesons travel hundreds of µm in the ATLAS Inner Detector before decaying to lighter hadrons resulting in a displaced secondary vertex as shown in Figure 36. Jets are flavor tagged using a multivariate discriminator which considers information on track displacement via their impact parameters, as well as secondary and tertiary decay vertices within the volume of the reconstructed jet cone. Several fixed efficiency working points are providing by the ATLAS JET $E_{\mathrm{T}}^{\mathrm{miss}}$ working group. The analyses described in this thesis use the 77% efficiency percent working point.

The MV2c10 b-tagging algorithm used in the direct stop search has a rejection of factor 110 and 5 for light-flavour jets and c-jets. This algorithm was superseded by the deep Recurrent Neural Network (RNN) based DL1r algorithm [58, 59] which is used in the dark meson search. DL1r uses an artificial deep neural network trained on a simulated hybrid sample composed of $t\bar{t}$ and Z' events. At the 77% efficiency working point this algorithm has a rejection factor of 170 and 5 on light-flavored and charm jets respectively.

3.3.6 Missing Transverse Energy

Standard Model neutrinos and many beyond the Standard Model final states such as neutralinos escape ATLAS without leaving tracks or energy deposits and must be inferred from a momentum imbalance in observed physics objects. This momentum imbalance allows Missing Transverse Energy ($E_{\mathrm{T}}^{\mathrm{miss}}$) to be measured [60] and the presence of an invisible particle inferred. In this thesis $E_{\mathrm{T}}^{\mathrm{miss}}$ is computed as the magnitude of a vectorial sum of the p_{T} of the jets, electrons and muons in the event and soft energy term,

$$E_{\mathrm{T}}^{\mathrm{miss}} = \left| \sum_{jets} \mathbf{p_T} + \sum_{leptons} \mathbf{p_T} + \sum_{soft} \mathbf{p_T} \right| \tag{3.6}$$

. The soft energy term accounts for tracks with p_T greater than 500 MeV and calorimeter clusters which are not selected as objects. $E_{\mathrm{T}}^{\mathrm{miss}}$ systematic uncertainty is dominated by this soft term.

3.3.7 Muon Reconstruction

Muon reconstruction [61] combines tracks from the Inner Detector and the Muon Spectrometer to provide identification and momentum measurement of muons. This reconstruction can be supplemented by calorimeter signals consistent with MIP energy deposits. A recommended ATLAS working point of MediumLH is used to veto baseline muons in the 0-lepton regions of this thesis with no additional isolation requirement. The details of the working points used in this thesis are described in the analysis chapters. Signal muons are also required to pass isolation and overlap removal requirement as described in these sections. The ATLAS Recommended overlap removal procedure is applied to veto muons likely to originate in hadronic showers.

Monte Carlo simulation is used to generate signal and background samples for Standard Model and beyond the Standard Model processes. This simulation has three steps:

1. Event generation using the Parton Distribution Function (PDF) for the protons and the hard scattering Matrix Element (ME) from initial to final states

2. Proton shower (PS) and hadronization.

3. Simulation of detector response to the event.

Figure 37 shows an diagram of an example $t\bar{t}H$ event. First, a ME generator code computes and samples the phase space of the hard process. Next, the QCD evolution is simulated with a parton showing algorithm and hadronization is simulated with phenomenological models. Steps 1 and 2 are implemented in dedicated or combined codes with afterburner codes such as EvtGen [62] used to supplement the generators of step 1.

Stop quark direct production is simulated using MadGraph5_aMC@NLO [63] at leading order (LO) in QCD. Pythia [64] is used for the parton showering (PS) and hadronisation. The dark meson signal points are simulated using at next-to-leading-order (NLO) with MadGraph5_aMC@NLO v2.4.3 [63] interfaced with Pythia8. Decay of bottom and charm hadrons are simulated with EvtGen [62]. The configuration of all nominal background samples used in this thesis are described in Tables 5 and 6. Samples used for estimating systematic uncertainties are described in the analysis chapters. $t\bar{t}$ and W/Z + jets are important backgrounds in both analysis.

3.4 Monte Carlo event simulation

The PowhegBox v2 [66, 67, 68, 69] generator is used to model $t\bar{t}$ production with matrix elements at next-to-leading order (NLO) in the strong coupling constant α_{S} with the `NNPDF3.0nlo` [70] parton distribution function (PDF). The h_{damp} parameter is set to 1.5 m_{top} [71], this controls the matching in Powheg and effectively regulates the high-$\mathrm{p_T}$ radiation against which the $t\bar{t}$ system recoils.

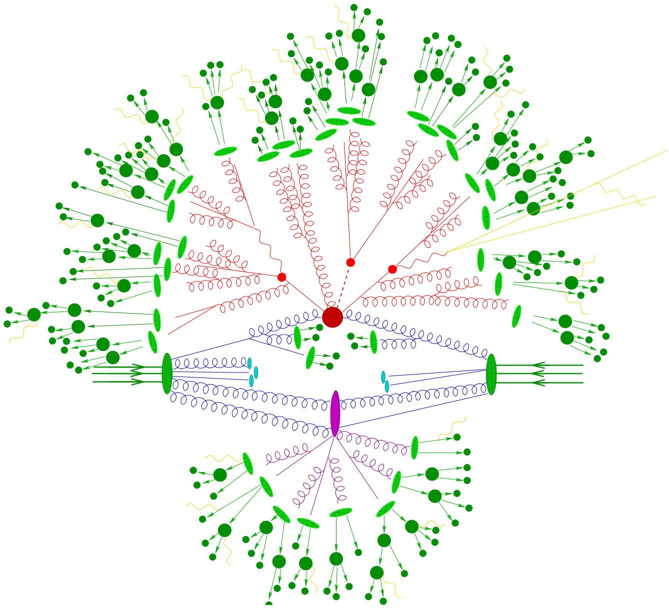

Figure 37. Diagram of a ttH event. The large red blob indicates the hard interaction and the small red blobs indicates the top and H decays. Hard QCD radiation (red) hadronizes to form the green blobs which then decay to additional hadrons. [65].

The production of V+jets ($V = W/Z$) is simulated with the Sherpa [72] generator using next-to-leading order (NLO) matrix elements (ME) for up to two partons, and leading order (LO) matrix elements for up to five partons calculated with the Comix [73] and OpenLoops 1 [74, 75, 76] libraries. They are matched with the Sherpa parton shower [77] using the MEPS@NLO prescription [78, 79, 80, 81] using the set of tuned parameters developed by the Sherpa authors. The Hessian `NNPDF3.0nnlo` set of PDFs [70, 82] is used and the samples are normalised to a next-to-next-to-leading order (NNLO) prediction [83].

The GEANT4 [84] code is used for full detector response simulation for most samples. This code propagates particles through the ATLAS detector and simulates their interactions and detection. Some systematic sample use Atlfast-II [85] fastsim where parameterized detector responses are used rather than full simulation for improved reconstruction computational efficiency.

Table 5. Overview of the simulated background samples used in Chapter IV.

Process	Generator	PDF	Showering	Tune	Cross section
W/Z + jets	Sherpa 2.2.1	NNPDF3.0 NNLO	Sherpa	Def.	NNLO
$t\bar{t}+V$	aMC@NLO 2.3.3	NNPDF3.0 NLO	Pythia 8.210	A14	NLO
$t\bar{t}$	Powheg-Box v2	NNPDF3.0 NNLO	Pythia 8.230	A14	NNLO+NNLL
Single top	Powheg-Box v2	NNPDF3.0 NNLO	Pythia 8.230	A14	NNLO+NNLL
Diboson	Sherpa 2.2.1-2.2.2	NNPDF3.0 NNLO	Sherpa	Def.	NLO
$t\bar{t}H$	aMC@NLO 2.2.3	NNPDF3.0 NLO	Pythia 8.230	A14	NLO
tWZ, tZ	aMC@NLO 2.3.3	NNPDF3.0 NLO	Pythia 8.212,8.230	A14	NLO

Table 6. Overview of the simulated background samples used in Chapter V.

Process	Generator	PDF	Showering	Tune	Cross section
$t\bar{t}$	PowhegBox v2	`NNPDF3.0nlo`	Pythia8	A14	NNLO+NNLL
$t\bar{t}$+HF	Powheg Box Res	`NNPDF3.0nlo`	Pythia8	A14	NNLO
W/Z + jets	Sherpa v2.2.11	`NNPDF3.0nnlo`	Sherpa	Def.	NLO
Single top	PowhegBox v2	`NNPDF3.0nlo`	Pythia8	A14	NLO+NNLL
$t\bar{t}t\bar{t}$	MadGraph5_aMC@NLO v2.4.3	`NNPDF3.1nlo`	Pythia8	A14	NLO
$t\bar{t}$ $+W/Z$	MadGraph5_aMC@NLO v2.3.3	`NNPDF3.0nlo`	Pythia8	A14	NLO
$t\bar{t}H$	PowhegBox v2	`NNPDF3.0nlo`	Pythia8	A14	NLO
Other $t\bar{t}$ + X	MadGraph5_aMC@NLO	`NNPDF2.3lo`	Pythia8	A14	NLO
Multiboson	Sherpa v2.2.1/v2.2.2	`NNPDF3.0nnlo`	Sherpa	Def.	NLO

CHAPTER IV

A SEARCH FOR THE SUPERSYMMETRIC PARTNER TO THE TOP QUARK IN THE JETS+$E_{\mathrm{T}}^{\mathrm{miss}}$ FINAL STATE

4.1 Introduction

Supersymmetry (SUSY) [86, 87, 88, 89, 90, 91] is an extension of the Standard Model (SM) that can resolve the gauge hierarchy problem [92, 93, 94, 95] by introducing supersymmetric partners of the SM bosons and fermions. The SUSY partner to the top quark, the top squark, plays an important role in cancelling out potentially large top-quark loop corrections to the Higgs boson mass [96, 97]. Naturalness arguments suggest that the superpartners of the third-generation quarks may be $O($ TeV$)$, and thus experimentally accessible at the Large Hadron Collider (LHC) [98, 99]. The superpartners of the left- and right-handed top quarks, $\tilde{t}_{\mathrm{L}}$ and $\tilde{t}_{\mathrm{R}}$, mix to form two mass eigenstates, $\tilde{t}_1$ and $\tilde{t}_2$, where $\tilde{t}_1$ is the lighter one. Throughout this paper, it is assumed that $\tilde{t}_2$ has sufficiently high mass such that the analysis is sensitive to $\tilde{t}_1$ only, which is labelled $\tilde{t}$ in the following.

R-parity-conserving SUSY models [100] may also provide a dark-matter candidate through the lightest supersymmetric particle (LSP), which is stable [101, 102]. In these models, the supersymmetric partners are produced in pairs. At the LHC, top squarks are produced mostly via gluon–gluon fusion as well as quark–antiquark annihilation. In a simplified scenario where the first- and second-generation squarks and gluinos are decoupled, the cross section of direct top squark pair production is largely decoupled from the specific choice of SUSY model parameters except for the top squark mass. This production cross section falls steeply with increasing top squark mass, ranging from 10.0 ± 6.7 pb for $m_{\tilde{t}} = 300$ GeV to 0.89 ± 0.13 fb for $m_{\tilde{t}} = 1300$ GeV [103, 104, 105, 106].

In this paper, each top squark is assumed to decay into a top quark (that may be either on-shell or off-shell) and the LSP, which is assumed to be the lightest neutral mass eigenstate of the partners of the electroweak gauge and Higgs bosons, i.e. the lightest neutralino, $\tilde{\chi}^0_1$. The degree to which the top quark is off-shell is directly related to the mass difference between $\tilde{t}$ and $\tilde{\chi}^0_1$. The top squark decay scenarios considered are shown in Figures 38(a)–38(c): the top quark is on-shell in two-body decays ($\tilde{t} \to t\tilde{\chi}^0_1$), three-body decays contain an off-shell top quark but the W boson is on-shell ($\tilde{t} \to t^*\tilde{\chi}^0_1 \to bW\tilde{\chi}^0_1$), and in four-body decays both the top quark and W boson are off-shell ($\tilde{t} \to t^*\tilde{\chi}^0_1 \to bW^*\tilde{\chi}^0_1 \to bff'\tilde{\chi}^0_1$, where f and f' are fermions originating from the off-shell W boson decay). Only hadronic W boson decays are considered in the following.

This paper presents a search for top squark pair production with an experimental signature of at least two jets, large missing transverse momentum, and no electrons or muons, using 139 fb^{-1} of proton–proton (pp) collision data provided by the LHC at a centre-of-mass energy of $\sqrt{s} = 13\,\text{TeV}$ and collected by the ATLAS detector in 2015–2018. Previous searches have been performed by both the ATLAS [107, 108, 109, 110, 111, 112, 13] and CMS [113, 114, 115, 116, 117, 118, 119, 120, 121] collaborations. In this search, enhanced sensitivity to two-body top squark decays, where $m_{\tilde{t}} - m_{\tilde{\chi}^0_1}$ is greater than the top quark mass, m_t, is achieved by the analysis of the full LHC Run 2 dataset and the exploitation of techniques designed to efficiently reconstruct top quarks that are Lorentz-boosted in the laboratory frame. Sensitivity to compressed scenarios, where $m_{\tilde{t}} - m_{\tilde{\chi}^0_1} \sim m_t$, is extended compared with previous searches through the analysis of events in which high-transverse-momentum jets from

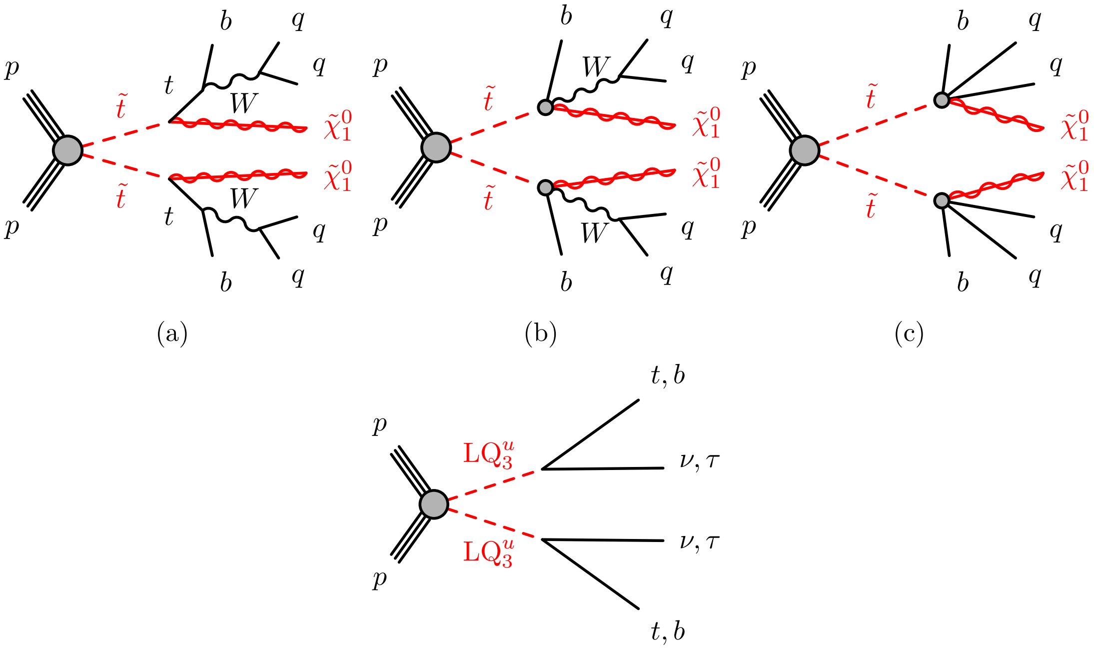

(a) (b) (c)

(d)

Figure 38. Decay topologies of the signal models considered in the analysis: (a) two-body, (b) three-body, (c) four-body top squark decays, the top quarks being produced in pairs, and (d) up-type, third-generation scalar leptoquark pair production, with both leptoquarks decaying into a top quark and a neutralino or a bottom quark and a τ-lepton. For simplicity, no distinction is made between particles and antiparticles. Only hadronic W boson decays are shown.

initial-state radiation (ISR) boost the top squark system in the transverse plane. Finally, sensitivity to the four-body decay scenario where $m_{\tilde{t}} - m_{\tilde{\chi}_1^0}$ is less than the sum of the W boson mass, m_W, and the b-quark mass, m_b, is achieved by extending the identification efficiency for low-transverse-momentum b-hadron decays through the use of charged-particle tracking information, adding sensitivity to the all-hadronic channel in comparison with previous searches. All sensitivities are also increased thanks to global enhancements in detector performance achieved by the end of LHC Run 2, including more precise estimates of the statistical significance of missing transverse momentum in an event [122] and improved identification efficiencies for jets containing b-hadrons [58]. The interpretation of the results uses simplified models [123, 124, 125].

As has been demonstrated previously [108, 109, 110, 126, 127], top squark searches are sensitive to a variety of additional signal models such as top squarks originating from gluino decays [123, 124, 125], top squark decays via charged electroweak SUSY partners [123, 124, 125], mediator-based dark-matter models [128, 129, 130, 131, 132, 133], scalar dark-energy models [134], and third-generation scalar leptoquarks [135, 136, 137, 138, 139, 140, 141]. In this paper, the results are interpreted in models considering the pair production of up-type, third-generation scalar leptoquarks (LQ_3^u), as shown in Figure 38(d), assuming that the LQ_3^u only interact with leptons and quarks from the same generation [142]. Similar LQ_3^u interpretations have been performed by both the ATLAS [127] and CMS [143] collaborations. The third-generation leptoquark production cross section is identical to that of top squark production and the $\mathrm{LQ}_3^\mathrm{u} \to t\nu$ decay channel has the same experimental signature as heavy top squarks decaying into massless neutralinos, and thus additional sensitivity is achieved compared with previous LQ_3^u results.

This chapter contains material coauthored with the ATLAS collaboration. Only signal regions A and B and their backgrounds are described in full detail in this chapter. All regions are described in [10].

4.2 ATLAS detector

The ATLAS experiment [32, 35, 144] at the LHC is a multipurpose particle detector with a cylindrical forward–backward- and ϕ-symmetric geometry and an approximate 4π coverage in solid angle.[1] It consists of an inner tracking detector surrounded by a thin superconducting solenoid providing a 2 T axial magnetic field, electromagnetic and hadron calorimeters, and a muon spectrometer. The inner tracking detector covers the pseudorapidity range $|\eta| < 2.5$. It consists of silicon pixel, silicon microstrip, and transition radiation tracking detectors. Lead/liquid-argon (LAr) sampling calorimeters provide electromagnetic (EM) energy measurements with high granularity. Hadronic calorimetry is provided by a steel/scintillator-tile calorimeter covering the central pseudorapidity range ($|\eta| < 1.7$). The endcap and forward regions are instrumented with LAr calorimeters for both the EM and hadronic energy measurements up to $|\eta| = 4.9$. The muon spectrometer surrounds the calorimeters and features three large air-core toroidal superconducting magnets with eight coils each, providing coverage up to $|\eta| = 2.7$, as well as a system of precision tracking chambers and fast detectors for triggering. The field integral of the toroids ranges between 2 and 6 T·m across most of the detector.

---

[1] ATLAS uses a right-handed coordinate system with its origin at the nominal interaction point (IP) in the centre of the detector and the z-axis along the beam pipe. The x-axis points from the IP to the centre of the LHC ring, and the y-axis points upwards. Cylindrical coordinates (r, ϕ) are used in the transverse plane, ϕ being the azimuthal angle around the z-axis. The pseudorapidity is defined in terms of the polar angle θ as $\eta = -\ln\tan(\theta/2)$. Angular distance is measured in units of $\Delta R \equiv \sqrt{(\Delta\eta)^2 + (\Delta\phi)^2}$.

4.3 Data collection and simulated event samples

The data were collected from 2015 to 2018 at a pp centre-of-mass energy of 13 TeV with 25 ns bunch spacing, resulting in a time-integrated luminosity of 139.0 ± 2.4 fb^{-1} [27], measured using the LUCID-2 detector [28]. Multiple pp interactions occur per bunch crossing (pile-up) and the average number of these interactions in the data was measured to be $\langle\mu\rangle = 34$. A two-level trigger system [145] is used to select events. The first-level trigger is implemented in hardware and uses a subset of the detector information to reduce the event rate to at most 100 kHz. This is followed by a software-based trigger that reduces the accepted event rate to 1 kHz (on average) for offline storage.

Selected events are required to pass a missing transverse momentum (whose magnitude is denoted by $E_{\mathrm{T}}^{\mathrm{miss}}$) trigger [146], which is fully efficient for events with reconstructed $E_{\mathrm{T}}^{\mathrm{miss}} > 250$ GeV (the $E_{\mathrm{T}}^{\mathrm{miss}}$ reconstruction is described in Section 4.4). In order to estimate the background originating from SM processes, events are also selected at lower values of $E_{\mathrm{T}}^{\mathrm{miss}}$ using single-electron, single-muon, and single-jet triggers. Electron and muon triggers yield an approximately constant efficiency in the presence of a single isolated electron or muon with transverse momentum (p_{T}) above 27 GeV (see Section 4.4 for details of the electron, muon, and jet reconstruction); these triggers are needed for the estimation of $Z \to \nu\bar{\nu}$ production in association with heavy-flavour jets (Z + jets) and top pair production in association with $Z \to \nu\bar{\nu}$ ($t\bar{t}$ $+Z$) backgrounds. Triggers based on the presence of a single jet were used to collect data samples for the estimation of the multijet and all-hadronic $t\bar{t}$ backgrounds. The jet p_{T} thresholds after energy calibration ranged from 50 to 400 GeV. In order to stay within the bandwidth limits of the trigger system, only a fraction of the events passing the jet triggers were recorded to permanent storage.

Monte Carlo (MC) simulations are used to model the SUSY and leptoquark signals, as well as to aid in the description of the background processes. SUSY signal models were all generated with MadGraph5_aMC@NLO 2.6.2 [63] at leading order (LO) in QCD, while leptoquark signals were generated with MadGraph5_aMC@NLO 2.4.3 at next-to-leading order (NLO) in QCD. All signal samples were interfaced to Pythia 8.230 [64] for the parton showering (PS) and hadronisation, and with EvtGen 1.6.0 [62] for the b- and c-hadron decays.

The parton distribution function (PDF) set used for the generation of the signal samples is NNPDF2.3 LO [147] for SUSY signals and NNPDF3.0 NLO [70] for leptoquark signals, with the A14 [148] set of tuned underlying-event and parton shower parameters (UE tune). Matching of the matrix element (ME) with parton showering was performed following the CKKW-L prescription [149], with a matching scale set to one quarter of the mass of the top squark or leptoquark. All signal cross sections are calculated to approximate next-to-next-to-leading order (NNLO) in the strong coupling constant, adding the resummation of soft gluon emission at next-to-next-to-leading-logarithm accuracy (approximate NNLO+NNLL) [150, 103, 104, 151].

The top squark mixing parameter between $\tilde{t}_{\mathrm{L}}$ and $\tilde{t}_{\mathrm{R}}$ was set to be maximal.[2] Finally, the top quark mass was set to 172.5 GeV in all simulated samples.

SM background samples were generated with different MC event generators depending on the process. Details of the generators and parton showering used for the different processes are shown in Table 7.

---

[2] This refers to the Higgs–top-squark trilinear mixing term; the scenario of maximal mixing allows the top squark masses to be as light as possible, given a 125 GeV Higgs mass [152].

Table 7. Overview of the simulated background samples.

Process	ME event generator	PDF	PS and hadronisation	UE tune	Cross-section calculation
V+jets	SHERPA 2.2.1 [153]	NNPDF3.0 NNLO	SHERPA	Def.	NNLO [154]
$t\bar{t}+V$	aMC@NLO 2.3.3	NNPDF3.0 NLO	PYTHIA 8.210	A14	NLO [63]
$t\bar{t}$	POWHEG-BOX v2 [69]	NNPDF3.0 NNLO	PYTHIA 8.230	A14	NNLO+NNLL [155, 156, 157, 158, 159, 160]
Single top	POWHEG-BOX v2	NNPDF3.0 NNLO	PYTHIA 8.230	A14	NNLO+NNLL [161, 162, 163]
Diboson	SHERPA 2.2.1-2.2.2	NNPDF3.0 NNLO	SHERPA	Def.	NLO
$t\bar{t}H$	aMC@NLO 2.2.3	NNPDF3.0 NLO	PYTHIA 8.230	A14	NLO [164, 165, 166, 167]
tWZ, tZ	aMC@NLO 2.3.3	NNPDF3.0 NLO	PYTHIA 8.212,8.230	A14	NLO

The detector simulation [168] was performed using either *GEANT*4 [169] or a fast simulation framework, where the showers in the electromagnetic and hadronic calorimeters are simulated with a parameterised description [170] and the rest of the detector is simulated with *GEANT*4. All signal samples were produced using the fast simulation, while SM background samples used the *GEANT*4 set-up. All MC samples were produced with a varying number of simulated minimum-bias interactions overlaid on the hard-scattering event, to account for pile-up. These interactions were produced using PYTHIA 8.2 with the A3 tune [171] and NNPDF2.3 LO PDF set. The simulated events are reweighted to match the distribution of the number of pp interactions per bunch crossing in data. Corrections are applied to the simulated events to account for differences between data and simulation for the lepton trigger, reconstruction, identification and isolation efficiencies, and for the lepton and jet momentum scale and energy resolution. Corrections are also applied to the efficiency of identifying jets containing b-hadrons (b-jets), the probability of mis-tagging jets containing only charm hadrons (c-jets) and only lighter hadrons (light-flavour jets), and the probability of mis-tagging jets originating from the hard pp scattering as pile-up jets.

4.4 Event reconstruction

Events are required to have a primary vertex [172, 173] reconstructed from at least two tracks [174] with $p_{\mathrm{T}} > 500$ MeV. Among the vertices found, the vertex with the largest summed p_{T}^2 of the associated tracks is designated as the primary vertex.

Calorimeter jets are built from topological clusters of energy in the calorimeter [175], calibrated to the electromagnetic scale, using the anti-k_t algorithm with radius parameter $R = 0.4$ [52, 176]. These types of jets are referred to as 'jets'. Jet transverse momenta are further corrected to the corresponding particle-level jet p_{T}, based on the simulation [54]. Remaining differences between data and simulated events are evaluated and corrected for using in situ techniques, which exploit the transverse momentum balance between a jet and a reference object such as a photon, Z boson, or multijet system in data. After these calibrations, all jets in the event with $p_{\mathrm{T}} > 20$ GeV and $|\eta| < 4.5$ must satisfy a set of loose jet-quality requirements [177]. In the four-body analysis, the leading jet in p_{T} must satisfy a set of tighter jet-quality requirements. These requirements are designed to reject jets originating from sporadic bursts of detector noise, large coherent noise or isolated pathological cells in the calorimeter system, hardware issues, beam-induced background or cosmic-ray muons [177]. If these jet requirements are not met, the event is discarded. All jets are required to have $p_{\mathrm{T}} > 20$ GeV and $|\eta| < 2.8$ to be considered in this analysis. In addition, the 'medium' working point of the track-based jet vertex tagger [178, 55] is required for jets with $p_{\mathrm{T}} < 120$ GeV and $|\eta| < 2.5$, to reject jets that originate from pile-up interactions.

Jets which contain b-hadrons and are within the inner-detector acceptance ($|\eta| < 2.5$) are identified as 'b-tagged' using a multivariate algorithm that exploits the impact parameters[3] of the charged-particle tracks, the presence of secondary vertices, and the reconstructed flight paths of b- and c-hadrons inside the jet [58]. The output of the multivariate algorithm is a single b-tagging output score, which signifies the likelihood of a jet to contain b-hadrons. The average identification efficiency of jets containing b-hadrons is 77% as determined in simulated $t\bar{t}$ events. Using the same simulated

---

[3] The transverse impact parameter, d_0, is defined as the distance of closest approach of a track to the beam-line, measured in the transverse plane. The longitudinal impact parameter, z_0, corresponds to the z-coordinate distance between the point along the track at which the transverse impact parameter is defined and the primary vertex.

sample, a rejection factor of approximately 110 (5) is reached for jets initiated by light quarks and gluons (charm quarks).

In order to identify low-p_{T} b-hadrons that are not contained in jets passing the $p_{\mathrm{T}} > 20$ GeV requirement, 'track-jets' are reconstructed from inner-detector tracks using the anti-$k_{\perp}$algorithm with radius parameter $R = 0.4$. Tracks considered for inclusion in track-jets are required to have $p_{\mathrm{T}} > 500$ MeV, $|\eta| < 2.5$, at least seven hits in the silicon microstrip and pixel detectors, no more than one hit shared by multiple tracks in the pixel detector, no more than one missing hit in the pixel detector, and no more than two missing hits in the silicon microstrip detector. Additional requirements on the longitudinal impact parameter projected along the beam direction ($|z_0 \sin(\theta)| <$ 3 mm) reduce the pile-up contributions and improve the efficiency in selecting tracks from the hard-scatter vertex. Track-jets are required to have $p_{\mathrm{T}} > 5$ GeV, more than one track within the jet radius, $|\eta| < 2.5$, and not overlap with the leading non-b-tagged jet in the event ($\Delta R > 0.4$). The standard b-tagging algorithm is employed for track-jets [179] and the selection requirement is tighter than for regular jets, due to the larger amount of background at low p_{T}. The average identification efficiency for jets containing b-hadrons is 70% as determined in simulated $t\bar{t}$ events. Using the same simulated sample, a rejection factor of approximately 200 (10) is reached for jets initiated by light quarks and gluons (charm quarks).

Electron candidates are reconstructed from clusters of energy deposits in the electromagnetic calorimeter that are matched to a track in the inner detector. They are required to have $|\eta| < 2.47$ and $p_{\mathrm{T}} > 4.5$ GeV, and must pass a loose likelihood-based selection [180, 181]. The impact parameter along the beam direction is required to be less than 0.5 mm. The electromagnetic shower of an electron can also be reconstructed as a jet such that a procedure is required to resolve this ambiguity. In the case where the separation[4] between an electron candidate and a non-b-tagged (b-tagged) jet is $\Delta R_y < 0.2$, the candidate is considered to be an electron (b-tagged jet). This procedure uses a b-tagged jet definition that is looser than the one described earlier, to avoid selecting electrons from heavy-flavour hadron decays. If the separation between an electron candidate and any jet satisfies $0.2 < \Delta R_y < 0.4$, the candidate is considered to be a jet, and the electron candidate is removed.

Muons are reconstructed by matching tracks in the inner detector to tracks in the muon spectrometer and are required to have $|\eta| < 2.7$ and $p_{\mathrm{T}} > 4$ GeV [61]. The impact parameter along the beam direction is required to be less than 0.5 mm. Events containing muons identified as originating from cosmic rays, $|d_0| > 0.2$ mm and $|z_0| > 1$ mm, or as poorly reconstructed, $\sigma(q/p)/|(q/p)| > 0.2$, are removed. Here, $\sigma(q/p)/|(q/p)|$ is a measure of the momentum uncertainty for a particle with charge q. Muons are discarded if they are within $\Delta R = 0.4$ of jets that survive the electron–jet overlap removal, except when the number of tracks associated with the jet is less than three, where the muon is kept and the jet discarded.

The requirements on electrons and muons are tightened for the selection of events in background control regions (described in Section 4.6) containing at least one electron or muon. The electrons and muons passing the tight selection are called 'control' electrons or muons in the following, as opposed to 'baseline' electrons and muons, which are only required to pass the requirements described above. Control electrons and muons are required to satisfy the 'FCLoose' p_{T}-dependent track-based and calorimeter-based isolation criteria [182]. The calorimeter-based isolation is determined by taking the ratio of the sum of energy deposits in a cone of $\Delta R = 0.2$

---

[4] For the overlap removal, rapidity (y) is used instead of pseudorapidity: $y = \frac{1}{2}\ln\frac{E+p_z}{E-p_z}$, where E is the energy and p_z is the z-component of the momentum of the object. The separation is then defined as $\Delta R_y \equiv \sqrt{(\Delta y)^2 + (\Delta\phi)^2}$.

around the electron or muon candidate to the sum of energy deposits associated with the electron or muon. The track-based isolation is estimated in a similar way but using a variable cone size with a maximum value of $\Delta R = 0.2$ for electrons and $\Delta R = 0.3$ for muons. Electron candidates are required to pass a 'tight' likelihood-based selection. The impact parameter of the electron in the transverse plane is required to be less than five times the transverse impact parameter uncertainty (σ_{d_0}). Further selection criteria are also imposed on reconstructed muons: muon candidates are required to pass a 'medium' quality selection and meet the $|d_0| < 3\sigma_{d_0}$ requirement.

The $\mathbf{p}_{\mathrm{T}}^{\mathrm{miss}}$ vector is the negative vector sum of the p_{T} of all selected and calibrated electrons, muons, and jets in the event, plus an extra term ('soft' term) added to account for energy depositions in the event that are not associated with any of the objects. The 'soft' term is calculated from inner-detector tracks ($p_{\mathrm{T}} > 500$ MeV and matched to the primary vertex, to make it resilient to pile-up contamination) not associated with selected objects [183, 60]. The missing transverse momentum calculated using only the tracking system (denoted by $\mathbf{p}_{\mathrm{T}}^{\mathrm{miss,track}}$, with magnitude $E_{\mathrm{T}}^{\mathrm{miss,track}}$) is computed from the vector sum of the inner-detector tracks with $p_{\mathrm{T}} > 500$ MeV and $|\eta| < 2.5$ that are associated with the event's primary vertex.

Hadronically decaying τ-lepton candidates are identified as non-b-tagged jets with $|\eta| < 2.5$ and a maximum of four inner-detector tracks matched to them. They are only used in some regions to veto events with τ-lepton candidates most likely originating from $W \rightarrow \tau\nu$ decays, which are identified with the additional requirement that the $\Delta\phi$ between the τ-lepton candidate and the $\mathbf{p}_{\mathrm{T}}^{\mathrm{miss}}$ is less than $\pi/5$.

4.5 Signal region definitions

The experimental signature of this search, for all signal topologies, consists of multiple jets, one or two of which are b-tagged, no electrons and muons (following the baseline definition described in Section 4.4), and large missing transverse momentum. The $E_{\mathrm{T}}^{\mathrm{miss}}$ trigger is used to collect the data in all signal regions.

Beyond these common requirements, four sets of signal regions (SRA–D) are defined to target each decay topology and kinematic regime, as shown in Figure 39. SRA (SRB) is sensitive to the production of high-mass $\tilde{t}$ pairs that each undergo a two-body decay with large (medium) $\Delta m(\tilde{t}, \tilde{\chi}_1^0)$, or the production of high-mass leptoquark pairs. Both SRA and SRB employ top-quark mass-reconstruction techniques to reject background, of which the dominant source is associated production of a Z boson with heavy-flavour jets, with the Z decaying into neutrinos ($Z+$jets). SRC targets compressed two/three-body top squark decays with $\Delta m(\tilde{t}, \tilde{\chi}_1^0) \sim m_t$ and has $t\bar{t}$ production as the dominant background contribution. A common preselection is defined for SRA–C: at least four jets are required ($\mathrm{N}_{\mathrm{jets}} \geq 4$), at least two of which must be b-tagged ($\mathrm{N}_{\mathrm{b-jet}} \geq 2$), and the leading four jets must satisfy $p_{\mathrm{T}} > 80, 80, 40, 40$ GeV. SRD targets highly compressed four-body top squark decays and uses track-jets to identify b-hadrons with low p_{T}. As in SRA and SRB, the dominant source of background in SRD is Z + jets. In both SRC and SRD, a high-p_{T} jet originating from ISR is used to improve sensitivity to the targeted decays. Only signal regions A and B and their backgrounds are described in detail in this chapter.

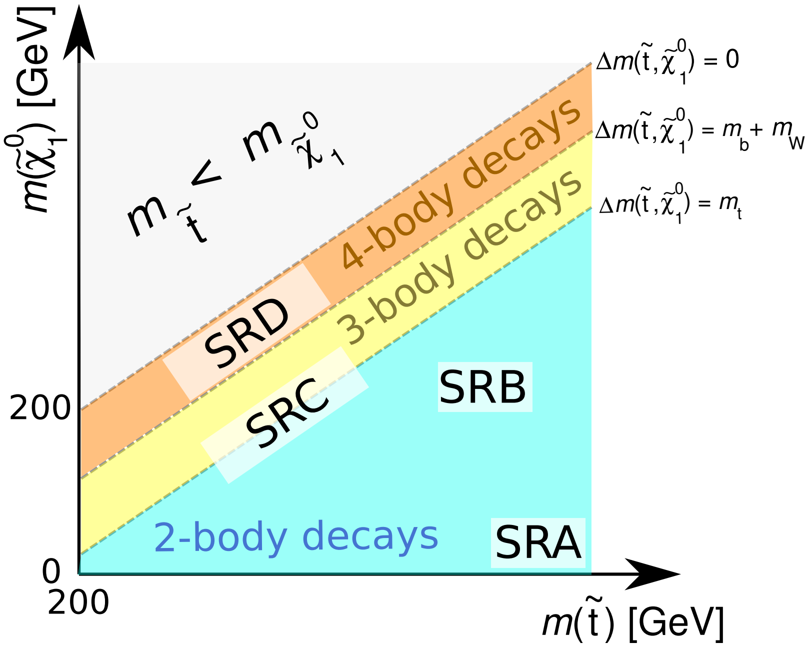

Figure 39. Schematic representation of the various topologies targeted by the different signal regions defined in the analysis (SRA, SRB, SRC, SRD). SRA and SRB are orthogonal and the exact requirements made in the signal regions are detailed in the text and Table 8.

4.5.1 Signal regions A and B

SRA is optimised for exclusion at 95% confidence level (CL) of the scenario where $m_{\tilde{t}} = 1300$ GeV and $m_{\tilde{\chi}_1^0} = 1$ GeV, while SRB is optimised for $m_{\tilde{t}} = 700$ GeV and $m_{\tilde{\chi}_1^0} = 400$ GeV. SRA and SRB have the best sensitivity to up-type, third-generation scalar leptoquarks, when leptoquarks decay via $\mathrm{LQ}_3^{\mathrm{u}} \rightarrow t\nu$.

To avoid a loss of efficiency when the top quark has $p_{\mathrm{T}} > 200$ GeV and its daughters are close to each other, the two hadronic top candidates are reconstructed by using the anti-k_{T} algorithm to cluster $R = 0.4$ jets, using radius parameters of $R = 0.8$ and $R = 1.2$, similar to the technique used in the previous ATLAS search [108]. Each reclustered jet is assigned a mass which is computed from the four-momenta of its jet constituents. Two $R = 1.2$ reclustered jets, representing top candidates, are required, and the leading reclustered $R = 1.2$ jet must have a mass ($m^{1}_{\text{jet},R=1.2}$) greater than 120 GeV. To optimise signal efficiency regardless of the subleading top candidate reconstruction success (measured by how close the candidate mass is to the top quark mass), the events are divided into three categories based on the subleading $R = 1.2$ reclustered jet mass ($m^{2}_{\text{jet},R=1.2}$): the 'TT' category includes events with $m^{2}_{\text{jet},R=1.2} > 120$ GeV, corresponding to successfully reconstructing a subleading top candidate; the 'TW' category contains events with $60 < m^{2}_{\text{jet},R=1.2} < 120$ GeV, corresponding to successfully reconstructing a subleading W candidate; and the 'T0' category represents events with $m^{2}_{\text{jet},R=1.2} < 60$ GeV, corresponding to not reconstructing a top nor a W candidate.

In SRA, in addition to using the mass of the reclustered jets, information about the flavour content of the reclustered jet is used to improve background rejection. For all SRA categories, a b-tagged jet is required to be within $\Delta R = 1.2$ of the leading reclustered $R = 1.2$ jet, $j_1^{R=1.2}(b)$, while in the SRA-TT category, the same selection is made for the subleading $R = 1.2$ jet, $j_2^{R=1.2}(b)$. A requirement is also made on the leading $R = 0.8$ reclustered jet mass ($m^{1}_{\text{jet},R=0.8} > 60$ GeV) in SRA.

In order to reject events with mismeasured $E_{\text{T}}^{\text{miss}}$ originating from multijet and hadronic $t\bar{t}$ decays, the minimum difference in azimuthal angle between the $\mathbf{p}_{\text{T}}^{\text{miss}}$ and the leading four jets ($|\Delta\phi\,(\text{jet}^{1-4}, E_{\text{T}}^{\text{miss}})|$) is required to be greater than 0.4.

The most powerful rejection of background comes from requiring that the object-based $E_{\text{T}}^{\text{miss}}$ significance (Object based $E_{\text{T}}^{\text{miss}}$ sig.) [122] is greater than 25 (14) in SRA (SRB). This variable characterises the $E_{\text{T}}^{\text{miss}}$ according to the p_{T}, p_{T} resolution, and ϕ resolution of all objects in the event, and is defined as:

$$\text{Object based}\, E_{\text{T}}^{\text{miss}}\, \text{sig.} \;=\; \frac{E_{\text{T}}^{\text{miss}}}{\sqrt{\sigma_{\text{L}}^{2}(1-\rho_{\text{LT}}^{2})}},$$

where σ_{L} is the expected resolution of the total longitudinal momentum (relative to the direction of $\mathbf{p}_{\mathrm{T}}^{\mathrm{miss}}$) of all objects in the event as a function of the p_{T} of each object. Likewise, ρ_{LT} is the correlation factor between the longitudinal and transverse momentum resolutions for all objects.

Substantial $t\bar{t}$ background rejection is provided by additional requirements to reject events in which one W boson decays via a lepton plus neutrino. The first requirement is that the transverse mass (m_{T}) calculated from the $E_{\mathrm{T}}^{\mathrm{miss}}$ and the b-tagged jet closest in ϕ to the $\mathbf{p}_{\mathrm{T}}^{\mathrm{miss}}$ direction and defined as:

$$m_{\mathrm{T}}^{b,\mathrm{min}} = \sqrt{2\, p_{\mathrm{T}}^{b}\, E_{\mathrm{T}}^{\mathrm{miss}} \left[1 - \cos\Delta\phi\left(\mathbf{p}_{\mathrm{T}}^{b}, \mathbf{p}_{\mathrm{T}}^{\mathrm{miss}}\right)\right]},$$

must be above 200 GeV. The second requirement consists of vetoing events containing hadronic τ-lepton candidates likely to have originated from a $W \to \tau\nu$ decay (τ-veto).

To reject events that contain b-tagged jets from gluon splitting, requirements are made on the angular distance between the two leading b-tagged jets, $\Delta R\,(b, b)$. In SRB, an additional requirement of $m_{\mathrm{T}}^{b,\mathrm{max}} > 200$ GeV is made, where $m_{\mathrm{T}}^{b,\mathrm{max}}$ is analogous to $m_{\mathrm{T}}^{b,\mathrm{min}}$ except that the transverse mass is computed with the b-tagged jet that has the largest $\Delta\phi$ relative to the $\mathbf{p}_{\mathrm{T}}^{\mathrm{miss}}$ direction. This requirement is a more stringent version of $m_{\mathrm{T}}^{b,\mathrm{min}}$, requiring that the leading two b-tagged jets are not near the $\mathbf{p}_{\mathrm{T}}^{\mathrm{miss}}$.

Finally, to allow the statistical combination of SRA and SRB, SRA is required to have the m_{T2,χ^2} variable greater than 450 GeV, while SRB is required to have $m_{\mathrm{T2},\chi^2} < 450$ GeV. The m_{T2,χ^2} variable is based on m_{T2} [184, 185] and is constructed from the direction and magnitude of $\mathbf{p}_{\mathrm{T}}^{\mathrm{miss}}$ and the direction of each of the top candidates, reconstructed using a χ^2-like method with $R = 0.4$ jets as inputs. The minimisation for finding the top candidates used in m_{T2,χ^2} is performed in terms of a χ^2-like penalty function, $\chi^2 = (m_{\mathrm{cand}} - m_{\mathrm{true}})^2/m_{\mathrm{true}}$, where m_{cand} is the top quark or W boson candidate mass and m_{true} is set to 80.4 GeV for W boson candidates and 173.2 GeV for top quark candidates.[5] Initially, single or pairs of $R = 0.4$ jets, whichever configuration results in a mass closest to m_W, form W boson candidates, which are then combined with additional b-tagged jets in the event to construct top quark candidates. When calculating m_{T2,χ^2} the momenta of top quark candidates selected by the χ^2 method are used, while the masses of the top quarks are set to 173.2 GeV and the invisible particles are assumed to be massless. Table 8 summarises all the selection criteria used in SRA and SRB.

In addition to SRA and SRB, which are optimised for high $m_{\tilde{t}}$ via a statistical combination, a signal region is optimised for discovery. This region, SRA-TT-Disc, has the same requirements as SRA-TT, with the exception of a less stringent requirement of Object based $E_{\mathrm{T}}^{\mathrm{miss}}$ sig. > 11. When setting exclusion limits on specific signal models, SRA-TT-Disc is not considered.

---

[5] These mass values were the world averages of the W boson and top quark masses at the time of the development of this method which was for the last iteration of this search [108]. Updated measurements of the masses of the W boson and top quark have a negligible effect on this method and thus were not included.

Table 8. Selection criteria for SRA and SRB. Each signal region is separated into three categories based on reconstructed top candidate masses. A dash indicates that no selection is applied.

Variable/SR	**SRA-TT**	**SRA-TW**	**SRA-T0**	**SRB-TT**	**SRB-TW**	**SRB-T0**
Trigger	$E_{\mathrm{T}}^{\mathrm{miss}}$					
$E_{\mathrm{T}}^{\mathrm{miss}}$	> 250 GeV					
N_{ℓ}	exactly 0					
$\mathrm{N}_{\mathrm{jets}}$	≥ 4					
p_{T}^{2}	> 80 GeV					
p_{T}^{4}	> 40 GeV					
$\lvert\Delta\phi\,(\mathrm{jet}^{1-4}, E_{\mathrm{T}}^{\mathrm{miss}})\rvert$	> 0.4					
$\mathrm{N}_{\mathrm{b-jet}}$	≥ 2					
$m_{\mathrm{T}}^{b,\mathrm{min}}$	> 200 GeV					
τ-veto	✓					
$m_{\mathrm{jet},R=1.2}^{1}$	> 120 GeV					
$m_{\mathrm{jet},R=1.2}^{2}$	> 120 GeV	60–120 GeV	< 60 GeV	> 120 GeV	60–120 GeV	< 60 GeV
$m_{\mathrm{jet},R=0.8}^{1}$	> 60 GeV			–		
$j_{1}^{R=1.2}(b)$	✓			–		
$j_{2}^{R=1.2}(b)$	✓	–				
$\Delta R\,(b, b)$	> 1.0	–		> 1.4		
$m_{\mathrm{T}}^{b,\mathrm{max}}$	–			> 200 GeV		
Object based $E_{\mathrm{T}}^{\mathrm{miss}}$ sig.	> 25			> 14		
$m_{\mathrm{T2},\chi^{2}}$	> 450 GeV			< 450 GeV		

4.6 Background estimation

The main SM background process in SRA, SRB, and SRD is $Z \to \nu\bar{\nu}$ production in association with heavy-flavour jets. In SRC, $t\bar{t}$ production dominates, including mostly events where one W boson decays hadronically and the other W boson decays via a τ-lepton and its corresponding neutrino (W + jets). Other important background processes include leptonic W decays produced in association with heavy-flavour jets, a single top quark produced with a W boson, and the irreducible background from $t\bar{t} + Z$, where the Z boson decays into two neutrinos.

Significant background contributions are estimated primarily from comparisons between data and simulation in specially designed 'control regions' (CRs), which have a selection orthogonal to all SRs and aim to enhance a particular background process, while probing a similar event topology. Sufficient data are needed to minimise the statistical uncertainties in the background estimates in the CRs, while the extrapolation from the CR to the SR, evaluated with simulated events, should be as small as possible to reduce the associated systematic uncertainties. Furthermore, CR selection criteria are chosen to minimise potential contamination by signal. The signal contamination is below 10% in all CRs for top squark and neutralino mass combinations that have not yet been excluded at 95% confidence level by previous ATLAS searches [107, 108, 109, 110, 112, 13].

Separate CRs are defined for SRA–B, SRC and SRD, with the observed number of events in each region included in one of the three dedicated binned profile likelihood fits [186] of the analysis (SRA–B fit, SRC fit, SRD fit). The CRs are defined so that all CRs associated with a given signal region are orthogonal to the other CRs for that specified region. Partial overlaps remain possible between regions included in different fits. Each likelihood function is built as the product of Poisson probability density functions, describing the observed and expected numbers of events in the control regions. Additional terms, constrained by Gaussian probability density functions accounting for MC statistics and common systematic uncertainties (discussed in Section 4.7) between the control and signal regions and their correlations, are included and treated as nuisance parameters in the fitting procedure.

Control regions targeting the Z + jets, $t\bar{t}$, W + jets, single-top and $t\bar{t}$ $+Z$ backgrounds are included in the SRA–B fit, while for the SRC fit only a $t\bar{t}$ control region is defined. For the SRD fit, control regions are defined for $Z +$ jets, $t\bar{t}$, and $W +$ jets backgrounds. For each fit (SRA–B, SRC, and SRD), the normalisations of these backgrounds are determined simultaneously in order to best match the observed data in each control region, including contributions from all backgrounds (background-only fit). No observed or expected number of events in the signal regions is considered at this stage. In cases where there are multiple control regions for one background in one fit, the fit yields one normalisation which best fits all regions.

Contributions from all-hadronic $t\bar{t}$ and multijet production are found to be negligible in all signal regions except for SRC, where they are subdominant. These backgrounds are estimated from data collected by single-jet triggers using a jet smearing procedure described in Ref. [187] and are fixed in the fit, with an uncertainty assigned to them (discussed in Section 4.7). The contributions from all other background processes (diboson, tZ, $t\bar{t}H$, $t\bar{t}W$, tWZ) are less than 15% of the total SM background expectations and are fixed at the value expected from the simulation, using the most accurate theoretical cross sections available, while their uncertainties are included as additional nuisance parameters in the fit. In the following, the multijet, diboson, tZ, $t\bar{t}H$, $t\bar{t}W$, and tWZ backgrounds are grouped together and referred to as 'other'.

Validation regions (VRs) are defined for the major sources of background in each signal region such that they are orthogonal to the control regions and the signal regions. They usually suffer from a higher signal contamination (up to 20%) than the CRs, but probe a kinematic region which is closer to that of the SRs. The background normalisation factors from the simultaneous fit are applied to their respective backgrounds and compared with data in each VR to verify good agreement and that the simultaneous fit is well-behaved.

Detailed CR definitions for the estimation of Z + jets (CRZ), $t\bar{t}$ +Z (CRTTZ), $t\bar{t}$ (CRT), W + jets (CRW), and single-top (CRST) backgrounds are described in the following subsections, while a summary of the control region strategy in the SRA–B and SRD fits is shown in Figure 40. The strategy for SRC only involves one control region (extrapolating from an electron or muon multiplicity of zero in the SR to an electron or muon multiplicity of one in the CR) and one validation region (extrapolating over $\Delta\phi_{\mathrm{ISR},E_{\mathrm{T}}^{\mathrm{miss}}}$) for the dominant $t\bar{t}$ background.

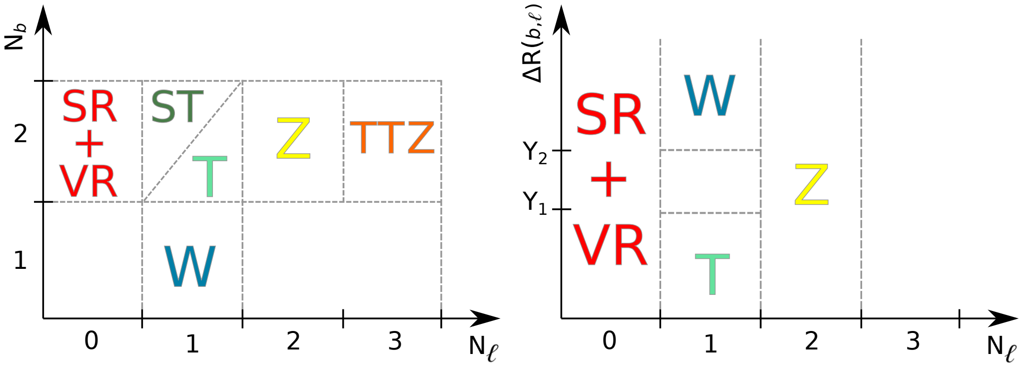

(a) (b)

Figure 40. A summary of the background control region strategy used in the (a) SRA–B and (b) SRD fits. The orthogonality between the Z + jets (Z), $t\bar{t}$ +Z (TTZ), $t\bar{t}$ (T), W + jets (W), and single-top (ST) backgrounds' control regions and the signal and validation regions (SR+VR) included in the SRA–B fit rely on the number of leptons, N_ℓ, and the number of b-tagged jets, N_b. T and ST are made orthogonal by selecting either low-p_{T} ($<$ 20 GeV) or high-p_{T} ($>$ 27 GeV) leptons, respectively. The orthogonality between the Z + jets (Z), $t\bar{t}$ (T), and W + jets (W) backgrounds' control regions and the signal and validation regions (SR+VR) included in the SRD fit relies on N_ℓ and, for $N_\ell = 1$, the angular distance between the lepton and the closest b-tagged jet (b-tagged track-jet in CRWD0), $\Delta R(b,\ell)$. Placeholders for the values of $\Delta R(b,\ell)$ are shown as Y_1 and Y_2 and vary in different SRD regions depending on N_b. Additional selections not appearing on the sketches ensure orthogonality between the SR and the VR. Additional extrapolations from CRs to SRs in other kinematic quantities not necessarily shown in this sketch are region-specific and detailed in the text.

4.6.1 Z + jets background estimation

The normalisation of the simulation of $Z \to \nu\bar{\nu}$ produced in association with heavy-flavour jets is estimated from $Z \to e^+e^-$ and $Z \to \mu^+\mu^-$ events produced in association with heavy-flavour jets, which is the strategy adopted for SRA–B (CRZAB) and SRD (CRZD). Data events passing a single-electron or single-muon trigger are considered, and events with two control electrons or two control muons with opposite charge are selected. In CRZAB (CRZD), $p_{\mathrm{T}}^{\ell} > 27, 20$ GeV ($p_{\mathrm{T}}^{\ell} > 30, 20$ GeV) is required for the leading and subleading leptons, respectively, which must also have an invariant mass within 10 GeV of the Z boson mass, $m_Z = 91$ GeV. Events with $E_{\mathrm{T}}^{\mathrm{miss}} > 50$ GeV ($E_{\mathrm{T}}^{\mathrm{miss}} > 70$ GeV) in CRZAB (CRZD) are discarded in order to reject $t\bar{t}$ events. The transverse momenta of the selected electrons or muons are vectorially added to the $\mathbf{p}_{\mathrm{T}}^{\mathrm{miss}}$ to mimic the $Z(\nu\nu)$ + jets decays in the SRs, forming the quantity $E_{\mathrm{T}}^{\mathrm{miss}\prime}$. High-$p_{\mathrm{T}}$ Z bosons are then effectively selected by requiring large $E_{\mathrm{T}}^{\mathrm{miss}\prime}$.

Recalculated quantities that use $E_{\mathrm{T}}^{\mathrm{miss}\prime}$ instead of $E_{\mathrm{T}}^{\mathrm{miss}}$ are identified by the addition of a prime (e.g. $m_{\mathrm{T}}^{b,\mathrm{min}\prime}$). Where possible, the CR selection criteria are identical to the criteria used in the signal region; however, the criteria for key variables such as $m_{\mathrm{T}}^{b,\mathrm{min}\prime}$ and Object based $E_{\mathrm{T}}^{\mathrm{miss}\prime}$ sig. for CRZAB, or $E_{\mathrm{T}}^{\mathrm{miss}}/\sqrt{H_{\mathrm{T}}'}$ for CRZD, are loosened to enhance the number of data events in the CR. The Z + jets CR included in the SRA–B (SRD) fit is split into two (three) categories depending on $m^2_{\mathrm{jet},R=1.2}$ ($\mathrm{N_{b-jet}}$), to minimise the extrapolation across the various SR categories. There are only two categories in CRZAB, CRZAB-TTTW (representing the background in the TT and TW signal categories) and CRZAB-T0, due to the limited number of data events. The detailed set of selection criteria for the Z + jets CRs are presented in

Table 9; representative distributions for CRZ variables that have looser requirements than in the SRs are shown in Figure 41.

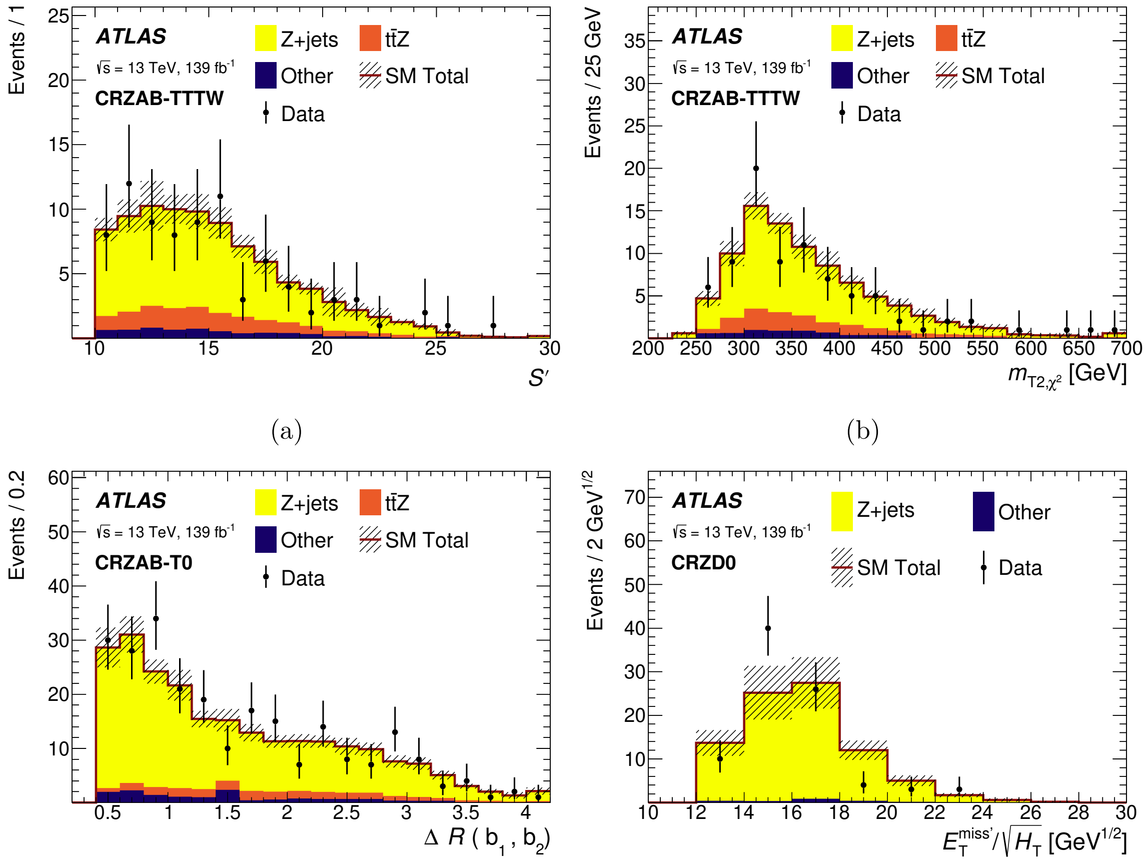

(a) (b)

(c) (d)

Figure 41. Distributions illustrating the level of agreement between data (points) and the SM expectation (stacked histograms, after simultaneously fitting to all backgrounds) in several Z + jets control regions: (a) Object based $E_{\mathrm{T}}^{\mathrm{miss}\prime}$ sig. and (b) m_{T2,χ^2} for CRZAB-TTTW, (c) $\Delta R\,(b, b)$ for CRZAB-T0, and (d) $E_{\mathrm{T}}^{\mathrm{miss}\prime}/\sqrt{H_{\mathrm{T}}}$ for CRZD0. The hatched uncertainty band around the SM expectation includes the combination of MC statistical, theory-related and detector-related systematic uncertainties. The rightmost bin in each plot includes all overflows.

Table 9. Selection criteria for the Z + jets control regions. The defining extrapolation for these control regions is over the number of leptons; two electrons or muons (ℓ) from Z decays are required, compared with zero leptons in the signal regions. A dash indicates that no selection is applied. Variables for which the signal and control region requirements differ are highlighted by a thick border around the cell that contains the requirement. Requirements are made on the following variables in the signal regions but have no equivalent requirement in the control regions: τ-veto, $m^1_{\text{jet},R=0.8}$, $j_1^{R=1.2}(b)$, $j_2^{R=1.2}(b)$, $\Delta R\,(b,b)$, $m_{\mathrm{T}}^{b,\max}$, m_{T2,χ^2}, $E_{\mathrm{T}}^{\text{miss,track}}$, and $\left|\Delta\phi\left(E_{\mathrm{T}}^{\text{miss}}, E_{\mathrm{T}}^{\text{miss,track}}\right)\right|$.

Variable/CR	**CRZAB-TTTW**	**CRZAB-T0**	**CRZD0**	**CRZD1**	**CRZD2**
Trigger	single electron or muon				
Control ℓ	exactly 2, same flavour / opposite sign				
Additional baseline ℓ	0				
$m(\ell,\ell)$	81–101 GeV				
$E_{\mathrm{T}}^{\text{miss}}$	< 50 GeV		< 70 GeV		
p_{T}^{ℓ}	> 27, > 20 GeV		> 30, > 20 GeV		
$E_{\mathrm{T}}^{\text{miss}\prime}$	> 200 GeV		> 250 GeV	> 150 GeV	> 200 GeV
$\mathrm{N_{jets}}$	≥ 4		–		
p_{T}^{2}	> 80 GeV		–		
p_{T}^{4}	> 40 GeV		–		
$\mathrm{N_{b-jet}}$	≥ 2		exactly 0	exactly 1	≥ 2
$m^1_{\text{jet},R=1.2}$	> 80 GeV		–		
$m^2_{\text{jet},R=1.2}$	> 60 GeV	< 60 GeV	–		
$m_{\mathrm{T}}^{b,\min\prime}$	> 150 GeV		–		
Object based $E_{\mathrm{T}}^{\text{miss}\prime}$ sig.	> 10		–		
$p_{\mathrm{T}}^{\text{jISR}}$	–		> 250 GeV	> 200 GeV	> 250 GeV
$\left\|\Delta\phi\left(\text{non}-\text{b}, E_{\mathrm{T}}^{\text{miss}}\right)\right\|$	–		> 2.4		
$\mathrm{N_{b-jet}^{VR}}$	–		≥ 1		–
$\left\|\Delta\phi\left(\text{jet}^{1-4}, E_{\mathrm{T}}^{\text{miss}}\right)\right\|$	–		> 0.4	–	
$\|\eta^{b_1,\text{VR}}\|$	–		< 1.2	–	
$\max\left\|\Delta\phi\left(\text{non}-\text{b}, \text{b}^{\text{VR}}\right)\right\|$	–		> 2.2	–	
$\left\|\Delta\phi\left(b_1^{\text{VR}}, b_2^{\text{VR}}\right)\right\|$	–		< 2.5	–	
$p_{\mathrm{T}}^{b_1,\text{VR}}$	–		< 50 GeV	> 10 GeV	–
$p_{\mathrm{T}}^{1,\text{VR}}$	–			< 40 GeV	–
$\min\left\|\Delta\phi\left(\text{jet}^{\text{VR }1-4}, \text{non}-\text{b}\right)\right\|$	–			> 1.2	–
$\|\eta^{b_1}\|$	–			< 1.6	–
$\|\Delta\phi\,(\text{non}-\text{b}, b_1)\|$	–			> 1.8	> 2.2
$\|\eta^{b_2}\|$	–				< 1.2
$p_{\mathrm{T}}^{b_1}$	–				< 175 GeV
$\|\Delta\phi\,(\text{non}-\text{b}, b_2)\|$	–				> 1.6
$E_{\mathrm{T}}^{\text{miss}\prime}/\sqrt{H_{\mathrm{T}}}$	–		$> 12\sqrt{\text{GeV}}$	$> 8\sqrt{\text{GeV}}$	

4.6.2 $\mathrm{t\bar{t}}$ + Z background estimation

The SM production of $t\bar{t}+Z$, where $Z \to \nu\bar{\nu}$, is a significant source of background in SRA and SRB and is largely irreducible. To estimate this background, a three-lepton (electrons and muons) region is defined, to maximise the purity of $t\bar{t} + Z$.

Events that pass a single-electron or single-muon trigger are selected. The trigger electron or muon must pass the requirements for a control electron or muon and have offline $p_{\mathrm{T}} > 27$ GeV. Exactly two additional control leptons (electrons or muons) with $p_{\mathrm{T}} > 20$ GeV are required. The sum of the charges of the three leptons is required to equal 1 or -1, while two of the leptons are required to have the same flavour and opposite charge. The pair of same-flavour, opposite-sign leptons that is most consistent with the Z boson mass forms the Z boson candidate and is required to have an invariant mass satisfying 81 GeV $< m(\ell,\ell) <$ 101 GeV. The Z boson candidate is required to have $p_{\mathrm{T}} > 200$ GeV. The remaining lepton and the $\mathbf{p}_{\mathrm{T}}^{\mathrm{miss}}$ are treated as non-b-tagged jets in the computation of all jet-related variables (such as p_{T}), to mimic hadronic W decays.

Four jets are required to be in the event, in addition to the lepton not associated with the Z boson candidate and the $\mathbf{p}_{\mathrm{T}}^{\mathrm{miss}}$, and two of the jets are required to be b-tagged jets. The selection criteria are summarised in Table 10. Representative distributions for CRTTZ variables that have looser requirements than in the SRs are shown in Figure 42.

Table 10. Selection criteria for the $t\bar{t}+Z$ control region. The defining extrapolation for these control regions is over the number of leptons; three leptons (a combination of electrons and muons) from W and Z decays is required, compared with zero leptons in the signal region. Variables for which the signal and control region requirements differ are highlighted by a thick border around the cell that contains the requirement. Requirements are made on the following variables in SRA and SRB but have no equivalent requirement in the control region: $|\Delta\phi\,(\text{jet}^{1-4}, E_{\mathrm{T}}^{\mathrm{miss}})|$, $m_{\mathrm{T}}^{b,\mathrm{min}}$, τ-veto, $m^{1}_{\mathrm{jet},R=1.2}$, $m^{2}_{\mathrm{jet},R=1.2}$, $m^{1}_{\mathrm{jet},R=0.8}$, $j_1^{R=1.2}(b)$, $j_2^{R=1.2}(b)$, $\Delta R\,(b,b)$, $m_{\mathrm{T}}^{b,\mathrm{max}}$, Object based $E_{\mathrm{T}}^{\mathrm{miss}}$ sig. , and m_{T2,χ^2}.

Variable/CR	**CRTTZ**
Trigger	single electron or muon
Control ℓ	exactly 3
Additional baseline ℓ	0
Sum of muon and electron charges	$+1$ or -1
ℓ associated with Z	exactly 2, same flavour / opposite sign
$m(\ell,\ell)$	81–101 GeV
p_{T}^{ℓ}	>27, >20, >20 GeV
$p_{\mathrm{T}(\ell,\ell)}$	>200 GeV
$\mathrm{N_{jets}}$	≥ 4
$\mathrm{N_{b-jet}}$	≥ 2
p_{T}^{2} (including $E_{\mathrm{T}}^{\mathrm{miss}}$ and non-Z ℓ)	>80 GeV
p_{T}^{4} (including $E_{\mathrm{T}}^{\mathrm{miss}}$ and non-Z ℓ)	>40 GeV

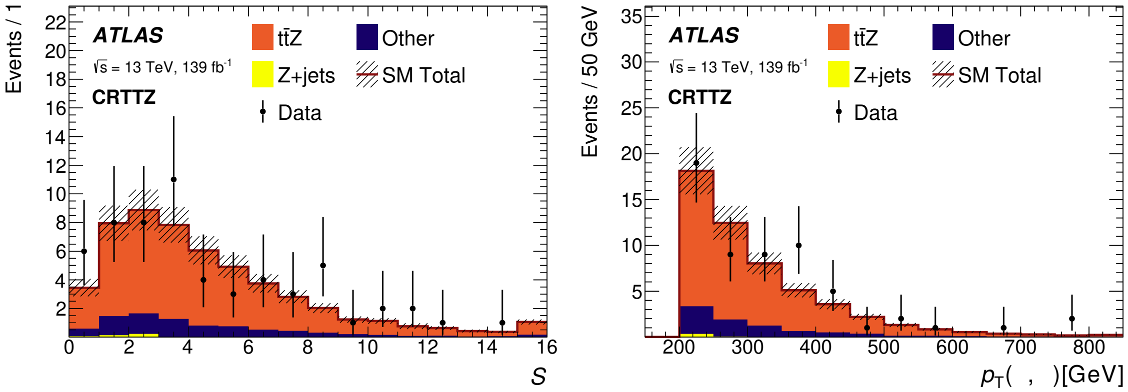

(a) (b)

Figure 42. Distributions illustrating the level of agreement between data (points) and the SM expectation (stacked histograms, after simultaneously fitting to all backgrounds) in the $t\bar{t}$ $+Z$ control region: (a) Object based $E_{\mathrm{T}}^{\mathrm{miss}}$ sig. and (b) $p_{\mathrm{T}(\ell,\ell)}$ for CRTTZ. The hatched uncertainty band around the SM expectation includes the combination of MC statistical, theory-related and detector-related systematic uncertainties. The rightmost bin in each plot includes all overflows.

4.6.3 t$\bar{\text{t}}$, W + jets, and single-top background estimation

The $t\bar{t}$ background in SRB, SRC, and SRD originates from events where a W boson decays into a hadronically decaying τ-lepton, where the τ-lepton is either not reconstructed (due to falling below the jet p_{T} threshold of 20 GeV), or is reconstructed as a jet. In order to model this process in the CRs, events that pass the same $E_{\mathrm{T}}^{\mathrm{miss}}$ trigger as the signal region, but also have a control electron or muon, are selected. The electron or muon is used as a proxy for the τ-lepton in the SRs.

In SRA and SRB, the hadronically decaying τ-leptons are most likely to have fallen below the jet $p_{\mathrm{T}} > 20$ GeV requirement, such that for the $t\bar{t}$ and W + jets control regions (CRTAB and CRWAB, respectively), exactly one control electron in the range $4.5 < p_{\mathrm{T}}^{e} < 20$ GeV or muon in the range $4.0 < p_{\mathrm{T}}^{\mu} < 20$ GeV is required. In SRC and SRD, the hadronically decaying τ-leptons have higher p_{T}, such that one control electron or muon with $p_{\mathrm{T}} > 20$ GeV is required, and is treated as a non-b-tagged jet in the computation of all jet-related variables.

In the $t\bar{t}$ control regions (CRTC, CRTD), the angular separation between the electron or muon and the b-tagged jet closest to the electron or muon, $\Delta R(b, \ell)$, is used to enhance the $t\bar{t}$ purity. In CRTD, $\Delta R(b, \ell)$ is also used to ensure orthogonality with the W + jets control region (CRWD). All $t\bar{t}$ control regions (CRTAB, CRTC, CRTD) have an upper bound on $m_{\mathrm{T}}\left(\ell, E_{\mathrm{T}}^{\mathrm{miss}}\right)$ to preserve orthogonality between the CRs and the signal regions of other ATLAS ongoing studies in the one-lepton plus missing transverse momentum channel, as well as to reduce potential signal contamination. In addition to the variables used in SRC, CRTC has a $m_{\mathrm{V}}/m_{\mathrm{S}} < 0.75$ requirement, where m_{S} is the variable used in SRC and m_{V} is the invariant mass of all visible objects, which provides additional signal rejection. The $t\bar{t}$ CR included in the SRD fit is split into two categories (CRTD1 or CRTD2, which require exactly one or at least two b-tagged jets, respectively) to minimise the extrapolation across the various SR categories. The various $t\bar{t}$ control regions designed for the analysis are defined in Table 11. Representative distributions are shown in Figure 43.

The W + jets background is important for SRA–B and SRD, while the single-top background is significant for SRA–B only; corresponding control regions (CRWAB, CRWD, and CRSTAB, respectively) are defined in Table 12. The W + jets background in SRA–B originates from W boson decays into low-p_{T} τ-leptons; thus, the strategy is similar to that described for CRTAB except that exactly one b-tagged jet is required, which makes CRWAB orthogonal to CRTAB. The single-top control region, CRSTAB, is defined as having exactly one control electron or muon with $p_{\mathrm{T}} > 20$ GeV (making CRSTAB orthogonal to both CRWAB and CRTAB) and two or more b-tagged jets. A requirement of $p_{\mathrm{T}} > 20$ GeV is used in CRWD because

Table 11. Selection criteria for the $t\bar{t}$ control regions. The defining extrapolation for these control regions is over the number of leptons; one electron or muon (ℓ) from W decays is required, compared with zero leptons in the signal region. A dash indicates that no selection is applied. Variables for which the signal and control region requirements differ are highlighted by a thick border around the cell that contains the requirement. Requirements are made on the following variables in the signal regions but have no equivalent requirement in the control regions: R_{ISR}, τ-veto, $m^{1}_{\mathrm{jet},R=0.8}$, $j_1^{R=1.2}(b)$, $j_2^{R=1.2}(b)$, $m_{\mathrm{T}}^{b,\mathrm{max}}$, m_{T2,χ^2}.

Variable/CR	**CRTAB**	**CRTC**
Trigger	$E_{\mathrm{T}}^{\mathrm{miss}}$	
$E_{\mathrm{T}}^{\mathrm{miss}}$	> 250 GeV	
Control ℓ	exactly 1	
Additional baseline ℓ	0	
p_{T}^{ℓ}	$4.5\,(4.0) < p_{\mathrm{T}}^{e\,(\mu)} < 20$ GeV	$p_{\mathrm{T}} > 20$ GeV
$m_{\mathrm{T}}\,(\ell, E_{\mathrm{T}}^{\mathrm{miss}})$	< 120 GeV	< 100 GeV
$\mathrm{N}_{\mathrm{jets}}$	≥ 4	
p_{T}^{2}	> 80 GeV	
p_{T}^{4}	> 40 GeV	
$\mathrm{N}_{\mathrm{b-jet}}$	≥ 2	
$\lvert\Delta\phi\,(\mathrm{jet}^{1-4}, E_{\mathrm{T}}^{\mathrm{miss}})\rvert$	> 0.4	–
$m^{1}_{\mathrm{jet},R=1.2}$	> 120 GeV	–
$m_{\mathrm{T}}^{b,\mathrm{min}}$	> 150 GeV	–
$\Delta R\,(b,b)$	> 1.4	–
Object based $E_{\mathrm{T}}^{\mathrm{miss}}$ sig.	> 14	–
$\lvert\Delta\phi\,(\mathrm{jet}^{1,2}, E_{\mathrm{T}}^{\mathrm{miss}})\rvert$	–	> 0.2
$N_{\mathrm{jet}}^{\mathrm{S}}$	–	≥ 4
$N_{\mathrm{b-jet}}^{\mathrm{S}}$	–	≥ 2
$p_{\mathrm{T}}^{\mathrm{ISR}}$	–	> 400 GeV
$p_{\mathrm{T},b}^{1,\mathrm{S}}$	–	> 40 GeV
$p_{\mathrm{T}}^{4,\mathrm{S}}$	–	> 50 GeV
m_{S}	–	> 400 GeV
$\Delta\phi_{\mathrm{ISR},E_{\mathrm{T}}^{\mathrm{miss}}}$	–	> 3.0
$m_{\mathrm{V}}/m_{\mathrm{S}}$	–	< 0.75
$\Delta R(b,\ell)$	–	< 2.0

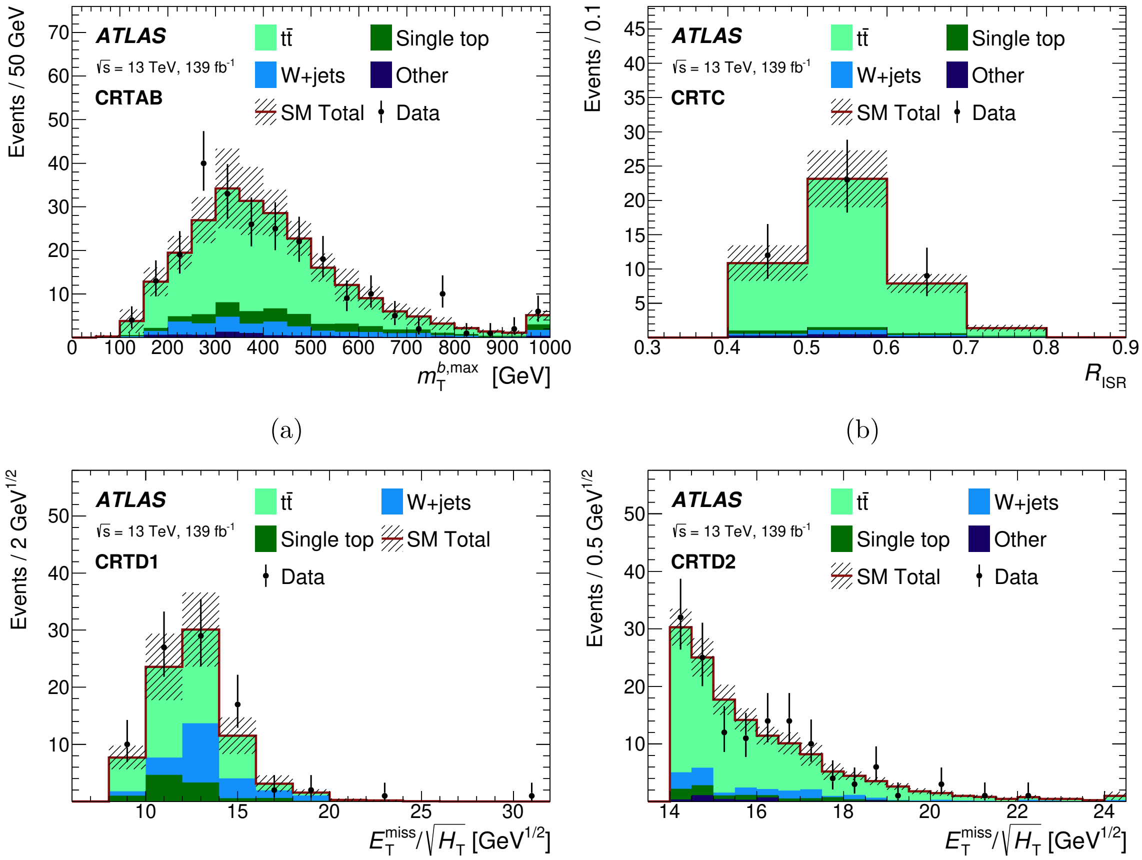

(a)

(b)

(c)

(d)

Figure 43. Distributions illustrating the level of agreement between data (points) and the SM expectation (stacked histograms, after simultaneously fitting to all backgrounds) in the $t\bar{t}$ control regions: (a) $m_{\mathrm{T}}^{b,\max}$ for CRTAB, (b) R_{ISR} for CRTC, and $E_{\mathrm{T}}^{\mathrm{miss}}/\sqrt{H_{\mathrm{T}}}$ for (c) CRTD1 and (d) CRTD2. The hatched uncertainty band around the SM expectation includes the combination of MC statistical, theory-related and detector-related systematic uncertainties. The rightmost bin in each plot includes all overflows.

the W + jets background in SRD is dominated by high-p_{T} electrons, muons, and τ-leptons. To enhance the purity of the W + jets background in CRWD and ensure orthogonality with CRTD, lower bounds are put on $\Delta R(b, \ell)$, which is defined with respect to the b-tagged jet (b-tagged track-jet) closest to the lepton in CRWD1–2 (CRWD0). Representative distributions for the various W + jets and single-top control regions defined in the analysis are shown in Figure 44.

Table 12. Selection criteria for the W + jets and single-top control regions. The defining extrapolation for these control regions is over the number of leptons; one electron or muon (ℓ) from W decays is required compared with zero leptons in the signal regions. A dash indicates that no selection is applied. Variables for which the signal and control region requirements differ are highlighted by a thick border around the cell that contains the requirement. Requirements are made on the following variables in the signal regions but have no equivalent requirement in the control regions: $m^{2}_{\mathrm{jet},R=1.2}$, $m^{1}_{\mathrm{jet},R=0.8}$, $j_1^{R=1.2}(b)$, $j_2^{R=1.2}(b)$, $m_{\mathrm{T}}^{b,\mathrm{max}}$, m_{T2,χ^2}.

<table>
<tr><th>Variable/CR</th><th>CRSTAB</th><th>CRWAB</th></tr>
<tr><td>Trigger</td><td colspan="2">$E_{\mathrm{T}}^{\mathrm{miss}}$</td></tr>
<tr><td>$E_{\mathrm{T}}^{\mathrm{miss}}$</td><td colspan="2">$> 250$ GeV</td></tr>
<tr><td>Control ℓ</td><td colspan="2">exactly 1</td></tr>
<tr><td>Additional baseline ℓ</td><td colspan="2">0</td></tr>
<tr><td>p_{T}^{ℓ}</td><td>$p_{\mathrm{T}} > 20$ GeV</td><td></td></tr>
<tr><td>$m_{\mathrm{T}}\left(\ell, E_{\mathrm{T}}^{\mathrm{miss}}\right)$</td><td colspan="2">$< 100$ GeV</td></tr>
<tr><td>$\mathrm{N_{jets}}$</td><td colspan="2">≥ 4</td></tr>
<tr><td>p_{T}^{2}</td><td colspan="2">> 80 GeV</td></tr>
<tr><td>p_{T}^{4}</td><td colspan="2">> 40 GeV</td></tr>
<tr><td>$\mathrm{N_{b-jet}}$</td><td>≥ 2</td><td>exactly 1</td></tr>
<tr><td>$\left|\Delta\phi\left(\mathrm{jet}^{1-4}, E_{\mathrm{T}}^{\mathrm{miss}}\right)\right|$</td><td colspan="2">$> 0.4$</td></tr>
<tr><td>$m^{1}_{\mathrm{jet},R=1.2}$</td><td>$> 120$ GeV</td><td>< 60 GeV</td></tr>
<tr><td>$m_{\mathrm{T}}^{b,\mathrm{min}}$</td><td colspan="2">$> 200$ GeV</td></tr>
<tr><td>$\Delta R\left(b, b\right)$</td><td>$> 1.4$</td><td>–</td></tr>
<tr><td>$m_{l,b,\mathrm{min}}$</td><td>> 100 GeV</td><td>–</td></tr>
<tr><td>τ-veto</td><td>yes</td><td>–</td></tr>
<tr><td>Object based $E_{\mathrm{T}}^{\mathrm{miss}}$ sig.</td><td colspan="2">> 14</td></tr>
<tr><td>$\Delta R(b, \ell)$</td><td>–</td><td>> 2.0</td></tr>
<tr><td>$p_{\mathrm{T}}^{\mathrm{j^{ISR}}}$</td><td colspan="2">–</td></tr>
</table>

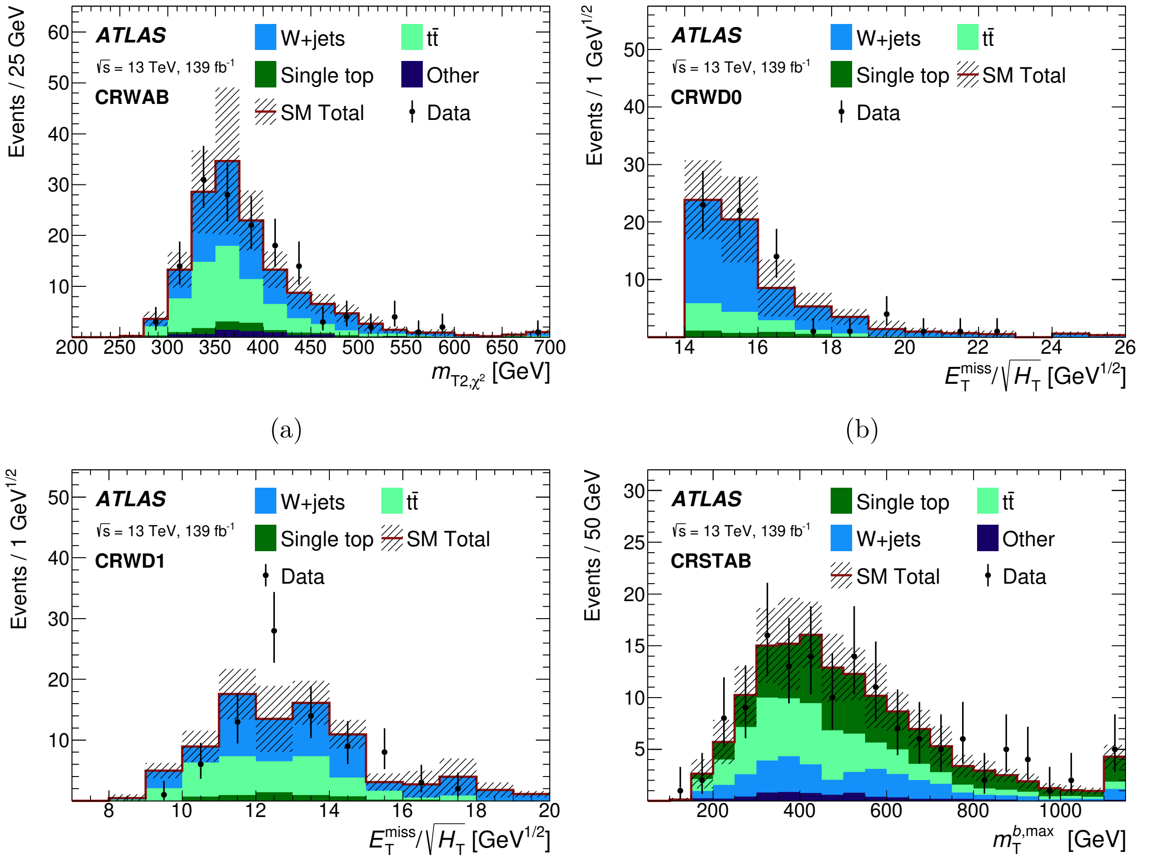

(a) (b)

(c) (d)

Figure 44. Distributions illustrating the level of agreement between data (points) and the SM expectation (stacked histograms, after simultaneously fitting to all backgrounds) in several W + jets and single-top control regions: (a) m_{T2,χ^2} for CRWAB, $E_{\mathrm{T}}^{\mathrm{miss}}/\sqrt{H_{\mathrm{T}}}$ for (b) CRWD0 and (c) CRWD1, and (d) $m_{\mathrm{T}}^{b,\max}$ for CRSTAB. The hatched uncertainty band around the SM expectation includes the combination of MC statistical, theory-related and detector-related systematic uncertainties. The rightmost bin in each plot includes all overflows.

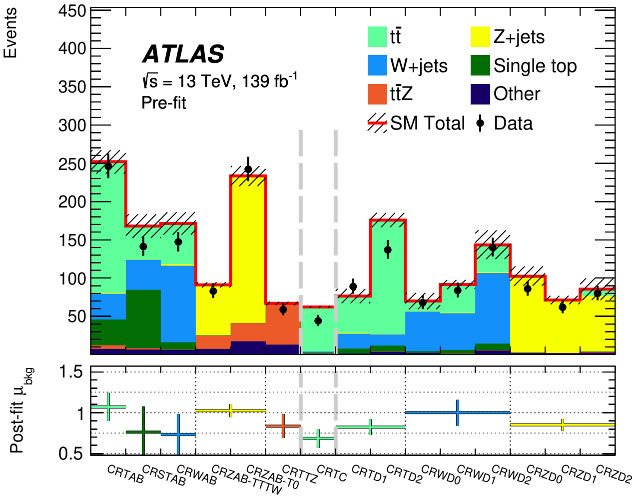

Figure 45. A summary of the normalisation factors determined from the various background-only fits. The total number of data events (points) and the SM expectation (stacked histograms) are shown in each control region before the fit. The uncertainty associated with the SM expectation includes the combination of MC statistical uncertainties, theory-related and detector-related systematic uncertainties. The normalisation factor applied to each background source (μ_{bkg}) after the fit and respective uncertainty, including the combination of MC statistical uncertainties, theory-related and detector-related systematic uncertainties, is shown in the lower panel. The control regions included in the SRA–B, SRC and SRD fits are separated by vertical dashed lines.

4.6.4 Validation of background estimates

The background normalisation factors derived from the SRA–B, SRC and SRD background-only fits are summarised in Figure 45. Most normalisation factors are within 1σ of unity, where σ denotes the total uncertainty, including the data statistical uncertainty in the CRs and the theory-related and detector-related systematic uncertainties (described in Section 4.7). However, the $t\bar{t}$ ($t\bar{t}$ and Z + jets) normalisation factors derived from the SRC (SRD) fit are lower than unity by one to two σ. Significant amounts of ISR radiation are required in SRC, SRD, and the associated control regions, unlike SRA–B and the associated control regions. The simulated event yields in $t\bar{t}$-enriched regions compare differently with data in SRA–B control regions and SRC–D control regions, overestimating the number of events in the latter, while fairly good agreement is observed in the former. A similar effect is observed in CRZAB and CRZD. These observations point to a mismodelling possibly related to the ISR system in $t\bar{t}$ and Z + jets events. The fitting procedure corrects for this mismodelling and is validated in the VRs discussed below.

Validation regions are defined to check the validity of the normalisation factors in the signal regions and to check the ability of the MC to describe the shapes of the kinematic variables over which extrapolations are made in propagating background estimates from the control regions to the signal regions. The defining extrapolation from control to signal regions is in the lepton multiplicity, whereas the validation regions include only events with zero leptons, as in the signal regions. Validation regions are designed for the Z + jets background in SRA (VRZA) and SRB (VRZB-TTTW, VRZB-T0) and SRD (VRZD0–2), as well as for the $t\bar{t}$ background in SRA–B (VRTAB), SRC (VRTC), and SRD (VRTD1–2). Requirements applied in the

SRs are modified in the VRs to ensure orthogonality with the SRs, to limit signal contamination, and to retain a sufficient number of events expected in data. Signal contamination in the VRs, for all signals considered in this search, is kept below 20%.

VRZA is made to be orthogonal to SRA–B by vetoing events where the leading reclustered jet contains a b-tagged jet while still requiring at least two b-tagged jets. Orthogonality between VRZB-TTTW and SRA–B is achieved by inverting the $\Delta R\,(b,b)$ requirement made in SRB, $\Delta R\,(b,b) < 1.4$, and selecting a lower Object based $E_{\mathrm{T}}^{\mathrm{miss}}$ sig. window than in SRA, $15 <$ Object based $E_{\mathrm{T}}^{\mathrm{miss}}$ sig. < 17.

Representative distributions for the validation regions defined in the analysis are shown in Figure 46. A summary of the expected and observed yields in the VRs after the SRA–B, SRC and SRD background-only fits is shown in Figure 47. All the background predictions in the VRs agree with the data within 1σ except the predictions in VRZD2, which agree with the data within 2σ.

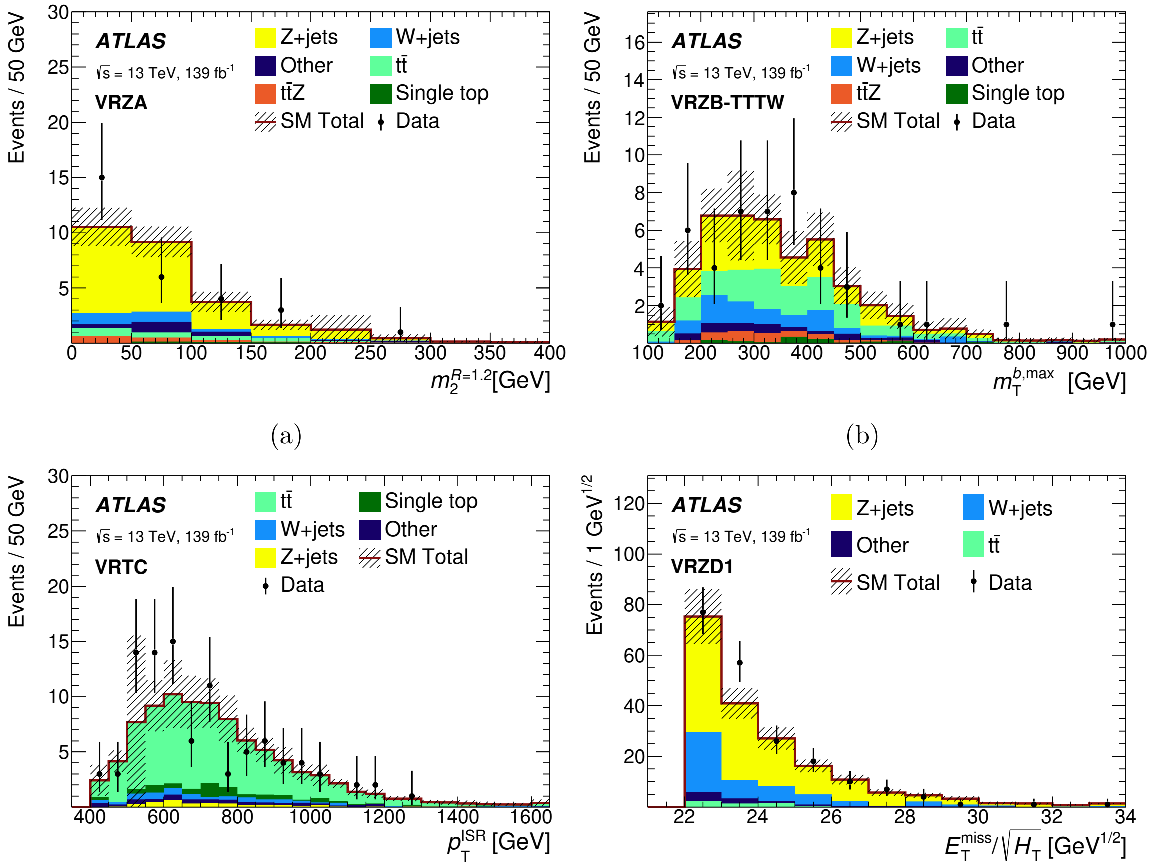

(a)

(b)

(c)

(d)

Figure 46. Distributions illustrating the level of agreement between data (points) and the SM expectation (stacked histograms, after simultaneously fitting to all backgrounds) in several validation regions: (a) $m^2_{\text{jet},R=1.2}$ in VRZA, (b) $m_{\mathrm{T}}^{b,\min}$ in VRZB-TTTW, (c) $p_{\mathrm{T}}^{\mathrm{ISR}}$ in VRTC, and (d) $E_{\mathrm{T}}^{\mathrm{miss}}/\sqrt{H_{\mathrm{T}}}$ in VRZD1. The hatched uncertainty band around the SM expectation includes the combination of MC statistical, theory-related and detector-related systematic uncertainties. The rightmost bin in each plot includes all overflows.

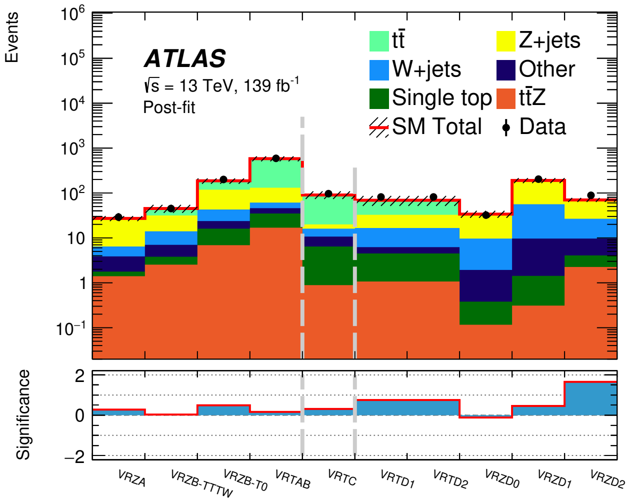

Figure 47. The total number of data events (points) and the SM expectation (stacked histograms) in all validation regions after the SRA–B, SRC and SRD background-only fits. The stacked histograms show the SM prediction and the hatched uncertainty band around the SM prediction shows the total uncertainty, which includes the MC statistical uncertainties, theory-related and detector-related systematic uncertainties. The lower panel shows the significance of the difference between data and the background prediction calculated with the method described in Ref. [188]. The validation regions considered in the SRA–B, SRC and SRD fits are separated by vertical dashed lines.

4.7 Systematic uncertainties

Uncertainties affecting the sensitivity of the analysis which originate from statistical sources are considered together with systematic uncertainties related to the detector calibration (detector-related uncertainties) and physics modelling of signal and background (theory-related uncertainties). The data statistical uncertainty in the number of events in the SRs dominates the total uncertainty in SRA and SRD, while uncertainties related to the physics modelling of the background play a significant role in SRB and SRC.

The impact of detector-related and theory-related systematic uncertainties in the background predictions are included in the profile likelihood fits (described in Section 4.6) as nuisance parameters constrained by Gaussian probability density functions. Their impact is reduced by scaling the dominant background components in the SRs using the data observed in the CRs via the introduction of free-floating normalisation parameters. After the SRA–B and SRD (SRC) background-only fit, none of the nuisance parameters are pulled significantly and most (all) of them are not constrained. The largest constraints are observed in the SRD fit and are on the $t\bar{t}$ modelling uncertainties and reach 30%.

The dominant systematic uncertainties in the background estimates in SRA and SRB (SRC and SRD), expressed as percentages of the total background expectations, are shown in Table 13 (Table 14). By convention, the data statistical uncertainty in the numbers of events in the CRs is accounted for as a systematic uncertainty and included in table rows indicated by the normalisation factors for each background source (μ_{bkg}).

Table 13. Systematic uncertainties (in percent) greater than 1% for at least one category within SRA and SRB. Uncertainties are expressed relative to the total background estimates. The uncertainties due to the scaling of background events based on data in control regions are indicated for each background component by $\mu_{t\bar{t}}$, $\mu_{t\bar{t}+Z}$, μ_Z, μ_W, and $\mu_{\text{single top}}$. The theory uncertainties quoted for each background include the different distribution shape uncertainties described in the text.

	SRA-TT	**SRA-TW**	**SRA-T0**	**SRB-TT**	**SRB-TW**	**SRB-T0**
Total syst. unc.	15	12	10	14	9	9
$t\bar{t}$ theory	2	2	1	11	6	4
Single-top theory	7	5	4	1	<1	1
$t\bar{t}Z$ theory	3	<1	<1	<1	<1	<1
Z theory	<1	<1	1	<1	<1	<1
$\mu_{t\bar{t}}$	<1	<1	<1	4	4	4
$\mu_{t\bar{t}+Z}$	6	2	2	4	3	1
μ_Z	3	5	5	3	3	3
μ_W	2	3	3	4	4	3
$\mu_{\text{single top}}$	6	4	5	3	4	5
JER	7	3	2	6	2	3
JES	4	4	2	2	<1	<1
b-tagging	5	3	3	2	1	2
$E_{\mathrm{T}}^{\mathrm{miss}}$ soft term	2	1	1	<1	<1	<1
MC statistics	7	7	5	3	3	2

Table 14. Systematic uncertainties (in percent) greater than 1% for at least one category within SRC and SRD. Uncertainties are expressed relative to the total background estimates. The uncertainties due to the scaling of background events based on data in control regions are indicated for each background component by $\mu_{t\bar{t}}$, μ_Z, and μ_W. The theory uncertainties quoted for each background include the different distribution shape uncertainties described in the text.

	SRC1	**SRC2**	**SRC3**	**SRC4**	**SRC5**	**SRD0**	**SRD1**	**SRD2**
Total syst. unc.	25	18	20	27	27	18	31	12
$t\bar{t}$ theory	20	11	12	16	21	4	9	5
Single-top theory	<1	<1	<1	<1	<1	<1	4	2
Z theory	<1	<1	1	2	4	7	3	2
W theory	<1	<1	1	2	3	<1	<1	<1
$\mu_{t\bar{t}}$	12	13	14	14	11	<1	2	5
μ_Z	<1	<1	<1	<1	<1	5	3	2
μ_W	<1	<1	<1	<1	<1	4	5	3
JER	5	<1	8	15	7	8	18	4
JES	<1	1	<1	4	6	1	4	2
b-tagging	2	2	2	2	2	3	5	7
Track-jet flavour	<1	<1	<1	<1	<1	4	7	<1
Track-jet flavour (low p_{T})	<1	<1	<1	<1	<1	7	4	1
$E_{\mathrm{T}}^{\mathrm{miss}}$ soft term	<1	<1	<1	<1	3	<1	<1	<1
Pile-up	<1	<1	<1	1	<1	2	12	<1
MC statistics	3	2	3	4	6	11	17	5

The dominant detector-related systematic uncertainty in the background estimates originates from sources related to the jet energy scale (JES) and resolution (JER) [54], which encompass both the modelling of the detector response and the analysis techniques used to derive the calibration, the b-tagging performance, which includes the uncertainty in the b-tagging efficiency of true b-jets [58] and in the b-tagging rate of light-flavour jets [189] and c-jets [190], and the energy scale and resolution of the $E_{\mathrm{T}}^{\mathrm{miss}}$ soft term [183, 60]. The uncertainty in the modelling of pile-up events contributes significantly to the total uncertainty only in SRD2.

The JES uncertainty is derived as a function of the p_{T} and η of each jet, the pile-up conditions, and the jet flavour. It is determined using a combination of simulated samples and collision data, including measurements of dijet, multijet, Z+jet, and γ+jet events. The JER uncertainty is derived as a function of the p_{T} and η of each jet, and is determined from a random cone technique applied to data recorded without selection bias, and studies of asymmetries in dijet events. The uncertainty in the JER is significant in many signal regions (maximally 18% in SRD1), while the most significant impact of the JES uncertainty reaches 6% in SRC5.

The uncertainty originating from the b-tagging performance of jets is estimated by varying the p_{T}- and flavour-dependent per-jet scale factors, applied to each jet, within predefined ranges determined from efficiency and mis-tag rate measurements in data. The b-tagging uncertainty is highest in SRA and SRD and does not exceed 7% (reached in SRD2).

Uncertainties in the b-tagging performance of track-jets, which are only relevant in SRD, are estimated for track-jets with $p_{\mathrm{T}} > 10$ GeV in the same way as for jets. The largest contribution from this systematic uncertainty is in SRD1, where it is 7%. For track-jets with $5 < p_{\mathrm{T}} < 10$ GeV, which may be selected in SRD0, no evaluation of the b-tagging performance in data is available, so the uncertainty is evaluated by comparing the b-tagging performance observed in $Z \to \ell\ell$ events generated with Sherpa and MadGraph interfaced with Pythia 8.2, resulting in an uncertainty of 7% in SRD0. The difference between the predictions of these two generators was found to always be larger than the difference between the predictions from extrapolation from the neighbouring bins, hence assigning the uncertainty based on the generator comparison is assumed to be conservative.

All jet-, electron-, and muon-related uncertainties are propagated to the calculation of the $E_{\mathrm{T}}^{\mathrm{miss}}$ when evaluated, and additional uncertainties in the energy scale and resolution of the $E_{\mathrm{T}}^{\mathrm{miss}}$ soft term are evaluated. The uncertainty in the soft term of the $E_{\mathrm{T}}^{\mathrm{miss}}$ is derived using $Z \to \mu^+\mu^-$ events and is less than 3% in all SRs. The uncertainty due to the reweighting of the simulated samples to match the distribution of pile-up in data is negligible in all SRs except SRD, where it is at most 12% (reached in SRD1).

Uncertainties in electron and muon reconstruction and identification uncertainties are also considered but have a negligible impact on the final background estimates. The uncertainty in the combined 2015–2018 integrated luminosity is 1.7% [27, 28] and has a negligible impact on the analysis.

Theoretical uncertainties in the physics modelling of the background processes are also evaluated for each background component. For the $t\bar{t}$ background, uncertainties are estimated from the comparison of different matrix-element calculations (Powheg-Box vs aMC@NLO), the choice of parton-showering model (Pythia vs Herwig 7), and the emission of ISR and final-state radiation (FSR) within Pythia 8 while leaving all other parameters for each comparison unchanged. The effects of ISR and FSR are explored by reweighting the nominal $t\bar{t}$ events in a manner that reduces (reduces and increases) initial-state (final-state) parton-shower radiation [71] and by using an alternative Powheg-Box v2 + Pythia 8.2 sample with h_{damp} set to $3m_t$ and parameter variation group Var3 (described in Ref. [71]) increased, leading to increased ISR. SRC is most sensitive to $t\bar{t}$ theory systematic uncertainties, ranging from 11% to 21%, followed by SRB, ranging from 4% to 11%.

Most of the single-top background events include a W boson in the final state (Wt). To account for the interference between Wt and $t\bar{t}$ production, yields in the signal and control regions are compared between a Wt simulated sample that uses the diagram-subtraction scheme, and the nominal sample that uses the diagram-removal scheme [191]. The final single-top uncertainty relative to the total background estimate is maximally 7% (in SRA-TT).

For the $t\bar{t}$ $+W/Z$ background, largely dominated by $t\bar{t} + Z$, the modelling uncertainty is estimated through variations of the renormalisation and factorisation scales simultaneously by factors of 2.0 and 0.5, and a comparison of parton-showering models (Pythia vs Herwig 7), resulting in a maximum uncertainty of 4% (in SRB-TT).

The modelling uncertainties for the W/Z + jets background processes due to missing higher orders are evaluated [192] using both coherent and independent variations of the QCD factorisation and renormalisation scales in the matrix elements by factors of 0.5 and 2, avoiding variations in opposite directions. The matrix-element matching scale between jets from the matrix element and the parton shower, and the resummation scale for soft gluon emission within Sherpa, are also varied by factors of 0.5 and 2. The resulting impact on the total background yields from the W/Z + jets modelling is at most 7% (in SRD0).

Uncertainties in each background from scale variations are fully correlated across regions and categories, and uncorrelated between processes. In some cases this may result in uncertainties cancelling out, while the higher-order corrections may not cancel out. The sensitivity of the results to the correlation assumptions was tested by redoing the fit with scale variations uncorrelated across all regions and categories, which resulted in negligible changes in the excluded cross sections near the edge of the exclusion region.

Detector and theory-related systematic uncertainties in signal yields are also evaluated when setting exclusion limits on specific signals (see Section 4.8). Detector-related uncertainties consider the same sources as for the background and are usually smaller than the modelling uncertainties. Signal theory uncertainties include sources related to signal acceptance, which are included in the profile likelihood fits as a single nuisance parameter, and the uncertainty in the total cross section, which is accounted for by repeating the exclusion procedure for the central and $\pm 1\sigma$ values of the cross section. The uncertainty in the total cross section is 7–16% for direct top squark production [150, 193, 194, 195, 196, 197, 198, 199], depending on the top squark mass. The same uncertainty is used for leptoquark production, due to the similarities between the two types of signals.

The main detector-related uncertainties in the signal yields originate from the JER, ranging from 2% to 15%, the JES, ranging from 2% to 20%, and the b-tagging performance (including track-jet b-tagging in SRD), ranging from 2% to 11%. Uncertainties in the signal acceptance due to variations of the renormalisation and factorisation scales and the matching scale (each varied up and down by a factor of two), and the parton-shower tune variations, are also taken into consideration. In regions where a high-p_{T} ISR system is selected (SRC and SRD), the p_{T} scale of the ISR is large enough such that the leading ISR jet is included in the matrix elements. The uncertainty in the ISR is therefore accounted for when varying the renormalisation and factorisation scales. The total uncertainty in the signal acceptance, considering the full range of $m_{\tilde{t}}$ and $m_{\tilde{\chi}_1^0}$ used in this search, is at most 12–13% in SRA–C, and 25% for SRD.

4.8 Results and interpretation

The background originating from SM processes is determined separately for each set of signal regions (SRA–B, SRC, SRD) from three profile likelihood 'background-only' fits (SRA–B fit, SRC fit, SRD fit) that include the relevant control regions as described in Section 4.6. The observed event yields in the various SRA–B, SRC and SRD categories are compared with the post-fit background estimates in Tables 15, 16, 17, and Figure 48. In the SRs optimised for discovery, SRA-TT-Disc and SRC-Disc, 14 and 28 events are observed, respectively, compared with 15.2 ± 1.8 and 28.0 ± 4.9 expected events, respectively. Figure 49 shows the distribution of Object based $E_{\mathrm{T}}^{\mathrm{miss}}$ sig. in SRA-TW, $m_{\mathrm{jet},R=1.2}^{1}$ in SRB-TT, R_{ISR} in SRC, and $E_{\mathrm{T}}^{\mathrm{miss}}/\sqrt{H_{\mathrm{T}}}$ in SRD0, SRD1 and SRD2. The background predictions are scaled to the values determined from the background-only fits.

Observed event yields are in good agreement with the background estimates in all the signal regions. The significance of a data excess with respect to the background predictions can be quantified by the probability (p) of a background-only hypothesis to be more signal-like than what is observed. To evaluate these probabilities in each signal region category, alternative fit configurations (discovery fits) are defined. Each discovery likelihood function is defined as the product of

Table 15. Observed event yields in SRA and SRB compared with the expected SM background yields in each signal region after the SRA–B background-only fit. The uncertainties include MC statistical uncertainties, detector-related systematic uncertainties, and theoretical uncertainties.

	SRA-TT	**SRA-TW**	**SRA-T0**	**SRB-TT**	**SRB-TW**	**SRB-T0**
Observed	4	8	11	67	84	292
Total SM	3.2 ± 0.5	5.6 ± 0.7	17.3 ± 1.7	46 ± 7	81 ± 7	276 ± 24
Z + jets	1.35 ± 0.28	3.2 ± 0.4	10.5 ± 1.3	15.6 ± 3.3	28.7 ± 3.4	117 ± 14
Single top	0.50 ± 0.31	0.59 ± 0.29	1.9 ± 0.8	3.5 ± 1.2	7.0 ± 3.0	31 ± 15
$t\bar{t}$	0.08 ± 0.07	0.16 ± 0.10	0.4 ± 0.4	10 ± 5	20 ± 6	72 ± 19
$t\bar{t}+Z$	1.05 ± 0.29	0.74 ± 0.17	1.50 ± 0.34	9.9 ± 1.9	12.5 ± 2.5	22 ± 4
W + jets	0.16 ± 0.07	0.53 ± 0.20	1.7 ± 0.6	4.9 ± 1.9	8 ± 4	22 ± 9
Other	0.080 ± 0.020	0.34 ± 0.24	1.32 ± 0.22	2.4 ± 0.4	4.7 ± 2.3	10.4 ± 1.3

Table 16. Observed event yields in SRC compared with expected SM background yields in each signal region after the background-only fit. The uncertainties include MC statistical uncertainties, detector-related systematic uncertainties, and theoretical uncertainties.

	SRC1	**SRC2**	**SRC3**	**SRC4**	**SRC5**
Observed	53	57	38	9	4
Total SM	46 ± 12	52 ± 9	32 ± 7	11.8 ± 3.1	2.5 ± 0.7
Z + jets	1.2 ± 0.5	1.4 ± 0.8	1.2 ± 0.5	0.67 ± 0.32	0.24 ± 0.12
Single top	0.90 ± 0.34	2.7 ± 0.6	1.1 ± 0.7	0.61 ± 0.33	0.25 ± 0.05
$t\bar{t}$	32 ± 11	40 ± 9	26 ± 6	9.5 ± 2.7	1.7 ± 0.6
$t\bar{t}$ $+Z$	0.74 ± 0.32	0.50 ± 0.31	0.24 ± 0.12	$0.09\,^{+\,0.11}_{-\,0.09}$	$0.010\,^{+\,0.030}_{-\,0.010}$
W + jets	1.3 ± 0.6	1.7 ± 0.6	1.5 ± 0.7	$0.4\,^{+\,0.6}_{-\,0.4}$	0.23 ± 0.09
Other	9.7 ± 2.9	5.6 ± 1.5	1.8 ± 0.5	0.51 ± 0.10	$0.08\,^{+\,0.19}_{-\,0.08}$

Table 17. Observed and expected yields after the background-only fit, for SRD. The uncertainties include MC statistical uncertainties, detector-related systematic uncertainties, and theoretical uncertainties.

	SRD0	**SRD1**	**SRD2**
Observed	5	4	10
Total SM	6.9 ± 1.3	3.1 ± 1.0	12.2 ± 1.5
Z + jets	4.2 ± 0.8	1.07 ± 0.25	3.5 ± 0.6
Single top	$0.020^{+0.030}_{-0.020}$	$0.10^{+0.16}_{-0.10}$	0.84 ± 0.31
$t\bar{t}$	0.36 ± 0.29	0.56 ± 0.31	5.1 ± 1.0
$t\bar{t}$ +Z	$0.02^{+0.04}_{-0.02}$	$0.010^{+0.010}_{-0.010}$	< 0.01
W + jets	1.9 ± 0.6	0.9 ± 0.6	2.0 ± 0.7
Other	0.44 ± 0.13	0.45 ± 0.21	0.76 ± 0.20

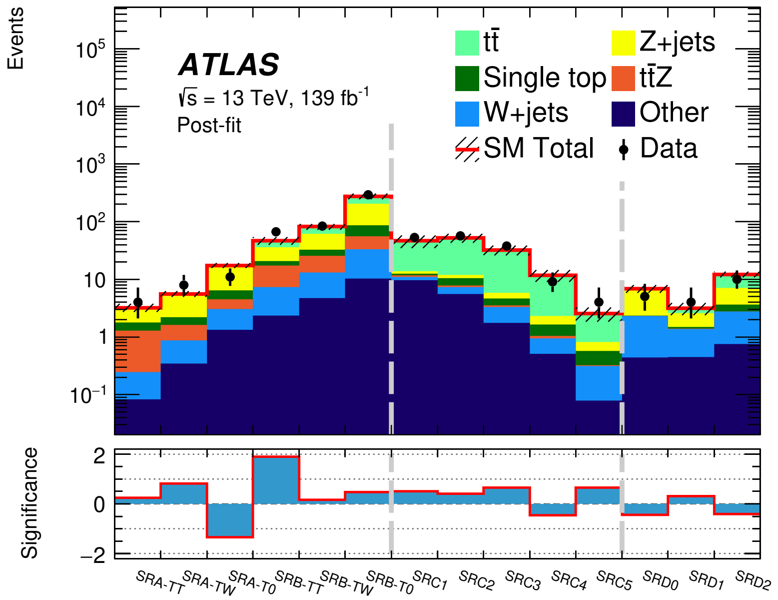

Figure 48. Event yields comparing data (points) to the SM prediction (stacked histograms) in all signal regions after the SRA–B, SRC and SRD background-only fits. The hatched uncertainty band around the SM prediction shows the total uncertainty, which includes the MC statistical uncertainties, detector-related systematic uncertainties, and theoretical uncertainties. The signal regions included in the SRA–B, SRC and SRD fits are separated by vertical dashed lines.

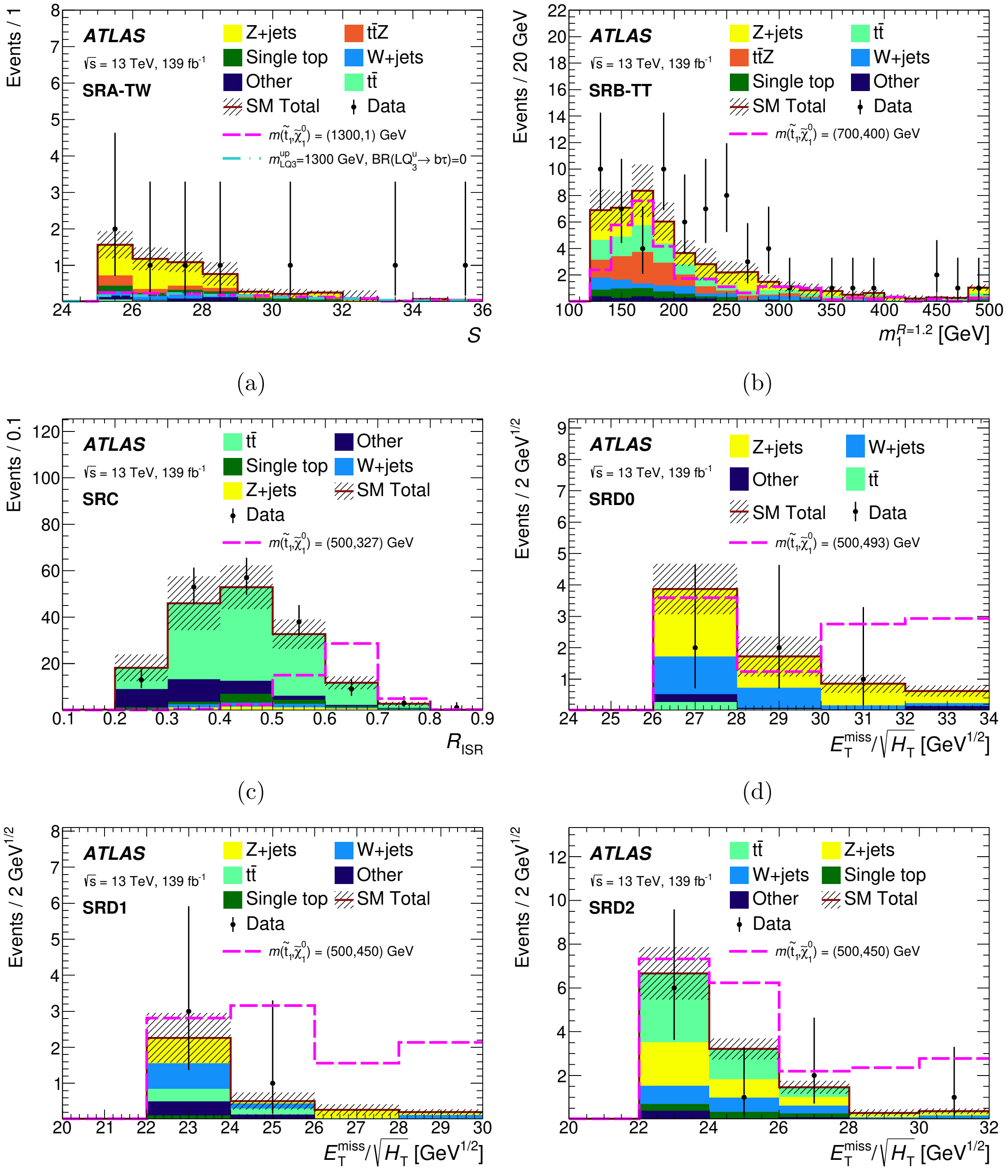

(a)

(b)

(c)

(d)

(e)

(f)

Figure 49. Distributions of (a) Object based $E_{\mathrm{T}}^{\mathrm{miss}}$ sig. in SRA-TW, (b) $m_{\mathrm{jet},R=1.2}^{1}$ in SRB-TT, (c) R_{ISR} in SRC, and (d–f) $E_{\mathrm{T}}^{\mathrm{miss}}/\sqrt{H_{\mathrm{T}}}$ in SRD0–2 after the SRA–B, SRC and SRD background-only likelihood fits. The stacked histograms show the SM prediction and the hatched uncertainty band around the SM prediction shows the total uncertainty, which includes the MC statistical uncertainties, detector-related systematic uncertainties, and theoretical uncertainties. The data (points) are overlaid. For each variable, the distribution for a representative signal hypothesis is overlaid as a dashed line. The rightmost bin includes overflow events.

the Poisson probability density function describing the numbers of events of a single signal region category and the background-only likelihood function associated with that signal region. An additional parameter, the signal strength, defined for positive values and corresponding to the signal normalisation in the signal region, is included and free-floating in the fit. The smallest p-value, assuming the background-only hypothesis, is 0.03, corresponding to 1.87σ, in SRB-TT. In this signal region, 67 events are observed compared with 46.7 ± 6.7 expected events. The largest deficit in the data is found in SRA-T0 where 11 events are observed compared with 17.3 ± 1.7 expected events.

Model-independent upper limits set at 95% CL on the number of beyond the SM (BSM) events in each signal region are derived using the $\mathrm{CL_s}$ prescription [200] and neglecting any possible signal contamination in the control regions. Normalising these by the integrated luminosity of the data sample, they are interpreted as upper limits on the visible BSM cross section, σ_{vis}, where σ_{vis} is defined as the product of the acceptance, reconstruction efficiency and production cross section. The results from the discovery fits are shown in Table 18, with SRA-TT having the lowest upper bound on the visible cross section of new physics phenomena of 0.04 fb.

A profile-likelihood-ratio test is defined in order to set limits on direct pair production of top squarks. A new fit configuration is defined (referred to as an exclusion fit) for each signal region category (SRA–B, SRC or SRD), where the Poisson probability density functions describing the observed and expected numbers of events in all relevant signal region bins are included in the likelihood function, and the signal-strength parameter, defined for positive values, is free-floating in the fit. Signal contamination in the CRs is taken into account. Limits are derived using the $\mathrm{CL_s}$ prescription and calculated from asymptotic formulae [201]. The nominal event

Table 18. Left to right: 95% CL upper limits on the visible cross section ($\langle\epsilon\sigma\rangle^{95}_{\rm obs}$) and on the number of signal events ($S^{95}_{\rm obs}$). The third column ($S^{95}_{\rm exp}$) shows the 95% CL upper limit on the number of signal events, given the expected number (and $\pm1\sigma$ excursions on the expectation) of background events. The last two columns indicate the $\rm CL_B$ value, i.e. the confidence level observed for the background-only hypothesis, the discovery p-value ($p(s=0)$), and the significance (Z). In cases where the observed data yields are less than the total expected background yields, the p-value is truncated to 0.5.

Signal Region	$\langle\epsilon\sigma\rangle^{\mathbf{95}}_{\rm obs}$ **[fb]**	$S^{95}_{\rm obs}$	$S^{95}_{\rm exp}$	$\rm CL_B$	$p(s=0)$ **(Z)**
SRA-TT	0.04	6.0	$5.2^{+2.7}_{-1.7}$	0.63	0.34 (0.40)
SRA-TW	0.06	8.6	$6.5^{+3.2}_{-1.6}$	0.78	0.18 (0.92)
SRA-T0	0.05	6.4	10^{+5}_{-3}	0.11	0.50 (0.00)
SRA-TT-Disc	0.06	8.4	9^{+4}_{-2}	0.39	0.50 (0.00)
SRB-TT	0.28	38.5	22^{+9}_{-6}	0.95	0.03 (1.87)
SRB-TW	0.21	28.6	27^{+10}_{-7}	0.57	0.42 (0.19)
SRB-T0	0.51	71.1	60^{+22}_{-16}	0.69	0.30 (0.53)
SRC1	0.19	26.0	22^{+4}_{-9}	0.75	0.49 (0.01)
SRC2	0.24	32.8	27^{+10}_{-7}	0.76	0.22 (0.77)
SRC3	0.17	24.0	20^{+7}_{-5}	0.76	0.23 (0.75)
SRC4	0.06	8.0	9^{+4}_{-2}	0.29	0.50 (0.00)
SRC5	0.05	6.6	$5.0^{+2.8}_{-1.2}$	0.73	0.22 (0.78)
SRC-Disc	0.11	15.4	15^{+6}_{-4}	0.53	0.49 (0.02)
SRD0	0.04	5.4	$6.8^{+3.3}_{-2.1}$	0.28	0.50 (0.00)
SRD1	0.04	6.2	$5.5^{+2.7}_{-1.8}$	0.63	0.34 (0.40)
SRD2	0.05	6.9	8^{+4}_{-2}	0.28	0.50 (0.00)

yield in each set of SRs is set using the background-level estimates obtained from a background-only fit to both the CRs and the SRs to determine the expected limits, while a coloured band that represents the $\pm 1\sigma$ of the total uncertainty (σ_{exp}) is also evaluated. The observed event yields and the same background estimates are used to determine the observed limits for each set of SRs (SRA–B, SRC and SRD); these are evaluated for the nominal signal cross sections as well as for $\pm 1\sigma$ theory uncertainties in those cross sections, denoted by $\sigma^{\mathrm{SUSY}}_{\mathrm{theory}}$.

Figure 50 shows the observed and expected exclusion contours at 95% CL as a function of (a) the $\tilde{\chi}^0_1$ mass vs the $\tilde{t}$ mass and (b) $\Delta m(\tilde{t}, \tilde{\chi}^0_1)$ vs the $\tilde{t}$ mass. The exclusion contour is obtained by choosing the exclusion fit configuration (SRA–B, SRC or SRD) with the best expected limit for each signal hypothesis. The data included in the SRA–B fit, together with previous limits from the overlay of zero-, one-, and two-lepton channels and other analyses [107, 108, 109, 110, 112, 13], exclude top squark masses up to 1250 GeV for $\tilde{\chi}^0_1$ masses below 200 GeV. Additional constraints are set by the SRC fit in the case where $\Delta m(\tilde{t}, \tilde{\chi}^0_1) \approx m_t$, for which top squark masses in the range $300-630$ GeV are excluded. Some structures in the expected exclusion contour are observed in this region and were traced back to the fixed R_{ISR}-binning adopted in SRC. Since the binning of R_{ISR} is fixed and does not depend on the signal considered, for some signals the peak is located at the boundary between two bins and therefore leads to a global lower signal over background ratio across all SRC bins. Finally, limits are set by the SRD fit in the case where $m_{\tilde{t}} - m_{\tilde{\chi}^0_1} < m_W + m_b$ (with $\Delta m(\tilde{t}, \tilde{\chi}^0_1) \geq 5$ GeV), for which top squark masses in the range $300-660$ GeV are excluded. The sharp structure in the middle of Figure 50 (b) is an artifact of stitching together the exclusion contours of SRC and SRD. Signals with $\Delta m(\tilde{t}, \tilde{\chi}^0_1) = 5$ GeV, which is the smallest $\Delta m(\tilde{t}, \tilde{\chi}^0_1)$ value considered, are excluded for $m_{\tilde{t}} < 490$ GeV. This is the first time that an ATLAS all-hadronic search reaches exclusion sensitivity in the four-body region. This is due to the newly introduced and dedicated SRD, which takes advantage of track-jet b-tagging to discriminate between signal and background. The exclusion limits shown in Figure 50 are derived for unpolarised top squarks. [6] The exclusion limit stays within ±25 GeV of top squark mass when varying the top squark polarisation, which is within the $\sigma^{\text{SUSY}}_{\text{theory}}$ uncertainty band; hadronic final states are less sensitive to polarisation effects than final states with one or more leptons.

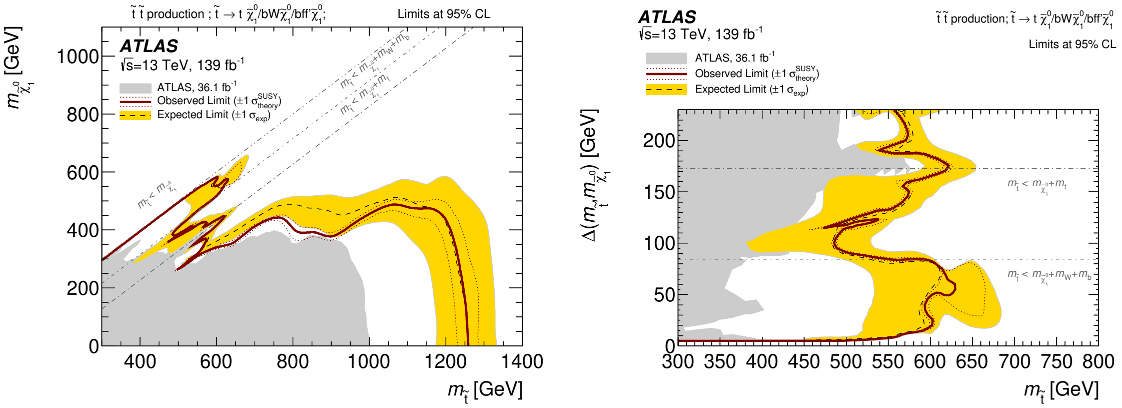

(a)

(b)

Figure 50. Observed (red solid line) and expected (black dashed line) exclusion contours at 95% CL as a function of the (a) $\tilde{\chi}^0_1$ vs $\tilde{t}$ masses and (b) $\Delta m(\tilde{t}, \tilde{\chi}^0_1)$ vs $\tilde{t}$ mass. Masses that are within the contours are excluded. Uncertainty bands corresponding to the ±1σ variation of the expected limit (yellow band) and the sensitivity of the observed limit to ±1σ variations of the signal total cross section (red dotted lines) are also indicated. Observed limits from previous ATLAS searches [107, 108, 109, 110, 112, 13] based on 36.1 fb^{-1} of pp collision data are provided for comparison in grey.

The SRA–B exclusion fit was repeated considering the analysis sensitivity to the production of up-type, third-generation scalar leptoquarks. The results are shown in Figure 51(a) as a function of the leptoquark branching ratio to charged leptons, $\mathcal{B}\,(\text{LQ}^{\text{u}}_3 \to b\tau)$ in this scenario, vs the leptoquark mass. For $\mathcal{B}\,(\text{LQ}^{\text{u}}_3 \to b\tau) = 0$, where

---

[6] The polarisation of the top squarks refers to the fraction of right-handed vs left-handed components in the $\tilde{t}_1$ mass eigenstate.

the leptoquarks decay into $t\nu$ 100% of the time, leptoquarks are excluded up to a mass of 1240 GeV as shown in Figure 51(b). The difference in exclusion reach at $\mathcal{B}\left(\mathrm{LQ}_3^{\mathrm{u}} \to b\tau\right) = 0$ between the leptoquark and top squark interpretations comes from the fact that top squark samples were produced at LO in QCD while the leptoquark samples were produced at NLO, which changes the kinematics slightly. This difference, however, is covered by the signal acceptance uncertainty (12% in SRA–B).

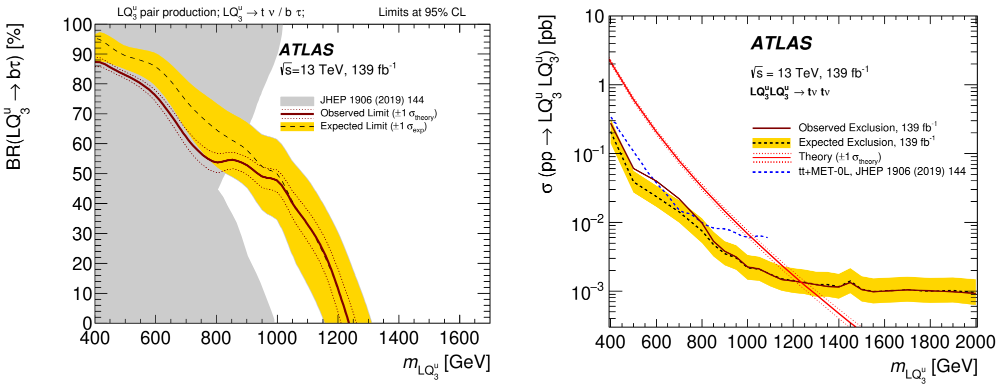

(a) (b)

Figure 51. Observed (red solid line) and expected (black dashed line) limits on up-type, third-generation leptoquarks. (a) Limits as a function of the branching ratio of leptoquarks decaying into $b\tau$ (with the only other decay allowed being into $t\nu$) vs leptoquark mass. (b) Limits on the production cross section at 95% CL as a function of leptoquark mass assuming that all leptoquarks decay into $t\nu$. Uncertainty bands corresponding to the $\pm 1\sigma$ variation of the expected limit (yellow band) and the sensitivity of the observed limit are also indicated. Observed limits from previous searches with the ATLAS detector at $\sqrt{s} = 13$ TeV [127] are overlaid (a) in grey and (b) as a blue dashed line.

4.9 Conclusion

Results from a search for a scalar partner of the top quark based on an integrated luminosity of 139 fb^{-1} of $\sqrt{s} = 13$ TeV proton–proton collision data recorded by the ATLAS experiment at the LHC from 2015 to 2018 are presented. Final states with high-p_{T} jets, large missing transverse momentum, and no electrons or muons are selected. The sensitivity of the search is enhanced by the analysis of the full LHC Run 2 dataset, improvements achieved in the detector performance by the end of the LHC Run 2, and new analysis techniques such as the use of b-tagged track-jets, which extend sensitivity to all-hadronic four-body decays.

Direct top squark pair production is considered, assuming both top squarks decay via $\tilde{t} \rightarrow t^{(*)}\tilde{\chi}_1^0$, and considering a large range of mass differences between the top squark and the neutralino. In particular, fully hadronic final states are used for the first time in an ATLAS analysis to set limits on the scenario where both the top quarks and W bosons originating from their decays are off-shell, $\Delta m(\tilde{t}, \tilde{\chi}_1^0) < m_W + m_b$, due to improvements in the identification efficiency of low-transverse-momentum b-hadrons. The results are also reinterpreted in the context of third-generation, up-type scalar leptoquark pair production, restricted to the scenario where the leptoquarks decay into $t\nu$ or $b\tau$ final states.

No significant excess above the expected SM background is observed. Exclusion limits at 95% confidence level are derived as a function of $m_{\tilde{t}}$ and $m_{\tilde{\chi}_1^0}$, resulting in the exclusion of top squark masses that extend up to 1.25 TeV for $\tilde{\chi}_1^0$ masses below 200 GeV. In the case where $m_{\tilde{t}} \sim m_t + m_{\tilde{\chi}_1^0}$, top squark masses in the range 300−630 GeV are excluded, while in the scenario where $m_{\tilde{t}} < m_W + m_b + m_{\tilde{\chi}_1^0}$ (with $\Delta m(\tilde{t}, \tilde{\chi}_1^0) \geq 5$ GeV), top squark masses in the range 300−660 GeV are excluded. Exclusion limits for up-type, third-generation scalar leptoquarks are extended to masses below 1240 GeV, assuming the leptoquarks can decay only via $t\nu$. Model-independent limits and p-values for each signal region are also reported, with 0.04 fb as the lowest upper bound on the visible cross section of new physics phenomena.

CHAPTER V

A SEARCH FOR DARK MESONS DECAYING TO TOP AND BOTTOM QUARKS

5.1 Introduction

The Standard Model (SM) can be extended by a new strongly-coupled, confining gauge theory with fermion representation which transforms under the electroweak group. The appeal of such an extension is that dark matter can arise in form of composite mesons or baryons of the new strongly-coupled theory, which additionally often exhibits an automatic accidental symmetry protecting against its decay. Consequently, a vast amount of research has been put into the study of strongly-coupled dark matter manifesting itself as dark mesons, dark baryons or dark quarkonia-like states [8]. One set of models incorporating this concept is Stealth Dark Matter [7]. Here, the new strongly-coupled dark sector consists of vector-like fermions which participate in interactions within the new dark as well as electroweak group, but also couple to the Higgs boson. The result is the emergence of a familiar-looking dark sector as the direct analogue to the QCD meson and baryon sector. This leads to several intriguing phenomenological consequences: As long as the vector-like mass is dominant, the new dark sector is under no constraints from precision electroweak or Higgs coupling measurements, while the Higgs interactions break the dark sector global symmetry and thus allow dark mesons to decay into pure Standard Model states [202]. The search focuses on low-energy effective theories developed in [6], which incorporate the leading interactions between dark mesons of a strongly-coupled, $SU(2)$ dark flavour symmetry preserving dark sector and the SM. Models like these rest on a solid theoretical motivation as they contain a stable dark scalar baryon which could account for the stable dark matter observed in cosmological measurements.

The simplified model targeted in this search contains only the two phenomenologically relevant sets of dark mesons: A lighter pseudoscalar triplet of dark pions and an additional triplet of dark rho vector mesons which are both kept at a scale around or slightly above the electroweak scale. Assuming completely mass degenerated triplets, the dark sectors can be fully described by three parameters: the mass of the dark pions m_{π_D}, the mass of the dark rhos m_{ρ_D} and the number of dark colours N_D. Since the phenomenological consequences remain unchanged for values of N_D that are not excessively large, we have chosen to fix $N_D = 4$ throughout this search, by which we follow the typical choice and considerations made for Stealth Dark Matter [7]. Contrary to QCD, the vector-like nature of the dark sector allows to either gauge the full $SU(2)_L$ weak interaction symmetry group or just the underlying $U(1)$ group, which leads to two distinct models of kinetic mixing of dark mesons with the SM. We are distinguishing the two models of kinetic mixing by the labels $SU(2)_L$ and $SU(2)_R$ respectively. The phenomenological consequences manifest themselves in the allowed decay channels and production cross sections of dark pions, where the

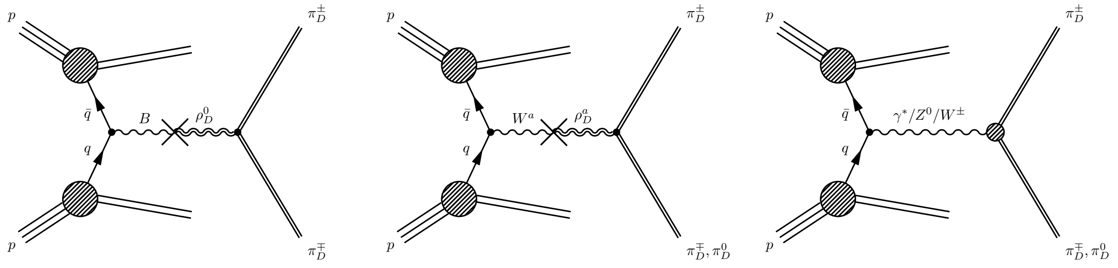

Figure 52. Feynman diagrams of dark pion pair production. The diagram on the left shows the resonant production via the kinetic mixing of the dark sector with the SM B-field resulting in an electrically neutral dark rho, the middle plot shows the kinetic mixing with the W-field resulting in either a neutral or charged dark rho, while the plot on the right shows Drell-Yan pair production of dark pions.

$SU(2)_L$ models result in considerably larger cross sections than the $SU(2)_R$ models. Dark pions are always pair-produced either via Drell-Yan processes or resonantly via kinetic mixing of SM electroweak gauge bosons with the dark rho that then subsequently decays into a pair of dark pions. Figure 52 shows three Feynman diagrams illustrating these mechanisms. Throughout nearly all of the parameter space investigated in this search, the resonant production dominates the production of dark pions. The production cross section therefore depends trivially on the ratio of the dark pion and dark rho masses for which we will use the symbol $\eta = m_{\pi_D}/m_{\rho_D}$. $SU(2)_L$ models can be further classified into two categories depending on whether the dark pion decays are gaugephobic, i.e. the preferred decay channels are to pairs of fermions, or gaugephilic, where the decay to Higgs, W and Z dominates if kinematically allowed. In $SU(2)_R$ models dark pions always decay gaugephobically. Consequently, there are three fundamentally distinct models of dark mesons to consider for a search. In all cases dark pions decay promptly back into pure SM states. Once the model of kinetic mixing, gaugephobic-ness of dark pion decays, dark pion mass and η-parameter are determined, the model is fully specified including the dark pion decay branching fractions.

For models with $\eta < 0.5$, the decay $\rho_D^{\pm} \to \pi_D^{\pm}\pi_D^{\mp,0}$ has a branching fraction of nearly 1.0, while for models with $\eta > 0.5$ this decay is kinematically forbidden and the ρ_D thus decays to pairs of leptons or quarks. Previous searches for resonances in the dilepton spectrum both in ATLAS and CMS have put heavy constraints on such models [203, 204]. The bounds for models with $\eta < 0.5$ are considerably weaker. Most previous searches fail to be sensitive to the dark meson models discussed here because they either require a large amount of missing energy in an event, consider single-production or are optimised for high-mass resonances and do not retain sensitivity

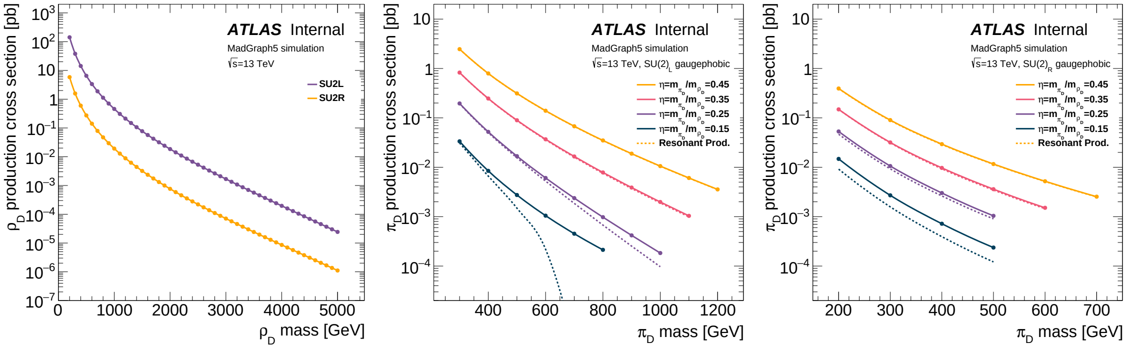

Figure 53. The left panel shows the production cross section of dark rhos separately for $SU(2)_L$ and $SU(2)_R$ kinetic mixing. The production cross sections of dark pions for four different values of η are plotted in the middle panel for $SU(2)_L$ and for $SU(2)_R$ in the right panel. The dashed coloured lines indicate the contribution of the resonant production mode to the total dark pion production cross section.

to the mass regime relevant for dark mesons. As a consequence this search considers only models with $\eta < 0.5$ where the exclusion limits are weakest.

Figure 53 shows the production cross sections for dark rhos and dark pions separately for $SU(2)_L$ and $SU(2)_R$ models. In general the cross sections are larger for the $SU(2)_L$ scenario, but get smaller the further the meson masses move away from the resonance at $\eta = 0.5$. The contribution of the resonant production to the total production cross section is indicated by the dashed lines. The mass points at $\eta = 0.15$ in $SU(2)_L$ and $SU(2)_R$ models are the only samples for which the Drell-Yan production mode dominates over the resonant production. This has kinematic consequences as the dark pions are much softer compared to those produced in the decay of a very heavy intermediate particle. For convenience, the cross sections for the signal points investigated in this analysis have been listed explicitely in appendix A.1.

A variety of different decay channels are open to dark pions in the available parameter space. The most relevant channels and their branching fractions are drawn in figure 54. For the gaugephobic models the decay to top and bottom quarks always dominates at high masses, while decays to bottom and charm quarks, taus and gauge

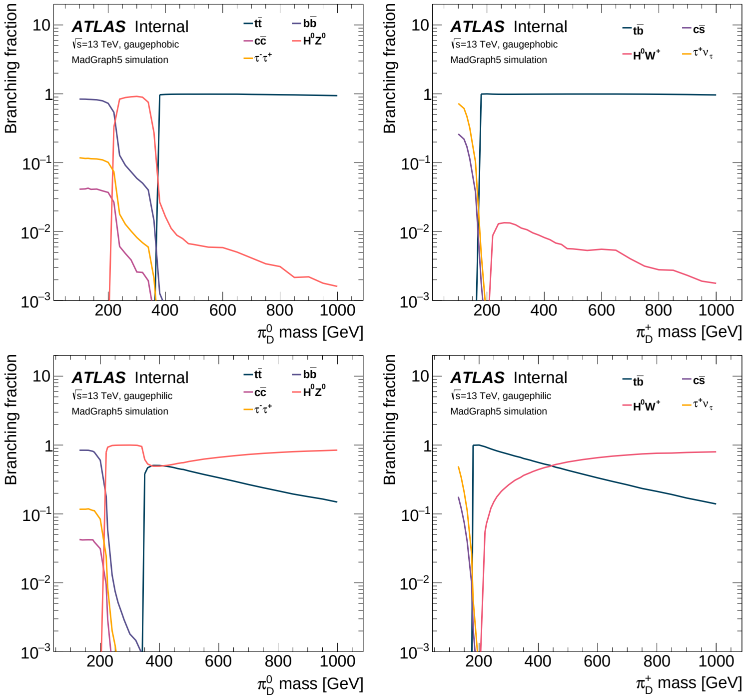

Figure 54. Branching fractions of the most relevant decay channels over the full dark pion mass range. The top two panels represent the available decays of dark pions from gaugephobic models. The bottom two panels show the same for dark pions originating from gaugephilic models. The left column only contains neutral dark pions, the right column the positively charged dark pions. Not all possible decay channels are drawn. Channels with small branching fractions are suppressed for clarity.

bosons are relevant at lower dark pion masses. For gaugephilic models the decay behaviour is more complex as the decays to gauge bosons and to top and bottom quarks simultaneously exhibit large branching fractions. This leads to very complex final states with several bosons, b-jets and top decays in the same event. For reasons of simplicity we will therefore focus exclusively on gaugephobic models in the remainder of this search and specifically target final states containing either three top- and one bottom-quark or two top- and two bottom-quarks.

The dark meson models investigated here have so far never been put to a dedicated experimental test at any collider experiment. The existing limits are therefore based solely on the reinterpretation of other analyses which are less than

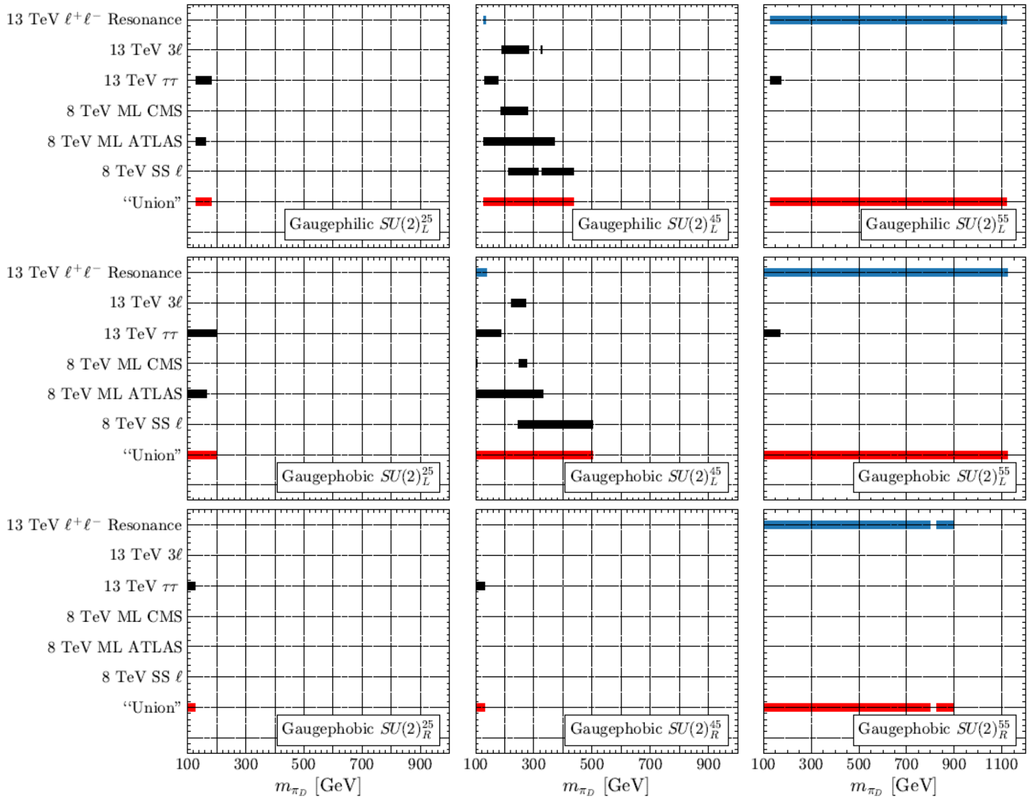

Figure 55. Overview of existing limits for several benchmark points of the proposed dark meson models. The top row corresponds to gaugephilic $SU(2)_L$ models, the middle to gaugephobic $SU(2)_L$ models and the bottom row for $SU(2)_R$ models. The three columns show different values for $\eta = m_{\pi_D}/m_{\rho_D}$. From left to right they are $\eta = 0.25$, $\eta = 0.45$ and $\eta = 0.55$. The black bars symbolise the excluded regions of dark pion mass space provided by a specific analysis, the red bars show the combination of all investigated analyses. Of interest for the present study are the four plots in the bottom left. For more details and the method see the original source of figure, published in [6].

ideal for dark meson models. As a result the limits are extremely weak and in some cases still set by 8 TeV searches as can be seen from figure 55.

The aim of this analysis is to provide the world's first dedicated experimental insights into the proposed dark meson models using the full run 2 dataset.

Signal dark mesons decay to pure standard model states consisting of top and bottom quarks. Here, dark mesons are always pair-produced resulting in the dominant analysis signature of *tttb* and *ttbb*.

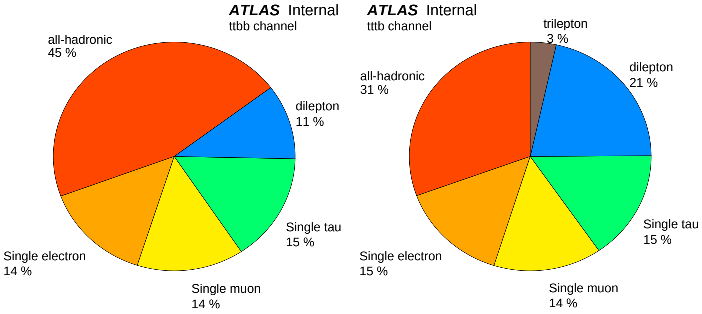

Figure 56. Fraction of events decaying to final states with no leptons, one lepton or multiple leptons in the $ttbb$ final state on the left and the $tttb$ final state on the right.

The majority of top quarks decay into purely hadronic final states. As a consequence, events containing a pair of dark pions often exhibit challenging signatures containing up to ten signal jets, four of which originate from a b quark. As shown in figure 56, decays involving an electron or a muon are less likely, but offer the advantage of a considerably cleaner event signature. In this search we consider both the all-hadronic and the 1-lepton final states ($l = e, \mu$), which will make use of a common analysis framework but employ different analysis strategies.

In the all-hadronic channel an AnalysisTop based framework is used to apply all recommended object calibrations and cleanings while simultaneously applying a channel-specific preselection to generate small sets of analysis ntuples. The dominant background originates from QCD multijet events, with further significant contributions from $t\bar{t}$ and V+jets. Further minor backgrounds are considered as well. With the exception of the multijet background, all backgrounds are estimated from simulation. For QCD multijets the pre-selected events are used to derive an estimate directly from data. A final cut-based selection is applied to suppress background events. The signal region consists of 9 bins defined by the masses of the leading and subleading large R-parameter jets in the event. Additionally, four validation regions with a binning matching the signal region are defined. Finally, a likelihood fit is performed over all signal region bins to assess the possible signal strength.

This chapter contains material coauthored with the ATLAS collaboration.

5.2 Data and Simulated Samples

5.2.1 Data sample

The analysis is based on the full run 2 proton–proton data sample recorded in 2015-2018 at $\sqrt{s} = 13$ TeV with a bunch spacing of 25 ns corresponding to an integrated luminosity of 139 fb^{-1}. The luminosity was determined using the LUCID-2 detector [205] following the methodology described in [206] and has an uncertainty of 2.4 fb^{-1}. The data are collected in the main physics stream and reconstructed offline using `athena release 21`. Calibrations of physics objects are applied in the derivation framework where the `TOPQ4` derivation format is predominantly[1] used for the all-hadronic channel and the `TOPQ1` derivation format for the one-lepton channel. The `TOPQ4` derivation slims unused containers, thins MC truth information and applies a basic event selection based on jets. Events are required to contain either at least one calibrated fat jet with R-parameter 1.0 and $p_T > 200$ GeV, or at least five calibrated jets with $R = 0.4$ and a minimal transverse momentum of 20 GeV, at least one of which has to be b-tagged. All jets have to be located in the central region of the detector where $\eta < 2.5$. The implementation of the `TOPQ4` derivation can be found in [207]. The `TOPQ1` derivation applies the same slimming and thinning as the `TOPQ4`

---

[1] For many top samples the derivations were produced in pass-through mode, i.e. unskimmed. In such a case the `TOPQ1` and `TOPQ4` derivations are identical and can therefore be used in both channels.

derivation but selects events based on leptons, where either an electron or a muon with $p_T > 20$ GeV in the central region of the detector where $|\eta| < 2.5$ is required. Electrons are required to be tagged at least DFCommonElectronsLHLoose, muons are required to have a full-detector combined track and to be quality tagged as DFCommonGoodMuon. The implementation of the `TOPQ1` derivation can be found in [208].

5.2.2 Signal Monte Carlo samples

Dark pions can be pair-produced via Drell-Yan and resonantly via the production of a dark rho. Both production channels are simulated in MadGraph5_aMC@NLO v2.4.3 [63], where the matrix elements are calculated to NLO, interfaced with Pythia8.212 [209] for hadronisation and showering using production tags `e8005` for $SU(2)_L$ and `e8207` for $SU(2)_R$ samples. Signal parameters were chosen to cover the relevant areas in (m_{π_D},η) space for $SU(2)_L$ and $SU(2)_R$ models. The number of dark colours N_D was set to 4 for all signal points, the dark pion decays were simulated using the narrow width approximation. All events are passed through a detailed simulation of the ATLAS detector in Geant4 [169, 168], where the detailed configuration is listed in tag `s3126`. The same reconstruction algorithms and the same `athena` software release is used for simulation and data. To mimic the pileup conditions during data taking, the simulated samples are overlaid with minimum-bias collisions, where the number of additional collisions approximate the pileup distributions observed in data. Since the pileup conditions changed over time, three distinct Monte Carlo campaigns are necessary to completely reproduce the pileup conditions in data. The mc16a campaign corresponds to data taken in 2015 and 2016 and is represented by tags `r9364_r9315`, mc16d corresponds to data taken in 2017 and is considered in tags `r10201_r10210`, while tags `r10724_r10726` are used for the mc16e campaign representing the 2018 data. 10K events are simulated for each signal point and Monte Carlo production campaign, with the exception of two samples per model for which 100K events per campaign have been simulated. These high-statistics samples are intended for detailed signal studies and correspond to ($m_{\pi_D} = 400$ GeV, $\eta = 0.45$) and ($m_{\pi_D} = 800$ GeV, $\eta = 0.25$) for $SU(2)_L$ models, and for $SU(2)_R$ models ($m_{\pi_D} = 300$ GeV, $\eta = 0.45$) and ($m_{\pi_D} = 400$ GeV, $\eta = 0.35$). All simulated signal samples are processed in an unskimmed `TOPQ1` derivation which can be used by both the all-hadronic and the 1-lepton channel. An overview of all simulated signal points and their distribution in η-m_{π_D} space can be found in figure 57.

The effect of multiple interactions in the same and neighbouring bunch crossings (pile-up) was modelled by overlaying the simulated hard-scattering event with inelastic proton–proton events generated with PYTHIA8.186 [209] using the `NNPDF2.3lo` set of parton distribution functions (PDF) [210] and the A3 set of tuned parameters [171].

Motivated by the expected limits of the all-hadronic channel (see section 5.9) the original $SU(2)_L$ signal grid has been extended by additional samples as also illustrated in figure 57. The signal samples of the extension were simulated using MADGRAPH5_aMC@NLO v2.9.9 interfaced with PYTHIA8.306 for hadronisation and showering, corresponding to event generation tag `e8419`. For each signal point of the extension a total of 20K events per MC campaign have been simulated. The simulation and reconstruction was done with the exact same configuration as the original signal grid.

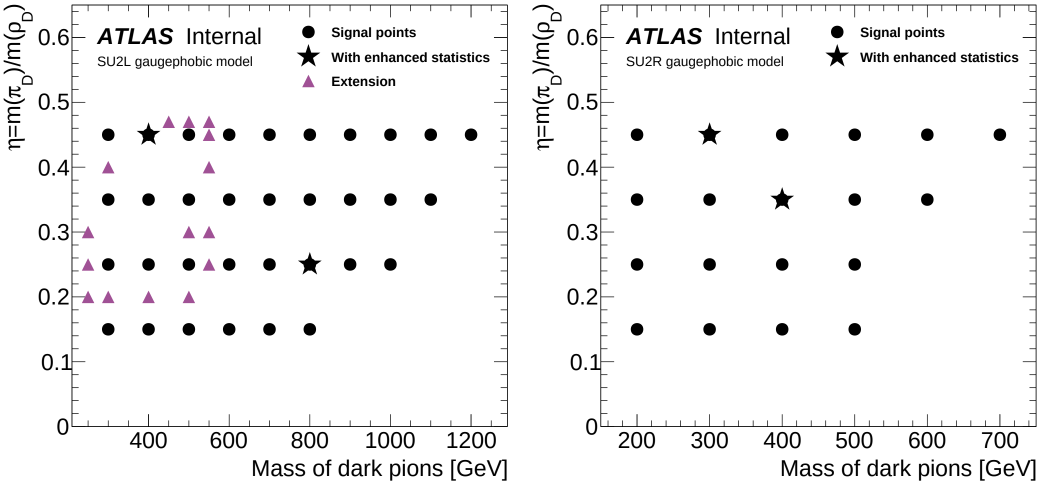

Figure 57. Distribution of simulated samples in η-m_{π_D} space. The left grid corresponds to $SU(2)_L$, the right to $SU(2)_R$ models. The black markers indicate the original signal grid, while the purple markers show the extension of the $SU(2)_L$ signal grid for the all-hadronic channel. The high-statistics data points have 100K events per campaign, the remainder of the original signal grid 10K and the extension 20K events per grid point.

5.2.3 Background Monte Carlo samples

All background MC samples are produced centrally for all three production campaigns. Depending on the intended use in the 1-lepton, all-hadronic or both channels, the samples are then processed into the `TOPQ1`, `TOPQ4` or both derivation formats. All derivations are processed either in a skimmed configuration which applies event skimming as described in section 5.2.1 (production tags `p4344` and `p4512` have predominantly been used here), or an unskimmed configuration which accepts every event into the derivation output and is typically used for all signal and top samples (predominantly production tags `p4346` and `p4514`).

The production of $t\bar{t}$ events is modelled using the PowhegBox v2 [66, 67, 68, 69] generator which provides matrix elements at next-to-leading order (NLO) in the strong coupling constant $\alpha_S$with the `NNPDF3.0nlo` [70] parton distribution function (PDF) and the h_{damp} parameter, which controls the matching in Powheg and effectively regulates the high-p_{T}radiation against which the $t\bar{t}$ system recoils, set to 1.5 m_{top} [71]. The functional form of the renormalisation and factorisation scale is set to the default scale $\sqrt{m_{\mathrm{top}}^2 + p_{\mathrm{T}}^2}$. The events are interfaced with PYTHIA8.230 [64] for the parton shower and hadronisation, using the A14 set of tuned parameters [148] and the `NNPDF2.3lo` set of PDFs [147]. The decays of bottom and charm hadrons are simulated using the EVTGEN v1.6.0 program [62].

The $t\bar{t}$ sample is normalised to the cross-section prediction at next-to-next-to-leading order (NNLO) in QCD including the resummation of next-to-next-to-leading logarithmic (NNLL) soft-gluon terms calculated using TOP++2.0 [211, 159, 158, 157, 156, 155, 160]. For proton–proton collisions at a centre-of-mass energy of $\sqrt{s} = 13\,\mathrm{TeV}$, this cross section corresponds to $\sigma(t\bar{t})_{\mathrm{NNLO+NNLL}} = 832 \pm 51$ fb using a top-quark mass of $m_{\mathrm{top}} = 172.5$ GeV. The uncertainties on the cross-section due to PDF and $\alpha_{\mathrm{S}}$are calculated using the PDF4LHC prescription [212] with the MSTW2008 68% CL NNLO [213, 214], CT10 NNLO [215, 216] and NNPDF2.3 5f FFN [147] PDF sets, and are added in quadrature to the scale uncertainty.

The uncertainty due to initial-state radiation (ISR) is estimated by comparing the nominal $t\bar{t}$ sample with additional samples [217]. To simulate higher parton radiation, the factorisation and renormalisation scales are varied by a factor of 0.5 while simultaneously increasing the h_{damp} value to 3.0 m_{top} and using the Var3c up variation from the A14 tune. For lower parton radiation, μ_{r} and μ_{f} are varied by a factor of two while keeping the h_{damp} value to 1.5 m_{top} and using the Var3c down variation in the parton shower. The Var3c A14 tune variation [148] largely corresponds to the variation of $\alpha_{\mathrm{S}}$for ISR in the A14 tune. The impact of final-state radiation (FSR) is evaluated by varying the renormalisation scale for emissions from the parton shower up and down by a factor of two.

The `NNPDF3.0lo` replicas are used to evaluate the PDF uncertainties for the nominal PDF. The central value of this PDF is further compared with the central values of the `CT14nnlo` [218] and `MMHT2014nnlo` [219] PDF sets.

Since the all-hadronic channel operates in an extreme region of phase space with very large H_{T}, a dedicated H_{T}-sliced sample is used that ensures sufficient statistics even at very large H_{T}. In the 1-lepton channel the bulk $t\bar{t}$ sample without slicing is used.

Samples for $t\bar{t}$+HF processes were produced with the Powheg Box Res [220] generator and OpenLoops 1 [74, 75, 76], using a pre-release of the implementation of this process in Powheg Box Res provided by the authors [221], with the `NNPDF3.0nlo` [70] PDF set. It was interfaced with Pythia8.240 [64], using the A14 set of tuned parameters [148] and the `NNPDF2.3lo` PDF set. The four-flavour scheme was used with the b-quark mass set to 4.95 GeV. The factorisation scale was set to $0.5 \times \Sigma_{i=t,\bar{t},b,\bar{b},j} m_{\mathrm{T},i}$, the renormalisation scale was set to $\sqrt[4]{m_{\mathrm{T}}(t) \cdot m_{\mathrm{T}}(\bar{t}) \cdot m_{\mathrm{T}}(b) \cdot m_{\mathrm{T}}(\bar{b})}$, and the h_{damp} parameter was set to $0.5 \times \Sigma_{i=t,\bar{t},b,\bar{b}} m_{\mathrm{T},i}$.

The production of $W/Z+$jetsis simulated with the Sherpa v2.2.11 [72] generator using next-to-leading order (NLO) matrix elements (ME) for up to two partons, and leading order (LO) matrix elements for up to five partons calculated with the Comix [73] and OpenLoops 1 [74, 75, 76] libraries. They are matched with the Sherpa parton shower [77] using the MEPS@NLO prescription [78, 79, 80, 81] using the set of tuned parameters developed by the Sherpa authors. The Hessian `NNPDF3.0nnlo` set of PDFs [70, 82] is used and the samples are normalised to a next-to-next-to-leading order (NNLO) prediction [83].

The associated production of top quarks with W bosons (tW) is modelled using the PowhegBox v2 [222, 67, 68, 69] generator at NLO in QCD using the five-flavour scheme and the `NNPDF3.0nlo` set of PDFs [70]. The diagram removal scheme [191] is used to remove interference and overlap with $t\bar{t}$ production. The related uncertainty is estimated by comparing with an alternative sample generated using the diagram subtraction scheme [191, 71]. The events are interfaced to PYTHIA8.230 [64] using the A14 tune [148] and the `NNPDF2.3lo` set of PDFs [147]. Single-top t-channel production is modelled using the POWHEGBOX v2 [223, 67, 68, 69] generator at NLO in QCD using the four-flavour scheme and the corresponding `NNPDF3.0nlo` set of PDFs [70]. The events are interfaced with PYTHIA8.230 [64] using the A14 tune [148] and the `NNPDF2.3lo` set of PDFs [147]. Single-top s-channel production is modelled using the POWHEGBOX v2 [224, 67, 68, 69] generator at NLO in QCD in the five-flavour scheme with the `NNPDF3.0nlo` [70] parton distribution function (PDF) set. The events are interfaced with PYTHIA8.230 [64] using the A14 tune [148] and the `NNPDF2.3lo` PDF set.

The production of $t\bar{t}t\bar{t}$ events is modelled using the MADGRAPH5_aMC@NLO v2.4.3 [63] generator which provides matrix elements at next-to-leading order (NLO) in the strong coupling constant $\alpha_{\mathrm{S}}$with the `NNPDF3.1nlo` [70] parton distribution function (PDF). The functional form of the renormalisation and factorisation scales are set to $0.25\times \sum_i \sqrt{m_i^2 + p_{\mathrm{T},i}^2}$, where the sum runs over all the particles generated from the matrix element calculation, following the Ref. [225]. Top quarks are decayed at LO using MADSPIN [226, 227] to preserve all spin correlations. The events are interfaced with PYTHIA8.230 [64] for the parton shower and hadronisation, using the A14 set of tuned parameters [148] and the `NNPDF2.3lo` [70] PDF set. The decays of bottom and charm hadrons are simulated using the EVTGEN v1.6.0 program [62].

The production of $t\bar{t}$ +W/Zevents is modelled using the MADGRAPH5_aMC@NLO v2.3.3 [63] generator at NLO with the `NNPDF3.0nlo` [70] parton distribution function (PDF). The events are interfaced to Pythia8.210 [64] using the A14 tune [148] and the `NNPDF2.3lo` [70] PDF set. The decays of bottom and charm hadrons are simulated using the EvtGen v1.2.0 program [62].

The production of $t\bar{t}H$ events is modelled using the PowhegBox v2 [66, 67, 68, 69, 228] generator at NLO with the `NNPDF3.0nlo` [70] PDF set. The events are interfaced to Pythia8.230 [64] using the A14 tune [148] and the `NNPDF2.3lo` [70] PDF set. The decays of bottom and charm hadrons are performed by EvtGen v1.6.0 [62].

The further rare backgrounds ttt, $t\bar{t}ZZ$, $t\bar{t}WW$, $t\bar{t}WZ$, $t\bar{t}WH$ and $t\bar{t}HH$ are all produced using the LO MadGraph5_aMC@NLO generator interfaced with Pythia8 using the A14 set of tuned parameters and scaled to NLO cross sections [229].

Samples of diboson final states (VV) are simulated with the Sherpa v2.2.1 or v2.2.2 [72] generator depending on the process, including off-shell effects and Higgs-boson contributions, where appropriate. Semileptonic final states, where one boson decays leptonically and the other hadronically, are generated using matrix elements at NLO accuracy in QCD for up to one additional parton and at LO accuracy for up to three additional parton emissions. Samples for the loop-induced processes $gg \to VV$ are generated using LO-accurate matrix elements for up to one additional parton emission. The matrix element calculations are matched and merged with the Sherpa parton shower based on Catani-Seymour dipole factorisation [73, 77] using the MEPS@NLO prescription [78, 79, 80, 81]. The virtual QCD correction are provided by the OpenLoops 1 library [74, 75, 76]. The `NNPDF3.0nnlo` set of PDFs is used [70], along with the dedicated set of tuned parton-shower parameters developed by the Sherpa authors.

Just like described for signal MC samples in section 5.2.2, all background MC samples are overlayed by simulated minimum-bias events to account for the effects of pileup. The same configuration as for signal was used.

The configurations of all background samples are summarised in table 19.

5.2.4 Pileup reweighting

Monte Carlo samples are generated using an expected pileup distribution, which typically differs from the actual distribution measured in data. The three MC campaigns account for the different pileup conditions over the four years of data taking in run 2 (mc16a corresponds to 2015+2016, mc16d to 2017 and mc16e emulates the pileup profile observed in 2018). All MC samples are reweighted using the PileUpReweightingTool to match the distributions in data. Samples of the mc16a campaign are reweighted based on the average number of interactions per bunch crossing, whereas the later campaigns use the actual μ distribution since the expected pileup profiles where generated from smeared actual μ data and using the average number of collisions would result in a loss of statistics. Following recommendation to improve data to MC agreement the μ profile in data is scaled by 1/1.03 before weight calculation.

5.2.5 $t\bar{t}$+HF overlap removal

As described in section 5.2.3, a dedicated sample in which a pair of top quarks is produced in association with two b-quarks can be used to supplement statistics in the phase space relevant for this analysis. Since the same diagrams are also contained

Table 19. Overview of the configuration of all nominal background samples used in the analysis.

Process	Generator	PDF	Showering	Tune	Cross section
$t\bar{t}$	PowhegBox v2	`NNPDF3.0nlo`	Pythia8	A14	NNLO+NNLL
$t\bar{t}$+HF	Powheg Box Res	`NNPDF3.0nlo`	Pythia8	A14	NNLO
W/Z + jets	Sherpa v2.2.11	`NNPDF3.0nnlo`	Sherpa	Def.	NLO
Single top	PowhegBox v2	`NNPDF3.0nlo`	Pythia8	A14	NLO+NNLL
$t\bar{t}t\bar{t}$	MadGraph5_aMC@NLO v2.4.3	`NNPDF3.1nlo`	Pythia8	A14	NLO
$t\bar{t}$ $+W/Z$	MadGraph5_aMC@NLO v2.3.3	`NNPDF3.0nlo`	Pythia8	A14	NLO
$t\bar{t}H$	PowhegBox v2	`NNPDF3.0nlo`	Pythia8	A14	NLO
Other $t\bar{t}$ + X	MadGraph5_aMC@NLO	`NNPDF2.3lo`	Pythia8	A14	NLO
Multiboson	Sherpa v2.2.1/v2.2.2	`NNPDF3.0nnlo`	Sherpa	Def.	NLO

within the inclusive $t\bar{t}$ samples an event overlap removal procedure is needed to avoid an overestimation of $t\bar{t}$+HF events. For this purpose, an event classification strategy analogous to [230] has been implemented.

After evaluating the event counts it was concluded that since the all-hadronic channel uses an H_{T}-sliced $t\bar{t}$ sample, the $t\bar{t}$+HF sample has insufficient statistics in the high-H_{T} phase space relevant for this channel. We therefore rely solely on the good statistics provided by the H_{T}-sliced $t\bar{t}$ sample.

5.3 Object Definitions and Reconstruction

5.3.1 Electrons

Electrons are identified using the likelihood-based (LH) electron identification (ID) recommended by the Electron Gamma Combined Performance group [231]. The LH method combines the signal and background probability densities for a given set of discriminating variables into a signal-background discriminator on which a cut is applied. There are five working points [232], each using different variables to build the discriminator, and three of which are used to define different types of electrons in this analysis. All electrons are furthermore required to fulfill the standard electron track to vertex association requirements recommended by the Electron Gamma Combined Performance group, and to have $|\eta| < 1.37$ or $1.52 < |\eta| < 2.47$, corresponding to the central region of the detector excluding the transition region between barrel and endcap regions, where the reconstruction efficiency is low[231].

In the all-hadronic channel, *loose electrons* are identified with the `LooseAndBLayerLH` working point and are used for vetoing events containing any leptons. They are also required to fulfill the isolation requirements defined by the `FCLoose` working point of the IsolationSelectionTool, recommended by the isolation forum [233]. In the 1-lepton channel, loose electrons are identified with the `MediumLH` working point of the LH-based electron ID and have no isolation requirement. They are used to veto events with any additional leptons. In both channels, loose electrons are required to have $\mathrm{p_T} >~ 10\,\mathrm{GeV}$. A summary of the loose electron requirements can be found in table 20.

Table 20. Selection criteria for *loose electrons* used for vetoing events containing any leptons in the all-hadronic channel and events with more than one lepton in the 1-lepton channel.

Feature	Criterion
Pseudorapidity range	$(\lvert\eta\rvert < 1.37) \quad \lvert\rvert \quad (1.52 < \lvert\eta\rvert < 2.47)$
Energy calibration	`es2018_R21_v0` (ESModel)
Transverse momentum	$p_\mathrm{T} > 10\,\mathrm{GeV}$
Track to vertex association	$\lvert d_0^{\mathrm{BL}}(\sigma)\rvert < 5$ $\lvert\Delta z_0^{\mathrm{BL}}\sin\theta\rvert < 0.5\,\mathrm{mm}$
Identification	`MediumLH` (1-lepton), `LooseAndBLayerLH` (all-hadronic)
Isolation	None (1-lepton), `FCLoose` (all-hadronic)

To account for reconstruction and selection efficiency differences between Monte Carlo and data, scale factors are applied to the weights of the Monte Carlo events.

5.3.2 Muons

Muons are identified by the quality working points provided by the Muon Combined Performance (MCP) group [234], which take information from both the Inner Detector and the Muon Spectrometer into account to reconstruct muons. All muons are required to be found within the acceptance region of the Inner Detector, $\lvert\eta\rvert < 2.5$, and to satisfy the MCP recommended vertex association criteria, $|d_0^{BL}/\sigma(d_0^{BL})| < 3$ and $\Delta z_0^{BL}\sin(\theta) < 0.5\,\mathrm{mm}$, as defined in [234].

Loose muons are identified in the all-hadronic channel by the `loose` quality working point and in the 1-lepton channel by the `medium` quality working point. In the all-hadronic channel they have to satisfy the `FCLoose` isolation criteria and in the 1-lepton channel there are no isolation criteria. They further have to satisfy $\mathrm{p_T} > 10$ GeV. The full definition can be found in table 21. Analogously to electrons, loose muons are used for vetoing events containing leptons in the all-hadronic channel and vetoing events with more than one lepton in the 1-lepton channel.

Table 21. Selection criteria for *loose muons*, used in the all-hadronic channel to veto events containing leptons and in the 1-lepton channel to veto events containing more than one lepton.

Feature	Criterion
Selection working point	`Loose` (all-hadronic), `Medium` (1-lepton)
Isolation working point	`FCLoose` (all-hadronic), None (1-lepton)
p_T	$> 10\,\mathrm{GeV}$
$\|\eta\|$	< 2.5
$\|d_0^{BL}/\sigma(d_0^{BL})\|$	< 3
$\Delta z_0^{BL}\sin(\theta)$	$< 0.5\,\mathrm{mm}$

To account for reconstruction and selection efficiency differences between Monte Carlo and data, scale factors are applied to the weights of the Monte Carlo events.

5.3.3 Small-R jets

Jets are reconstructed from topological clusters of cells in the calorimeters and from inner detector tracks using the particle flow (PFlow) algorithm [53], which helps to suppress energy deposits in the calorimeters originating from charged pileup particles. The algorithm further allows for taking momentum measurements from tracking information whenever the tracker resolution outperforms the calorimeter resolution. Jets are found using the Anti-$k_\perp$algorithm [52] implemented in the FastJet package [?] with a fixed radius parameter of $R = 0.4$ using charged constituents associated with the primary vertex and neutral PFlow objects as inputs. The most up-to-date recommendations are applied to calibrate all jets [235]. After calibration all jets are required to have p_T >20 GeV. In the all-hadronic channel, they are also required to be central in the detector where $|\eta| < 2.8$ to use the same η range as seen by the H_T trigger described in section 5.4.1. In the 1-lepton channel, the H_T trigger is not used, and the jets are required to satisfy $|\eta| < 2.5$. In order to minimise the effects of pileup, a jet vertex tagger (JVT) [178] is used to make sure matched inner detector tracks are consistent with the primary vertex. The `tight` working point is used in the central region of the detector where $|\eta| < 2.5$, while for jets with $2.5 < |\eta| < 2.8$ the `tight` working point of the forward jet vertex tagger [236] is required.

5.3.4 Large-R reclustered jets

Large-R jets are reclustered from calibrated R=0.4 PFlow jets using the Anti-$k_\perp$algorithm with an R parameter of R=1.2. These jets reconstruct dark pion candidates and the R parameter has been optimized for the dark pion mass and boost of the targeted signal points as described in appendix A.2.

Figure 58 shows the reconstruction efficiency for a range of R parameters for two reference signal points. The two large-R jets with the highest $p_\mathrm{T}$are required to have jet mass greater than 190 GeV as part of the preselection.

Table 22. Jet reconstruction criteria.

Feature	Criterion
Algorithm	Anti-$k_{\perp}$
R-parameter	0.4
Input constituent	EMPFlow
Analysis release number	21.2.200
`CalibArea` tag	00-04-82
Calibration configuration	`JES_MC16Recommendation_Consolidated_PFlow_Apr2019_Rel21.config`
Calibration sequence (Data)	`JetArea_Residual_EtaJES_GSC_Insitu`
Calibration sequence (MC)	`JetArea_Residual_EtaJES_GSC_Smear`
Selection requirements	
Observable	requirement
Jet cleaning	`LooseBad`
BatMan cleaning	No
p_{T}	$> 20\,\mathrm{GeV}$
$\|\eta\|$	< 2.8 (All hadronic) or < 2.5 (One lepton)

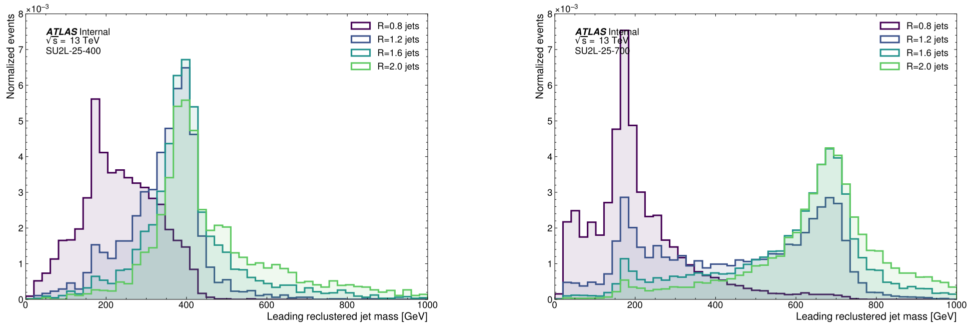

Figure 58. Jet reclustering for a range of R parameters for an $SU(2)_L$ signal point with $\eta = 0.25$ and $m_{\pi_D} = 400$ GeV on the left and on the right for an $SU(2)_L$ sample with $\eta = 0.25$ and $m_{\pi_D} = 700$ GeV. R=1.2 jets provide good signal reconstruction while limiting multijet background events.

5.3.5 Flavour tagging

Jets originating from the decay of a b quark can be identified as such through the signature of their slightly longer lifetime by employing an algorithm based on multivariate analysis techniques which considers information on track displacement via their impact parameters, as well as secondary and tertiary decay vertices within the volume of the reconstructed jet cone. While different algorithms to perform such b-tagging exist, this analysis uses the `DL1r` algorithm based on an artificial deep neural network trained on a simulated hybrid sample composed of $t\bar{t}$ and Z' events [58, 59]. The algorithm has a multidimensional output corresponding to the probabilities for a jet to originate from a b quark (in the following referred to as b-tagged jet), c quark, or any light flavour. The flavour probabilities are then used to define a single cut value on the b-tagged jetprobability. The ATLAS Flavour Tagging Group maintains various operating points to provide a specific b-tagged jettagging efficiency of 60%, 70%, 77% or 85% in a simulated $t\bar{t}$ sample. For this analysis the all-hadronic channel makes use of the 77% working point, which has a rejection factor of 5 and 170 on charm and light-flavoured jets, respectively. The 1 lepton channel uses the 70% working point, which has a rejection factor of 10 and 417 on charm and light-flavoured jets, respectively [237].

Uncertainties on the correction factors for the b-tagging identification response are applied to the simulated event samples by looking at dedicated flavour-enriched samples in data. An additional term is included to extrapolate the measured uncertainties to the high-p_{T}region of interest. This term is calculated from simulated events by considering variations on the quantities affecting the b-tagging performance such as the impact parameter resolution, percentage of poorly measured tracks, description of the detector material, and track multiplicity per jet. The dominant effect on the uncertainty when extrapolating to high-$p_{\mathrm{T}}$is related to the different tagging efficiencies when smearing the track impact parameters based on the resolution measured in data and simulation.

5.3.6 Overlap removal

It is possible that reconstructed candidate objects overlap with each other and that the same tracks or energy deposits are therefore associated to multiple objects. As a result an overlapping procedure must be applied which removes all but one of the overlapping objects from the event. The metric used to evaluate whether objects overlap is defined as $\Delta R = \sqrt{\Delta y^2 + \Delta\phi^2}$, where Δy is the rapidity distance between two objects. The sequence of removal of overlapping objects is summarised in table 23 and corresponds to the procedure labelled `recommended` within `AnalysisTop` defined and documented in [238].

Table 23. Sequence of the `recommended` object overlap removal procedure used in this analysis.

Reject	Against	Criteria
Electron	Electron	Shared track, higher-p_{T}electron kept
Muon	Electron	Calo-tagged muon and shared ID track
Electron	Muon	Shared ID track
Photon	Electron	$\Delta R < 0.4$
Photon	Muon	$\Delta R < 0.4$
Jet	Electron	$\Delta R < 0.2$
Electron	Jet	$\Delta R < 0.4$
Jet	Muon	numTrack < 3 and (ghost-associated OR $\Delta R < 0.2$)
Muon	Jet	$\Delta R < 0.4$
Photon	Jet	$\Delta R < 0.4$
Fat Jet	Electron	$\Delta R < 0.1$
Jet	Fat Jet	$\Delta R < 1.0$

5.4 Event and object selection

5.4.1 Online event selection

Because of the high expected jet multiplicity in the signal the all-hadronic channel relies on triggers on H_{T}, where H_{T} is defined as the scalar sum of the transverse energies of all the reconstructed jets in the event with $|\eta_{\mathrm{jet}}| < 2.8$. H_{T} triggers are built on top of L1 single-jet trigger items. To cope with the rising luminosities during run 2, the trigger H_{T} threshold has been increased from 850 GeVin 2015 to 1 TeVin the latter half of 2016. Since the trigger decision is based on H_{T} computed from online jet momenta, which is not identical to the jet momenta computed offline from fully calibrated jets, the triggers show a slow onset behaviour with respect to offline H_{T} as can be seen in figure 59 (left). While an offline H_{T} cut is applied for all fully-hadronic signal regions, the cut does not ensure fully effcient triggers. Therefore, the onset behaviour and especially its modelling in simulation has to be taken into account.

period	run numbers	lowest-unprescaled trigger	Int. Lum. [fb^{-1}]
2015	276262-284484	HLT_ht850_L1J75	3.2
2016	297730-300279	HLT_ht850_L1J75	0.6
	300345-311481	HLT_ht1000_L1J100	32.5
2017	325713-340453	HLT_ht1000_L1J100	44.3
2018	349169-364292	HLT_ht1000_L1J100	58.5

Table 24. List of all lowest unprescaled H_{T} triggers alongside the data-taking periods during which they were used and the corresponding integrated luminosity.

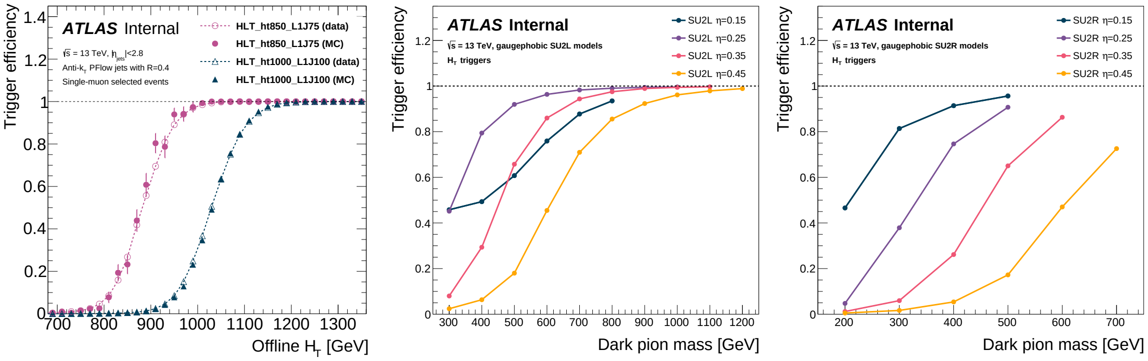

Figure 59. Left: Comparison of H_{T} trigger onsets between data and simulation for all H_{T} triggers used in the analysis. The onsets were produced from events that were selected by single-muon triggers. Middle and right: H_{T} trigger efficiencies as function of dark pion mass and η parameter. All simulated $SU(2)_L$ signal points are plotted in the middle panel, the $SU(2)_R$ efficiencies are shown on the right.

It is studied in detail in section 5.7.2.7. A full list of all used H_{T} triggers is given in table 24 alongside the relevant datataking period and corresponding integrated luminosities.

The efficiencies of H_{T} triggers in selecting signal are plotted in Figure 59 for all simulated signal samples. The triggers reach 100% efficiency for the highest dark pion masses, but have low to zero efficiency for low masses. Just like for single-lepton triggers the efficiency generally increases for lower η values since topologies tend to be very boosted after the decay of the heavy dark rho. The efficiency is only reduced for those mass points which have a large contribution from Drell-Yan production, especially the $\eta = 0.15$ mass points in the $SU(2)_L$ models.

5.4.2 Offline event selection

Only events recorded in the `physics_Main` stream are considered for this search. The debug stream, which contains events for which the HLT has timed out or crashed, will be used for an independent check.

Interaction vertices are reconstructed from ID tracks, where the tracks are required to have transverse momentum $p_T^{\text{trk}} > 500$ MeV [173]. Candidates for the primary vertex are required to have at least two associated tracks. The candidate with the largest $\sum(p_T^{\text{trk}})^2$, where p_T^{trk} is the transverse momentum of an associated track, is labelled the primary vertex (PV). Events that fail the reconstruction of a PV are rejected.

All data events are required to pass the standard good run list (GRL) selection, which allows for the rejection of individual lumi blocks within the data taking of an LHC fill. The lists recommended by the DataPreparation Group [239] are used. They correspond to versions 20170619 for data recorded in 2015, 20180129 for 2016 data, 20180619 for 2017 data and 20190318 for data from 2018.

Furthermore, a number of event-level vetos are applied to reject bad or corrupted events. This includes checks for LAr noise bursts (`xAOD::EventInfo::LAr`), corruptions in the Tile calorimeter (`xAOD::EventInfo::Tile`), events affected by the recovery procedure for single-event upsets in the SCT (`xAOD::EventInfo::SCT`), and incomplete events due to a TTC (Timing, Trigger and Control) restart (`xAOD::EventInfo::Core`).

5.4.3 Discriminating variables

The analysis uses a collection of discriminating variables, some common to both channels, some specific for each of them. The variables are listed and described below:

- H_{T} is the scalar sum of transverse momentum for jets in an event.
- $\mathrm{N}_{\mathrm{jets}}$ is the number of jets in the event, reconstructed and identified as described in section 5.3.3
- $\mathrm{N}_{\mathrm{b-jet}}$ is the number of jets identified as coming from a b-decay using a 77% efficiency working point, following section 5.3.5
- $m_{\mathrm{jet,R=1.2}}$ is the re-clustered anti-$k_{\mathrm{T}}R = 1.2$ jet mass
- $m_{bb}/p_{T,bb}$ for a large-R jet is the ratio of mass to $p_{\mathrm{T}}$for the system of the two closest b-tagged jets to the large-R jet
- $\Delta R\left(j, b_2\right)$ for a large-R jet is the distance between the second closest b-tagged jet and the large-R jet

$m_{bb}/p_{T,bb}$ is computed for a large-R jet by adding the 4-vectors of the two closest (smallest ΔR) b-tagged jets and then dividing the mass of this object by its p_{T}. The mass of both b-jets is set to 5 GeV for this calculation only. The all-hadronic signal region selection uses $m_{bb}/p_{T,bb}$ and $\Delta R\left(j, b_2\right)$ to require two well-separated, b-tagged jets in both large-R jets in an event to suppress the QCD multijet background.

5.4.4 Object selection

5.4.4.1 All-hadronic channel

In addition to the trigger, good run list, jet/muon cleaning, and derivation requirements, the selections listed in table 25 are applied for all all-hadronic studies shown in this note. This preselection requires zero loose-leptons, H_{T} greater than 1150 GeV and at least six jets in an event with $p_T > 25$ GeV. This H_{T} selection has been chosen to exclude the vast majority of the trigger onset region where the H_{T} trigger does not have full efficiency yet and where the analysis would be susceptible to a mismodeling of the onset behaviour in simulation. A flavour tagging requirement of three b-tagged jets is applied to reject low b-tag backgrounds. The two large-R jets with the largest $p_{\mathrm{T}}$are required to have mass over 190 GeV to exclude SM processes.

Table 25. Summary of the preselection cuts used in the all-hadronic channel.

Cut	Preselection
loose ℓ	0
H_{T}	$>$ 1150 GeV
$p^{6}_{T,jet}$	> 25 GeV
$\mathrm{N}_{\mathrm{b-jet}}$	≥ 3
$m^{1}_{\mathrm{jet,R=1.2}}$	> 190 GeV
$m^{2}_{\mathrm{jet,R=1.2}}$	> 190 GeV

Event yields with this preselection applied are shown in table 26. SM processes with final states containing multiple top or bottom quarks were investigated as potential backgrounds and are included in this table. The dominant background originates from QCD multijet events as can be inferred by the large data yield compared to the sum of MC backgrounds. In signal and validation regions this QCD multijet background is determined through a data driven method. The major MC background is $t\bar{t}$, with additional contributions from W/Z + jets, single-top and $t\bar{t}$ +X. Multiboson backgrounds are almost entirely excluded by the preselection.

Table 26. All-hadronic preselection yields for data and Monte Carlo samples.

Sample	Yield	Percent SM MC sum
$t\bar{t}$	8690.6	81.7
W/Z + jets	1167.8	11.0
$t\bar{t}$ + X	402.5	3.8
SingleTop	372.1	3.5
Multiboson	0.8	« 1
SM sum	10633.8	100
SU2L-25-400	1276.2	
SU2L-25-500	484.1	
SU2L-25-600	176.9	
Data	67339	

Applying the event quality, trigger, and preselection cuts results in the data, MC and example signal point yields listed in the cutflow in table 27. Each row of this table shows the weighted events yields after application of all cuts listed above. Appendix A.4 contains additional cutflows for all SM backgrounds and additional signal points.

Signal yields across the signal point grid with the preselection applied are shown in Figure 60. The preselection cuts were optimised using the η = 0.25 and m_{π_D} = 500 GeV signal point as a benchmark. The signal yields drop significantly at high dark pion masses and for small η values due to the large decrease in production cross section as shown in Figure 53. Additionally, for the samples with η = 0.15 Drell-Yan dark pion production becomes relevant and takes over as dominant production mechanism for $m_{\pi_D} > 400$ GeV resulting in further reduced signal yields.

Distributions of all-hadronic preselection and signal region discriminating variables are shown in figures 61-63. These plots compare normalized distributions of MC backgrounds to three reference signal points. No multijet background estimate

Table 27. All-hadronic preselection cutflow for data and all considered simulated backgrounds at 139 fb^{-1} integrated luminosity.

Cut	Data	All MC	$t\bar{t}$ allhad	$t\bar{t}$ leptonic	V+jets	$t\bar{t}+X$	Single top	Multiboson	Signal-25-500
Derivation	4854707771	55906050.1	694738.7	481928.0	34144700.6	232261.6	20227153.6	125267.6	2334.7
GRL	4712276790	55906050.1	694738.7	481928.0	34144700.6	232261.6	20227153.6	125267.6	2334.7
Good Calo	4707661650	55906050.1	694738.7	481928.0	34144700.6	232261.6	20227153.6	125267.6	2334.7
Primary vertex	4707659559	55906050.0	694738.7	481928.0	34144700.6	232261.6	20227153.5	125267.6	2334.7
Trigger	205205611	2023505.2	644911.2	416308.9	809064.8	20854.6	131120.3	1245.5	2170.9
Bad muon veto	205203444	2023355.4	644901.9	416200.1	809052.8	20851.3	131104.9	1244.5	2170.7
Jet cleaning	202840649	2016338.2	642644.4	414750.2	806313.6	20775.2	130613.9	1241.0	2164.6
$H_T > 1150$ GeV	87703211	1077894.6	396149.0	256362.1	352814.7	10616.4	61433.6	518.8	1999.9
$N_{\text{jets}} \geq 6$	45304007	847490.9	360951.1	205735.7	226798.4	9865.0	43921.0	219.6	1797.1
$N_{\text{jets, R=1.2}} \geq 2$	45005443	838487.0	360365.9	200019.5	225162.2	9715.7	43007.9	215.8	1758.5
$N_{\text{b-jets}} \geq 3$	576239	86552.0	48503.7	24585.3	6318.3	2675.1	4449.2	20.4	1181.3
electron veto	568304	79540.4	48351.5	18454.4	6311.1	2341.1	4061.9	20.4	998.9
muon veto	561409	72769.1	48305.5	12428.6	6304.3	2032.2	3678.2	20.4	829.5
$m^{1,2}_{\text{jet},1.2} > 190$ GeV	69879	10806.7	7151.2	1647.1	1220.6	405.8	381.2	0.8	493.3
$p^{6}_{T,\text{jet}} > 25$ GeV	67339	10633.8	7074.2	1616.4	1167.8	402.5	372.1	0.8	484.1
preselected	67339	10633.8	7074.2	1616.4	1167.8	402.5	372.1	0.8	484.1

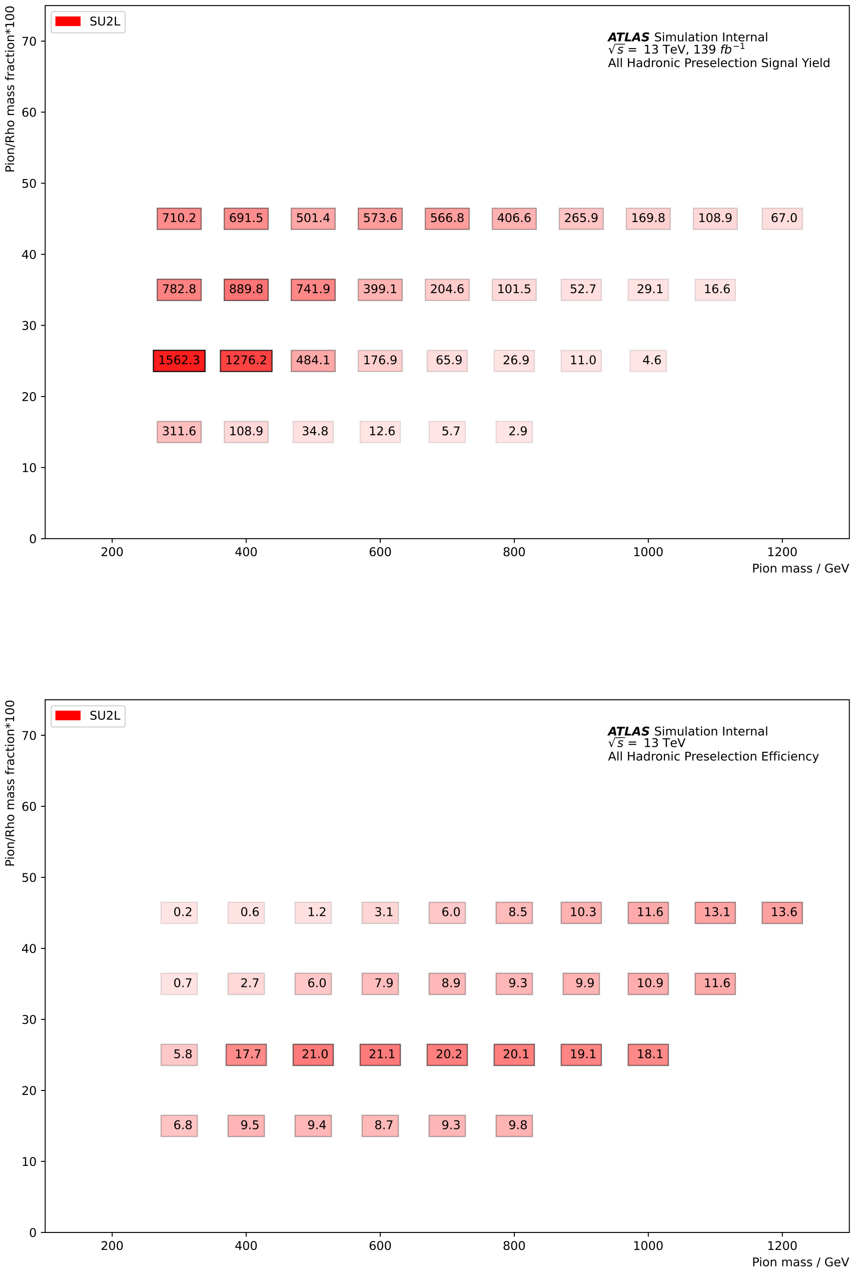

Figure 60. All-hadronic preselection yield and efficiency for $SU(2)_L$ signal points. The signal region has been optimized for $\eta = 0.25$ and $m_{\pi_D} = 500$ GeV. $SU(2)_R$ is not targeted in the all hadronic channel due to the low cross section at large π_D and ρ_D masses in this model.

is included in these plots as they are intended to show signal discrimination from MC backgrounds. Kinematic distributions of jets in preselected data events and their stability over time have been studied in appendix A.5, the sensitivity of the key preselection quantities to pileup were investigated more closely in appendix A.6.

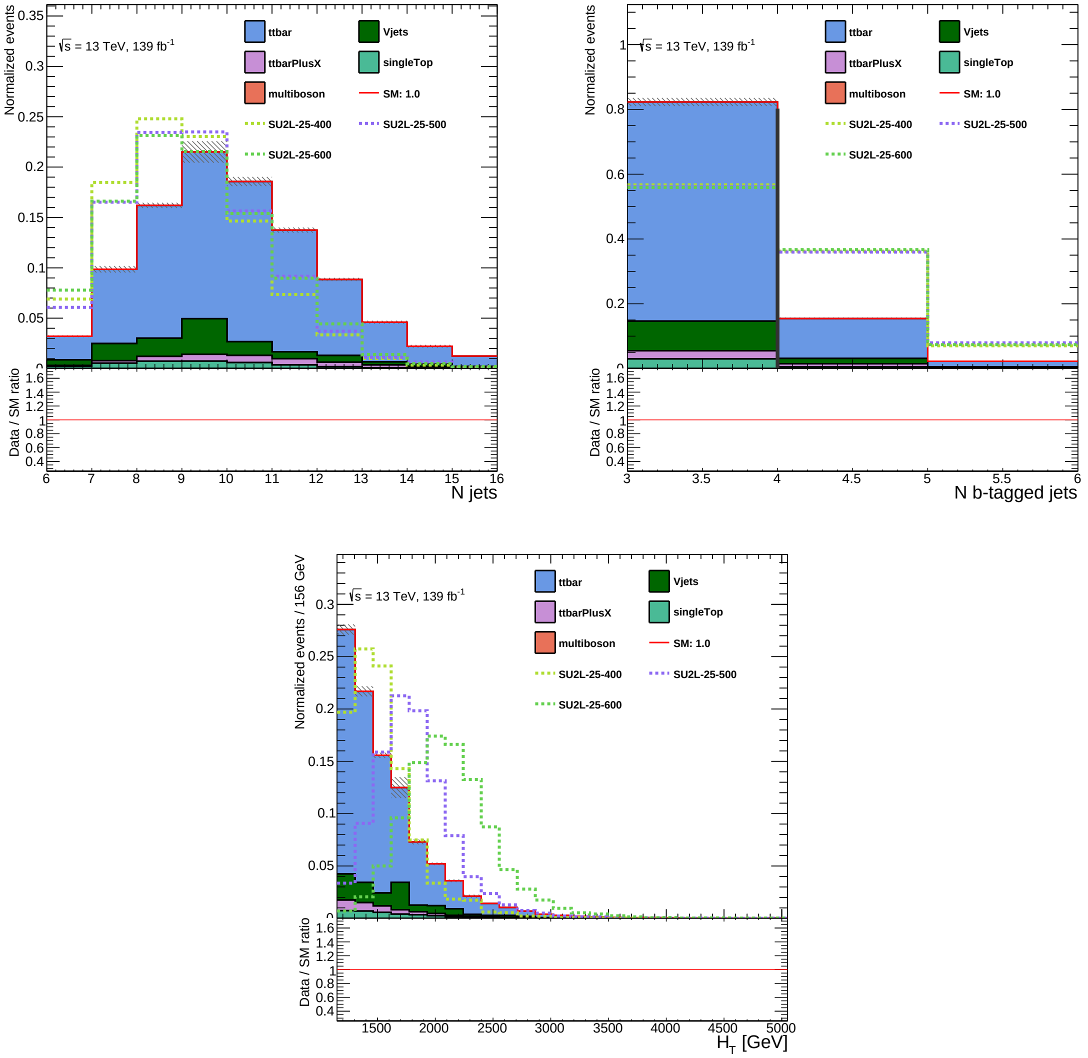

Figure 61. Plots of the all-hadronic preselection variables with the last bin including overflow events. Statistical uncertainties are indicated by the shaded region. The QCD multijet background is not calculated at the preselection stage. The η = 0.25 signal points shown are highly boosted which results in merging of R=0.4 jets and a reduced number of jets.

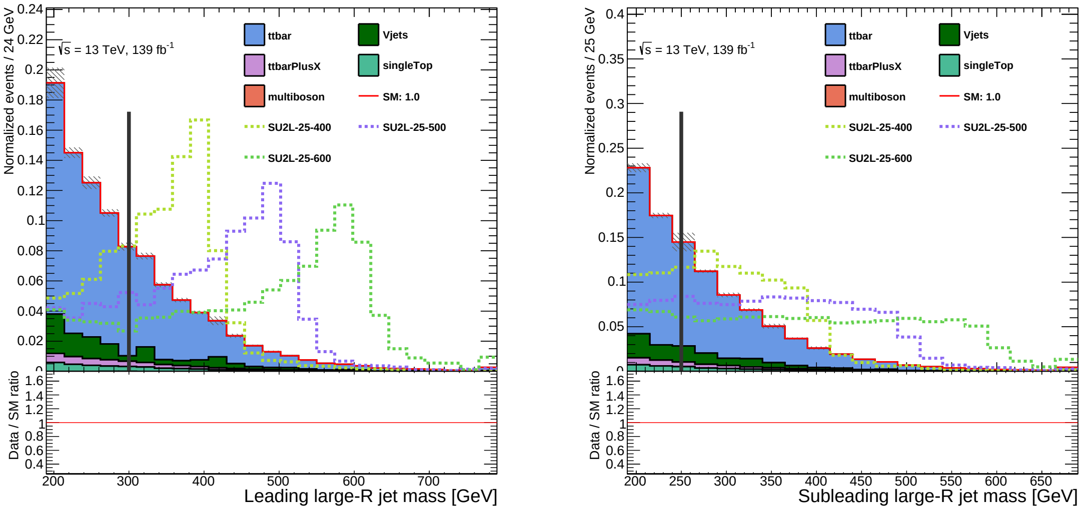

Figure 62. Plots of the all-hadronic preselection variables with the last bin including overflow events. Statistical uncertainties are indicated by the shaded region. The QCD multijet background is not calculated at the preselection stage. Signal region selections as described by table 28 are indicated with a vertical line. Individual SR bins select sub-regions of leading and sub-leading large-R jet mass for improved background discrimination.

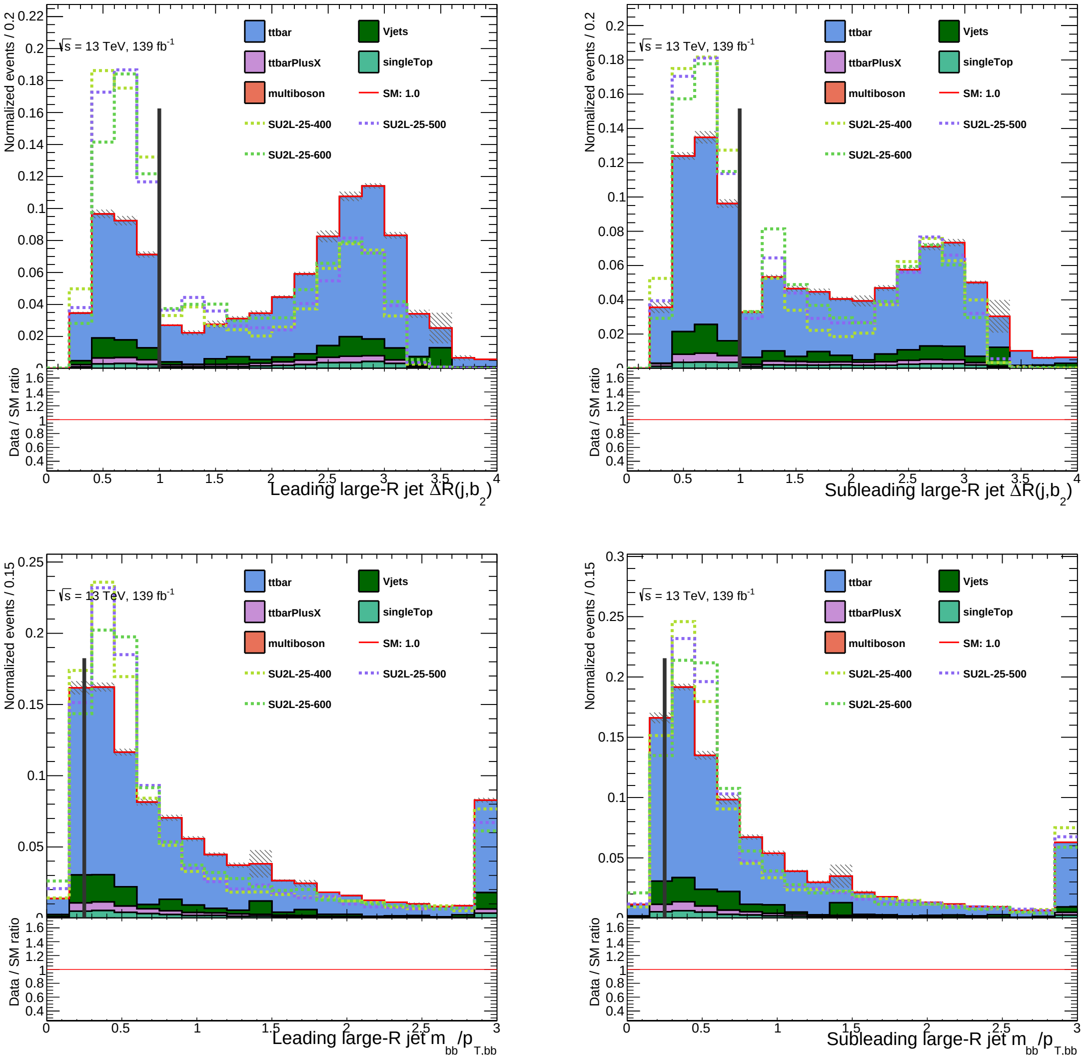

Figure 63. Plots of the all-hadronic preselection variables with the last bin including overflow events. The Multijet background is not estimated for this selection. The $m_{bb}/p_{T,bb}> 0.25$ selection is intended to suppress QCD multijet events. Signal region selections as described by table 28 are indicated with a vertical line. Leading and sub-leading large-R jet $\Delta\mathrm{R}(\mathrm{J}, \mathrm{b}_2)$ is required to be less than 1.0. Statistical uncertainties are indicated by the shaded band.

5.5 Signal region definitions

5.5.1 All-hadronic channel

The all-hadronic signal region (SR) is optimized for medium to low η values and dark pion masses larger than 400 GeV. In particular, the signal point with $\eta = 0.25$ and $m_{\pi_D} = 500$ GeV was used as benchmark. This selection adds requirements on large-R jet kinematics, b-jet kinematics, and b-tag matching requirements to both large-R jets in addition to the preselection. The signal region is binned in leading and subleading large-R jet mass to improve the sensitivity of the all-hadronic channel. From here on the bins of the SR are treated individually. Specifically this means the QCD multijet estimation is performed individually for each SR bin, and the final selection therefore has to account for the different leading and subleading jet mass requirements in each of these SR bins. Two tagging selections are applied to each of the leading two large-R jets in order to reconstruct two dark pions in the event as described in appendix A.2. A large-R jet is considered bb_i tagged if the ΔR between the large-R jet and the second closest b-tagged jet is less than 1.0. Here and in the following the subscript i identifies the jet. A large-R jet is considered $\pi_{D,i}$ tagged if its mass falls into the mass window which defines the current SR bin. The tag definitions are summarised in table 28.

The signal region requires both large-R jets to pass both tagging selections. The remaining events with one or two tags form the regions used for the data driven QCD extrapolation, the three-tag events are used as validation. This will be discussed in detail in section 5.6. To further exclude multijet events a common selection of $m_{bb}/p_{T,bb} > 0.25$ is applied to both large-R jets in the SR and all extrapolation regions, where $m_{bb}/p_{T,bb}$ is defined as the ratio of the mass to the transverse momentum of the pair of b-tagged jets closest to a large-R jet. Only the leading and subleading jet are considered in this evaluation. Additional reclustered jets with lower $p_{\mathrm{T}}$are not included even if the leading jets should fail the selection cuts.

Table 28. The all-hadronic SR selection is specified by four tag selections. The SR is divided into nine bins for improved sensitivity and the tag selections depend on the bin.

Large-R jet	tag	variable	selection
Both leading large-R jets		$m_{bb}/p_{T,bb}$	> 0.25
Leading large-R jet	$\pi_{D,1}$	$m_{\mathrm{jet,R=1.2}}$	bin selection
Subleading large-R jet	$\pi_{D,2}$	$m_{\mathrm{jet,R=1.2}}$	bin selection
Leading large-R jet	bb_1	$\Delta R\,(j, b_2)$	< 1.0
Subleading large-R jet	bb_2	$\Delta R\,(j, b_2)$	< 1.0

This region has been optimized for the SU2L-25-500 signal point, with a pion mass of 500 GeV and an η value of 0.25. The high boost from the small η results in a relatively small ΔR for the dark pion constituents allowing efficient pion reconstruction via the reclustered large-R jet mass, as can be judged from 62.

Each SR bin selects a window in leading and sub-leading large-R jet mass providing sensitivity to a range of η and dark pion masses as well as greater sensitivity to the targeted optimization point. Figure 64 shows the signal region bin definitions and the yields for the benchmark SU2L-25-500 signal point. Yields for additional signal points are shown in appendix A.7.

The large-R jet tags were selected for background discriminating power and suitability for an extended ABCD QCD multijet estimate. The extrapolation regions used for this data driven estimate use the already introduced tag selections and their corresponding anti-tags, which will be defined in section 5.6. These selections were optimized by independently varying each cut in a reference signal region, computing a full background estimate including MC and multijet background, and

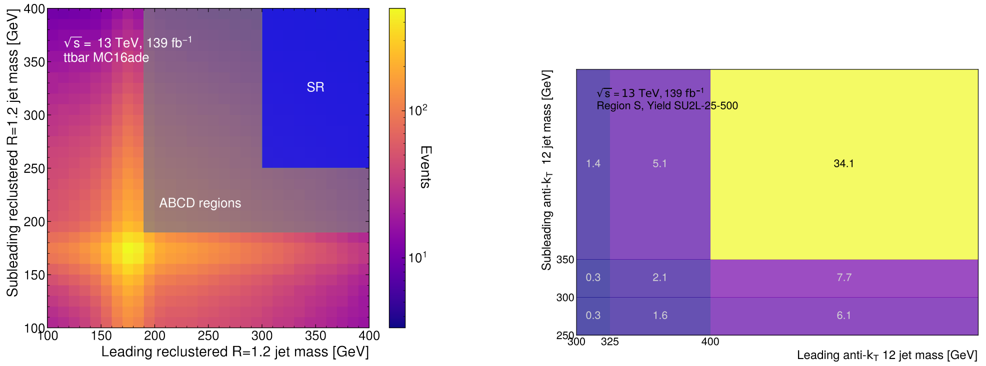

Figure 64. SR mass selection (left) and signal yield for point SU(2)$_\mathrm{L}$ 25 500 in each SR bin (right). The ABCD regions selection was chosen to exclude ttbar from all regions. The SR bins are open ended for the largest leading and subleading jet masses.

then maximizing the expected significance. A cutflow and example plots from this optimization with an unbinned signal region are shown in appendix A.8.

5.6 Background estimation

5.6.1 Background estimation in the all-hadronic channel

QCD multijet is the dominant background for the all-hadronic channel. A data-driven method is used to estimate this background, while MC simulation is used to estimate the remaining SM processes as described in section 5.2.2. Typical ABCD extrapolations are based on two discriminating variables. Here, however, we employ an extended ABCD method that relies on four instead of two discriminating variables, which allows the correction of correlations between pairs of discriminating variables and provide validation regions close to the signal region selection. Because MC backgrounds make up less than 20% of the total SM background in the SR, no control regions are used to scale the MC estimates. The multijet estimate extrapolates from regions with small leading and sub-leading $m_{\mathrm{jet,R=1.2}}$ and large $\Delta R\,(j, b_2)$ to SR bins with large leading and sub-leading $m_{\mathrm{jet,R=1.2}}$ and small $\Delta R\,(j, b_2)$. The SR bin selections are defined by two tag selections for each of two large-R jets as described in section 5.5. Anti-tags, denoted by a slashed tag label, are orthogonal selections which invert the selection or select a small large-R jet mass for $\pi_{D,i}$ tags. The combinations of possible tags and anti-tags in an event result in the 16 regions shown in figure 65. The extended ABCD method extrapolates from regions with one tag to the signal region bins. Two tag regions are used to determine correlation correction factors and three tag regions are used for validation of the estimate.

The SR is divided into leading and sub-leading jet mass bins in order to improve analysis sensitivity. For each of these nine bins the multijet background is estimated using an ABCD extrapolation. The $\pi_{D,i}$ tagging in these extrapolations selects one of these bins while the bb tagging is independent of bin selection. Table 29 shows the binned tag and anti-tag selections.

Table 29. All-hadronic binned tag selections. All of these selections are applied for each bin of the signal region.

Large-R jet	Tag	Variable	Tag selection	Anti-tag selection
Both large-R jets		$m_{bb}/p_{T,bb}$	> 0.25	
Leading large-R jet	$\pi_{D,1}$	$m_{\mathrm{jet,R=1.2}}$	bin selection	=< 300 GeV
Subleading large-R jet	$\pi_{D,2}$	$m_{\mathrm{jet,R=1.2}}$	bin selection	=< 250 GeV
Leading large-R jet	bb_1	$\Delta R\,(j, b_2)$	< 1.0	>= 1.0
Subleading large-R jet	bb_2	$\Delta R\,(j, b_2)$	< 1.0	>= 1.0

This data driven multijet extrapolation is a four variable generalization of the ABCD method based on the QCD estimate described in [240], where the top tags are replaced by $\pi_{D,i}$ tags and single b tags by bb tags to select for dark pions rather than top quarks. Region labels used in the present analysis follow the same naming convention as introduced in the reference.

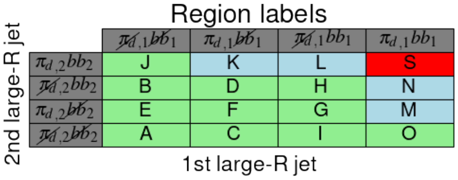

	$\not\pi_{d,1}\not{bb}_1$	$\pi_{d,1}\not{bb}_1$	$\not\pi_{d,1}bb_1$	$\pi_{d,1}bb_1$
$\pi_{d,2}bb_2$	J	K	L	S
$\not\pi_{d,2}bb_2$	B	D	H	N
$\pi_{d,2}\not{bb}_2$	E	F	G	M
$\not\pi_{d,2}\not{bb}_2$	A	C	I	O

Figure 65. Tagging states for the 16 regions used to estimate QCD in the SR. Region S labels a SR bin, regions BCEI are used for the ABCD extrapolation, regions DFGHJO are used to compute correlation correction factors and regions KLMN are validation regions. The estimate is done independently for all SR bins.

The extended ABCD method is a complex procedure, only the general concepts of which are outlined here. For a more comprehensive explanations and additional information and calculations we refer to appendix A.3.

To estimate the QCD multijet background a four variable ABCD estimate $\hat{S}'$ is computed from data - MC counts in regions A, B, C, E, and I according to

$$\hat{S}' = \frac{BCEI}{A^3} \quad , \tag{5.1}$$

where the letters represent the event counts in the respective regions. The estimate is then multiplied by six k factors to correct for correlations between regions,

$$\hat{S} = \hat{S}' \cdot k_{\pi_{D,1},bb_1} \cdot k_{\pi_{D,2},bb_2} \cdot k_{\pi_{D,1},bb_2} \cdot k_{\pi_{D,2},bb_1} \cdot k_{\pi_{D,1},\pi_{D,2}} \cdot k_{bb_1,bb_2}. \tag{5.2}$$

A correlation factor is computed for each of the regions D, F, G, H, J and O. Each correlation factor, k_{t_1,t_2} (where t denotes either a $\pi_{D,i}$ or bb_i tag), is computed by comparing its two variable (conventional) ABCD estimate to data - MC in the region with both of these tags,

$$k_{t_1,t_2} = \frac{N_{t_1,t_1} \cdot N_{\not{t}_1,\not{t}_2}}{N_{\not{t}_1,t_1} \cdot N_{t_1,\not{t}_2}} \quad , \tag{5.3}$$

where the slash indicates an anti-tag and N the even counts. If the region counts are independent for these tag selection than the expectation value of the corresponding k factor will be 1. Correlation factors around 1.5 are observed between the $\pi_{D,1}$ and bb_1 tags as well as the $\pi_{D,2}$ and bb_2 tags. The bb_1 and bb_2 tags are highly correlated with a k factor of 0.1 due to the preselection requirement of 3 b-tagged jets. This could be mitigated by requiring 4 b-tagged jets, however, this would result in low statistics and high signal contamination for the 4D ABCD extrapolation regions.

For each validation region, a three variable ABCD estimate is computed with two correlation correction factors. For example, in region K where the leading jet is tagged as $\pi_{D,1}$ and $\not{bb}_1$, and the sub-leading jet has tags $\pi_{D,2}$ and bb_2, the QCD multijet estimate is

$$\hat{K} = \frac{J \cdot C}{A} k_{\pi_{D,1},\pi_{D,2}} \cdot k_{\pi_{D,1},bb_2} \quad . \tag{5.4}$$

Data yields in all 1, 2, and 3 tag ABCD regions are shown in figure 66 individually for each bin in the plane of leading and sub-leading $m_{\mathrm{jet,R=1.2}}$.

Full tables of data, SM MC, QCD multijet estimates, signal yields, signal contaminations and k factors for each SR bin are shown in appendix A.9. Signal contamination is less than 15% for all extrapolation regions. This contamination results mainly from weak exclusion limits for the dark pion signal point with $m_{\pi_D} = 300$ GeV and $\eta = 0.25$. For all signal points the ratio of signal to background in the extrapolation regions is small compared to the ratio of signal to background in the most sensitive bin,

$$S_{CR}/B_{CR} \ll S_{SR}/B_{CR} \quad . \tag{5.5}$$

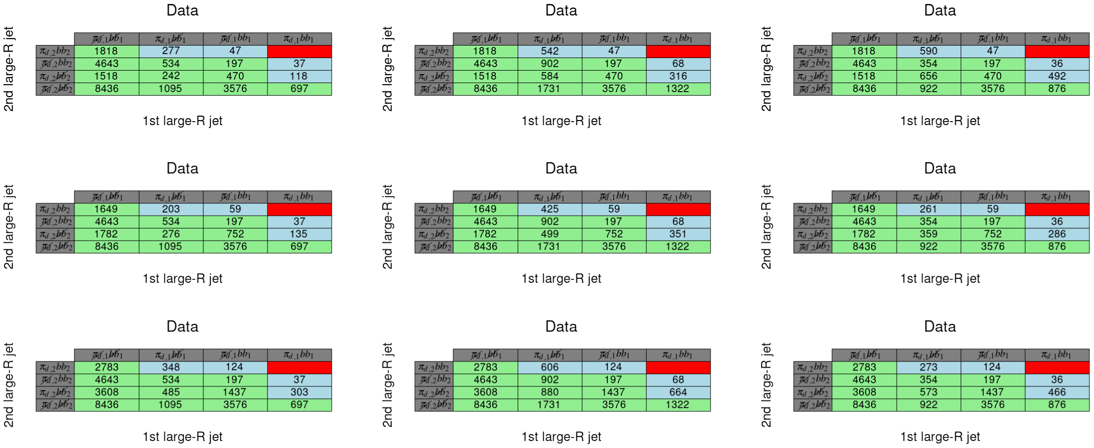

Data

	$\not\pi_{d,1}\not{b}b_1$	$\pi_{d,1}\not{b}b_1$	$\not\pi_{d,1}bb_1$	$\pi_{d,1}bb_1$
$\pi_{d,2}bb_2$	1818	277	47	🟥
$\not\pi_{d,2}bb_2$	4643	534	197	37
$\pi_{d,2}\not{b}b_2$	1518	242	470	118
$\not\pi_{d,2}\not{b}b_2$	8436	1095	3576	697

Data

	$\not\pi_{d,1}\not{b}b_1$	$\pi_{d,1}\not{b}b_1$	$\not\pi_{d,1}bb_1$	$\pi_{d,1}bb_1$
$\pi_{d,2}bb_2$	1818	542	47	🟥
$\not\pi_{d,2}bb_2$	4643	902	197	68
$\pi_{d,2}\not{b}b_2$	1518	584	470	316
$\not\pi_{d,2}\not{b}b_2$	8436	1731	3576	1322

Data

	$\not\pi_{d,1}\not{b}b_1$	$\pi_{d,1}\not{b}b_1$	$\not\pi_{d,1}bb_1$	$\pi_{d,1}bb_1$
$\pi_{d,2}bb_2$	1818	590	47	🟥
$\not\pi_{d,2}bb_2$	4643	354	197	36
$\pi_{d,2}\not{b}b_2$	1518	656	470	492
$\not\pi_{d,2}\not{b}b_2$	8436	922	3576	876

Data

	$\not\pi_{d,1}\not{b}b_1$	$\pi_{d,1}\not{b}b_1$	$\not\pi_{d,1}bb_1$	$\pi_{d,1}bb_1$
$\pi_{d,2}bb_2$	1649	203	59	🟥
$\not\pi_{d,2}bb_2$	4643	534	197	37
$\pi_{d,2}\not{b}b_2$	1782	276	752	135
$\not\pi_{d,2}\not{b}b_2$	8436	1095	3576	697

Data

	$\not\pi_{d,1}\not{b}b_1$	$\pi_{d,1}\not{b}b_1$	$\not\pi_{d,1}bb_1$	$\pi_{d,1}bb_1$
$\pi_{d,2}bb_2$	1649	425	59	🟥
$\not\pi_{d,2}bb_2$	4643	902	197	68
$\pi_{d,2}\not{b}b_2$	1782	499	752	351
$\not\pi_{d,2}\not{b}b_2$	8436	1731	3576	1322

Data

	$\not\pi_{d,1}\not{b}b_1$	$\pi_{d,1}\not{b}b_1$	$\not\pi_{d,1}bb_1$	$\pi_{d,1}bb_1$
$\pi_{d,2}bb_2$	1649	261	59	🟥
$\not\pi_{d,2}bb_2$	4643	354	197	36
$\pi_{d,2}\not{b}b_2$	1782	359	752	286
$\not\pi_{d,2}\not{b}b_2$	8436	922	3576	876

Data

	$\not\pi_{d,1}\not{b}b_1$	$\pi_{d,1}\not{b}b_1$	$\not\pi_{d,1}bb_1$	$\pi_{d,1}bb_1$
$\pi_{d,2}bb_2$	2783	348	124	🟥
$\not\pi_{d,2}bb_2$	4643	534	197	37
$\pi_{d,2}\not{b}b_2$	3608	485	1437	303
$\not\pi_{d,2}\not{b}b_2$	8436	1095	3576	697

Data

	$\not\pi_{d,1}\not{b}b_1$	$\pi_{d,1}\not{b}b_1$	$\not\pi_{d,1}bb_1$	$\pi_{d,1}bb_1$
$\pi_{d,2}bb_2$	2783	606	124	🟥
$\not\pi_{d,2}bb_2$	4643	902	197	68
$\pi_{d,2}\not{b}b_2$	3608	880	1437	664
$\not\pi_{d,2}\not{b}b_2$	8436	1731	3576	1322

Data

	$\not\pi_{d,1}\not{b}b_1$	$\pi_{d,1}\not{b}b_1$	$\not\pi_{d,1}bb_1$	$\pi_{d,1}bb_1$
$\pi_{d,2}bb_2$	2783	273	124	🟥
$\not\pi_{d,2}bb_2$	4643	354	197	36
$\pi_{d,2}\not{b}b_2$	3608	573	1437	466
$\not\pi_{d,2}\not{b}b_2$	8436	922	3576	876

Figure 66. Data yields for QCD estimate extrapolation regions. The nine tables correspond to the signal region bins in the plane of leading and sub-leading $m_{\mathrm{jet,R=1.2}}$, i.e. in the left column the leading jet has 300 GeV $< m_{\mathrm{jet,R=1.2}} <$ 325 GeV, in the middle column 325 GeV $< m_{\mathrm{jet,R=1.2}} <$ 400 GeV and in the right column $m_{\mathrm{jet,R=1.2}} >$ 400 GeV, while in the lowest row the sub-leading jet has 250 GeV $< m_{\mathrm{jet,R=1.2}} <$ 300 GeV, in the middle row 300 GeV $< m_{\mathrm{jet,R=1.2}} <$ 350 GeV and in the upper row $m_{\mathrm{jet,R=1.2}} >$ 350 GeV

Satisfying this condition insures that any systematic contribution of a possible signal to the ABCD estimate will not impact the sensitivity of the analysis. This criterion was chosen following the discussion in [241].

Applying equation 5.2 to the data - MC counts in each of the extrapolation regions for each of the SR bins results in a per bin QCD multijet estimate as shown in figure 67. This data driven background estimation method extrapolates over four discriminating variables with correction terms for correlation between any two of these variables and can be validated through the closure of the estimate in the four 3-tag validation regions K, L, M and N, which will be discussed in detail in the immediately following chapter.

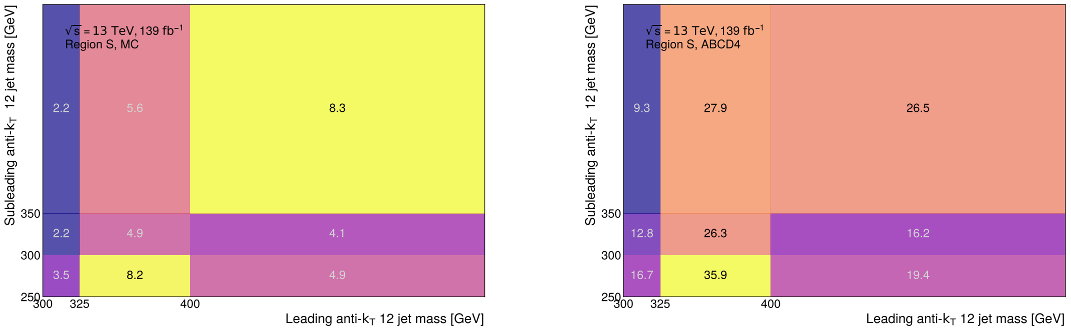

Figure 67. Background estimates for binned all-hadronic SR, MC contribution on the left, estimated QCD multijet yields on the right. The multijet background is estimated for each bin of the SR using the ABCD method.

5.6.2 Background validation in the all-hadronic channel

Four QCD multijet validation regions are defined with the same binning as the all-hadronic SR. Data is compared to SM MC plus the QCD multijet estimate in these regions to validate the ABCD extrapolation and to provide a non-closure systematic uncertainty. These VRs are defined by applying three tags and one anti-tag in order to create validation regions as close to the SR as possible. The VRs are labeled K, L, M and N with tag selections shown in figure 65.

Figure 68 compares data to SM estimated yields for each VR in each SR bin. Data yields are within the uncertainty band for all of these regions, where the size of the uncertainty band is determined and discussed in chapter 5.7.4.

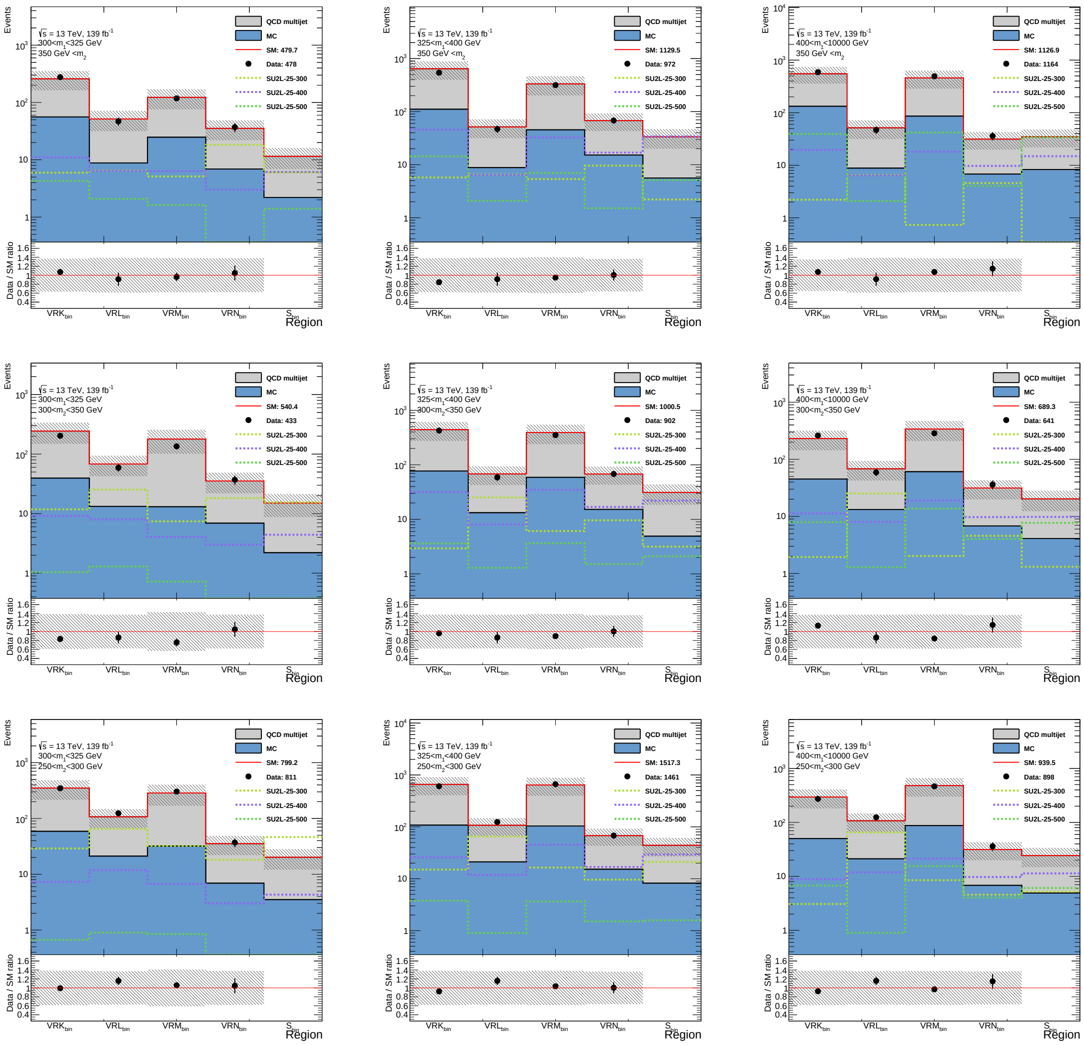

Figure 68. Validation regions for each signal region bin. The shaded region indicates BG uncertainty including statistical uncertainties and a 48% systematic non-closure error on the QCD multijet estimate. Full systematic uncertainties are included in the results section plots. Each validation region differs from the signal region by having exactly one anti-tag. VRK requires less than 2 b-tagged jets matched to the leading large-R jet (the $\cancel{bb}_1$ tag). VRL requires $m_{\mathrm{jet,R=1.2}} < 300$ GeV for the leading large-R jet (the $\cancel{\pi}_{D,1}$ tag). VRM requires less than 2 b-tagged jets matched to the sub-leading large-R jet (the $\cancel{bb}_2$ tag). VRN requires $m_{\mathrm{jet,R=1.2}} < 250$ GeV for the sub-leading large-R jet (the $\cancel{\pi}_{D,2}$ tag).

5.7 Systematic uncertainties

5.7.1 Summary of systematics

There are a multitude of different sources of potential systematic variations to consider in this analysis. They have been split up into three groups. Uncertainties arising from instrumental origins are discussed in section 5.7.2, systematic uncertainties from theoretical considerations are detailed in 5.7.3 and section 5.7.4 deals with the uncertainty on the QCD multijet background estimation relevant only in the all-hadronic channel.

For a better overview a list of all considered uncertainties is given in table 30.

5.7.2 Instrumental uncertainties

5.7.2.1 Luminosity uncertainty

The integrated luminosity of the full dataset used in this analysis was determined with the LUCID-2 detector [205] following the method detailed in [27]. The uncertainty on this value is determined to be 1.7% by using beam-separation scans in x and y. The uncertainty value is applied to all simulated samples in the analysis and is labelled `Luminosity`.

5.7.2.2 Pileup reweighting uncertainty

As described in section 5.2.4, all simulated samples are reweighted to match the pileup profile observed in data. To estimate a systematic variation that might be introduced by this procedure the scale factor applied to the pileup distributions is varied from its nominal value of 1.0/1.03 to 1.0/0.99 to account for the up systematics

Table 30. Overview of all considered systematic uncertainties. Some of the systematics consist of several components, in such a case the number of components is indicated in the right column. A star indicates that these components have been combined by adding the uncertainties in quadrature before the final statistical analysis.

Source of uncertainty	Components
Instrumental uncertainties	
Luminosity	1
Pileup reweighting	1
Leptons	
Electron scale factors	4
Electron resolution and scale	3
Muon scale factors	8
Muon resolution and scale	4
Jets	
Jet vertex tagging	1
Flavour-tagging	22
Jet energy scale	23
Jet energy resolution	8
H_{T} trigger efficiency	1
Theoretical uncertainties	
$t\bar{t}$ **modeling**	
μ_R and μ_F variations	1*
PDF+α_S variations	1*
m_{top} variations	1*
Generator	1
Parton shower	1
Choice of h_{damp}	1
QCD multijet estimate	1

and 1.0/1.07 for the down systematic. The corresponding uncertainty is labelled `Pileup_Reweighting`

5.7.2.3 Lepton uncertainty

Uncertainties on leptons arise from multiple sources around identification, isolation, reconstruction, trigger as well as momentum scale and resolution.

Slight performance differences between data and simulation in lepton reconstruction, identification, isolation and triggering are corrected by the application of scale factors that have been estimated from tag-and-probe experiments in $Z \to l^+l^-$ events in data and simulation [242, 234]. The scale factors constitute a potential source of systematic variation. The uncertainties on the scale factors can be propagated to the analysis in form of a set of alternative event weights. For electrons this results in four individual variations labelled `EL_SF_[ID/Isol/Reco/Trigger]`. For muons eight components arise from ID, isolation, track-to-vertex association and trigger (`MU_SF_[ID/Isol/TTVA/Trigger]`). Each of these four is in itself split up into a statistical and a systematic component.

In simulation the lepton momentum scale and resolution is corrected to match the distribution in data. This is a source of a potential systematic variation. To evaluate the impact of scale systematics the lepton energy or momentum is varied by $\pm 1\sigma$ and the signal selection redone. For resolution uncertainties the lepton energy or momentum is smeared and the signal selection redone. For electrons this results in three individual components, `EG_RESOLUTION_ALL` and `EG_SCALE_[ALL/AFII]`, while for muons fourparate components exist (`MUON_[CB/SCALE]` and `MUON_SAGITTA_[DATASTAT/RESBIAS]`).

5.7.2.4 Jet vertex tagging uncertainty

Slight differences in efficiency of the jet vertex tagging (JVT) method in data and simulation are addressed by applying scale factors to simulation. In [178] systematic variations on these scale factors have been explored in different simulated $Z \rightarrow \mu\mu$+jets samples. These uncertainties are propagated to the analysis in form of additional event weights that are applied to all samples. The corresponding uncertainty is labelled `JET_Vertex_Tagging`.

5.7.2.5 Flavour-tagging uncertainty

Flavour-tagging efficiency differences between data and simulation are corrected by a reweighting of events. This introduces a source of potential systematic variations. Uncertainties on the corrections are derived from dedicated flavour-enriched subsets of the data which are propagated to the analysis in form of alternative sets of event weights. All flavour tagging uncertainties are stored in the central file `2019-21-13TeV-MC16-CDI-2019-10-07_v1.root`. It comprises nine independent NPs for b-tagged jets(labelled `BTag_B_NP[1-9]`), five parameters for c-jets (`BTag_C_NP[1-5]`) and six parameters from light jets (`BTag_Light_NP[1-6]`). Additionally there are two more NPs to extrapolate the measured uncertainties to the high-p_{T}region labelled `BTag_Extrapolation` and `BTag_Extrapolation_From_Charm`.

5.7.2.6 Jet Energy Scale and Resolution for small-R jets

The determination of jet energy scale (JES) and jet energy resolution (JER) is done by combining information from actual collision data, test beam data and simulation as described in [243, 54]. The Jet/EtMiss group provides different types of JES and JER systematics configurations where either all nuisance parameters (NP) are kept independently or whether some of them are grouped [244]. For JES a total of nearly 100 NPs exists that can be reduced by category to roughly 30, by a global reduction to about 20, or through a strong reduction to 6 or 7. In this analysis we use the global reduction which is recommended for analyses that do not intend to perform combinations with CMS.

JER has a total of 34 individual NPs that can be reduced to 13 in the FullJER scheme, where the smearing is done both (pseudo-)data and simulation, or 8 NPs in the SimpleJER scheme, where the smearing is done exclusively in simulation. Here we use the SimpleJER scheme.

In section 5.9.1.1 we will see that all jet related systematics are unconstrained in the Asimov fit, thus giving us confirmation that our choice of reduction scheme was good and no additional parameters are needed.

5.7.2.7 H_T trigger efficiency

The H_T triggers used in the all-hadronic channel are sensitive to the scalar sum of jet momenta and therefore blind to muons which allows us to use events triggered by single-muon triggers to study systematic uncertainties associated to H_T triggers. In order to characterise the trigger behaviour the onset functions have been evaluated for events containing at least five jets with $p_\mathrm{T} > 20$ GeV or at least one large-R parameter jet with $R = 1.0$ and $p_\mathrm{T} > 200$ GeV, where all jets are required to be within $|\eta| < 2.5$. The onset functions are then built by plotting the trigger efficiencies as function of the reconstructed offline H_T constructed from all jets within $|\eta| < 2.8$ in the event for data and $t\bar{t}$ MC. The resulting trigger onset functions are shown in figure 69, where they are fitted with an error function of the form

$$\epsilon(H_\mathrm{T}\text{-trigger}) = \frac{A}{2}\left[1 + \mathrm{erf}\left(\frac{H_\mathrm{T}^{\mathrm{offline}} - B}{\sqrt{2}C}\right)\right] \tag{5.6}$$

where the parameter A corresponds to the plateau value of the trigger and is fixed to 1.0, parameter B represents the effective threshold for which the H_T-trigger reaches

50% efficiency and parameter C the resolution as the width of a Gaussian that cumulatively models the slope of the fit.

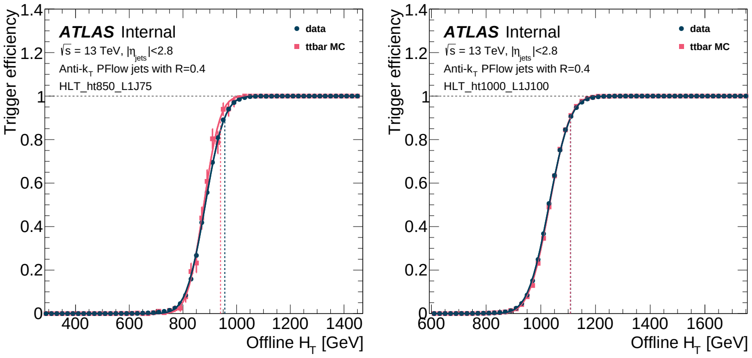

Figure 69. Onsets for HLT_ht850_L1J75 (left) and HLT_ht1000_L1J100 (right) in data and $t\bar{t}$ MC. The onsets were produced from single-muon triggered events with a jet multiplicity selection. See text for more details. The dashed vertical lines correspond to the offline H_{T} values for which the triggers reach 90% efficiency.

As can be seen in figure 69 the trigger reaches full efficiency for data and MC. However, since the offline H_{T} cut does not necessarily guarantee a working point in the plateau region, the differences in the onset behaviour between data and MC have to be considered as a systematic uncertainty on the expected signal yield. This is estimated by folding the onsets with the offline H_{T} spectrum for all signal MC samples. In this process the $t\bar{t}$ MC events are solely used to obtain the shape of the simulated onset of a given trigger chain to assess its differences with the shape in data. The total uncertainty is estimated from three individual components: the relative difference between the signal yields obtained from using the onset fit from data and $t\bar{t}$ MC, the maximal relative effect of independent $\pm 1\sigma$ variations of the fit parameters B and C on the fit in data, and independent fit parameter variations on the fit in MC. The abolute uncertainty is then calculated by adding the three components in quadrature.

The uncertainties are estimated for all signal points and both used H_T triggers where the signal offline H_T distributions were built from events with the same pileup profile as expected during the periods during which the relevant trigger was active. Offline H_T cuts in various signal regions have also been taken into account. To get meaningful uncertainties for each mass points the derived uncertainties per trigger are weighted according to the integrated luminosities during which the trigger was used for data taking, as can be extracted from table 24. Figure 70 shows the individual uncertainties for all H_T triggers and all signal points as well as their luminosity-weighted combination. As can be easily seen the systematic uncertainties due to the $H_\mathrm{T}$trigger onset are small for all signal samples. We apply a flat systematic of 0.04% labelled `HT_trigger`.

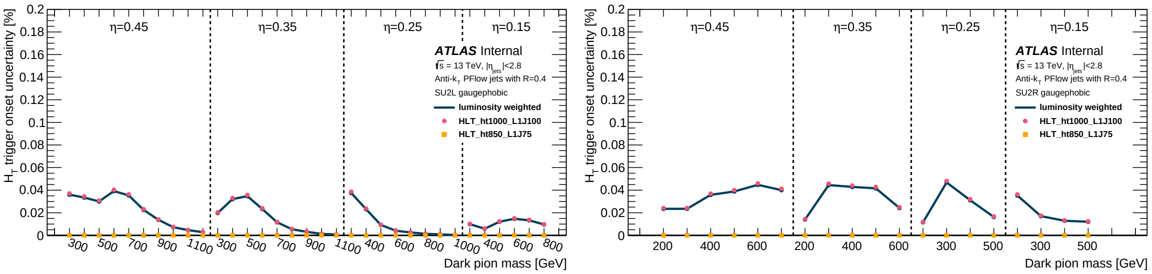

Figure 70. Estimated systematic uncertainties on the H_T trigger efficiency evaluated for all $SU(2)_L$ samples of the original signal grid on the left and all $SU(2)_R$ samples on the right. The uncertainties derived from the onset for individual triggers are shown with coloured markers, while the solid line indicates the luminosity-weighted combination of both triggers.

5.7.3 Theoretical cross sections

5.7.3.1 $t\bar{t}$ uncertainty

The leading simulated background in both analysis channels is $t\bar{t}$. It is affected by a number of systematic uncertainties that impact both scale and shape of distributions.

An uncertainty of ±6% is assigned on the inclusive $t\bar{t}$ production cross-section at NNLO+NNLL which is the result of adding in quadrature contributions from renormalisation and factorisation scale variations (obtained by independently varying the parameters μ_R and μ_F by a factor 0.5 and 2.0 and taking the envelope), PDF and α_S variations (where variations follow the PDF4LHC treatment [245] with the typical `Var3c` variations of the strong coupling constant α_S) and mass uncertainty (which follows from variations of the top mass by ±1 GeV) [246]. The associated systematic is labelled `ttbar_cross_section`.

An uncertainty introduced by the choice of generator is estimated by comparing the nominal $t\bar{t}$ samples with a different set of samples that were generated using MadGraph5_aMC@NLO. It is subsequently denoted by `ttbar_matching_scheme`

A further source of systematic uncertainty is the choice of parton showering model in the samples. To assess the impact the nominal samples are compared with an alternative set of samples where the parton showering was done using Herwig7. The associated systematic uncertainty is labelled `ttbar_parton_shower`.

The impact of a variation of the h_{damp} parameter is assessed by comparing the nominal samples to an alternative set of samples for which h_{damp} has been set to $3.0 \cdot m_{\text{top}}$. The corresponding uncertainty is identified as `ttbar_hdamp`.

5.7.3.2 Minor simulated backgrounds

All other simulated backgrounds are negligible in the all-hadronic channel and we therefore assign no systematic uncertainty on them.

5.7.4 QCD multijet background estimation

Deviations of the ratio between data and SM estimate from unity, denoted $k_{VR} =$ (data-MC)/QCD, are used to estimate a non-closure systematic uncertainty for the 4D ABCD method. The factors are multiplied together and the absolute value of the deviation of this product from 1 is used as the systematic uncertainty,

$$\sigma_{ABCD} = |1 - k_K k_L k_M k_N|. \tag{5.7}$$

This quantity is computed for each bin of the SR to produced the values shown in figure 71. The worst case, 48%, is applied as a non-closure systematic uncertainty for all bins and can subsequently be identified via the label `ABCD`.

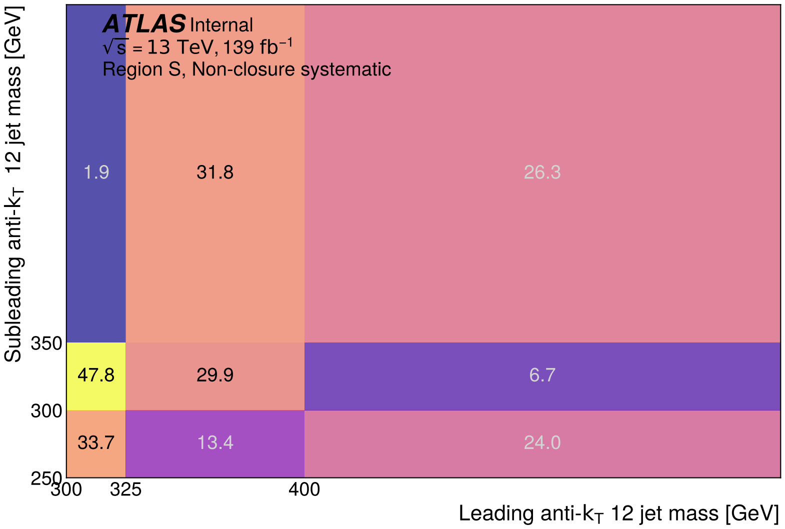

Figure 71. ABCD non-closure systematic uncertainty for each bin of the SR. All shown numbers are given in percent.

5.8 Unblinding Strategy

According to common practise this analysis has been conducted in a blinded manner, which means at no point have data events in the signal regions been examined. This was ensured by dedicated blinding algorithms which have prevented that data events in the signal regions were carried through to the analysis ntuples to prevent any accidental unblinding. Our blinding strategy was developed early on in the analysis process and consists of the following steps:

1. Development of a strategy to select dark meson events based on simulated samples and define signal regions for the search.

2. Estimate the expected SM backgrounds in the signal regions, optimise selection for maximum sensitivity to dark meson events, and derive dedicated control and validation regions by creating orthogonal selections where the signal contribution is negligible.

3. Use data in the control regions to validate the background estimate in the 1-lepton channel. In the all-hadronic channel the control regions are used to estimate QCD contributions directly from data. The background estimate is validated in dedicated validation regions.

4. Evaluate the expected signal and background contributions in the signal regions to calculate the sensitivity of the analysis only considering pseudo data.

After the completion of all four steps and the appropriate approval procedures from the editorial board and the HQT group we feel confident to unblind data in the signal regions and run the same statistical analysis tools as before with real data instead of pseudo data. Depending on the results two different interpretations can be considered:

If a significant excess of events beyond the prediction from SM expectation is observed, we will test all signal hypothesis against the observed data distribution using the TRExFitter framework as described below to determine the statistical significance of the data excess. In the absence of a significant excess, the same statistical analysis framework can be used to derive 95% confidence level exclusion limits on the considered signal models. In either case we plan to ultimately combine the results of the all-hadronic and the 1-lepton channel.

5.9 Final statistical analysis

5.9.1 All-hadronic Channel

The statistical analysis in the all-hadronic channel relies on a profile-likelihood fit over all nine signal region bins defined by the leading and subleading jet mass. Figure 72 shows an example of the predicted SM background and its composition in the SR alongside the expected event yields from three different signal+background hypotheses to illustrate how a potential signal would manifest itself. As expected, the dominant background originates from QCD events with an additional significant contribution coming from $t\bar{t}$ events. The red dashed line corresponds to the signal point for which the signal selection was primarily optimised.

Two different versions of the fit are performed. They are described below in dedicated chapters.

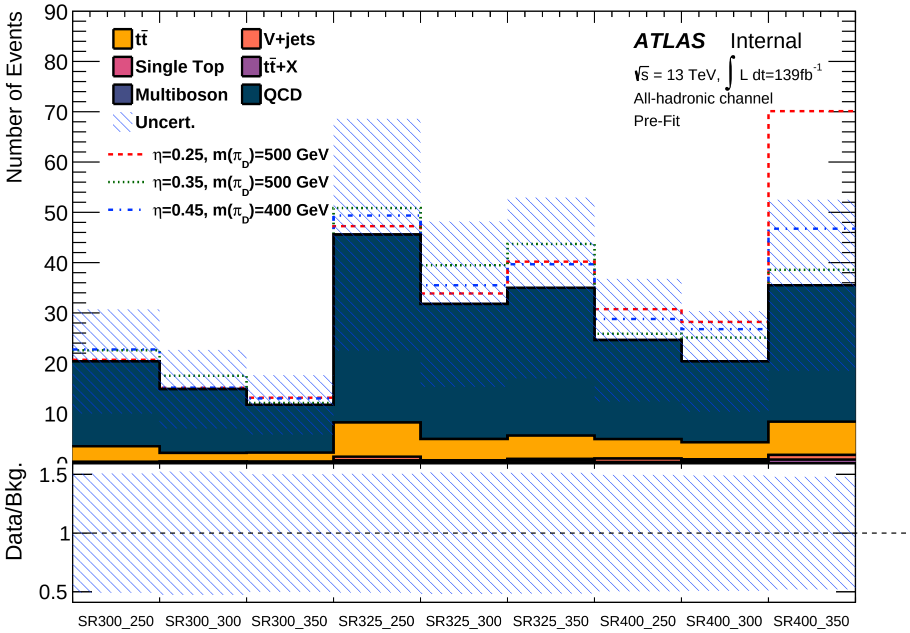

Figure 72. Predicted background in the signal region of the all-hadronic channel. Three different signal hypotheses are stacked onto the SM prediction to illustrate how signal would manifest itself. The shown uncertainty is a combination of statistical and systematic uncertainties. The x-axis labels reflect the different SR bins with the first number indicating the lower cut on the leading large-R jet mass and the second number the cut on the subleading large-R jet mass (compare e.g. to figure 67).

5.9.1.1 Asimov fit

For the Asimov fit no real data is considered and it is therefore possible to perform this fit while the analysis is still in a blinded state. Instead a set of pseudo-data which corresponds exactly to the background prediction ("Asimov data") is generated and fitted in all signal region bins. This allows to probe and cross-check two aspects of the fit model: First, the expected constraints on all fitted nuisance parameters and second, the expected sensitivity of the analysis to all considered signal points.

The fit itself is performed as if the Asimov data were real data. This means all signal hypotheses are evaluated against the pseudo-experiment to derive 95% confidence level intervals on the possible signal strength using the CL_S method defined in [201], which can in turn be converted into expected limits by multiplying them with the cross section of the signal hypothesis. The fit is conducted using the TRExFitter package which interfaces with HistFactory [247] and RooStats [248]. All estimated systematic uncertainties are included in the fit and TRExFitter automatically evaluates whether the systematic is kept as a whole, its shape dropped, or dropped altogether[2]. This step is referred to as "systematics pruning" and is applied individually for each signal and background component as well as each signal region. Since most systematics have a very limited impact on the present analysis, the majority of them are dropped at this stage. Figure 73 gives an overview of the results of the pruning step in the Asimov fit. As can be expected, no lepton systematic plays any role for the fit and even the majority of the jet systematics have too small an impact to be of relevance to the analysis. This is mainly due to the compensating nature of the multijet background estimate. Any variation in simulated

---

[2] Due to the special nature of the QCD estimate of this analysis no shape information is relevant here since each signal region consists only of a single bin. Hence TRExFitter drops the shape of all systematics without loss of information.

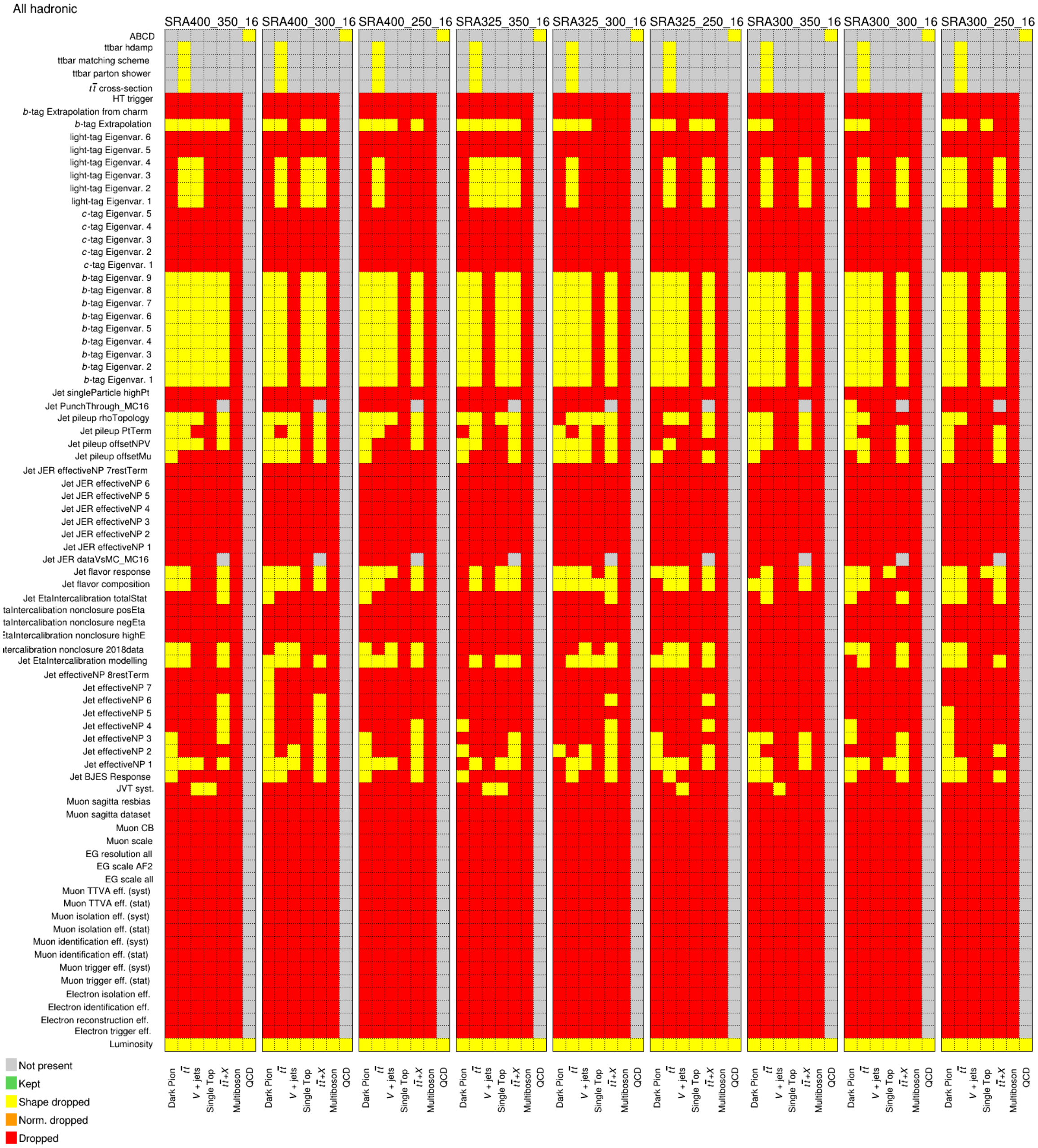

Figure 73. Summary of the results of the systematics pruning in the fit on Asimov data. Each panel represents one bin of the signal region, while the columns within each panel represent the individual background components or signal. As an example the dark pion signal point with $\eta = 0.25$ and $m_{\pi_D} = 400$ GeV was added here. Red boxes indicate that a systematic is negligible for a specific signal region bin and component. Yellow boxes indicate that the systematic is kept and considered as a nuisance parameter in the fitting (the reason these do not appear green is because all signal regions are one-bin regions which TRExFitter treats as if it dropped the shape, hence the yellow colour code). Grey boxes indicate that the systematic does not apply to this signal or background component. A technical issue caused the absence of two systematics for the $t\bar{t} + X$ sample, however, we expect this to have no bearing on the results of the analysis.

event counts gets compensated for by the multijet estimate as it is constrained directly to data.

A binned likelihood function operates by minimising the quantity $q(\mu) = -2\log\mathcal{L}$. Here, the likelihood $\mathcal{L}$ is defined as

$$\mathcal{L}(\mu,\theta|S,B,N) = \prod_{i\in\text{bins}} \mathcal{P}\left(N_i|\mu S_i + B_i\right) \times \mathcal{P}\left(S_i + B_i|\gamma_i\right) \prod_{j\in\text{syst.}} \mathcal{G}\left(\theta_j,\sigma_j\right) \tag{5.8}$$

where N is the number of data events, S the number of predicted signal events, B the expected background events, θ the set of nuisance parameters corresponding to systematic uncertainties (the systematics are scaled in such a fashion that before the fit all uncertainties have $\theta_j = 0$), γ the set of statistical uncertainties on the number of predicted events (also here the scaling is done to make $\gamma_i = 1$) and σ The uncertainties in the nuisance parameters modelling the systematic uncertainties (scaled so $\sigma_j = 1$ before the fit). The quantities indexed with i refer to the quantity in a specific bin, while the index j refers to a specific systematic. Statistical and systematic uncertainties are taken to be Poissonian ($\mathcal{P}$) and Gaussian ($\mathcal{G}$) distributed nuisance parameters.

The fit is performed under the background plus signal (S+B) hypothesis. The minimisation is done using the MINUIT2 minimisation package [249], which yields the optimal values for μ and the set of nuisance parameters θ_i, γ_i and σ_i. From these parameters it is possible to create a modified set of plots showing the post-fit distributions. Figure 74 contains a direct comparison of the pre-fit and post-fit distributions in all signal region bins. As expected, the post-fit plots show a significant reduction in the size of the uncertainty band due to constraints and (anti-)correlations of systematic uncertainties revealed by the fit.

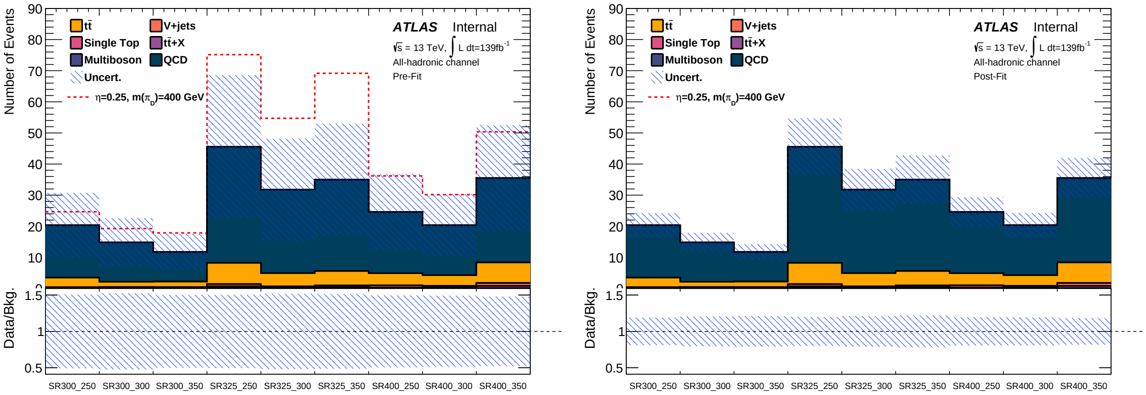

Figure 74. Pre-fit background estimate in all bins of the signal region on the left, the right plot shows the same after the fit was performed. The red dashed line shows an example $SU(2)_L$ signal point with $\eta = 0.25$ and $m_{\pi_D} = 400$ GeV. The uncertainty bands contain all statistical and systematic uncertainties. The x-axis labels reflect the different SR bins with the first number indicating the lower cut on the leading large-R jet mass and the second number the cut on the subleading large-R jet mass (compare e.g. to figure 67).

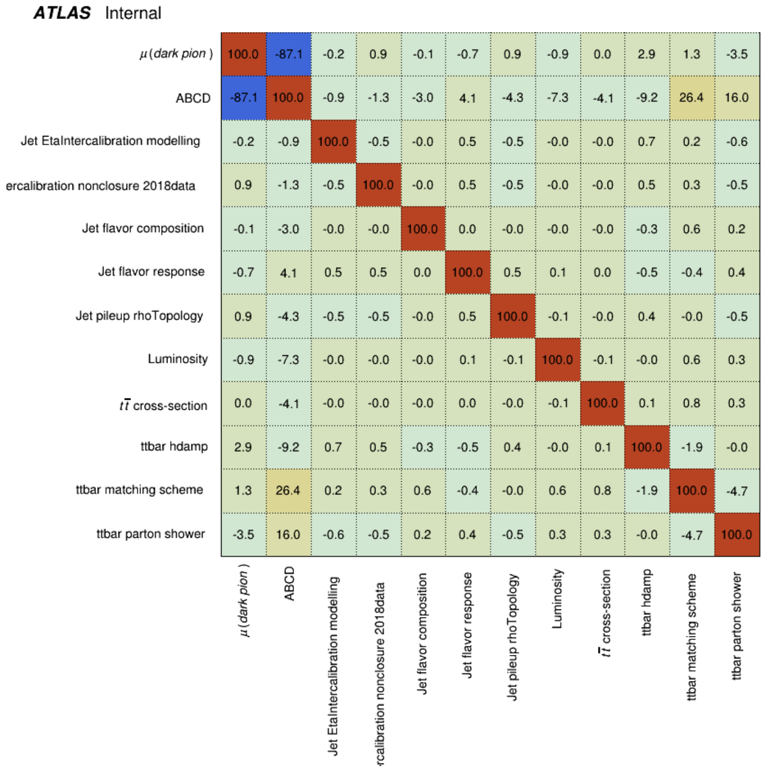
ATLAS Internal

	μ(dark pion)	ABCD	Jet EtaIntercalibration modelling	rcalibration nonclosure 2018data	Jet flavor composition	Jet flavor response	Jet pileup rhoTopology	Luminosity	$t\bar{t}$ cross-section	ttbar hdamp	ttbar matching scheme	ttbar parton shower
μ(dark pion)	100.0	-87.1	-0.2	0.9	-0.1	-0.7	0.9	-0.9	0.0	2.9	1.3	-3.5
ABCD	-87.1	100.0	-0.9	-1.3	-3.0	4.1	-4.3	-7.3	-4.1	-9.2	26.4	16.0
Jet EtaIntercalibration modelling	-0.2	-0.9	100.0	-0.5	-0.0	0.5	-0.5	-0.0	-0.0	0.7	0.2	-0.6
ercalibration nonclosure 2018data	0.9	-1.3	-0.5	100.0	-0.0	0.5	-0.5	-0.0	-0.0	0.5	0.3	-0.5
Jet flavor composition	-0.1	-3.0	-0.0	-0.0	100.0	0.0	-0.0	-0.0	-0.0	-0.3	0.6	0.2
Jet flavor response	-0.7	4.1	0.5	0.5	0.0	100.0	0.5	0.1	0.0	-0.5	-0.4	0.4
Jet pileup rhoTopology	0.9	-4.3	-0.5	-0.5	-0.0	0.5	100.0	-0.1	-0.0	0.4	-0.0	-0.5
Luminosity	-0.9	-7.3	-0.0	-0.0	-0.0	0.1	-0.1	100.0	-0.1	-0.0	0.6	0.3
$t\bar{t}$ cross-section	0.0	-4.1	-0.0	-0.0	-0.0	0.0	-0.0	-0.1	100.0	0.1	0.8	0.3
ttbar hdamp	2.9	-9.2	0.7	0.5	-0.3	-0.5	0.4	-0.0	0.1	100.0	-1.9	-0.0
ttbar matching scheme	1.3	26.4	0.2	0.3	0.6	-0.4	-0.0	0.6	0.8	-1.9	100.0	-4.7
ttbar parton shower	-3.5	16.0	-0.6	-0.5	0.2	0.4	-0.5	0.3	0.3	-0.0	-4.7	100.0

Figure 75. Correlation matrix of the Asimov fit in the all-hadronic channel. Shown are only parameters that have at least a 2% correlation with any of the other nuisance parameters. All shown numbers are given in percentages.

An easy way to visualise the correlations between nuisance parameters is to plot them in a correlation matrix. This was done in figure 75 and shows a strong correlation of the signal strength μ with the uncertainty on the QCD multijet estimate (listed as `ABCD`). This correlation is to be expected as the multijet uncertainty is designed in a very conservative way and in the absence of real data is very sensitive to variations in the signal strength. This also results in large constraints as described below. Further smaller and therefore tolerable correlations can be observed for the $t\bar{t}$ theory uncertainties (parton shower, matching scheme and hdamp parameter) with the systematic on the multijet estimate. All remaining parameters are virtually uncorrelated.

The fitted nuisance parameters are shown in figure 76. As the fit is performed on Asimov data we do not expect to see pulls for any of the nuisance parameters, but constraints on the parameter imposed by the fit. Only two systematics show any constraint at all: a negligible constraint for the $t\bar{t}$ matching scheme and a significant constraint on the uncertainty on the QCD multijet estimation. The constraint on the matching scheme likely results out of the correlation with the QCD multijet systematic, while the constraints on the multijet estimation themselves are a consequence of the Asimov fit: in the absence of real data the fairly large uncertainty can be reduced quite dramatically resulting in the observed constraints.

In order to estimate which parameters have the largest impact on signal, each nuisance parameter is pulled one sigma up and down while re-doing the minimisation of the likelihood. The change in the signal strength parameter μ is noted which corresponds to the uncertainty on μ from this parameter. It is now possible to plot these nuisance parameters ranked according to their impact on the signal strength. This was done in figure 77. As expected, the largest impact comes from the QCD

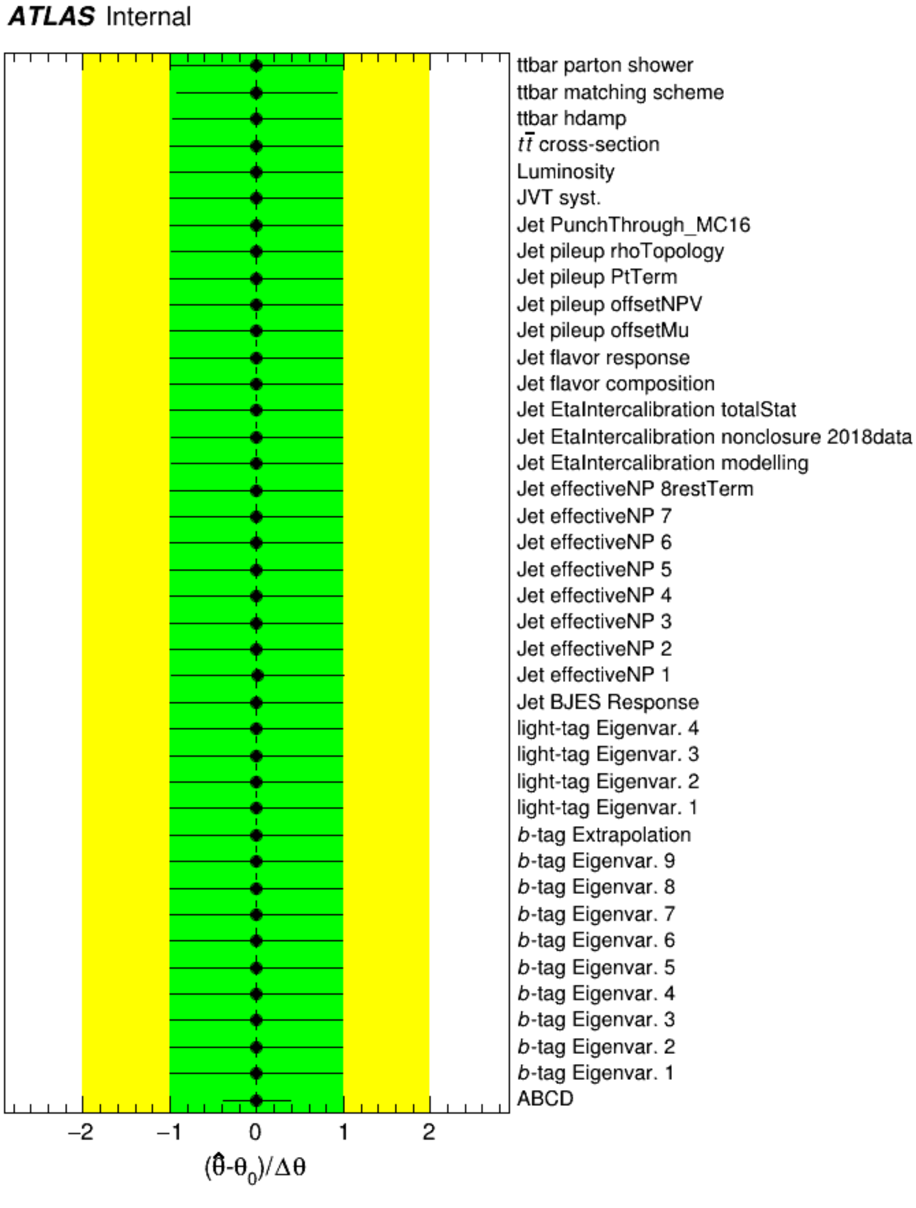

Figure 76. Nuisance parameters for the Asimov fit in the all-hadronic channel. Constraints are only visible to the $t\bar{t}$ matching scheme systematic and the parameter associated with the QCD multijet background estimation (ABCD).

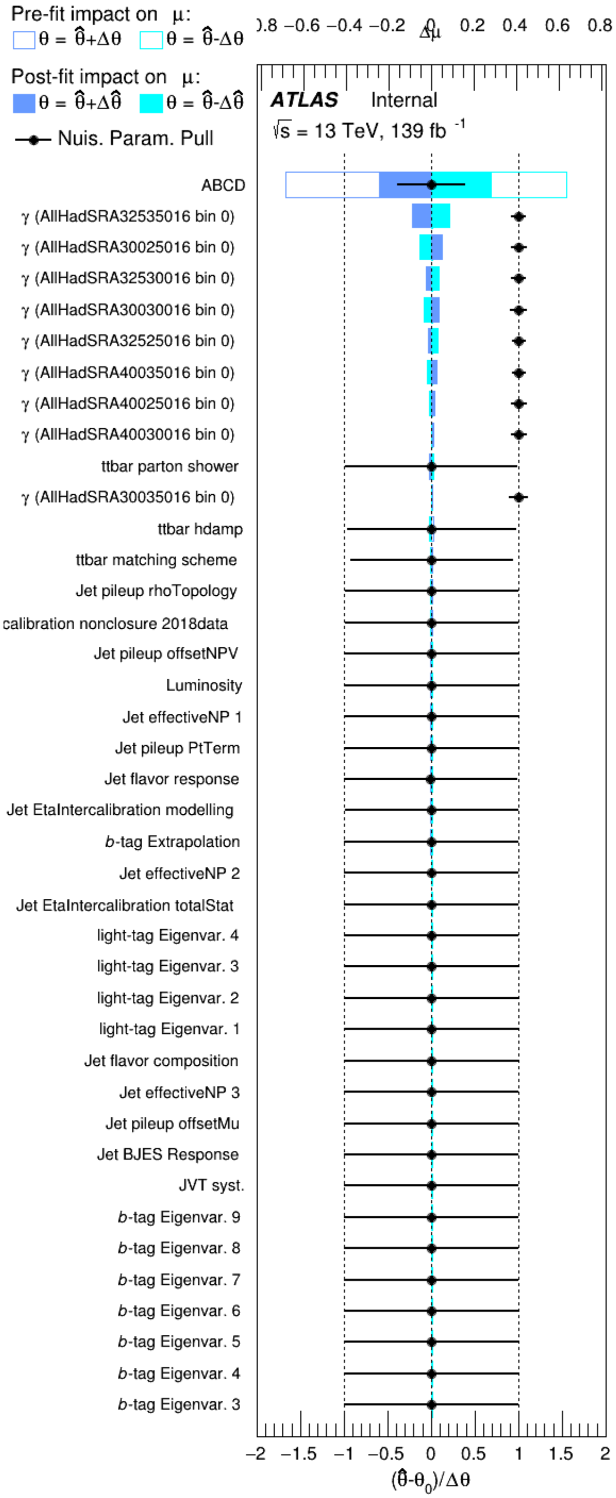

Figure 77. Ranking plot of the most impactful nuisance parameters in the fit to Asimov data.

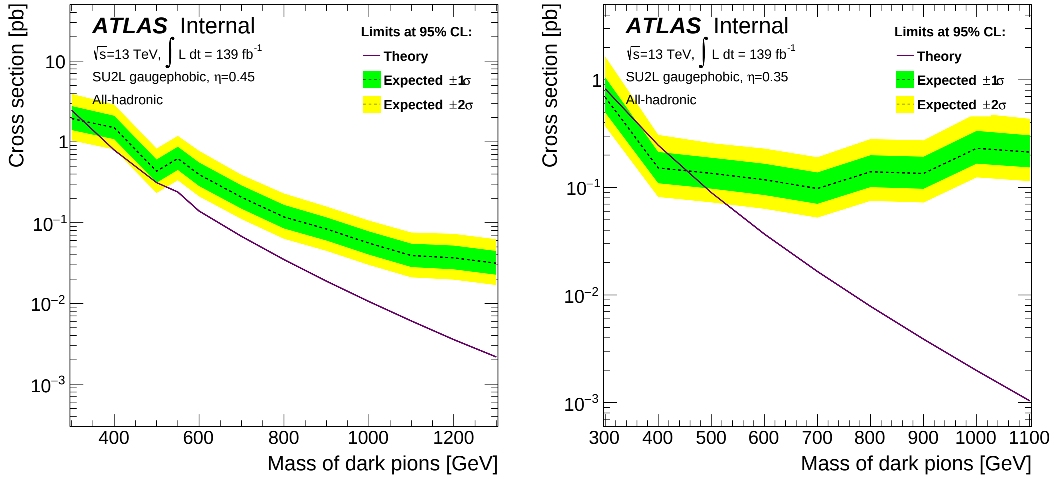

(a) η=0.45 (b) η=0.35

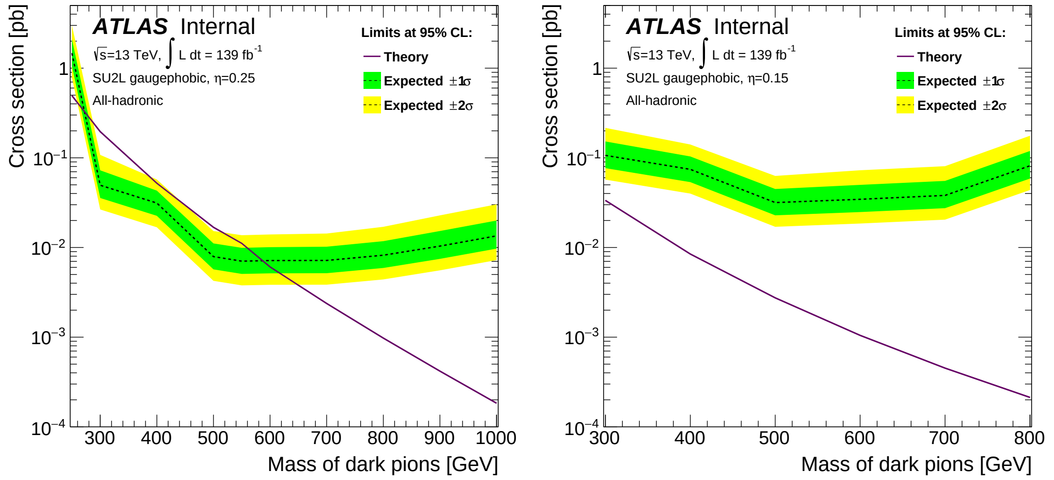

(c) η=0.25 (d) η=0.15

Figure 78. Expected upper limits on the dark pion production cross sections in the all-hadronic channel using the CL$_S$ method for all $SU(2)_L$ models in four slices of η. The dashed line represents the expected limit derived from the background-only hypothesis with the one and two sigma uncertainty bands shown in green and yellow. The solid purple line is the dark pion cross section prediction from theory. The shown uncertainties correspond to statistical plus systematic uncertainties.

multijet estimation uncertainty with the γ_i from the signal region bins showing up next. All remaining parameters have virtually no impact on the signal strength.

The results of the fit are used to derive expected upper limits on the production cross sections of dark pions. In figure 78 the limits are drawn in four slices of η

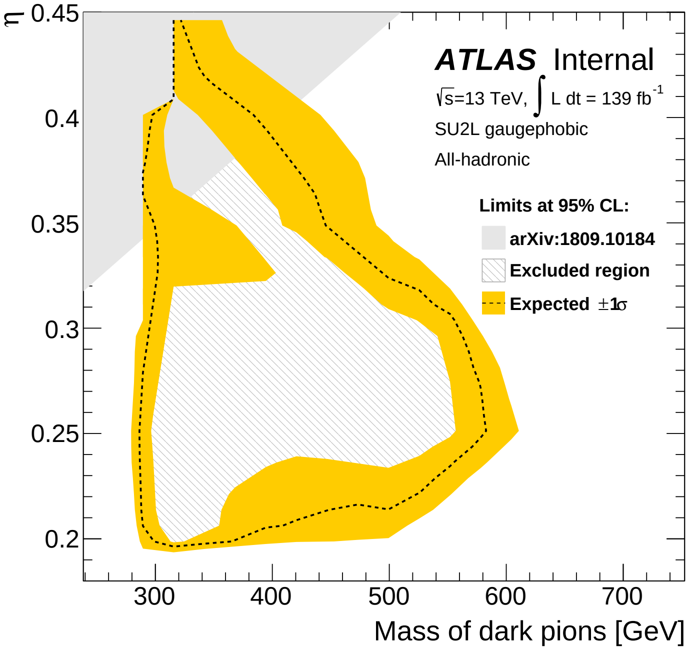

Figure 79. Expected exclusion limits in the η–m_{π_D}–plane for $SU(2)_L$ signal models in the all-hadronic channel.

corresponding to the values $\eta = 0.45$, 0.35, 0.25 and 0.15 in the $SU(2)_L$ models. The jagged shape of the exclusion band for $\eta = 0.45$ is mainly caused by a lack of statistics due to the very low signal efficiency in this extreme corner of signal phase space. The corresponding expected exclusion limits in the two-dimensional η–m_{π_D}–plane are drawn in figure 79.

As can be seen, it is possible to make statistically significant observations of dark pion events in the all-hadronic channel over a broad range of η and dark pion mass values. Comparing the expected limits to existing limits in figure 55 or the grey area in figure 79, it becomes clear that the all-hadronic channel is able to stand by itself and deliver not just a significant improvement over existing limits, but a worlds first. Since the production cross sections for dark pions from $SU(2)_R$ models are significantly smaller than for $SU(2)_L$ models, the all-hadronic channel has no sensitivity to any $SU(2)_R$ signal points.

CHAPTER VI

CONCLUSION

In this thesis I describe two searches which aim to discover or exclude dark matter signals. Excluding these signals allows us to constrain beyond the Standard Model parameter space and informs future searches. In the search for direct production of the supersymmetric partner to the top in the all-hadronic Jets+$E_{\mathrm{T}}^{\mathrm{miss}}$ final state we did not find any significant excess over Standard Model predictions and we are able to exclude stop masses up to 1.25 TeV for neutralino ($\tilde{\chi}_1^0$) masses below 200 GeV. This search significantly extends exclusion limits from the previous search at 36.2 fb^{-1} search as shown in Figure 81.

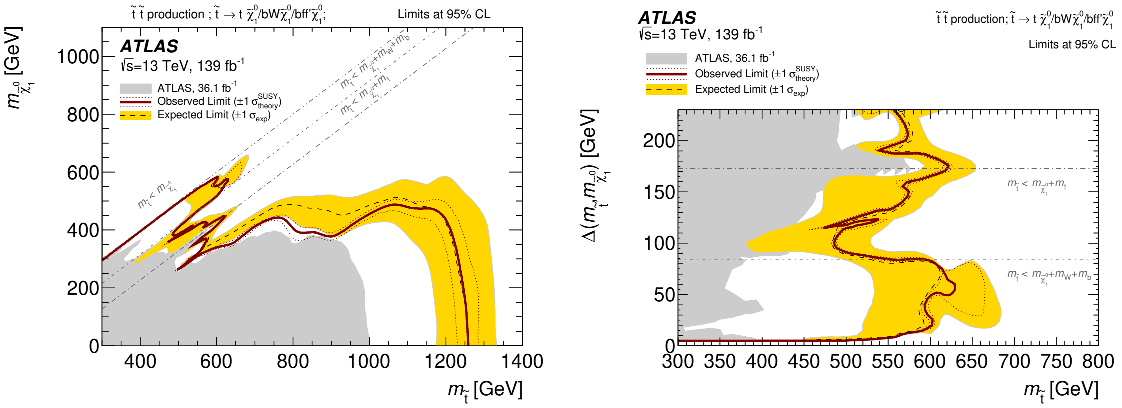

(a)

(b)

Figure 80. Observed (red solid line) and expected (black dashed line) exclusion contours at 95% CL as a function of the (a) $\tilde{\chi}_1^0$ vs $\tilde{t}$ masses and (b) $\Delta m(\tilde{t}, \tilde{\chi}_1^0)$ vs $\tilde{t}$ mass. Masses that are within the contours are excluded. Uncertainty bands corresponding to the $\pm 1\sigma$ variation of the expected limit (yellow band) and the sensitivity of the observed limit to $\pm 1\sigma$ variations of the signal total cross section (red dotted lines) are also indicated. Observed limits from previous ATLAS searches [107, 108, 109, 110, 112, 13] based on 36.1 fb^{-1} of *pp* collision data are provided for comparison in grey.

The search for dark mesons decaying to top and bottoms quarks is in editorial review and the signal regions are blinded at the time of this writing. This search

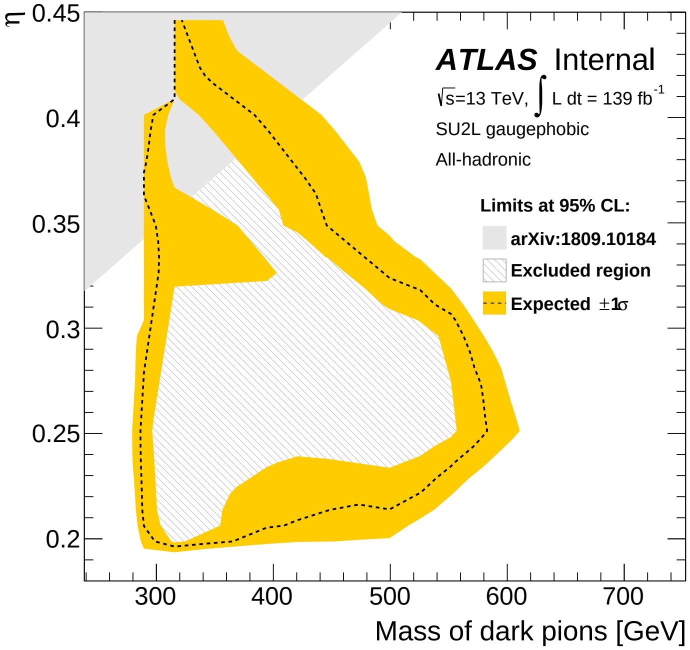

Figure 81. Run 2 expected exclusion limits in the η–m_{π_D}–plane for $SU(2)_L$ signal models in the all-hadronic channel.

is expected to exclude dark pion masses up to 500 GeV for 2 TeV dark rho mesons. Although observed limits cannot be shown for this search, the sensitivity for discovery or exclusion is expected to exclude dark pion masses up to 500 GeV for 2 TeV dark rho mesons as shown in Figure 81. A single-lepton channel search is also in progress and we intend to combine these analysis for greater statistical power and coverage of the dark meson parameter space.

LHC Run 3 is now in progress and is projected to produce 250 fb^{-1} of proton-proton collisions at $\sqrt{s} = 13.6\,\text{TeV}$ by its conclusion in 2025 [14]. The scaling of search sensitivity with luminosity of an example dark meson signal point is shown in Figure 82 for a range of multijet systematic uncertainties. We expect a Run 3 all-hadronic dark meson analysis to excluded dark pion masses up to 700 GeV. The HL-LHC [15] will increase collision rate and center of mass energy to allow collection of

$3000 - 4000\ \mathrm{fb}^{-1}$ of proton-proton collisions at $\sqrt{s} = 14\,\mathrm{TeV}$. Extrapolated exclusion and discovery sensitivity for direct stop production using HL-LHC data is shown in Figure 83. Future searches for the direct stop production and dark mesons will make use of higher center of mass energies, increased luminosity and improved analysis strategies to further contribute to our understanding of dark matter.

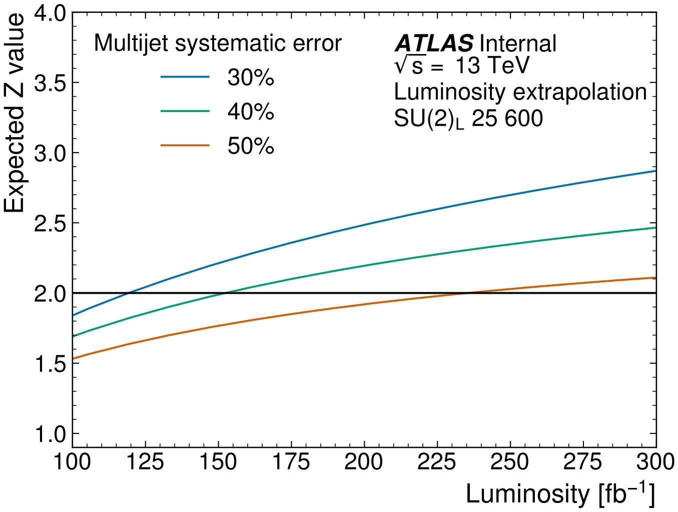

Figure 82. Extrapolated search sensitivity for an example $SU(2)_L$ signal point with a 600 GeV dark pion and 2.4 TeV dark rho for a range of multijet systematic uncertainties (this uncertainty is 48% in the Run 2 analysis). The black line indicates expected exclusion at 95% confidence. Multijet statistical and systematic uncertainties only are included in these binomial expected Z estimates.

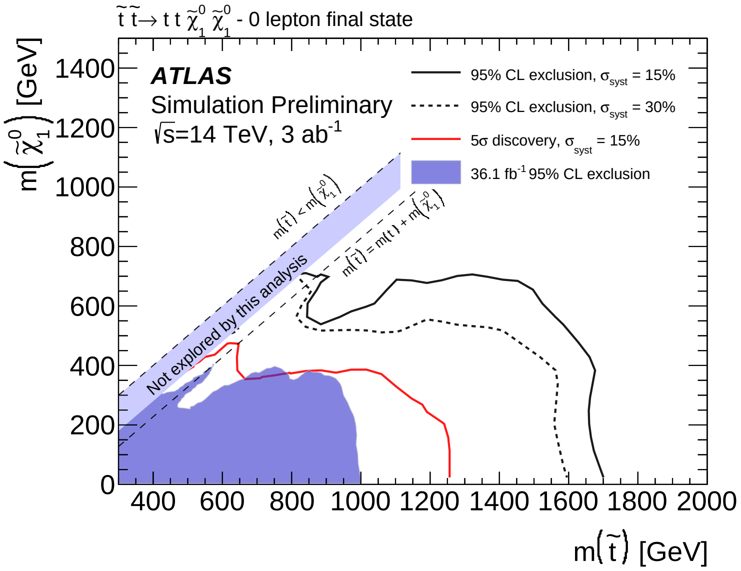

Figure 83. Final 95% CL exclusion reach and 5σ discovery contour corresponding to $3000-4000$ fb^{-1} of proton-proton collisions collected by ATLAS at the HL-LHC. Figure from [250].

APPENDIX

DARK MESON SEARCH ADDITIONAL STUDIES

A.1 Dark pion production cross sections

$SU(2)_L$ and $SU(2)_R$ cross sections depend on the mass of the dark rhos and pions, with $SU(2)_L$ models having larger cross sections at similar masses. This can be seen in 2D grids of η vs dark pion/rho mass, which are plotted in figure A.1 for convenience.

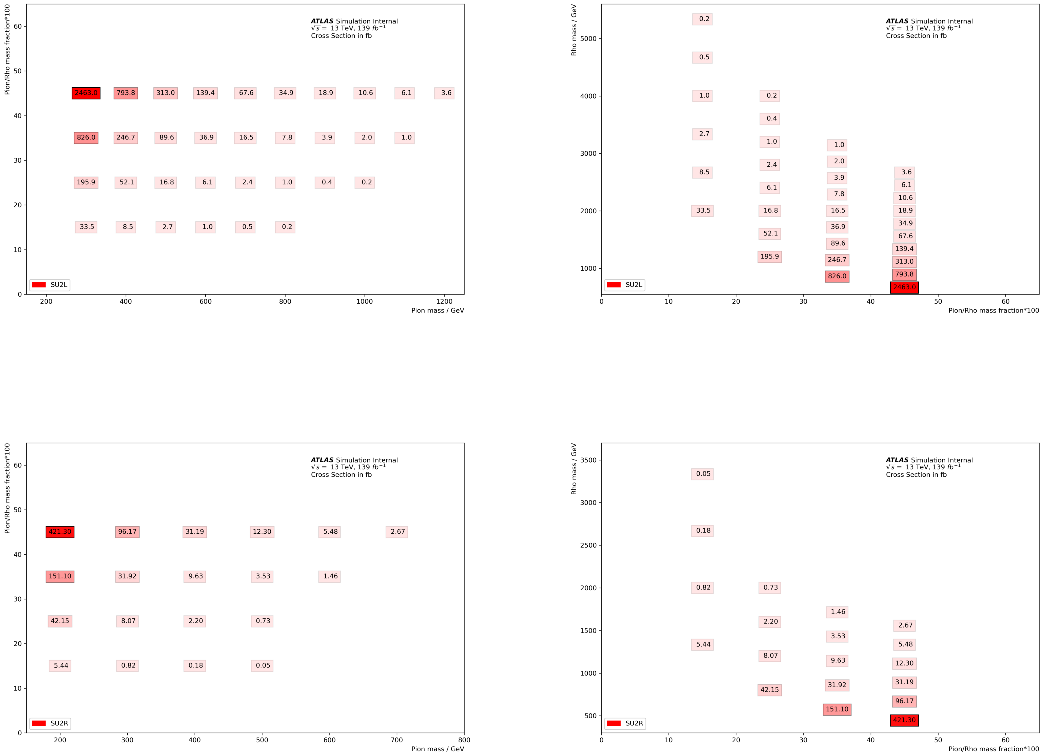

Figure A.1. Signal cross sections plotted on η vs dark pion/rho mass gridpoints for $SU(2)_L$ (top row) and $SU(2)_R$ (bottom row). Note that the axes are flipped for the rho mass dependence in the plots on the right.

A.2 Dark pion reconstruction

The all-hadronic dark pion signature consists of up to ten jets with four of these from B-mesons. In this analysis dark pions are reconstructed using large-R jet reclustering of R=0.4 jets and matched to b-tagged R=0.4 jets. The large-R jets are reclustered with a distance parameter R chosen for efficient dark pion reconstruction. The optimal R value of a signal point depends on the dark pion mass and boost (set by the ρ parameter).Figure A.3 shows the dependence of the distance in ΔR between the top and bottom decay products of dark pions on their p_T for two signal points. R=1.2 has good efficiency for these signal points and this efficiency increases with dark pion boost.

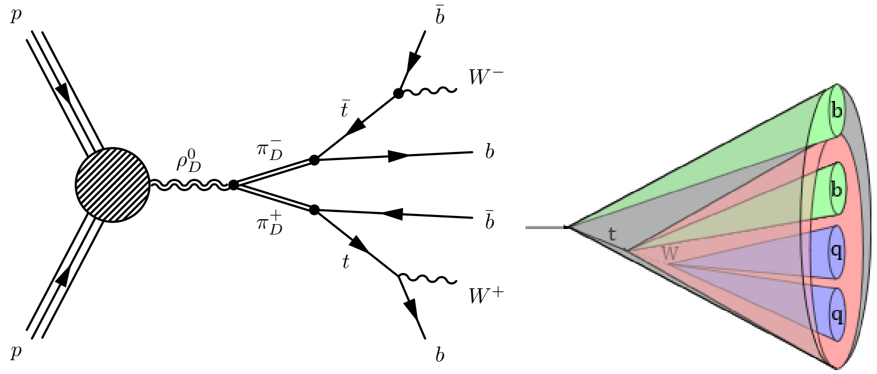

Figure A.2. Dark pions can decay into a top and a bottom quark (left). The dark pion can be identified from jet mass and the flavor tagging of its constituents.

R values of 0.8,1.2, and 1.4 were considered for dark pion reconstruction. An R value of 1.2 was chosen to capture dark pion decay products for the targeted $SU(2)_L$ signal point with $\eta = 0.25$ and $m_{\pi_D} = 500$ GeV while minimizing acceptance of multi-jet and pile-up jets. Figures A.4 and A.5 compare large-R jet reconstruction for different R values. The leading and subleading jet masses of these large-R jets are the primary discriminating variables for this analysis.

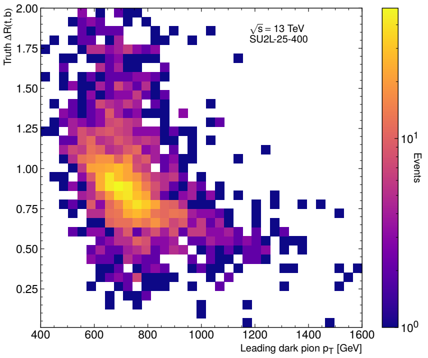

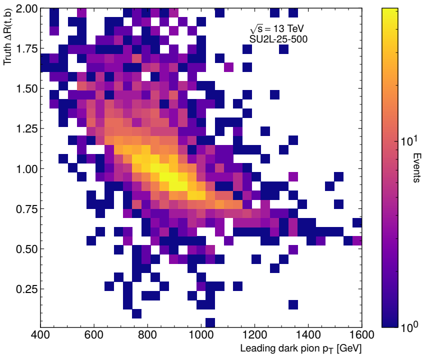

Figure A.3. Leading dark pion truth p_T compared to the ΔR of the its decay products for two signal points.

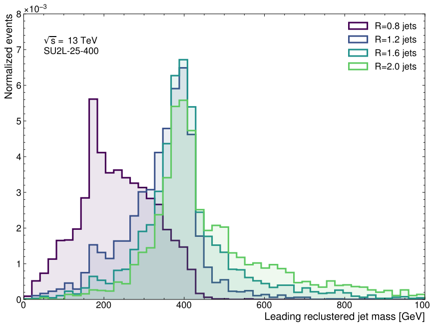

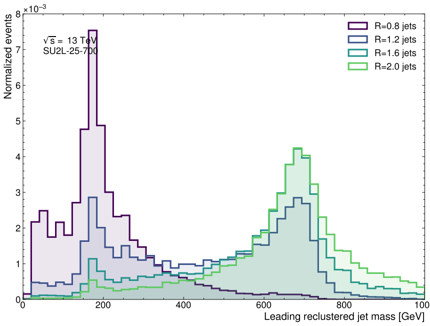

Figure A.4. Jet reclustering for a range of R parameters. R=1.2 jets provide good signal reconstruction while limiting multijet background events.

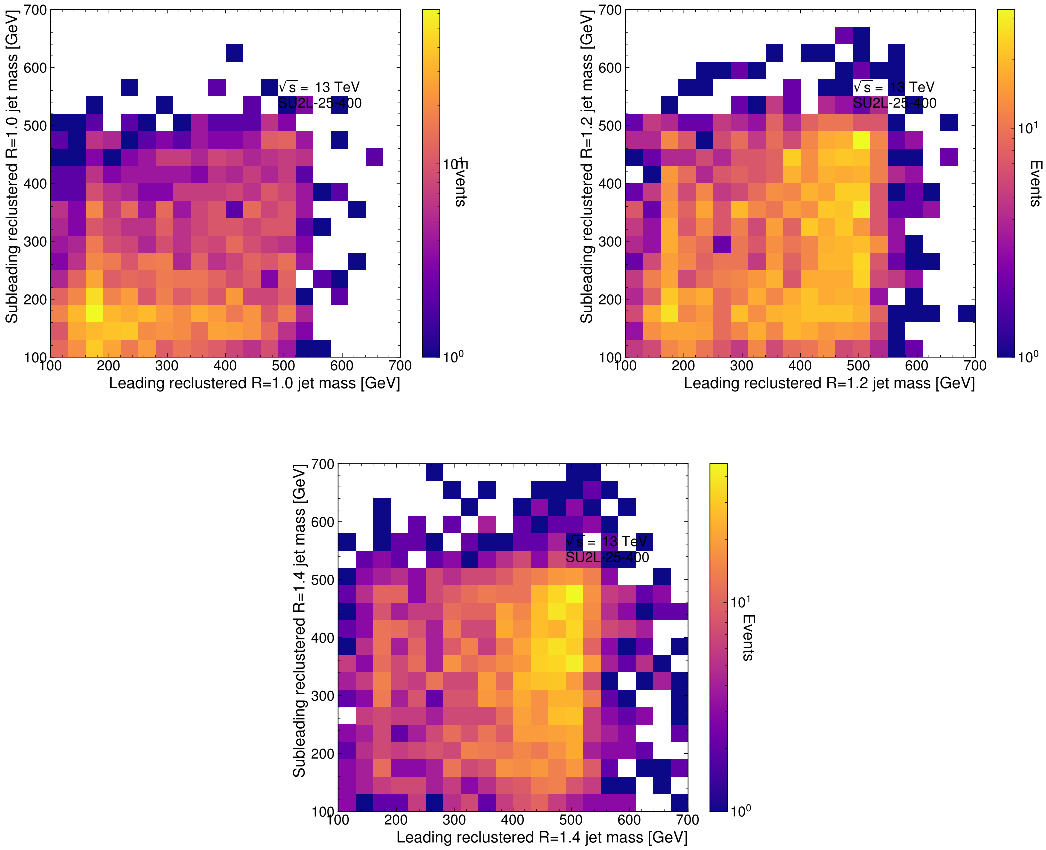

Figure A.5. Reclustered leading and subleading jet masses for three R parameters for the SU2L signal point with $\eta = 0.25$ and $m_{\pi_D} = 400$ GeV. The subleading jet mass reconstruction results in a broad peak and requires a looser selection. The R=1.2 parameter was chosen for efficient dark pion reconstruction.

A.3 The extended ABCD method

The dominant background for this analysis, QCD mutli-jet, is estimated using a data-driven approach to extrapolate from the observed contribution in low signal contamination regions to an estimate in the signal region. This four feature generalization of the ABCD method is similar to multi-jet estimation described in [240], but with tag definitions which select dark pions rather than tops. The top tags are replaced by π_d tags and single b-tags by bb-tags.

Figure A.6. 4D ABCD estimate region definitions. These labels have been chosen to agree with the notation used in [240]. Tag definitions are described in the main body 28.

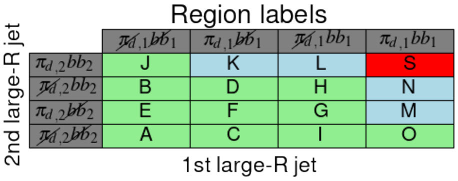

	$\cancel{\pi_d}_{,1}\cancel{bb}_1$	$\pi_{d,1}\cancel{bb}_1$	$\cancel{\pi_d}_{,1}bb_1$	$\pi_{d,1}bb_1$
$\pi_{d,2}bb_2$	J	K	L	S
$\cancel{\pi_d}_{,2}bb_2$	B	D	H	N
$\pi_{d,2}\cancel{bb}_2$	E	F	G	M
$\cancel{\pi_d}_{,2}\cancel{bb}_2$	A	C	I	O

For defined by selections on N_D features. For $N_D = 2$, define N_{11} as the number of events passing both selections and N_{ij} as the number of events passing some combination of selections and inverse selections specified by 1 or 0 for the N subscripts. Define f_i as the ratio of event passing to not passing selection i,

$$f_1 = \frac{N_{10}}{N_{00}} \tag{A.1}$$

$$f_2 = \frac{N_{01}}{N_{00}}. \tag{A.2}$$

In the case of uncorrelated selections,

$$f_1 = \frac{N_{11}}{N_{01}}, \tag{A.3}$$

$$f_2 = \frac{N_{11}}{N_{10}}, \tag{A.4}$$

and

$$N_{10} = f_1 N_{00}, \tag{A.5}$$

$$\hat{N}_{11} = f_2 N_{10}, \tag{A.6}$$

$$= f_2 f_1 N_{00}, \tag{A.7}$$

$$= \frac{N_{10} N_{01}}{N_{00}}. \tag{A.8}$$

Which reproduces the conventional 2D ABCD method (with different notation) for extrapolating into signal region A,

$$\hat{N}_{A^*} = \frac{N_{B^*} N_{C^*}}{N_{D^*}}. \tag{A.9}$$

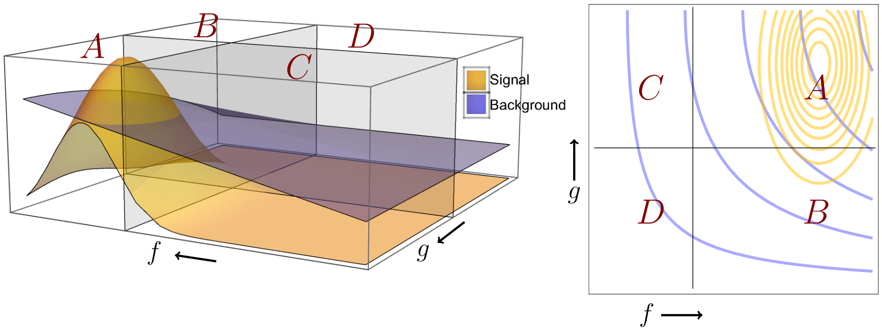

Figure A.7. Regions used in a conventional 2D ABCD estimate. Figure taken from [241]. Discriminating variables are f and g in this plot.

The ratio of the estimated region yield N_{11} to the observed yield $\hat{N}_{11}$ is defined as the correlation between this selections,

$$k_{12} = \frac{N_{11}}{\hat{N}_{11}} \qquad = \frac{N_{11}N_{00}}{N_{10}N_{01}}. \tag{A.10}$$

In the notation of A.6 there are 6 k factors which are each determined by comparing the 2D ABCD estimate of the QCD multijet background to data - MC in the two tag region,

$$k_{\pi_{d1},\pi_{d2}} = \frac{FA}{CE}, \tag{A.11}$$

$$k_{\pi_{d1},bb1} = \frac{OA}{CI}, \tag{A.12}$$

$$k_{\pi_{d1},bb2} = \frac{DA}{BC}, \tag{A.13}$$

$$k_{\pi_{d2},bb1} = \frac{GA}{EI}, \tag{A.14}$$

$$k_{\pi_{d2},bb2} = \frac{JA}{BE}, \tag{A.15}$$

$$k_{bb1,bb2} = \frac{HA}{BI}. \tag{A.16}$$

In the case of three discriminating variables with correlations between pairs of features,

$$f_1 = \frac{N_{100}}{N_{000}}, \tag{A.17}$$

$$f_2 = \frac{N_{010}}{N_{000}}, \tag{A.18}$$

$$f_3 = \frac{N_{001}}{N_{000}}, \tag{A.19}$$

$$k_{12} = \frac{N_{110}}{f_1 f_2 N_{000}}, \tag{A.20}$$

$$k_{13} = \frac{N_{101}}{f_1 f_3 N_{000}}, \tag{A.21}$$

$$k_{23} = \frac{N_{011}}{f_2 f_3 N_{000}}. \tag{A.22}$$

The expectation value of the two tag correlation terms k_{ij} is 1 for the case of uncorrelated variables.

Assuming that the correlation between any two 2-features does not depend on the third feature,

$$\hat{N}_{111} = f_1 f_2 f_3 k_{12} k_{23} k_{13} N_{000}. \tag{A.23}$$

In the notation of A.6 there are four 3-tag regions which are estimated using the six k-factors defined in A.16. The four region VR region estimates are,

$$\hat{K} = \frac{JC}{A} k_{\pi_{d,1},\pi_{d,2}} k_{\pi_{d,1},bb_2}, \tag{A.24}$$

$$\hat{L} = \frac{JI}{A} k_{\pi_{d,2},bb_1} k_{bb_1,bb_2}, \tag{A.25}$$

$$\hat{M} = \frac{OE}{A} k_{\pi_{d,1},\pi_{d,2}} k_{\pi_{d,2},bb_1}, \tag{A.26}$$

$$\hat{N} = \frac{OB}{A} k_{\pi_{d,1},bb_2} k_{bb_1,bb_2}. \tag{A.27}$$

These QCD multijet estimates are used to estimate the SM background in the VRs and defined a non-closure systematic uncertainty,

$$\sigma_{ABCD} = |1 - k_K k_L k_M k_N|. \tag{A.28}$$

The VR k-factor are estimates of the 3-tag correlations,

$$k_{VR} = \frac{N_{VR}}{\hat{N}_{VR}}. \tag{A.29}$$

Where N is the data - SM MC yield for a region.

Extending to 4 variables and assuming that there are no 4-correlations,

$$\hat{N}_{1111} = f_1 f_2 f_3 f_4 k_{12} k_{13} k_{14} k_{23} k_{24} k_{34} N_{0000}, \tag{A.30}$$

$$= \frac{N_{1000} N_{0100} N_{0010} N_{0001}}{N_{0000}^3} k_{12} k_{13} k_{14} k_{23} k_{24} k_{34}. \tag{A.31}$$

Expressing this relation in the region notation used in this analysis, $\pi_1, bb_1, \pi_2, bb_2 =$ 1, 2, 3, 4,

$$\hat{S}'_{\leq 1\ tag} = \prod_{tags=1} \frac{N_{(j)}}{N_A^3}, \tag{A.32}$$

$$\hat{S}'_{\leq 1\ tag} = \frac{N_B N_E N_C N_I}{N_A^3}, \tag{A.33}$$

$$\hat{S} = \hat{S}'_{\leq 1\ tag} k_{\pi_{d,1}, bb_1} k_{\pi_{d,2}, bb_2} k_{\pi_{d,1}, bb_2} k_{\pi_{d,2}, bb_1} k_{\pi_{d,1}, \pi_{d,2}} k_{bb_1, bb_2}. \tag{A.34}$$

This is the 4-variable 2-correlation corrected ABCD estimate. The statistical uncertainty of this estimates is computed from the data - SM MC uncertainties for each 1 and 2 tag regions,

$$\sigma_S^2 = \Sigma_{1tag,2tag}(\frac{\partial S}{\partial N_i})^2\sigma_{N_i}^2. \tag{A.35}$$

A.4 All-hadronic preselection full cutflow

For the benchmark $SU(2)_L$ signal point with $\eta = 0.25$ and $m_{\pi_D} = 500$ GeV (SU2L-25-500) table A.1 shows the weighted and unweighted yields for the full SR selection.

Table A.2 shows the raw event count cutflow for the all-hadronic preselection.

Table A.1. All-hadronic full selection cutflow for the benchmark $SU(2)_L$ signal point with $\eta = 0.25$ and $m_{\pi_D} = 500$ GeV at 139 fb^{-1} integrated luminosity.

Cut	Unweighted events	weighted events
Sample	29000	2335.2
INITIAL	29000	2335.2
GRL	29000	2335.2
GOODCALO	29000	2335.2
PRIVTX	29000	2335.2
TRIGDEC	27041	2173.0
NOBADMUON	37038	2172.8
JETCLEAN LooseBad	26951	2165.7
HT >= 1150 GeV	24763	1994.2
JET-N 20000 >= 6	22159	1786.2
JET-N-BTAG DL1r:FixedCutBEff-85 >= 3	18701	1506.9
JET-N-BTAG DL1r:FixedCutBEff-77 >= 2	18198	1466.5
EL-N 10000 == 0	15239	1227.3
MU-N 10000 == 0	12576	1013.0
Both leading R=1.2 jet masses > 60 GeV and Both R=1.0 jets pT > 350 GeV	10754	865.3
Jets-12-mptbbp-0 > 0.25	9732	786.4
Jets-12-mptbbp-1 > 0.25	8975	726.8
Jets-12-ttag-0 == 1	5115	414.6
Jets-12-m-0 > 300 GeV	3455	279.2
Jets-12-dRb1-0 < 1.0	1677	134.3
Jets-12-ttag-1 == 1	905	72.0
Jets-12-m-1 > 250 GeV	562	44.4
Jets-12-dRb1-1 < 1.0	221	16.9

Table A.2. Raw event counts of the all-hadronic preselection cutflow for data and all considered simulated backgrounds

Cut	data	All MC	$t\bar{t}$ allhad	$t\bar{t}$ leptonic	V+jets	$t\bar{t}+X$	Single top	Multiboson	Signal-25-500
Derivation	559740475	682840317	57192450	215064436	48651152	81415000	280271750	245529	29000
GRL	417309494	682840317	57192450	215064436	48651152	81415000	280271750	245529	29000
Good Calo	412694354	682840317	57192450	215064436	48651152	81415000	280271750	245529	29000
Primary vertex	412692263	682840267	57192450	215064436	48651152	81415000	280271700	245529	29000
Trigger	205205611	254120215	53933259	185397518	5201298	8270470	1315147	2523	27041
Bad muon veto	205203444	254068626	53932474	185348212	5201225	8269230	1314964	2521	27038
Jet cleaning	202840649	253105520	53728488	184645446	5182136	8237292	1309645	2513	26951
$H_T > 1150$ GeV	87703211	152615079	37783115	107035542	2872401	4327289	595737	995	24862
$N_{\text{jets}} \geq 6$	45304007	125406172	33898061	86082271	933154	4079547	412708	431	22365
$N_{\text{jets, R=1.2}} \geq 2$	45005443	122644447	33849331	83450772	928876	4011718	403326	424	21875
$N_{\text{b-jets}} \geq 3$	576239	16248091	4553902	10218764	28962	1403902	42517	44	14659
electron veto	568304	13488657	4538150	7664957	28874	1218783	37849	44	12423
muon veto	561409	10791469	4533759	5147049	28860	1048648	33109	44	10313
$t\bar{t}b\bar{b}$ overlap removal	561409	10791469	4533759	5147049	28860	1048648	33109	44	10313
$m^{1,2}_{\text{jet},1.2} > 190$ GeV	69879	1697903	830056	627586	3853	232924	3482	2	6212
$p^{6}_{T,\text{jet}} > 25$ GeV	67339	1674960	820466	616028	3678	231394	3392	2	6098
preselected	67339	1674960	820466	616028	3678	231394	3392	2	6098

A.5 All-hadronic preselection data studies

This appendix shows histograms of jet variables in data with the preselection as summarized in table 25 applied.

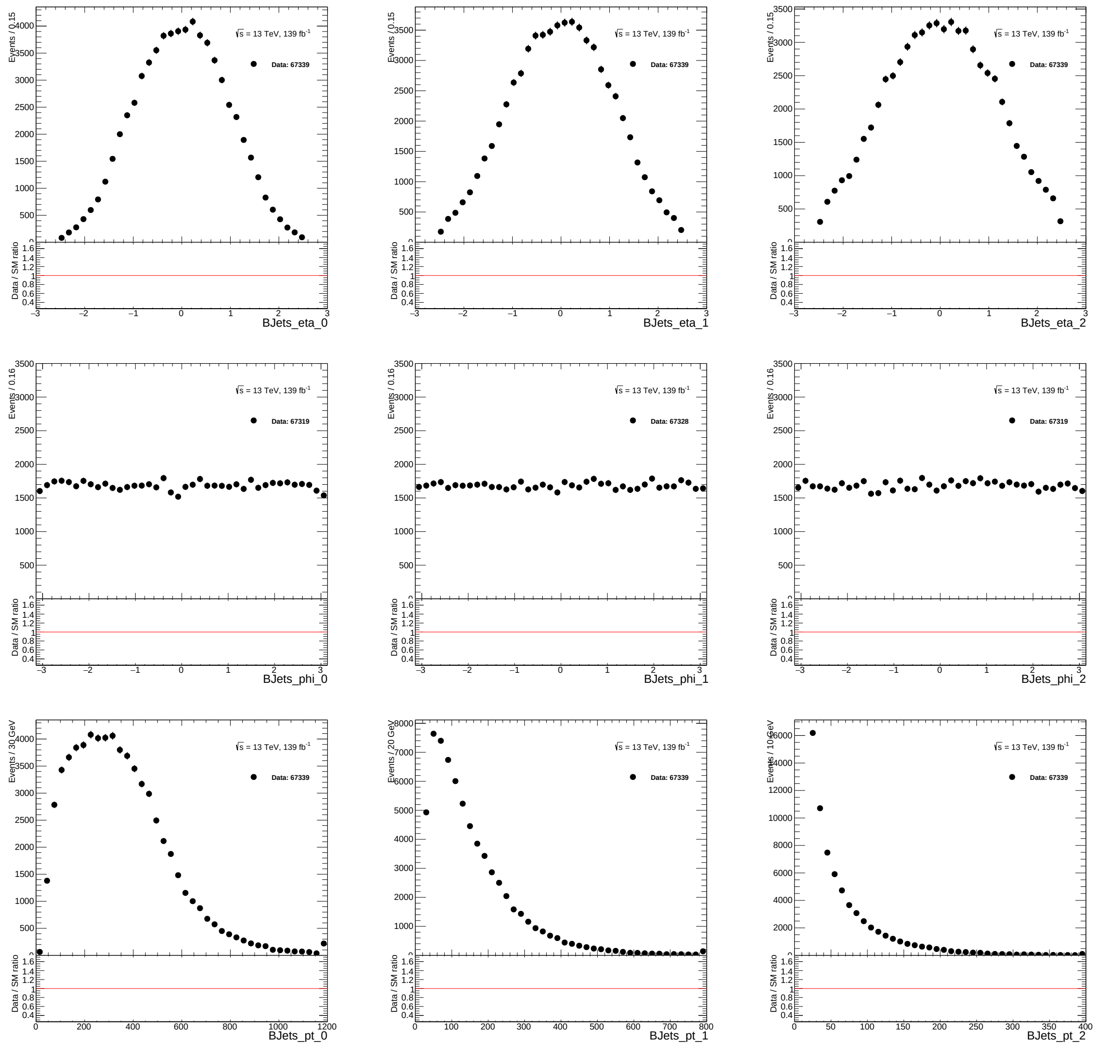

Figure A.8. All-hadronic pre-selection plots of b-jet kinematic variables.

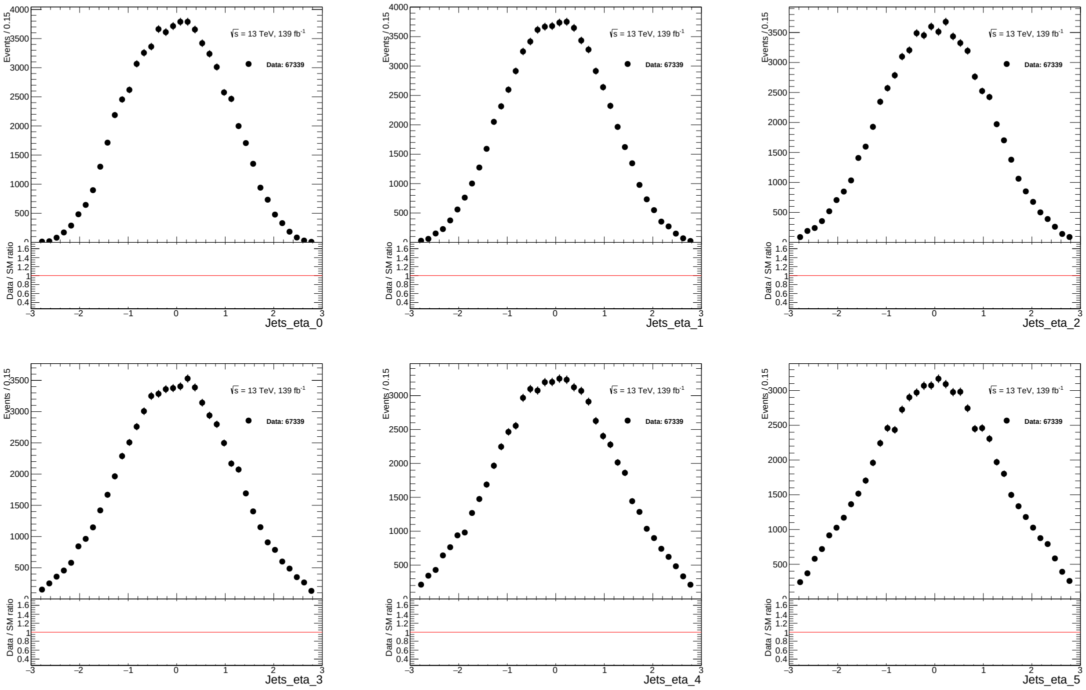

Figure A.9. All-hadronic pre-selection plots of the η of the leading six jets.

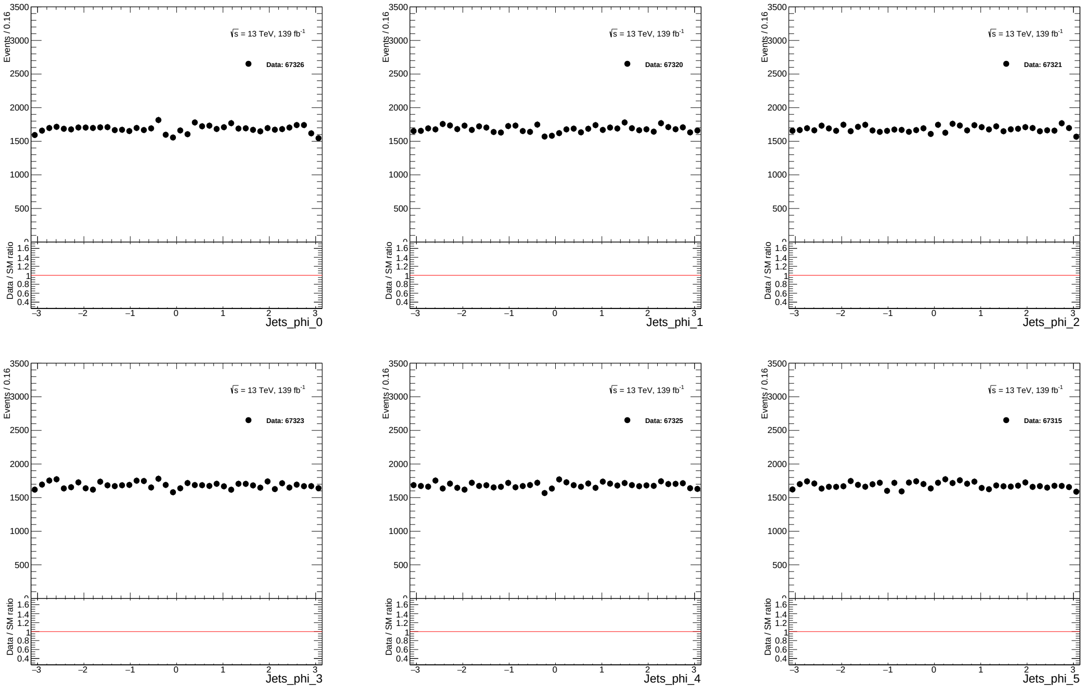

Figure A.10. All-hadronic pre-selection plots of the ϕ of the leading six jets.

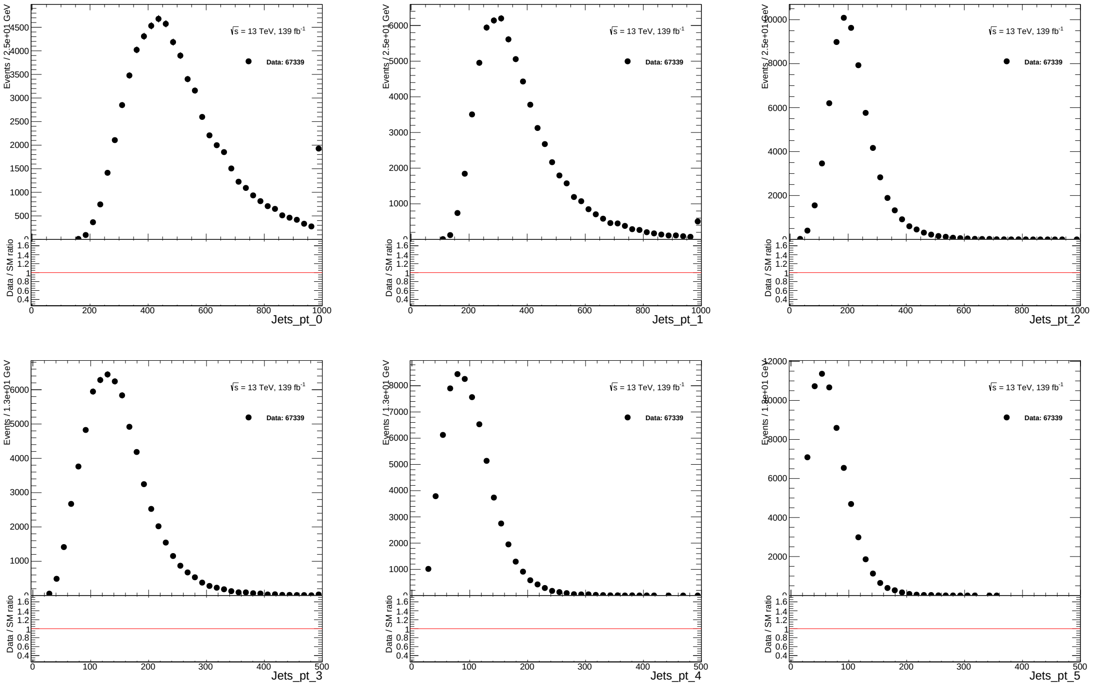

Figure A.11. All-hadronic pre-selection plots of the p_T of the leading six jets.

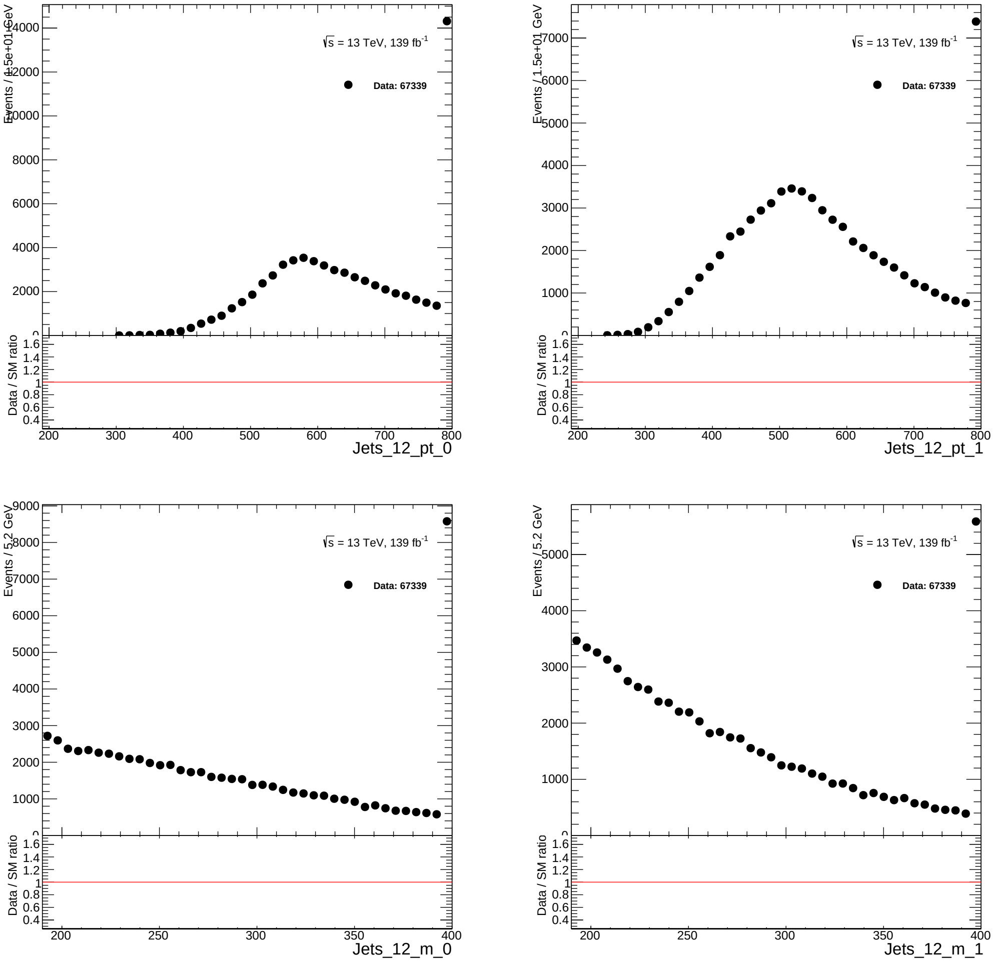

Figure A.12. All-hadronic pre-selection plots of leading and subleading large-R jet mass and p_T. The final bin contains the overflow.

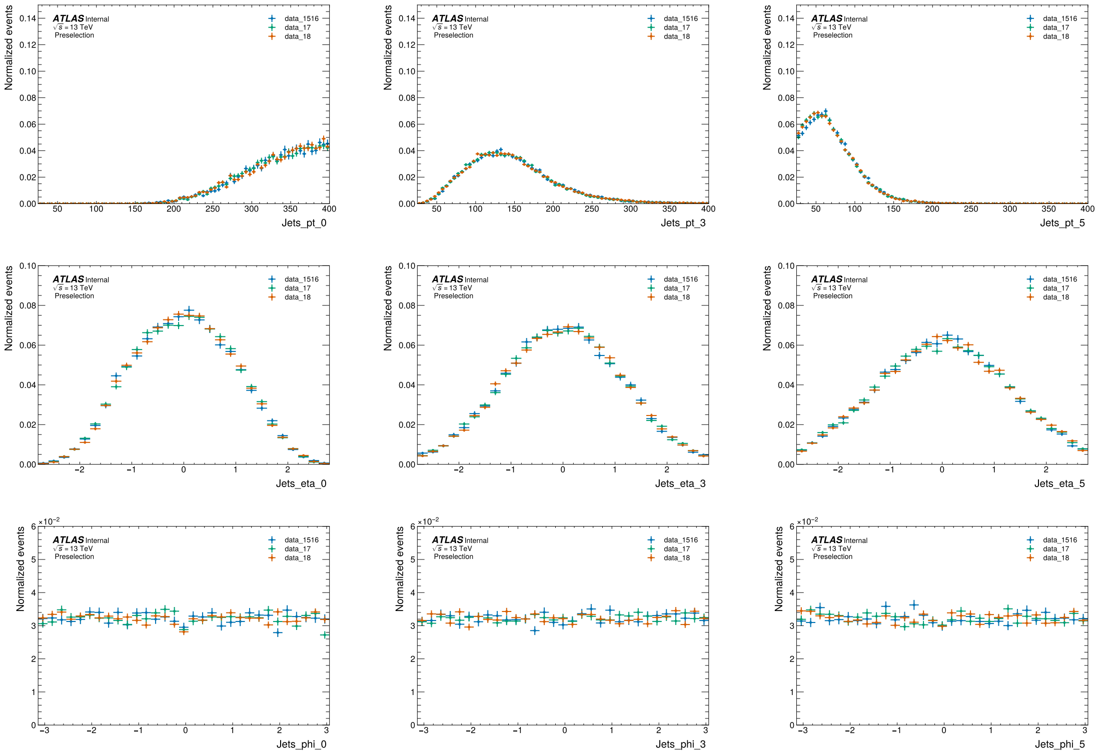

Figure A.13. Normalized plots of jet p_T, η and ϕ by year.

A.6 All-hadronic pile up sensitivity studies

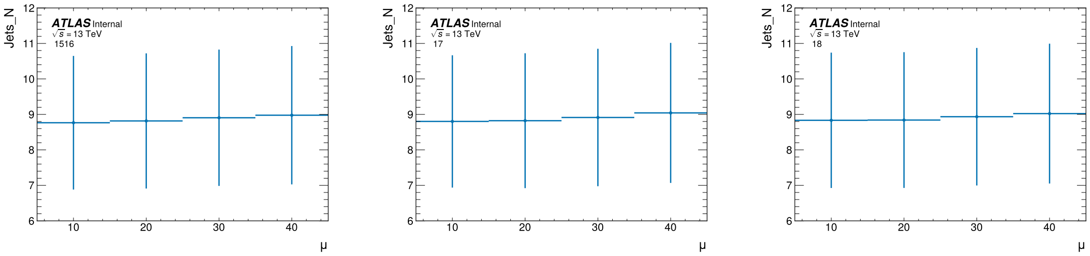

Figure A.14. Njets yields by μ bin by run year.

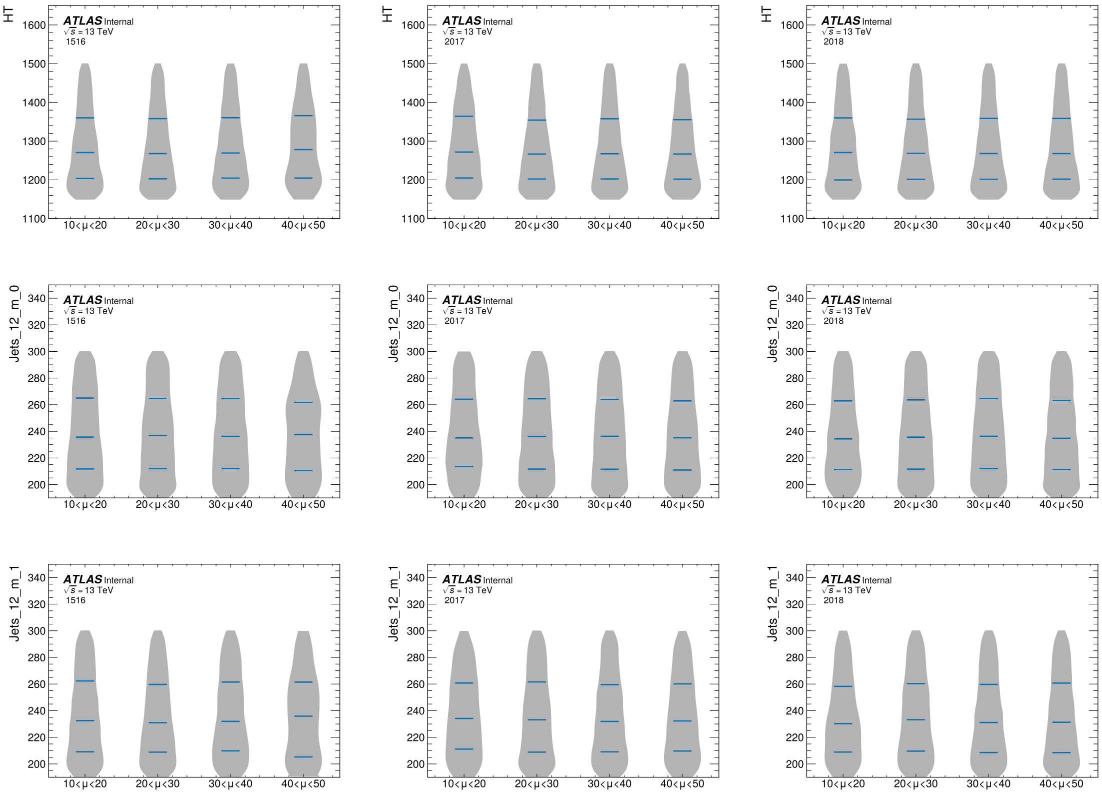

Figure A.15. Data event yields by μ bin by run year. A kernel density estimate of the variable distribution is shown for each bin. The horizontal blue lines indicate distribution quartiles

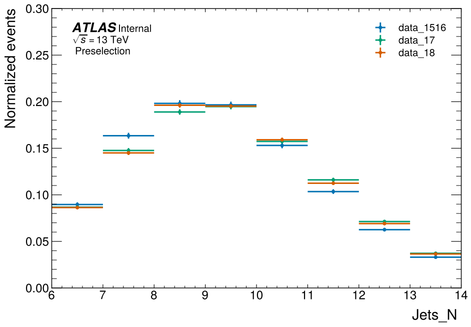

Figure A.16. Preselection Njets histograms by run year.

A.7 All-hadronic signal region signal and background yields

This appendix contains plots of signal and background yields for the all-hadronic SR.

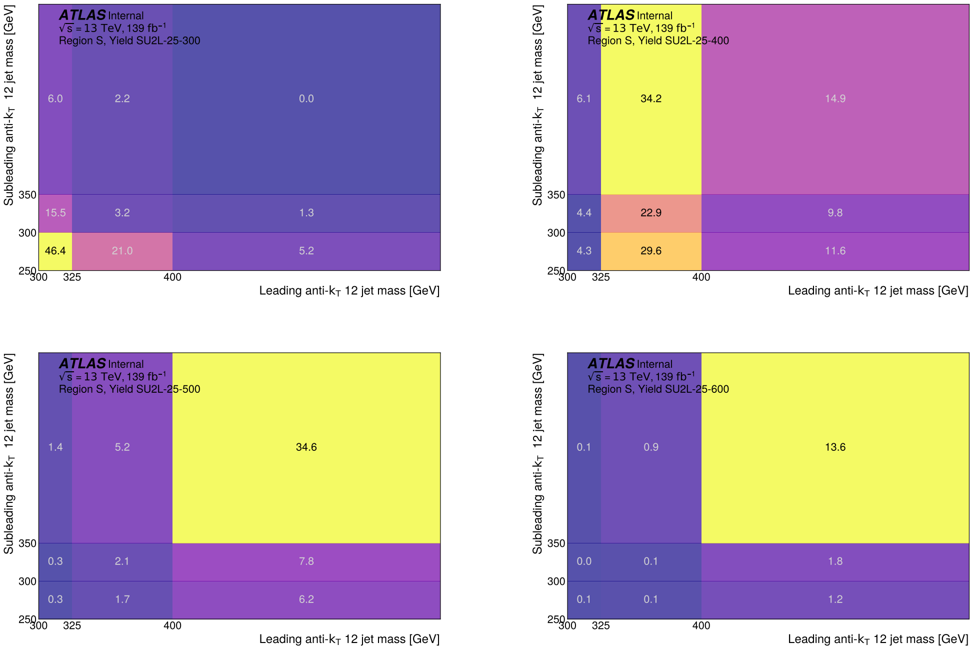

Figure A.17. Signal yield for SR bins for four $\eta = 0.25$ points.

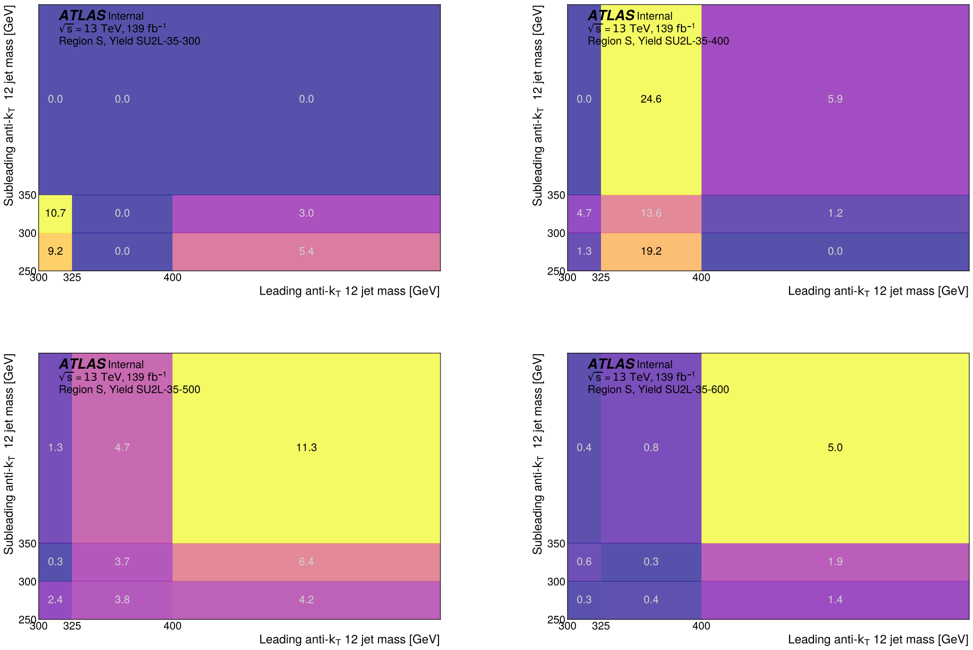

Figure A.18. Signal yield for SR bins for four $\eta = 0.35$ points.

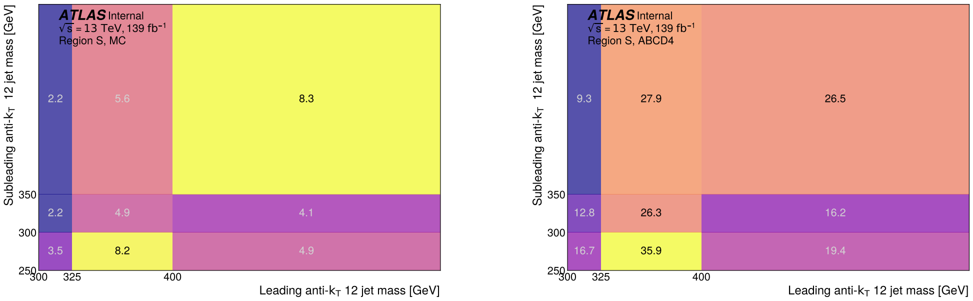

Figure A.19. MC and QCD multijet yield SR bins.

A.8 All-hadronic signal region optimization

The all-hadronic signal region was developed by evaluating physically motivated ttbar and QCD multijet discriminating variables to find variables with strong multijet exclusion and that are suited to the 4D ABCD background estimate. The 4 strong discriminating variables (leading and subleading $m_{\mathrm{jet,R=1.2}}$ and $\Delta R\,(j, b_2)$) and the weaker variables used in preselection definition (leading and subleading $m_{bb}/p_{T,bb}$) were optimized through estimating SR significance for a reference signal point as they are independently varied.

Figure A.20 shows three example plots used for this optimization

The Signal and MC background yields with each SR selection applied sequentially for the sum of SR bins are shown in table A.3

Table A.3. Weighted event cutflow for single bin SR. The QCD multijet background is not included in this cutflow. The selection used in this table includes a requirement 6 jets with $p_T > 20$ GeV instead of 6 jets with $p_T > 25$ GeV.

Selection	ttbar	Vjets	singleTop	ttbarPlusX	SU2L-25-500
Preselection	8800.0	1220.9	381.3	405.8	493.3
Leading $m_{bb}/p_{T,bb} > 0.25$	7864.8	1079.6	341.9 365.0	442.2	
Subleading $m_{bb}/p_{T,bb} > 0.25$	7104.9	940.2	307.9	330.0	403.4
Leading $m_{\mathrm{jet,R=1.2}} > 300$ GeV	2665.4	301.3	129.6	138.3	325.7
Subleading $m_{\mathrm{jet,R=1.2}} > 250$ GeV	1356.4	176.4	65.0	73.3	242.1
Leading $\Delta R\,(j, b_2) < 1.0$	323.4	39.4	13.4	18.7	126.3
Subleading $\Delta R\,(j, b_2) < 1.0$	30.5	4.1	1.0	2.9	53.9

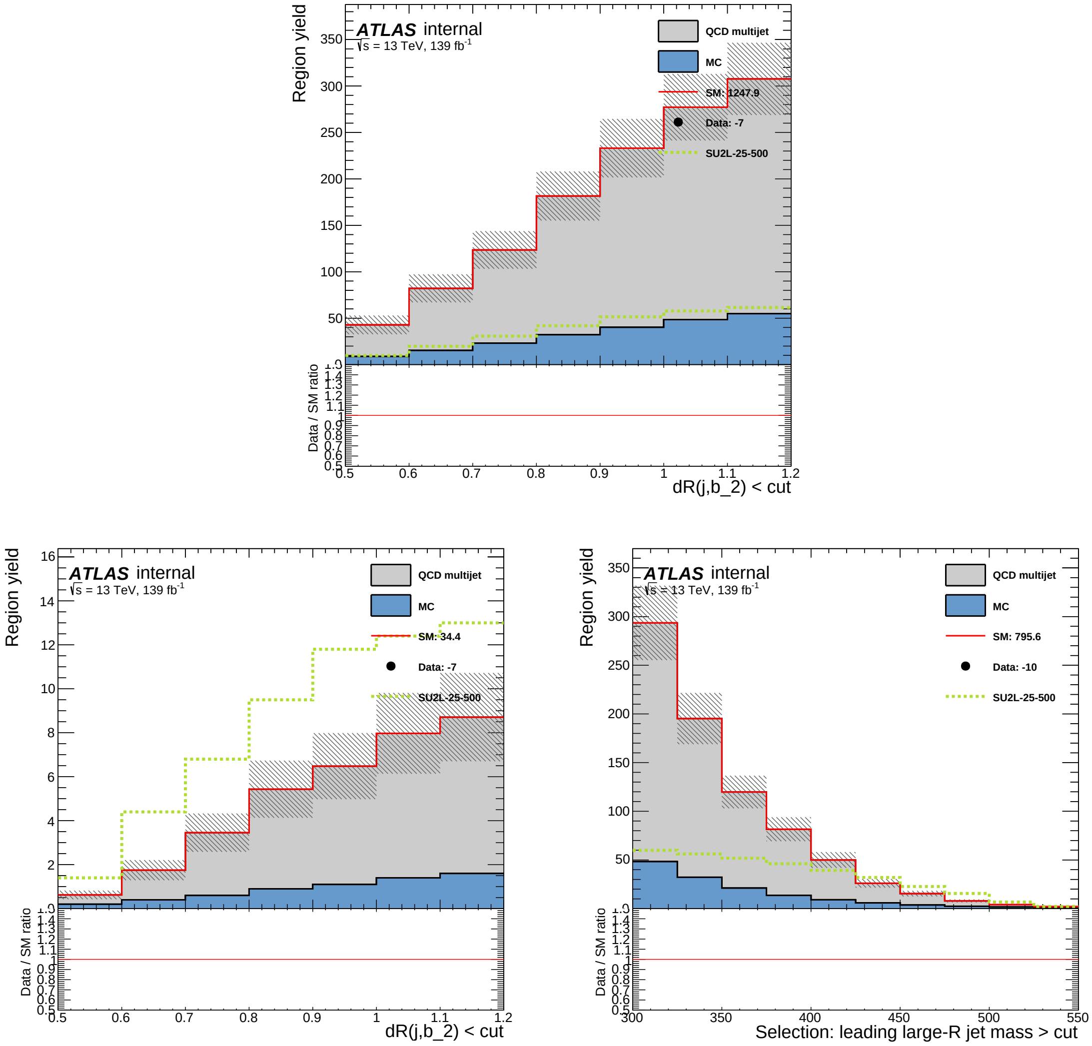

Figure A.20. Plots for optimization of SM backgrounds. Each bin shows the estimated SR yield for a choice of discriminating variable. The top plot shows an optimization of leading large-R jet $\Delta R(j, b_2)$ for the unbinned all-hadronic SR. The bottom plots show an example optimization for an SR leading and subleading jet mass subselection: 450 < leading $m^2_{\text{jet,R=1.2}}$ < 550 GeV, 350 < subleading $m^2_{\text{jet,R=1.2}}$ < 450 GeV. IN the right plot the leading large-R jet selection is varied as shown and the subleading large R jet selection is set to the leading selection + 100 GeV. The selection used in these plot includes a requirement 6 jets with $p_T > 20$ GeV instead of 6 jets with $p_T > 25$ GeV.

A.9 All-hadronic tables of ABCD regions by SR bin

This appendix shows data, SM MC, QCD multijet estimates, signal yields, signal contamination and k factors for each SR bin. Signal yields are shown for the $SU(2)_L$ optimization point, additional signal yield plots are shown in appendix A.7. The k factor tables show the ratio of the QCD multijet estimate to data-MC for the 4D ABCD method extrapolation and validation regions.

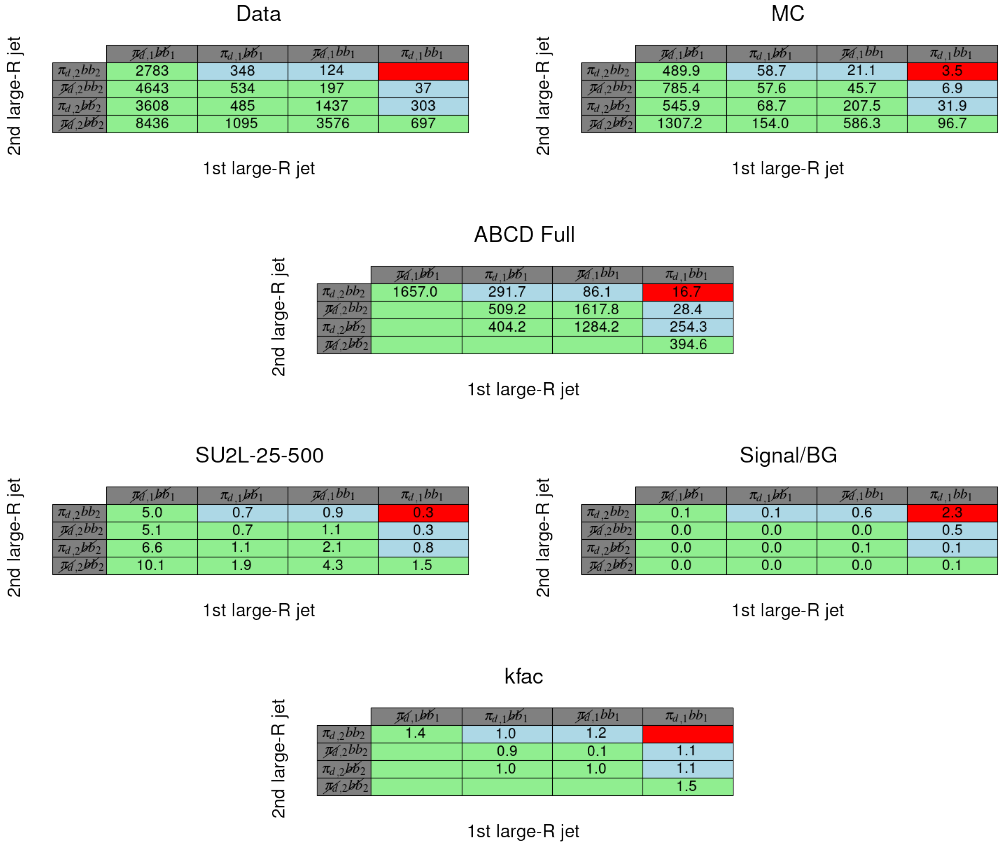

Data

2nd large-R jet

	$\not\pi_{d,1}\not{bb}_1$	$\pi_{d,1}\not{bb}_1$	$\not\pi_{d,1}bb_1$	$\pi_{d,1}bb_1$
$\pi_{d,2}bb_2$	2783	348	124	
$\not\pi_{d,2}bb_2$	4643	534	197	37
$\pi_{d,2}\not{bb}_2$	3608	485	1437	303
$\not\pi_{d,2}\not{bb}_2$	8436	1095	3576	697

1st large-R jet

MC

2nd large-R jet

	$\not\pi_{d,1}\not{bb}_1$	$\pi_{d,1}\not{bb}_1$	$\not\pi_{d,1}bb_1$	$\pi_{d,1}bb_1$
$\pi_{d,2}bb_2$	489.9	58.7	21.1	3.5
$\not\pi_{d,2}bb_2$	785.4	57.6	45.7	6.9
$\pi_{d,2}\not{bb}_2$	545.9	68.7	207.5	31.9
$\not\pi_{d,2}\not{bb}_2$	1307.2	154.0	586.3	96.7

1st large-R jet

ABCD Full

2nd large-R jet

	$\not\pi_{d,1}\not{bb}_1$	$\pi_{d,1}\not{bb}_1$	$\not\pi_{d,1}bb_1$	$\pi_{d,1}bb_1$
$\pi_{d,2}bb_2$	1657.0	291.7	86.1	16.7
$\not\pi_{d,2}bb_2$		509.2	1617.8	28.4
$\pi_{d,2}\not{bb}_2$		404.2	1284.2	254.3
$\not\pi_{d,2}\not{bb}_2$				394.6

1st large-R jet

SU2L-25-500

2nd large-R jet

	$\not\pi_{d,1}\not{bb}_1$	$\pi_{d,1}\not{bb}_1$	$\not\pi_{d,1}bb_1$	$\pi_{d,1}bb_1$
$\pi_{d,2}bb_2$	5.0	0.7	0.9	0.3
$\not\pi_{d,2}bb_2$	5.1	0.7	1.1	0.3
$\pi_{d,2}\not{bb}_2$	6.6	1.1	2.1	0.8
$\not\pi_{d,2}\not{bb}_2$	10.1	1.9	4.3	1.5

1st large-R jet

Signal/BG

2nd large-R jet

	$\not\pi_{d,1}\not{bb}_1$	$\pi_{d,1}\not{bb}_1$	$\not\pi_{d,1}bb_1$	$\pi_{d,1}bb_1$
$\pi_{d,2}bb_2$	0.1	0.1	0.6	2.3
$\not\pi_{d,2}bb_2$	0.0	0.0	0.0	0.5
$\pi_{d,2}\not{bb}_2$	0.0	0.0	0.1	0.1
$\not\pi_{d,2}\not{bb}_2$	0.0	0.0	0.0	0.1

1st large-R jet

kfac

2nd large-R jet

	$\not\pi_{d,1}\not{bb}_1$	$\pi_{d,1}\not{bb}_1$	$\not\pi_{d,1}bb_1$	$\pi_{d,1}bb_1$
$\pi_{d,2}bb_2$	1.4	1.0	1.2	
$\not\pi_{d,2}bb_2$		0.9	0.1	1.1
$\pi_{d,2}\not{bb}_2$		1.0	1.0	1.1
$\not\pi_{d,2}\not{bb}_2$				1.5

1st large-R jet

Figure A.21. Data, MC, QCD multijet estimate, signal yield, signal contamination, and k-factor for each of the 16 regions used in the ABCD QCD multijet estimate. Estimate for SR bin $300 < m_1 < 325$ GeV, $250 < m_2 < 300$ GeV

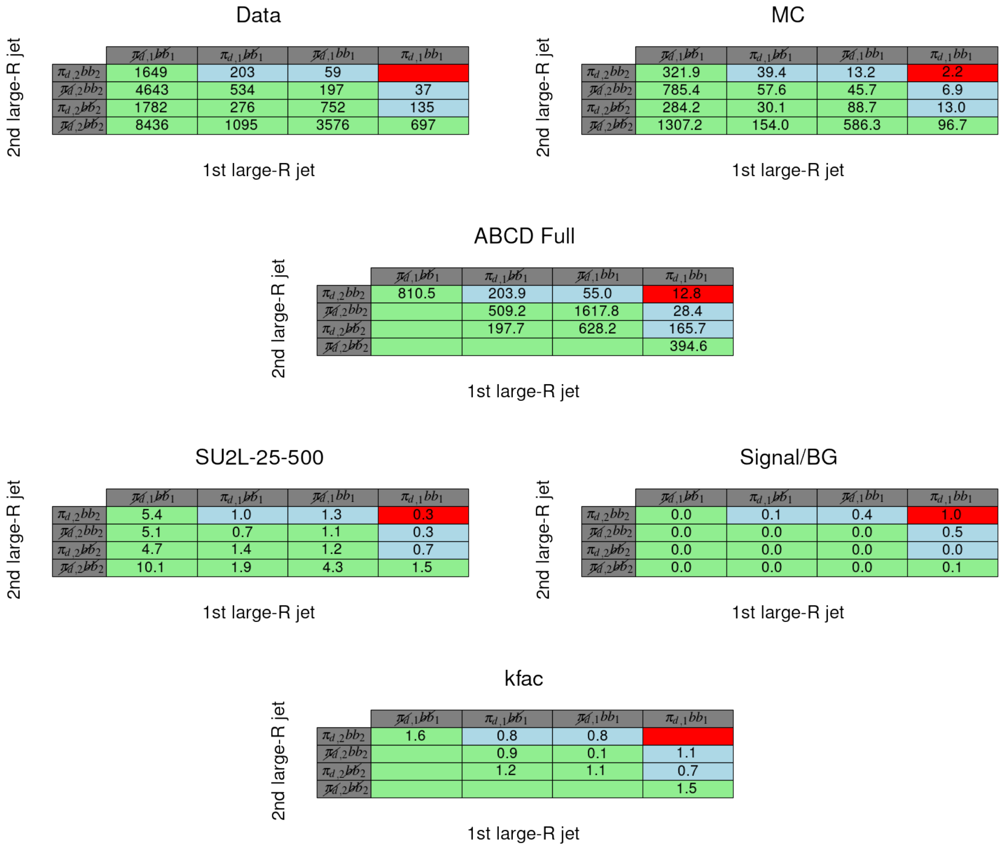

Data

	$\not\pi_{d,1}b\not b_1$	$\pi_{d,1}b\not b_1$	$\not\pi_{d,1}bb_1$	$\pi_{d,1}bb_1$
$\pi_{d,2}bb_2$	1649	203	59	
$\not\pi_{d,2}bb_2$	4643	534	197	37
$\pi_{d,2}b\not b_2$	1782	276	752	135
$\not\pi_{d,2}b\not b_2$	8436	1095	3576	697

2nd large-R jet

1st large-R jet

MC

	$\not\pi_{d,1}b\not b_1$	$\pi_{d,1}b\not b_1$	$\not\pi_{d,1}bb_1$	$\pi_{d,1}bb_1$
$\pi_{d,2}bb_2$	321.9	39.4	13.2	2.2
$\not\pi_{d,2}bb_2$	785.4	57.6	45.7	6.9
$\pi_{d,2}b\not b_2$	284.2	30.1	88.7	13.0
$\not\pi_{d,2}b\not b_2$	1307.2	154.0	586.3	96.7

2nd large-R jet

1st large-R jet

ABCD Full

	$\not\pi_{d,1}b\not b_1$	$\pi_{d,1}b\not b_1$	$\not\pi_{d,1}bb_1$	$\pi_{d,1}bb_1$
$\pi_{d,2}bb_2$	810.5	203.9	55.0	12.8
$\not\pi_{d,2}bb_2$		509.2	1617.8	28.4
$\pi_{d,2}b\not b_2$		197.7	628.2	165.7
$\not\pi_{d,2}b\not b_2$				394.6

2nd large-R jet

1st large-R jet

SU2L-25-500

	$\not\pi_{d,1}b\not b_1$	$\pi_{d,1}b\not b_1$	$\not\pi_{d,1}bb_1$	$\pi_{d,1}bb_1$
$\pi_{d,2}bb_2$	5.4	1.0	1.3	0.3
$\not\pi_{d,2}bb_2$	5.1	0.7	1.1	0.3
$\pi_{d,2}b\not b_2$	4.7	1.4	1.2	0.7
$\not\pi_{d,2}b\not b_2$	10.1	1.9	4.3	1.5

2nd large-R jet

1st large-R jet

Signal/BG

	$\not\pi_{d,1}b\not b_1$	$\pi_{d,1}b\not b_1$	$\not\pi_{d,1}bb_1$	$\pi_{d,1}bb_1$
$\pi_{d,2}bb_2$	0.0	0.1	0.4	1.0
$\not\pi_{d,2}bb_2$	0.0	0.0	0.0	0.5
$\pi_{d,2}b\not b_2$	0.0	0.0	0.0	0.0
$\not\pi_{d,2}b\not b_2$	0.0	0.0	0.0	0.1

2nd large-R jet

1st large-R jet

kfac

	$\not\pi_{d,1}b\not b_1$	$\pi_{d,1}b\not b_1$	$\not\pi_{d,1}bb_1$	$\pi_{d,1}bb_1$
$\pi_{d,2}bb_2$	1.6	0.8	0.8	
$\not\pi_{d,2}bb_2$		0.9	0.1	1.1
$\pi_{d,2}b\not b_2$		1.2	1.1	0.7
$\not\pi_{d,2}b\not b_2$				1.5

2nd large-R jet

1st large-R jet

Figure A.22. Data, MC, QCD multijet estimate, signal yield, signal contamination, and k-factor for each of the 16 regions used in the ABCD QCD multijet estimate. Estimate for SR bin $300 < m_1 < 325$ GeV, $300 < m_2 < 350$ GeV

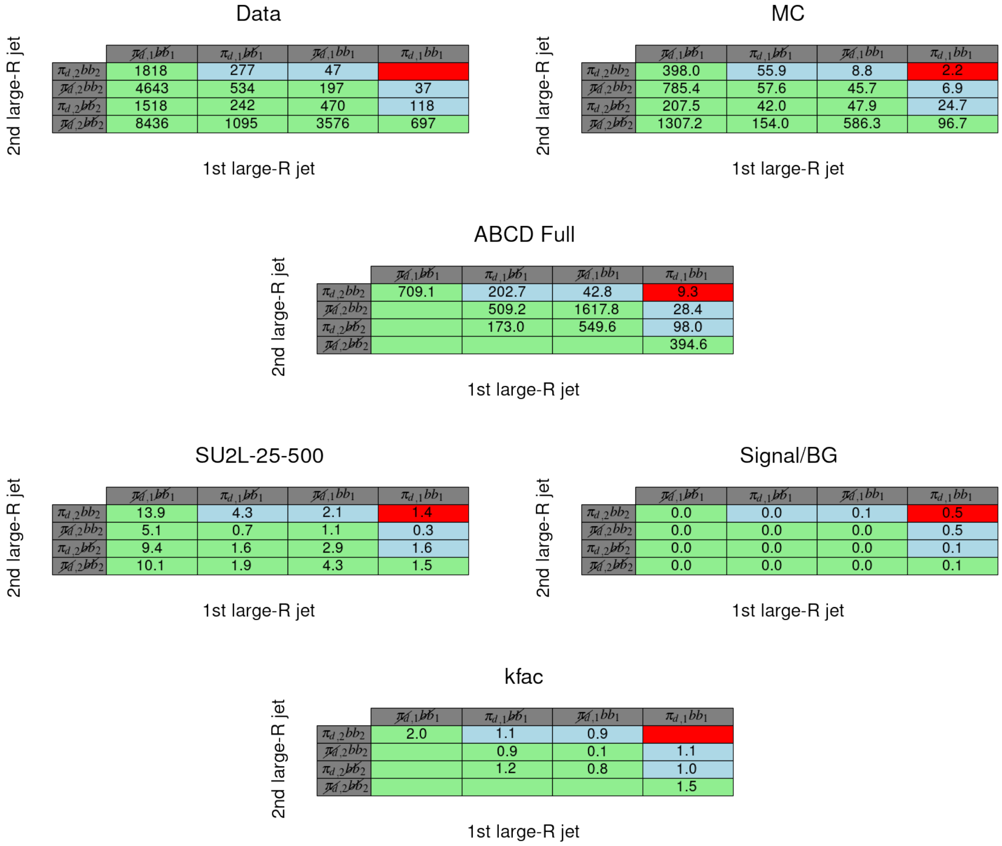

Data

2nd large-R jet

	$\not{\pi}_{d,1}\not{bb}_1$	$\pi_{d,1}\not{bb}_1$	$\not{\pi}_{d,1}bb_1$	$\pi_{d,1}bb_1$
$\pi_{d,2}bb_2$	1818	277	47	
$\not{\pi}_{d,2}bb_2$	4643	534	197	37
$\pi_{d,2}\not{bb}_2$	1518	242	470	118
$\not{\pi}_{d,2}\not{bb}_2$	8436	1095	3576	697

1st large-R jet

MC

2nd large-R jet

	$\not{\pi}_{d,1}\not{bb}_1$	$\pi_{d,1}\not{bb}_1$	$\not{\pi}_{d,1}bb_1$	$\pi_{d,1}bb_1$
$\pi_{d,2}bb_2$	398.0	55.9	8.8	2.2
$\not{\pi}_{d,2}bb_2$	785.4	57.6	45.7	6.9
$\pi_{d,2}\not{bb}_2$	207.5	42.0	47.9	24.7
$\not{\pi}_{d,2}\not{bb}_2$	1307.2	154.0	586.3	96.7

1st large-R jet

ABCD Full

2nd large-R jet

	$\not{\pi}_{d,1}\not{bb}_1$	$\pi_{d,1}\not{bb}_1$	$\not{\pi}_{d,1}bb_1$	$\pi_{d,1}bb_1$
$\pi_{d,2}bb_2$	709.1	202.7	42.8	9.3
$\not{\pi}_{d,2}bb_2$		509.2	1617.8	28.4
$\pi_{d,2}\not{bb}_2$		173.0	549.6	98.0
$\not{\pi}_{d,2}\not{bb}_2$				394.6

1st large-R jet

SU2L-25-500

2nd large-R jet

	$\not{\pi}_{d,1}\not{bb}_1$	$\pi_{d,1}\not{bb}_1$	$\not{\pi}_{d,1}bb_1$	$\pi_{d,1}bb_1$
$\pi_{d,2}bb_2$	13.9	4.3	2.1	1.4
$\not{\pi}_{d,2}bb_2$	5.1	0.7	1.1	0.3
$\pi_{d,2}\not{bb}_2$	9.4	1.6	2.9	1.6
$\not{\pi}_{d,2}\not{bb}_2$	10.1	1.9	4.3	1.5

1st large-R jet

Signal/BG

2nd large-R jet

	$\not{\pi}_{d,1}\not{bb}_1$	$\pi_{d,1}\not{bb}_1$	$\not{\pi}_{d,1}bb_1$	$\pi_{d,1}bb_1$
$\pi_{d,2}bb_2$	0.0	0.0	0.1	0.5
$\not{\pi}_{d,2}bb_2$	0.0	0.0	0.0	0.5
$\pi_{d,2}\not{bb}_2$	0.0	0.0	0.0	0.1
$\not{\pi}_{d,2}\not{bb}_2$	0.0	0.0	0.0	0.1

1st large-R jet

kfac

2nd large-R jet

	$\not{\pi}_{d,1}\not{bb}_1$	$\pi_{d,1}\not{bb}_1$	$\not{\pi}_{d,1}bb_1$	$\pi_{d,1}bb_1$
$\pi_{d,2}bb_2$	2.0	1.1	0.9	
$\not{\pi}_{d,2}bb_2$		0.9	0.1	1.1
$\pi_{d,2}\not{bb}_2$		1.2	0.8	1.0
$\not{\pi}_{d,2}\not{bb}_2$				1.5

1st large-R jet

Figure A.23. Data, MC, QCD multijet estimate, signal yield, signal contamination, and k-factor for each of the 16 regions used in the ABCD QCD multijet estimate. Estimate for SR bin $300 < m_1 < 325$ GeV, 350 GeV $< m_2$

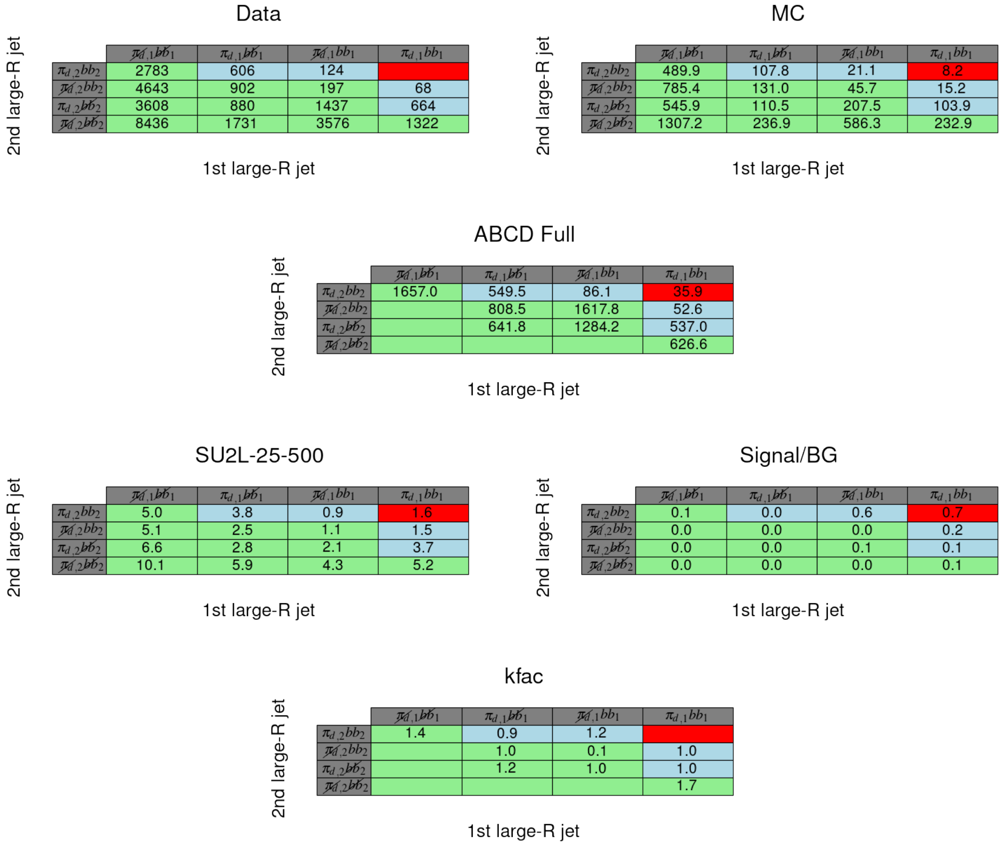

Data

	$\not\pi_{d,1}b\not b_1$	$\pi_{d,1}b\not b_1$	$\not\pi_{d,1}bb_1$	$\pi_{d,1}bb_1$
$\pi_{d,2}bb_2$	2783	606	124	
$\not\pi_{d,2}bb_2$	4643	902	197	68
$\pi_{d,2}b\not b_2$	3608	880	1437	664
$\not\pi_{d,2}b\not b_2$	8436	1731	3576	1322

MC

	$\not\pi_{d,1}b\not b_1$	$\pi_{d,1}b\not b_1$	$\not\pi_{d,1}bb_1$	$\pi_{d,1}bb_1$
$\pi_{d,2}bb_2$	489.9	107.8	21.1	8.2
$\not\pi_{d,2}bb_2$	785.4	131.0	45.7	15.2
$\pi_{d,2}b\not b_2$	545.9	110.5	207.5	103.9
$\not\pi_{d,2}b\not b_2$	1307.2	236.9	586.3	232.9

ABCD Full

	$\not\pi_{d,1}b\not b_1$	$\pi_{d,1}b\not b_1$	$\not\pi_{d,1}bb_1$	$\pi_{d,1}bb_1$
$\pi_{d,2}bb_2$	1657.0	549.5	86.1	35.9
$\not\pi_{d,2}bb_2$		808.5	1617.8	52.6
$\pi_{d,2}b\not b_2$		641.8	1284.2	537.0
$\not\pi_{d,2}b\not b_2$				626.6

SU2L-25-500

	$\not\pi_{d,1}b\not b_1$	$\pi_{d,1}b\not b_1$	$\not\pi_{d,1}bb_1$	$\pi_{d,1}bb_1$
$\pi_{d,2}bb_2$	5.0	3.8	0.9	1.6
$\not\pi_{d,2}bb_2$	5.1	2.5	1.1	1.5
$\pi_{d,2}b\not b_2$	6.6	2.8	2.1	3.7
$\not\pi_{d,2}b\not b_2$	10.1	5.9	4.3	5.2

Signal/BG

	$\not\pi_{d,1}b\not b_1$	$\pi_{d,1}b\not b_1$	$\not\pi_{d,1}bb_1$	$\pi_{d,1}bb_1$
$\pi_{d,2}bb_2$	0.1	0.0	0.6	0.7
$\not\pi_{d,2}bb_2$	0.0	0.0	0.0	0.2
$\pi_{d,2}b\not b_2$	0.0	0.0	0.1	0.1
$\not\pi_{d,2}b\not b_2$	0.0	0.0	0.0	0.1

kfac

	$\not\pi_{d,1}b\not b_1$	$\pi_{d,1}b\not b_1$	$\not\pi_{d,1}bb_1$	$\pi_{d,1}bb_1$
$\pi_{d,2}bb_2$	1.4	0.9	1.2	
$\not\pi_{d,2}bb_2$		1.0	0.1	1.0
$\pi_{d,2}b\not b_2$		1.2	1.0	1.0
$\not\pi_{d,2}b\not b_2$				1.7

Figure A.24. Data, MC, QCD multijet estimate, signal yield, signal contamination, and k-factor for each of the 16 regions used in the ABCD QCD multijet estimate. Estimate for SR bin $325 < m_1 < 400$ GeV, $250 < m_2 < 300$ GeV

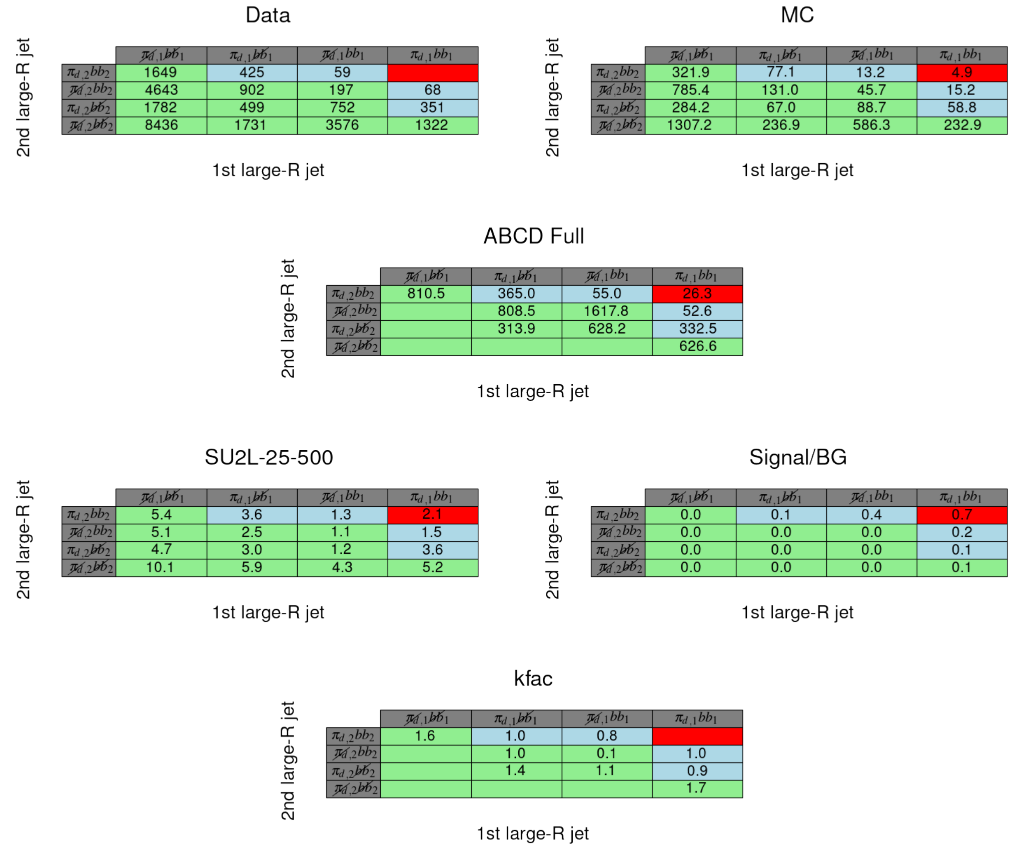

Data

2nd large-R jet

	$\not{\pi}_{d,1}\not{b}b_1$	$\pi_{d,1}\not{b}b_1$	$\not{\pi}_{d,1}bb_1$	$\pi_{d,1}bb_1$
$\pi_{d,2}bb_2$	1649	425	59	
$\not{\pi}_{d,2}bb_2$	4643	902	197	68
$\pi_{d,2}\not{b}b_2$	1782	499	752	351
$\not{\pi}_{d,2}\not{b}b_2$	8436	1731	3576	1322

1st large-R jet

MC

2nd large-R jet

	$\not{\pi}_{d,1}\not{b}b_1$	$\pi_{d,1}\not{b}b_1$	$\not{\pi}_{d,1}bb_1$	$\pi_{d,1}bb_1$
$\pi_{d,2}bb_2$	321.9	77.1	13.2	4.9
$\not{\pi}_{d,2}bb_2$	785.4	131.0	45.7	15.2
$\pi_{d,2}\not{b}b_2$	284.2	67.0	88.7	58.8
$\not{\pi}_{d,2}\not{b}b_2$	1307.2	236.9	586.3	232.9

1st large-R jet

ABCD Full

2nd large-R jet

	$\not{\pi}_{d,1}\not{b}b_1$	$\pi_{d,1}\not{b}b_1$	$\not{\pi}_{d,1}bb_1$	$\pi_{d,1}bb_1$
$\pi_{d,2}bb_2$	810.5	365.0	55.0	26.3
$\not{\pi}_{d,2}bb_2$		808.5	1617.8	52.6
$\pi_{d,2}\not{b}b_2$		313.9	628.2	332.5
$\not{\pi}_{d,2}\not{b}b_2$				626.6

1st large-R jet

SU2L-25-500

2nd large-R jet

	$\not{\pi}_{d,1}\not{b}b_1$	$\pi_{d,1}\not{b}b_1$	$\not{\pi}_{d,1}bb_1$	$\pi_{d,1}bb_1$
$\pi_{d,2}bb_2$	5.4	3.6	1.3	2.1
$\not{\pi}_{d,2}bb_2$	5.1	2.5	1.1	1.5
$\pi_{d,2}\not{b}b_2$	4.7	3.0	1.2	3.6
$\not{\pi}_{d,2}\not{b}b_2$	10.1	5.9	4.3	5.2

1st large-R jet

Signal/BG

2nd large-R jet

	$\not{\pi}_{d,1}\not{b}b_1$	$\pi_{d,1}\not{b}b_1$	$\not{\pi}_{d,1}bb_1$	$\pi_{d,1}bb_1$
$\pi_{d,2}bb_2$	0.0	0.1	0.4	0.7
$\not{\pi}_{d,2}bb_2$	0.0	0.0	0.0	0.2
$\pi_{d,2}\not{b}b_2$	0.0	0.0	0.0	0.1
$\not{\pi}_{d,2}\not{b}b_2$	0.0	0.0	0.0	0.1

1st large-R jet

kfac

2nd large-R jet

	$\not{\pi}_{d,1}\not{b}b_1$	$\pi_{d,1}\not{b}b_1$	$\not{\pi}_{d,1}bb_1$	$\pi_{d,1}bb_1$
$\pi_{d,2}bb_2$	1.6	1.0	0.8	
$\not{\pi}_{d,2}bb_2$		1.0	0.1	1.0
$\pi_{d,2}\not{b}b_2$		1.4	1.1	0.9
$\not{\pi}_{d,2}\not{b}b_2$				1.7

1st large-R jet

Figure A.25. Data, MC, QCD multijet estimate, signal yield, signal contamination, and k-factor for each of the 16 regions used in the ABCD QCD multijet estimate. Estimate for SR bin $325 < m_1 < 400$ GeV, $300 < m_2 < 350$ GeV

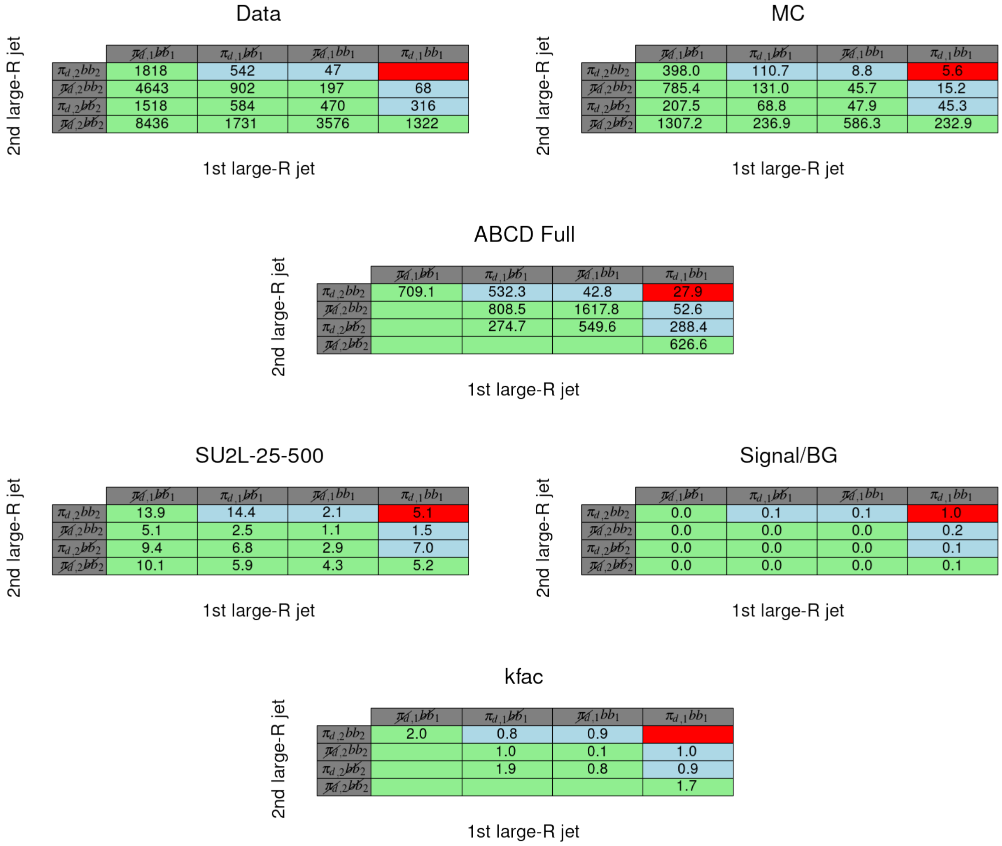

Data

	$\not\pi_{d,1}\not{bb}_1$	$\pi_{d,1}\not{bb}_1$	$\not\pi_{d,1}bb_1$	$\pi_{d,1}bb_1$
$\pi_{d,2}bb_2$	1818	542	47	
$\not\pi_{d,2}bb_2$	4643	902	197	68
$\pi_{d,2}\not{bb}_2$	1518	584	470	316
$\not\pi_{d,2}\not{bb}_2$	8436	1731	3576	1322

2nd large-R jet

1st large-R jet

MC

	$\not\pi_{d,1}\not{bb}_1$	$\pi_{d,1}\not{bb}_1$	$\not\pi_{d,1}bb_1$	$\pi_{d,1}bb_1$
$\pi_{d,2}bb_2$	398.0	110.7	8.8	5.6
$\not\pi_{d,2}bb_2$	785.4	131.0	45.7	15.2
$\pi_{d,2}\not{bb}_2$	207.5	68.8	47.9	45.3
$\not\pi_{d,2}\not{bb}_2$	1307.2	236.9	586.3	232.9

2nd large-R jet

1st large-R jet

ABCD Full

	$\not\pi_{d,1}\not{bb}_1$	$\pi_{d,1}\not{bb}_1$	$\not\pi_{d,1}bb_1$	$\pi_{d,1}bb_1$
$\pi_{d,2}bb_2$	709.1	532.3	42.8	27.9
$\not\pi_{d,2}bb_2$		808.5	1617.8	52.6
$\pi_{d,2}\not{bb}_2$		274.7	549.6	288.4
$\not\pi_{d,2}\not{bb}_2$				626.6

2nd large-R jet

1st large-R jet

SU2L-25-500

	$\not\pi_{d,1}\not{bb}_1$	$\pi_{d,1}\not{bb}_1$	$\not\pi_{d,1}bb_1$	$\pi_{d,1}bb_1$
$\pi_{d,2}bb_2$	13.9	14.4	2.1	5.1
$\not\pi_{d,2}bb_2$	5.1	2.5	1.1	1.5
$\pi_{d,2}\not{bb}_2$	9.4	6.8	2.9	7.0
$\not\pi_{d,2}\not{bb}_2$	10.1	5.9	4.3	5.2

2nd large-R jet

1st large-R jet

Signal/BG

	$\not\pi_{d,1}\not{bb}_1$	$\pi_{d,1}\not{bb}_1$	$\not\pi_{d,1}bb_1$	$\pi_{d,1}bb_1$
$\pi_{d,2}bb_2$	0.0	0.1	0.1	1.0
$\not\pi_{d,2}bb_2$	0.0	0.0	0.0	0.2
$\pi_{d,2}\not{bb}_2$	0.0	0.0	0.0	0.1
$\not\pi_{d,2}\not{bb}_2$	0.0	0.0	0.0	0.1

2nd large-R jet

1st large-R jet

kfac

	$\not\pi_{d,1}\not{bb}_1$	$\pi_{d,1}\not{bb}_1$	$\not\pi_{d,1}bb_1$	$\pi_{d,1}bb_1$
$\pi_{d,2}bb_2$	2.0	0.8	0.9	
$\not\pi_{d,2}bb_2$		1.0	0.1	1.0
$\pi_{d,2}\not{bb}_2$		1.9	0.8	0.9
$\not\pi_{d,2}\not{bb}_2$				1.7

2nd large-R jet

1st large-R jet

Figure A.26. Data, MC, QCD multijet estimate, signal yield, signal contamination, and k-factor for each of the 16 regions used in the ABCD QCD multijet estimate. Estimate for SR bin $325 < m_1 < 400\ \ \text{GeV}, 350\ \ \text{GeV} < m_2$

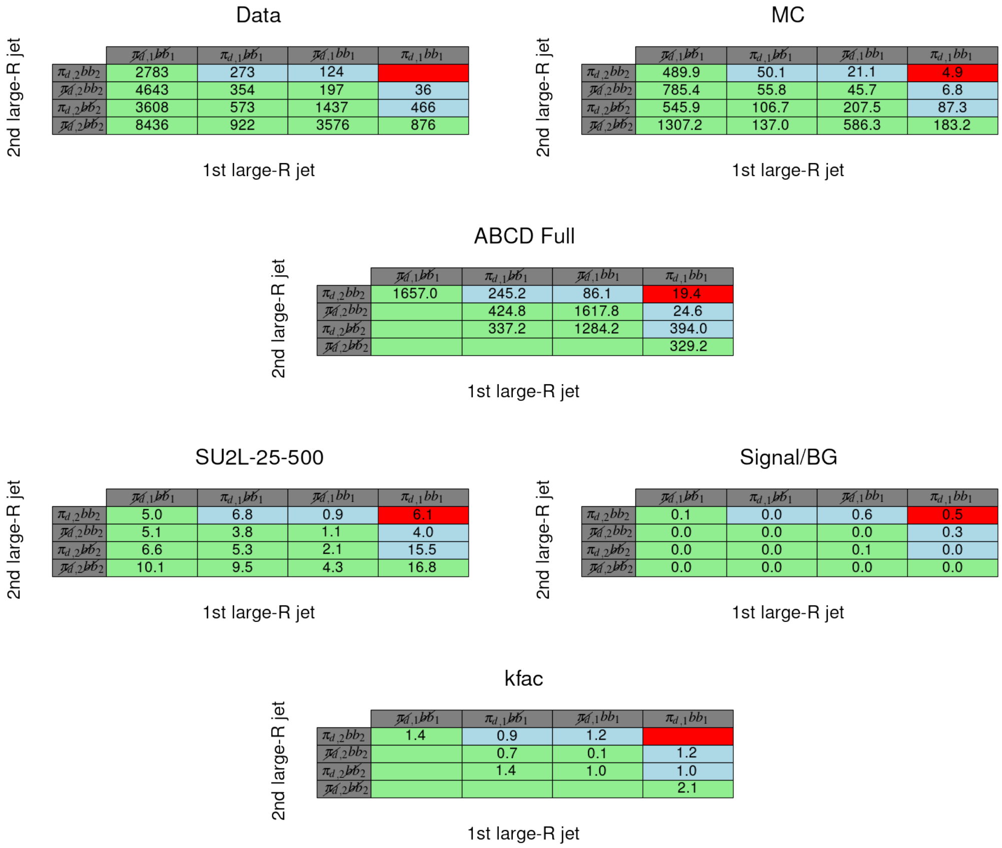

Data

	$\cancel{\pi}_{d,1}\cancel{bb}_1$	$\pi_{d,1}\cancel{bb}_1$	$\cancel{\pi}_{d,1}bb_1$	$\pi_{d,1}bb_1$
$\pi_{d,2}bb_2$	2783	273	124	
$\cancel{\pi}_{d,2}bb_2$	4643	354	197	36
$\pi_{d,2}\cancel{bb}_2$	3608	573	1437	466
$\cancel{\pi}_{d,2}\cancel{bb}_2$	8436	922	3576	876

MC

	$\cancel{\pi}_{d,1}\cancel{bb}_1$	$\pi_{d,1}\cancel{bb}_1$	$\cancel{\pi}_{d,1}bb_1$	$\pi_{d,1}bb_1$
$\pi_{d,2}bb_2$	489.9	50.1	21.1	4.9
$\cancel{\pi}_{d,2}bb_2$	785.4	55.8	45.7	6.8
$\pi_{d,2}\cancel{bb}_2$	545.9	106.7	207.5	87.3
$\cancel{\pi}_{d,2}\cancel{bb}_2$	1307.2	137.0	586.3	183.2

ABCD Full

	$\cancel{\pi}_{d,1}\cancel{bb}_1$	$\pi_{d,1}\cancel{bb}_1$	$\cancel{\pi}_{d,1}bb_1$	$\pi_{d,1}bb_1$
$\pi_{d,2}bb_2$	1657.0	245.2	86.1	19.4
$\cancel{\pi}_{d,2}bb_2$		424.8	1617.8	24.6
$\pi_{d,2}\cancel{bb}_2$		337.2	1284.2	394.0
$\cancel{\pi}_{d,2}\cancel{bb}_2$				329.2

SU2L-25-500

	$\cancel{\pi}_{d,1}\cancel{bb}_1$	$\pi_{d,1}\cancel{bb}_1$	$\cancel{\pi}_{d,1}bb_1$	$\pi_{d,1}bb_1$
$\pi_{d,2}bb_2$	5.0	6.8	0.9	6.1
$\cancel{\pi}_{d,2}bb_2$	5.1	3.8	1.1	4.0
$\pi_{d,2}\cancel{bb}_2$	6.6	5.3	2.1	15.5
$\cancel{\pi}_{d,2}\cancel{bb}_2$	10.1	9.5	4.3	16.8

Signal/BG

	$\cancel{\pi}_{d,1}\cancel{bb}_1$	$\pi_{d,1}\cancel{bb}_1$	$\cancel{\pi}_{d,1}bb_1$	$\pi_{d,1}bb_1$
$\pi_{d,2}bb_2$	0.1	0.0	0.6	0.5
$\cancel{\pi}_{d,2}bb_2$	0.0	0.0	0.0	0.3
$\pi_{d,2}\cancel{bb}_2$	0.0	0.0	0.1	0.0
$\cancel{\pi}_{d,2}\cancel{bb}_2$	0.0	0.0	0.0	0.0

kfac

	$\cancel{\pi}_{d,1}\cancel{bb}_1$	$\pi_{d,1}\cancel{bb}_1$	$\cancel{\pi}_{d,1}bb_1$	$\pi_{d,1}bb_1$
$\pi_{d,2}bb_2$	1.4	0.9	1.2	
$\cancel{\pi}_{d,2}bb_2$		0.7	0.1	1.2
$\pi_{d,2}\cancel{bb}_2$		1.4	1.0	1.0
$\cancel{\pi}_{d,2}\cancel{bb}_2$				2.1

Figure A.27. Data, MC, QCD multijet estimate, signal yield, signal contamination, and k-factor for each of the 16 regions used in the ABCD QCD multijet estimate. Estimate for SR bin $400 < m_1 < 10000$ GeV, $250 < m_2 < 300$ GeV

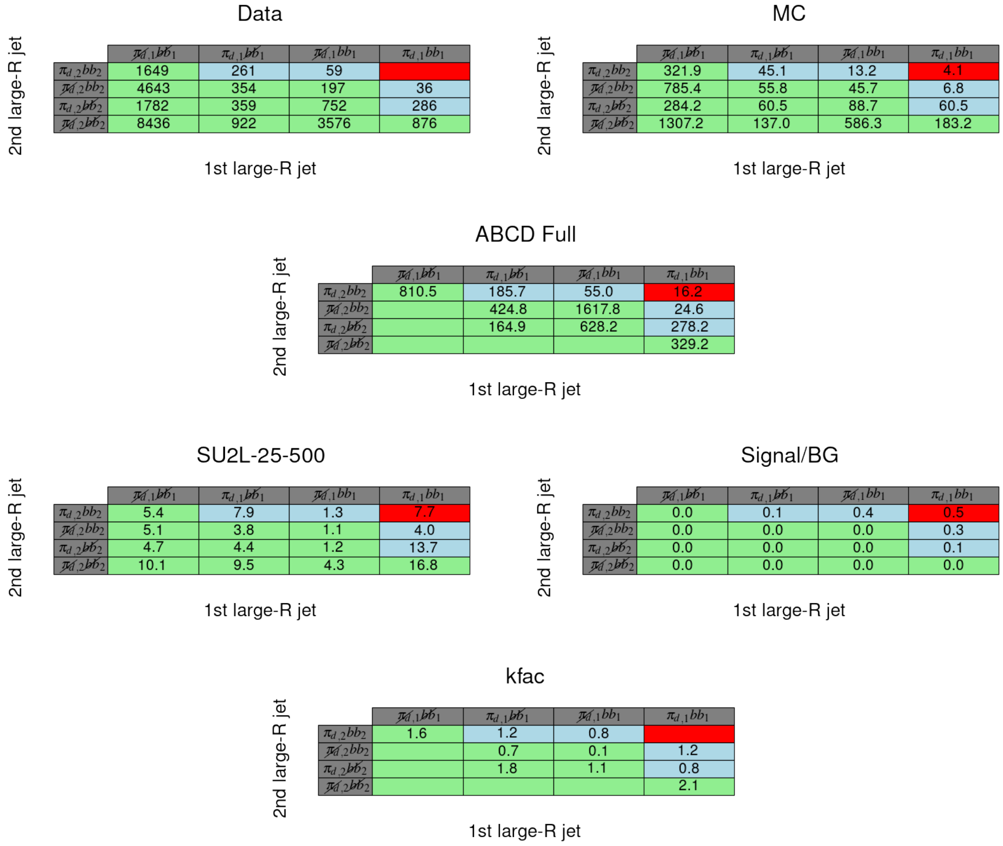

Data

	$\not{\pi}_{d,1}\not{bb}_1$	$\pi_{d,1}\not{bb}_1$	$\not{\pi}_{d,1}bb_1$	$\pi_{d,1}bb_1$
$\pi_{d,2}bb_2$	1649	261	59	
$\not{\pi}_{d,2}bb_2$	4643	354	197	36
$\pi_{d,2}\not{bb}_2$	1782	359	752	286
$\not{\pi}_{d,2}\not{bb}_2$	8436	922	3576	876

MC

	$\not{\pi}_{d,1}\not{bb}_1$	$\pi_{d,1}\not{bb}_1$	$\not{\pi}_{d,1}bb_1$	$\pi_{d,1}bb_1$
$\pi_{d,2}bb_2$	321.9	45.1	13.2	4.1
$\not{\pi}_{d,2}bb_2$	785.4	55.8	45.7	6.8
$\pi_{d,2}\not{bb}_2$	284.2	60.5	88.7	60.5
$\not{\pi}_{d,2}\not{bb}_2$	1307.2	137.0	586.3	183.2

ABCD Full

	$\not{\pi}_{d,1}\not{bb}_1$	$\pi_{d,1}\not{bb}_1$	$\not{\pi}_{d,1}bb_1$	$\pi_{d,1}bb_1$
$\pi_{d,2}bb_2$	810.5	185.7	55.0	16.2
$\not{\pi}_{d,2}bb_2$		424.8	1617.8	24.6
$\pi_{d,2}\not{bb}_2$		164.9	628.2	278.2
$\not{\pi}_{d,2}\not{bb}_2$				329.2

SU2L-25-500

	$\not{\pi}_{d,1}\not{bb}_1$	$\pi_{d,1}\not{bb}_1$	$\not{\pi}_{d,1}bb_1$	$\pi_{d,1}bb_1$
$\pi_{d,2}bb_2$	5.4	7.9	1.3	7.7
$\not{\pi}_{d,2}bb_2$	5.1	3.8	1.1	4.0
$\pi_{d,2}\not{bb}_2$	4.7	4.4	1.2	13.7
$\not{\pi}_{d,2}\not{bb}_2$	10.1	9.5	4.3	16.8

Signal/BG

	$\not{\pi}_{d,1}\not{bb}_1$	$\pi_{d,1}\not{bb}_1$	$\not{\pi}_{d,1}bb_1$	$\pi_{d,1}bb_1$
$\pi_{d,2}bb_2$	0.0	0.1	0.4	0.5
$\not{\pi}_{d,2}bb_2$	0.0	0.0	0.0	0.3
$\pi_{d,2}\not{bb}_2$	0.0	0.0	0.0	0.1
$\not{\pi}_{d,2}\not{bb}_2$	0.0	0.0	0.0	0.0

kfac

	$\not{\pi}_{d,1}\not{bb}_1$	$\pi_{d,1}\not{bb}_1$	$\not{\pi}_{d,1}bb_1$	$\pi_{d,1}bb_1$
$\pi_{d,2}bb_2$	1.6	1.2	0.8	
$\not{\pi}_{d,2}bb_2$		0.7	0.1	1.2
$\pi_{d,2}\not{bb}_2$		1.8	1.1	0.8
$\not{\pi}_{d,2}\not{bb}_2$				2.1

Figure A.28. Data, MC, QCD multijet estimate, signal yield, signal contamination, and k-factor for each of the 16 regions used in the ABCD QCD multijet estimate. Estimate for SR bin $400 < m_1 < 10000$ GeV, $300 < m_2 < 350$ GeV

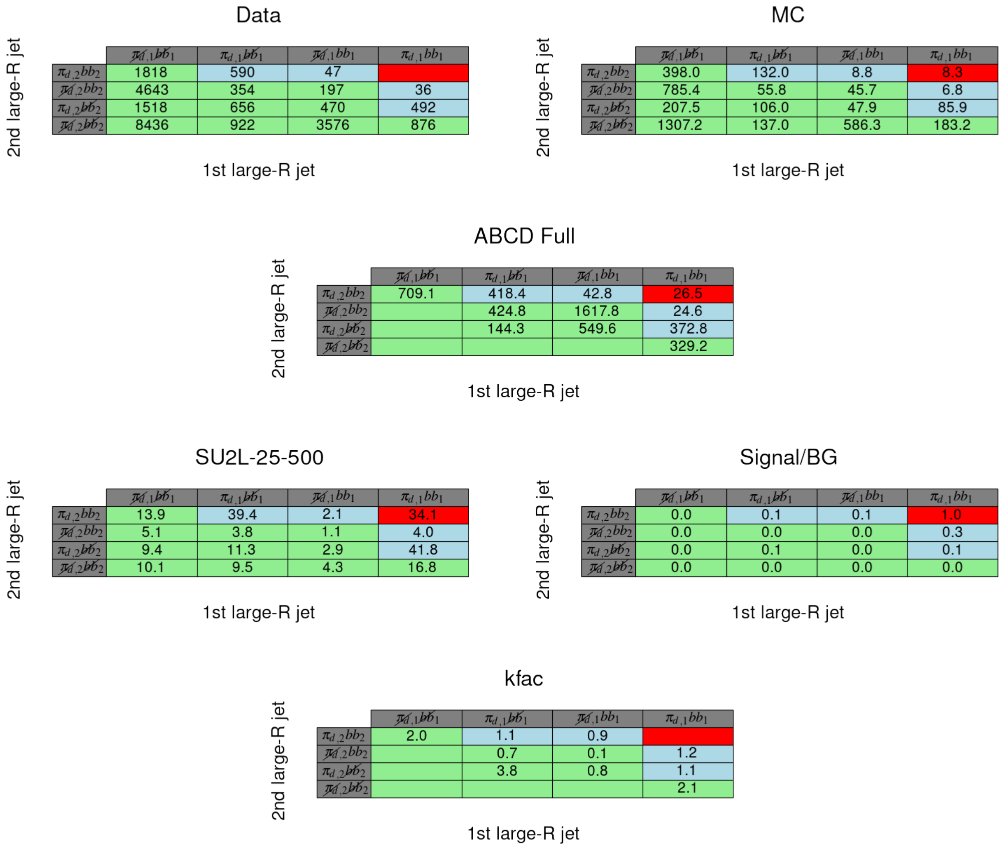

Data

	$\not{\pi}_{d,1}\not{bb}_1$	$\pi_{d,1}\not{bb}_1$	$\not{\pi}_{d,1}bb_1$	$\pi_{d,1}bb_1$
$\pi_{d,2}bb_2$	1818	590	47	
$\not{\pi}_{d,2}bb_2$	4643	354	197	36
$\pi_{d,2}\not{bb}_2$	1518	656	470	492
$\not{\pi}_{d,2}\not{bb}_2$	8436	922	3576	876

2nd large-R jet

1st large-R jet

MC

	$\not{\pi}_{d,1}\not{bb}_1$	$\pi_{d,1}\not{bb}_1$	$\not{\pi}_{d,1}bb_1$	$\pi_{d,1}bb_1$
$\pi_{d,2}bb_2$	398.0	132.0	8.8	8.3
$\not{\pi}_{d,2}bb_2$	785.4	55.8	45.7	6.8
$\pi_{d,2}\not{bb}_2$	207.5	106.0	47.9	85.9
$\not{\pi}_{d,2}\not{bb}_2$	1307.2	137.0	586.3	183.2

2nd large-R jet

1st large-R jet

ABCD Full

	$\not{\pi}_{d,1}\not{bb}_1$	$\pi_{d,1}\not{bb}_1$	$\not{\pi}_{d,1}bb_1$	$\pi_{d,1}bb_1$
$\pi_{d,2}bb_2$	709.1	418.4	42.8	26.5
$\not{\pi}_{d,2}bb_2$		424.8	1617.8	24.6
$\pi_{d,2}\not{bb}_2$		144.3	549.6	372.8
$\not{\pi}_{d,2}\not{bb}_2$				329.2

2nd large-R jet

1st large-R jet

SU2L-25-500

	$\not{\pi}_{d,1}\not{bb}_1$	$\pi_{d,1}\not{bb}_1$	$\not{\pi}_{d,1}bb_1$	$\pi_{d,1}bb_1$
$\pi_{d,2}bb_2$	13.9	39.4	2.1	34.1
$\not{\pi}_{d,2}bb_2$	5.1	3.8	1.1	4.0
$\pi_{d,2}\not{bb}_2$	9.4	11.3	2.9	41.8
$\not{\pi}_{d,2}\not{bb}_2$	10.1	9.5	4.3	16.8

2nd large-R jet

1st large-R jet

Signal/BG

	$\not{\pi}_{d,1}\not{bb}_1$	$\pi_{d,1}\not{bb}_1$	$\not{\pi}_{d,1}bb_1$	$\pi_{d,1}bb_1$
$\pi_{d,2}bb_2$	0.0	0.1	0.1	1.0
$\not{\pi}_{d,2}bb_2$	0.0	0.0	0.0	0.3
$\pi_{d,2}\not{bb}_2$	0.0	0.1	0.0	0.1
$\not{\pi}_{d,2}\not{bb}_2$	0.0	0.0	0.0	0.0

2nd large-R jet

1st large-R jet

kfac

	$\not{\pi}_{d,1}\not{bb}_1$	$\pi_{d,1}\not{bb}_1$	$\not{\pi}_{d,1}bb_1$	$\pi_{d,1}bb_1$
$\pi_{d,2}bb_2$	2.0	1.1	0.9	
$\not{\pi}_{d,2}bb_2$		0.7	0.1	1.2
$\pi_{d,2}\not{bb}_2$		3.8	0.8	1.1
$\not{\pi}_{d,2}\not{bb}_2$				2.1

2nd large-R jet

1st large-R jet

Figure A.29. Data, MC, QCD multijet estimate, signal yield, signal contamination, and k-factor for each of the 16 regions used in the ABCD QCD multijet estimate. Estimate for SR bin $400 < m_1 < 10000\ \ \text{GeV}, 350\ \ \text{GeV} < m_2$

REFERENCES CITED

[1] Planck collaboration. Planck 2018 results: I. overview and the cosmological legacy of planck. *Astronomy and astrophysics (Berlin)*, 641:1–56, 2020.

[2] Richard Massey, Thomas Kitching, and Johan Richard. The dark matter of gravitational lensing. *Rept. Prog. Phys.*, 73:086901, 2010.

[3] V. C. Rubin, Jr. Ford, W. K., and N. Thonnard. Rotational properties of 21 SC galaxies with a large range of luminosities and radii, from NGC 4605 ($R = 4kpc$) to UGC 2885 ($R = 122kpc$). *apj*, 238:471–487, June 1980.

[4] Douglas Clowe, Marusa Bradac, Anthony H. Gonzalez, Maxim Markevitch, Scott W. Randall, Christine Jones, and Dennis Zaritsky. A direct empirical proof of the existence of dark matter. *Astrophys. J. Lett.*, 648:L109–L113, 2006.

[5] Stephen P. Martin. A Supersymmetry primer. *Adv. Ser. Direct. High Energy Phys.*, 18:1–98, 1998.

[6] Graham D. Kribs, Adam Martin, and Tom Tong. Effective Theories of Dark Mesons with Custodial Symmetry. *JHEP*, 08:020, 2019.

[7] Thomas Appelquist et al. Stealth Dark Matter: Dark scalar baryons through the Higgs portal. *Phys. Rev. D*, 92(7):075030, 2015.

[8] Graham D. Kribs and Ethan T. Neil. Review of strongly-coupled composite dark matter models and lattice simulations. *Int. J. Mod. Phys. A*, 31(22):1643004, 2016.

[9] Oleg Antipin, Michele Redi, Alessandro Strumia, and Elena Vigiani. Accidental Composite Dark Matter. *JHEP*, 07:039, 2015.

[10] ATLAS collaboration. Search for a scalar partner of the top quark in the all-hadronic $t\bar{t}$ plus missing transverse momentum final state at $\sqrt{s} = 13$ TeV with the ATLAS detector. *Eur. Phys. J. C*, 80(8):737, 2020.

[11] ATLAS Collaboration. Search for new phenomena with top quark pairs in final states with one lepton, jets, and missing transverse momentum in pp collisions at $\sqrt{s}$= 13 TeV with the ATLAS detector. *JHEP*, 2104:174, 2021.

[12] ATLAS collaboration. Search for new phenomena in events with two opposite-charge leptons, jets and missing transverse momentum in pp collisions at $\sqrt{s} = 13$ TeV with the ATLAS detector. *JHEP*, 2104:165, 2021.

[13] ATLAS Collaboration. Measurements of top-quark pair spin correlations in the $e\mu$ channel at $\sqrt{s} = 13$ TeV using pp collisions in the ATLAS detector. 2019.

[14] ATLAS Collaboration. The ATLAS Experiment at the CERN Large Hadron Collider: A Description of the Detector Configuration for Run 3, 2022.

[15] Andrea Dainese, Michelangelo Mangano, Andreas B Meyer, Aleandro Nisati, Gavin Salam, and Mika Anton Vesterinen. Report on the Physics at the HL-LHC, and Perspectives for the HE-LHC. Technical report, Geneva, Switzerland, 2019.

[16] CDF collaboration. Observation of top quark production in $\bar{p}p$ collisions. *Phys. Rev. Lett.*, 74:2626–2631, 1995.

[17] D0 collaboration. Observation of the top quark. *Phys. Rev. Lett.*, 74:2632–2637, 1995.

[18] ATLAS Collaboration. Observation of a new particle in the search for the Standard Model Higgs boson with the ATLAS detector at the LHC. *Phys. Lett. B*, 716:1–29, 2012.

[19] CMS collaboration. Observation of a New Boson at a Mass of 125 GeV with the CMS Experiment at the LHC. *Phys. Lett. B*, 716:30–61, 2012.

[20] CDF collaboration. High-precision measurement of the W boson mass with the CDF II detector. *Science*, 376(6589):170–176, 2022.

[21] Pedro A. N. Machado. Neutrino Properties and Interactions. 6 2022.

[22] EROS-2 collaboration. Limits on the Macho Content of the Galactic Halo from the EROS-2 Survey of the Magellanic Clouds. *Astron. Astrophys.*, 469:387–404, 2007.

[23] R. L. Workman and Others. Review of Particle Physics. *PTEP*, 2022:083C01, 2022.

[24] Sidney Coleman and Jeffrey Mandula. All possible symmetries of the s matrix. *Phys. Rev.*, 159:1251–1256, Jul 1967.

[25] Lyndon Evans and Philip Bryant. LHC Machine. *JINST*, 3:S08001, 2008.

[26] Cinzia De Melis. The CERN accelerator complex. Complexe des accélérateurs du CERN. General Photo, 2016.

[27] Luminosity determination in pp collisions at $\sqrt{s} = 13$ TeV using the ATLAS detector at the LHC. Technical Report ATLAS-CONF-2019-021, CERN, Geneva, Jun 2019.

[28] G. Avoni et al. The new lucid-2 detector for luminosity measurement and monitoring in atlas. *JINST*, 13(07):P07017, 2018.

[29] ATLAS Collaboration. `https://twiki.cern.ch/twiki/bin/view/AtlasPublic/LuminosityPublicResultsRun2`. Online; accessed 24 October, 2022.

[30] ATLAS Collaboration. `https://twiki.cern.ch/twiki/bin/view/AtlasPublic/LuminosityPublicResultsRun2`. Online; accessed 24 October, 2022.

[31] ATLAS Collaboration. `https://twiki.cern.ch/twiki/bin/view/AtlasPublic/LuminosityPublicResultsRun2`. Online; accessed 24 October, 2022.

[32] ATLAS Collaboration. The ATLAS Experiment at the CERN Large Hadron Collider. *JINST*, 3:S08003, 2008.

[33] ATLAS Collaboration. ATLAS Inner Detector: Technical Design Report, 1. ATLAS-TDR-4, 1997.

[34] ATLAS Collaboration. Production and Integration of the ATLAS Insertable B-Layer. *JINST*, 13:T05008. 90 p, Mar 2018.

[35] ATLAS Collaboration. ATLAS Insertable B-Layer Technical Design Report. ATLAS-TDR-19, 2010.

[36] ATLAS Collaboration. ATLAS Insertable B-Layer Technical Design Report. Technical report, CERN, 2010.

[37] ATLAS Collaboration. The ATLAS TRT Barrel Detector. *JINST*, 3:P02014, 2008.

[38] ATLAS Collaboration. ATLAS Transition Radiation Tracker (TRT): Straw tubes for tracking and particle identification at the Large Hadron Collider. Technical report, CERN, Geneva, 2017.

[39] ATLAS Collaboration. ATLAS Liquid Argon Calorimeter Phase-I Upgrade: Technical Design Report. Technical report, CERN, 2013. Final version presented to December 2013 LHCC.

[40] ATLAS Collaboration. ATLAS Liquid-Argon Calorimeter: Technical Design Report. ATLAS-TDR-2, 1996.

[41] ATLAS Collaboration. `https://twiki.cern.ch/twiki/bin/view/AtlasPublic/ApprovedPlotsLAr`. Online; accessed 24 October, 2022.

[42] ATLAS Collaboration. ATLAS Tile Calorimeter: Technical Design Report. ATLAS-TDR-3, 1996.

[43] ATLAS Collaboration. *ATLAS muon spectrometer: Technical Design Report.* Technical design report. ATLAS. CERN, Geneva, 1997.

[44] ATLAS Collaboration. Performance of the ATLAS muon trigger in pp collisions at $\sqrt{s} = 8\,\text{TeV}$. *Eur. Phys. J. C*, 75:120, 2015.

[45] ATLAS Collaboration. The ATLAS Data Acquisition and High Level Trigger system. *JINST*, 11(06):P06008, 2016.

[46] ATLAS Collaboration. Performance of the ATLAS Trigger System in 2015. *Eur. Phys. J. C*, 77(5):317, 2017.

[47] Joao Pequenao and Paul Schaffner. How ATLAS detects particles: diagram of particle paths in the detector. Jan 2013.

[48] ATLAS Collaboration. Electron efficiency measurements with the ATLAS detector using the 2015 LHC proton–proton collision data. ATLAS-CONF-2016-024, 2016.

[49] Peter Loch. Lectures on Hadronic Final State Reconstruction at LHC. `http://atlas.physics.arizona.edu/~loch`.

[50] S. D. Ellis, J. Huston, K. Hatakeyama, P. Loch, and M. Tonnesmann. Jets in hadron-hadron collisions. *Prog. Part. Nucl. Phys.*, 60:484–551, 2008.

[51] ATLAS Collaboration. Topological cell clustering in the ATLAS calorimeters and its performance in LHC Run 1. *Eur. Phys. J. C*, 77:490, 2017.

[52] Matteo Cacciari, Gavin P. Salam, and Gregory Soyez. The anti-k_t jet clustering algorithm. *JHEP*, 04:063, 2008.

[53] ATLAS Collaboration. Jet reconstruction and performance using particle flow with the ATLAS Detector. *Eur. Phys. J. C*, 77:466, 2017.

[54] M. Aaboud et al. Jet energy scale measurements and their systematic uncertainties in proton-proton collisions at $\sqrt{s} = 13$ TeV with the ATLAS detector. *Phys. Rev.*, D96(7):072002, 2017.

[55] ATLAS Collaboration. Tagging and suppression of pileup jets with the ATLAS detector. ATLAS-CONF-2014-018, 2014.

[56] ATLAS Collaboration. Identification and rejection of pile-up jets at high pseudorapidity with the ATLAS detector. *Eur. Phys. J. C*, 77:580, 2017.

[57] Per Ola Hansson Adrian. The ATLAS b-Jet Trigger. Technical report, CERN, Geneva, 2011. Comments: 4 pages, 6 figures, conference proceedings for PIC2011.

[58] ATLAS Collaboration. ATLAS b-jet identification performance and efficiency measurement with $t\bar{t}$ events in pp collisions at $\sqrt{s} = 13\,\text{TeV}$. *Eur. Phys. J. C*, 79(11):970, 2019.

[59] ATLAS Collaboration. Optimisation and performance studies of the ATLAS b-tagging algorithms for the 2017-18 LHC run. Technical Report ATL-PHYS-PUB-2017-013, CERN, Geneva, Jul 2017.

[60] The ATLAS Collaboration. $E_{\mathrm{T}}^{\mathrm{miss}}$ performance in the ATLAS detector using 2015-2016 LHC p-p collisions. Technical Report ATLAS-CONF-2018-023, CERN, Geneva, Jun 2018.

[61] ATLAS Collaboration. Muon reconstruction performance of the ATLAS detector in proton–proton collision data at $\sqrt{s} = 13\,\text{TeV}$. *Eur. Phys. J. C*, 76:292, 2016.

[62] D. J. Lange. The EvtGen particle decay simulation package. *Nucl. Instrum. Meth. A*, 462:152, 2001.

[63] J. Alwall, R. Frederix, S. Frixione, V. Hirschi, F. Maltoni, et al. The automated computation of tree-level and next-to-leading order differential cross sections, and their matching to parton shower simulations. *JHEP*, 07:079, 2014.

[64] Torbjörn Sjöstrand, Stefan Ask, Jesper R. Christiansen, Richard Corke, Nishita Desai, Philip Ilten, Stephen Mrenna, Stefan Prestel, Christine O. Rasmussen, and Peter Z. Skands. An Introduction to PYTHIA 8.2. *Comput. Phys. Commun.*, 191:159, 2015.

[65] T. Gleisberg, Stefan. Hoeche, F. Krauss, M. Schonherr, S. Schumann, F. Siegert, and J. Winter. Event generation with SHERPA 1.1. *JHEP*, 02:007, 2009.

[66] Stefano Frixione, Paolo Nason, and Giovanni Ridolfi. A positive-weight next-to-leading-order Monte Carlo for heavy flavour hadroproduction. *JHEP*, 09:126, 2007.

[67] Paolo Nason. A new method for combining NLO QCD with shower Monte Carlo algorithms. *JHEP*, 11:040, 2004.

[68] Stefano Frixione, Paolo Nason, and Carlo Oleari. Matching NLO QCD computations with parton shower simulations: the POWHEG method. *JHEP*, 11:070, 2007.

[69] Simone Alioli, Paolo Nason, Carlo Oleari, and Emanuele Re. A general framework for implementing NLO calculations in shower Monte Carlo programs: the POWHEG BOX. *JHEP*, 06:043, 2010.

[70] Richard D. Ball et al. Parton distributions for the LHC Run II. *JHEP*, 04:040, 2015.

[71] ATLAS Collaboration. Studies on top-quark Monte Carlo modelling for Top2016. ATL-PHYS-PUB-2016-020, 2016.

[72] Enrico Bothmann et al. Event Generation with Sherpa 2.2. *SciPost Phys.*, 7(3):034, 2019.

[73] Tanju Gleisberg and Stefan Höche. Comix, a new matrix element generator. *JHEP*, 12:039, 2008.

[74] Federico Buccioni, Jean-Nicolas Lang, Jonas M. Lindert, Philipp Maierhöfer, Stefano Pozzorini, Hantian Zhang, and Max F. Zoller. OpenLoops 2. *Eur. Phys. J. C*, 79(10):866, 2019.

[75] Fabio Cascioli, Philipp Maierhofer, and Stefano Pozzorini. Scattering Amplitudes with Open Loops. *Phys. Rev. Lett.*, 108:111601, 2012.

[76] Ansgar Denner, Stefan Dittmaier, and Lars Hofer. Collier: A fortran-based complex one-loop library in extended regularizations. *Comput. Phys. Commun.*, 212:220–238, 2017.

[77] Steffen Schumann and Frank Krauss. A Parton shower algorithm based on Catani-Seymour dipole factorisation. *JHEP*, 03:038, 2008.

[78] Stefan Höche, Frank Krauss, Marek Schönherr, and Frank Siegert. A critical appraisal of NLO+PS matching methods. *JHEP*, 09:049, 2012.

[79] Stefan Höche, Frank Krauss, Marek Schönherr, and Frank Siegert. QCD matrix elements + parton showers: The NLO case. *JHEP*, 04:027, 2013.

[80] S. Catani, F. Krauss, R. Kuhn, and B. R. Webber. QCD Matrix Elements + Parton Showers. *JHEP*, 11:063, 2001.

[81] Stefan Höche, Frank Krauss, Steffen Schumann, and Frank Siegert. QCD matrix elements and truncated showers. *JHEP*, 05:053, 2009.

[82] Stefano Carrazza, Stefano Forte, Zahari Kassabov, José Ignacio Latorre, and Juan Rojo. An unbiased hessian representation for monte carlo PDFs. *The European Physical Journal C*, 75(8), aug 2015.

[83] Charalampos Anastasiou, Lance J. Dixon, Kirill Melnikov, and Frank Petriello. High precision QCD at hadron colliders: Electroweak gauge boson rapidity distributions at NNLO. *Phys. Rev. D*, 69:094008, 2004.

[84] S. Agostinelli et al. Geant4 - a simulation toolkit. *Nuclear Instruments and Methods in Physics Research Section A: Accelerators, Spectrometers, Detectors and Associated Equipment*, 506(3):250–303, 2003.

[85] ATLAS Collaboration. Fast Simulation for ATLAS: Atlfast-II and ISF. Technical report, CERN, Geneva, 2012.

[86] family=Golfand given=Yuri A, given-i=Yu A and family=Likhtman given=Evgeny P, given-i=EP. Extension of the Algebra of Poincare Group Generators and Violation of P Invariance. *JETP Lett.*, 13:323, 1971. [Pisma Zh. Eksp. Teor. Fiz. **13** (1971) 452].

[87] D. V. Volkov and V. P. Akulov. Is the neutrino a Goldstone particle? *Phys. Lett. B*, 46:109, 1973.

[88] J. Wess and B. Zumino. Supergauge transformations in four dimensions. *Nucl. Phys. B*, 70:39, 1974.

[89] J. Wess and B. Zumino. Supergauge invariant extension of quantum electrodynamics. *Nucl. Phys. B*, 78:1, 1974.

[90] S. Ferrara and B. Zumino. Supergauge invariant Yang-Mills theories. *Nucl. Phys. B*, 79:413, 1974.

[91] Abdus Salam and J. Strathdee. Super-symmetry and non-Abelian gauges. *Phys. Lett. B*, 51:353, 1974.

[92] Savas Dimopoulos and Howard Georgi. Softly broken supersymmetry and SU(5). *Nucl. Phys. B*, 193:150, 1981.

[93] N. Sakai. Naturalness in supersymmetric GUTS. *Z. Phys. C*, 11:153, 1981.

[94] S. Dimopoulos, S. Raby, and Frank Wilczek. Supersymmetry and the scale of unification. *Phys. Rev. D*, 24:1681, 1981.

[95] Luis E. Ibáñez and Graham G. Ross. Low-energy predictions in supersymmetric grand unified theories. *Phys. Lett. B*, 105:439, 1981.

[96] Kenzo Inoue, Akira Kakuto, Hiromasa Komatsu, and Seiichiro Takeshita. Aspects of Grand Unified Models with Softly Broken Supersymmetry. *Prog. Theor. Phys.*, 68:927, 1982.

[97] John R. Ellis and Serge Rudaz. Search for supersymmetry in toponium decays. *Phys. Lett. B*, 128:248, 1983.

[98] Riccardo Barbieri and G. F. Giudice. Upper bounds on supersymmetric particle masses. *Nucl. Phys. B*, 306:63, 1988.

[99] B. de Carlos and J. A. Casas. One-loop analysis of the electroweak breaking in supersymmetric models and the fine-tuning problem. *Phys. Lett. B*, 309:320, 1993.

[100] Glennys R. Farrar and Pierre Fayet. Phenomenology of the production, decay, and detection of new hadronic states associated with supersymmetry. *Phys. Lett. B*, 76:575, 1978.

[101] H. Goldberg. Constraint on the Photino Mass from Cosmology. *Phys. Rev. Lett.*, 50:1419, 1983.

[102] John Ellis, J. S. Hagelin, Dimitri V. Nanopoulos, Keith Olive, and M. Srednicki. Supersymmetric relics from the big bang. *Nucl. Phys. B*, 238:453, 1984.

[103] W. Beenakker, M. Kramer, T. Plehn, M. Spira, and P. M. Zerwas. Stop production at hadron colliders. *Nucl. Phys.*, B515:3–14, 1998.

[104] Wim Beenakker, Silja Brensing, Michael Krämer, Anna Kulesza, Eric Laenen, and Irene Niessen. Supersymmetric top and bottom squark production at hadron colliders. *JHEP*, 08:098, 2010.

[105] W. Beenakker et al. Squark and gluino hadroproduction. *Int. J. Mod. Phys. A*, 26:2637, 2011.

[106] Christoph Borschensky, Michael Krämer, Anna Kulesza, Michelangelo Mangano, Sanjay Padhi, Tilman Plehn, and Xavier Portell. Squark and gluino production cross sections in pp collisions at $\sqrt{s} = 13, 14, 33$ and $100\,\text{TeV}$. *Eur. Phys. J. C*, 74:3174, 2014.

[107] ATLAS Collaboration. ATLAS Run 1 searches for direct pair production of third-generation squarks at the Large Hadron Collider. *Eur. Phys. J. C*, 75:510, 2015.

[108] ATLAS Collaboration. Search for a scalar partner of the top quark in the jets plus missing transverse momentum final state at $\sqrt{s} = 13\,\text{TeV}$ with the ATLAS detector. *JHEP*, 12:085, 2017.

[109] ATLAS Collaboration. Search for top-squark pair production in final states with one lepton, jets, and missing transverse momentum using $36\,\text{fb}^{-1}$ of $\sqrt{s} = 13\,\text{TeV}$ pp collision data with the ATLAS detector. *JHEP*, 06:108, 2018.

[110] ATLAS Collaboration. Search for direct top squark pair production in final states with two leptons in $\sqrt{s} = 13\,\text{TeV}$ pp collisions with the ATLAS detector. *Eur. Phys. J. C*, 77:898, 2017.

[111] ATLAS Collaboration. Search for supersymmetry in final states with charm jets and missing transverse momentum in 13 TeV pp collisions with the ATLAS detector. *JHEP*, 09:050, 2018.

[112] ATLAS Collaboration. Search for dark matter and other new phenomena in events with an energetic jet and large missing transverse momentum using the ATLAS detector. *JHEP*, 01:126, 2018.

[113] CMS Collaboration. Inclusive search for supersymmetry using razor variables in pp collisions at $\sqrt{s} = 13\,\text{TeV}$. *Phys. Rev. D*, 95:012003, 2017.

[114] CMS Collaboration. A search for new phenomena in pp collisions at $\sqrt{s} = 13\,\text{TeV}$ in final states with missing transverse momentum and at least one jet using the α_{T} variable. *Eur. Phys. J. C*, 77:294, 2017.

[115] CMS Collaboration. Searches for pair production of third-generation squarks in $\sqrt{s} = 13\,\text{TeV}$ pp collisions. *Eur. Phys. J. C*, 77:327, 2017.

[116] CMS Collaboration. Search for direct production of supersymmetric partners of the top quark in the all-jets final state in proton–proton collisions at $\sqrt{s} = 13\,\text{TeV}$. *JHEP*, 10:005, 2017.

[117] CMS Collaboration. Search for top squark pair production in pp collisions at $\sqrt{s} = 13\,\text{TeV}$ using single lepton events. *JHEP*, 10:019, 2017.

[118] CMS Collaboration. Search for top squarks and dark matter particles in opposite-charge dilepton final states at $\sqrt{s} = 13\,\text{TeV}$. *Phys. Rev. D*, 97:032009, 2018.

[119] CMS Collaboration. Searches for physics beyond the standard model with the M_{T2} variable in hadronic final states with and without disappearing tracks in proton–proton collisions at $\sqrt{s} = 13\,\text{TeV}$. *Eur. Phys. J. C*, 80(1):3, 2020.

[120] CMS Collaboration. Search for supersymmetry in proton–proton collisions at 13 TeV in final states with jets and missing transverse momentum. *JHEP*, 10:244, 2019.

[121] CMS collaboration. Search for direct top squark pair production in events with one lepton, jets, and missing transverse momentum at 13 TeV with the CMS experiment. *JHEP*, 05:032, 2020.

[122] ATLAS Collaboration. Object-based missing transverse momentum significance in the ATLAS Detector. ATLAS-CONF-2018-038, 2018.

[123] Johan Alwall, My-Phuong Le, Mariangela Lisanti, and Jay G. Wacker. Searching for directly decaying gluinos at the Tevatron. *Phys. Lett. B*, 666:34, 2008.

[124] Johan Alwall, Philip Schuster, and Natalia Toro. Simplified models for a first characterization of new physics at the LHC. *Phys. Rev. D*, 79:075020, 2009.

[125] Daniele Alves et al. Simplified models for LHC new physics searches. *J. Phys. G*, 39:105005, 2012.

[126] ATLAS Collaboration. Constraints on mediator-based dark matter and scalar dark energy models using $\sqrt{s} = 13\,\text{TeV}$ pp collision data collected by the ATLAS detector. *JHEP*, 05:142, 2019.

[127] ATLAS Collaboration. Searches for third-generation scalar leptoquarks in $\sqrt{s} = 13\,\text{TeV}$ pp collisions with the ATLAS detector. *JHEP*, 06:144, 2019.

[128] Patrick J. Fox and Erich Poppitz. Leptophilic dark matter. *Phys. Rev. D*, 79:083528, 2009.

[129] S. Cassel, D. M. Ghilencea, and G. G. Ross. Electroweak and dark matter constraints on a Z' in models with a hidden valley. *Nucl. Phys. B*, 827:256–280, 2010.

[130] Yang Bai, Patrick J. Fox, and Roni Harnik. The Tevatron at the frontier of dark matter direct detection. *JHEP*, 12:048, 2010.

[131] Jalal Abdallah et al. Simplified models for dark matter searches at the LHC. *Phys. Dark Univ.*, 9-10:8–23, 2015.

[132] Daniel Abercrombie et al. Dark Matter benchmark models for early LHC Run-2 Searches: Report of the ATLAS/CMS Dark Matter Forum. *Phys. Dark Univ.*, 26:100371, 2019.

[133] Tomohiro Abe et al. LHC Dark Matter Working Group: Next-generation spin-0 dark matter models. 2018.

[134] Philippe Brax, Clare Burrage, Christoph Englert, and Michael Spannowsky. LHC signatures of scalar dark energy. *Phys. Rev. D*, 94(8):084054, 2016.

[135] Savas Dimopoulos and Leonard Susskind. Mass Without Scalars. *Nucl. Phys. B*, 155:237–252, 1979.

[136] Savas Dimopoulos. Technicolored Signatures. *Nucl. Phys. B*, 168:69–92, 1980.

[137] E. Eichten and K. Lane. Dynamical breaking of weak interaction symmetries. *Phys. Lett. B*, 90(1,2):125–130, 1980.

[138] V. D. Angelopoulos et al. Search for new quarks suggested by the superstring. *Nucl. Phys. B*, 292:59–92, 1987.

[139] W. Buchmüller and D. Wyler. Constraints on SU(5)-type leptoquarks. *Phys. Lett. B*, 177:377–382, 1986.

[140] J. C. Pati and A. Salam. Lepton number as the fourth "colour". *Phys. Rev. D*, 10:275–289, 1974.

[141] H. Georgi and S. L. Glashow. Unity of All Elementary-Particle Forces. *Phys. Rev. Lett.*, 32:438–441, 1974.

[142] W. Buchmüller, R. Rückl, and D. Wyler. Leptoquarks in lepton - quark collisions. *Phys. Lett. B*, 191:442–448, 1987.

[143] CMS Collaboration. Constraints on models of scalar and vector leptoquarks decaying to a quark and a neutrino at $\sqrt{s} = 13\,\mathrm{TeV}$. *Phys. Rev. D*, 98:032005, 2018.

[144] B. Abbott et al. Production and integration of the ATLAS Insertable B-Layer. *JINST*, 13:T05008, 2018.

[145] ATLAS Collaboration. Performance of the ATLAS trigger system in 2015. *Eur. Phys. J. C*, 77:317, 2017.

[146] ATLAS Collaboration. 2015 start-up trigger menu and initial performance assessment of the ATLAS trigger using Run-2 data. ATL-DAQ-PUB-2016-001, 2016.

[147] Richard D. Ball et al. Parton distributions with LHC data. *Nucl. Phys. B*, 867:244, 2013.

[148] ATLAS Collaboration. ATLAS Pythia 8 tunes to 7 TeV data. ATL-PHYS-PUB-2014-021, 2014.

[149] Leif Lönnblad and Stefan Prestel. Merging multi-leg NLO matrix elements with parton showers. *JHEP*, 03:166, 2013.

[150] Wim Beenakker, Christoph Borschensky, Michael Krämer, Anna Kulesza, and Eric Laenen. NNLL-fast: predictions for coloured supersymmetric particle production at the LHC with threshold and Coulomb resummation. *JHEP*, 12:133, 2016.

[151] Wim Beenakker, Christoph Borschensky, Raphael Heger, Michael Krämer, Anna Kulesza, and Eric Laenen. NNLL resummation for stop pair-production at the LHC. *JHEP*, 05:153, 2016.

[152] Marcela Carena, S. Heinemeyer, C. E. M. Wagner, and G. Weiglein. Suggestions for benchmark scenarios for MSSM Higgs boson searches at hadron colliders. *Eur. Phys. J. C*, 26:601–607, 2003.

[153] T. Gleisberg, S. Höche, F. Krauss, M. Schönherr, S. Schumann, et al. Event generation with SHERPA 1.1. *JHEP*, 02:007, 2009.

[154] Stefano Catani, Leandro Cieri, Giancarlo Ferrera, Daniel de Florian, and Massimiliano Grazzini. Vector boson production at hadron colliders: a fully exclusive QCD calculation at NNLO. *Phys. Rev. Lett.*, 103:082001, 2009.

[155] Michał Czakon, Paul Fiedler, and Alexander Mitov. Total Top-Quark Pair-Production Cross Section at Hadron Colliders Through $\mathcal{O}(\alpha_S^4)$. *Phys. Rev. Lett.*, 110:252004, 2013.

[156] Michal Czakon and Alexander Mitov. NNLO corrections to top pair production at hadron colliders: the quark-gluon reaction. *JHEP*, 01:080, 2013.

[157] Michal Czakon and Alexander Mitov. NNLO corrections to top-pair production at hadron colliders: the all-fermionic scattering channels. *JHEP*, 12:054, 2012.

[158] Peter Bärnreuther, Michal Czakon, and Alexander Mitov. Percent Level Precision Physics at the Tevatron: First Genuine NNLO QCD Corrections to $q\bar{q} \to t\bar{t} + X$. *Phys. Rev. Lett.*, 109:132001, 2012.

[159] Matteo Cacciari, Michal Czakon, Michelangelo Mangano, Alexander Mitov, and Paolo Nason. Top-pair production at hadron colliders with next-to-next-to-leading logarithmic soft-gluon resummation. *Phys. Lett.*, B710:612–622, 2012.

[160] Michal Czakon and Alexander Mitov. Top++: A Program for the Calculation of the Top-Pair Cross-Section at Hadron Colliders. *Comput. Phys. Commun.*, 185:2930, 2014.

[161] Nikolaos Kidonakis. Next-to-next-to-leading-order collinear and soft gluon corrections for t-channel single top quark production. *Phys. Rev.*, D83:091503, 2011.

[162] Nikolaos Kidonakis. Two-loop soft anomalous dimensions for single top quark associated production with a W- or H-. *Phys. Rev.*, D82:054018, 2010.

[163] Nikolaos Kidonakis. NNLL resummation for s-channel single top quark production. *Phys. Rev.*, D81:054028, 2010.

[164] W. Beenakker, S. Dittmaier, M. Kramer, B. Plumper, M. Spira, and P. M. Zerwas. NLO QCD corrections to t $\bar{t}$ H production in hadron collisions. *Nucl. Phys. B*, 653:151–203, 2003.

[165] S. Dawson, C. Jackson, L. H. Orr, L. Reina, and D. Wackeroth. Associated Higgs boson production with top quarks at the CERN Large Hadron Collider: NLO QCD corrections. *Phys. Rev. D*, 68:034022, 2003.

[166] Yu Zhang, Wen-Gan Ma, Ren-You Zhang, Chong Chen, and Lei Guo. QCD NLO and EW NLO corrections to $t\bar{t}H$ production with top quark decays at hadron collider. *Phys. Lett. B*, 738:1–5, 2014.

[167] S. Frixione, V. Hirschi, D. Pagani, H.-S. Shao, and M. Zaro. Electroweak and QCD corrections to top-pair hadroproduction in association with heavy bosons. *JHEP*, 06:184, 2015.

[168] ATLAS Collaboration. The ATLAS Simulation Infrastructure. *Eur. Phys. J. C*, 70:823, 2010.

[169] S. Agostinelli et al. GEANT4: A Simulation toolkit. *Nucl. Instrum. Meth. A*, 506:250, 2003.

[170] ATLAS Collaboration. The simulation principle and performance of the ATLAS fast calorimeter simulation FastCaloSim. ATL-PHYS-PUB-2010-013, 2010.

[171] ATLAS Collaboration. The Pythia 8 A3 tune description of ATLAS minimum bias and inelastic measurements incorporating the Donnachie-Landshoff diffractive model. Technical report, CERN, Geneva, Aug 2016. All figures including auxiliary figures are available at https://atlas.web.cern.ch/Atlas/GROUPS/PHYSICS/PUBNOTES/ATL-PHYS-PUB-2016-017.

[172] ATLAS Collaboration. Reconstruction of primary vertices at the ATLAS experiment in Run 1 proton–proton collisions at the LHC. *Eur. Phys. J. C*, 77:332, 2017.

[173] ATLAS Collaboration. Vertex Reconstruction Performance of the ATLAS Detector at $\sqrt{s} = 13$ TeV. Jul 2015.

[174] ATLAS Collaboration. Performance of the ATLAS track reconstruction algorithms in dense environments in LHC Run 2. *Eur. Phys. J. C*, 77:673, 2017.

[175] ATLAS Collaboration. Topological cell clustering in the ATLAS calorimeters and its performance in LHC Run 1. *Eur. Phys. J. C*, 77:490, 2017.

[176] Matteo Cacciari, Gavin P. Salam, and Gregory Soyez. FastJet User Manual. *Eur. Phys. J. C*, 72:1896, 2012.

[177] ATLAS Collaboration. Selection of jets produced in 13 TeV proton–proton collisions with the ATLAS detector. ATLAS-CONF-2015-029, 2015.

[178] ATLAS Collaboration. Performance of pile-up mitigation techniques for jets in pp collisions at $\sqrt{s} = 8\,\text{TeV}$ using the ATLAS detector. *Eur. Phys. J. C*, 76:581, 2016.

[179] ATLAS Collaboration. Soft b-hadron tagging for compressed SUSY scenarios. ATLAS-CONF-2019-027, 2019.

[180] ATLAS Collaboration. Electron reconstruction and identification in the ATLAS experiment using the 2015 and 2016 LHC proton-proton collision data at $\sqrt{s} = 13$ TeV. *Submitted to: Eur. Phys. J.*, 2019.

[181] ATLAS Collaboration. Electron and photon energy calibration with the ATLAS detector using 2015–2016 LHC proton–proton collision data. *JINST*, 14:P03017, 2019.

[182] ATLAS Collaboration. Electron and photon performance measurements with the ATLAS detector using the 2015-2017 LHC proton–proton collision data. *JINST*, 14(12):P12006, 2019.

[183] ATLAS Collaboration. Performance of missing transverse momentum reconstruction with the ATLAS detector using proton–proton collisions at $\sqrt{s} = 13\,\text{TeV}$. *Eur. Phys. J. C*, 78:903, 2018.

[184] C. G. Lester and D. J. Summers. Measuring masses of semi-invisibly decaying particle pairs produced at hadron colliders. *Phys. Lett. B*, 463:99–103, 1999.

[185] Alan Barr, Christopher Lester, and P. Stephens. A variable for measuring masses at hadron colliders when missing energy is expected; m_{T2}: the truth behind the glamour. *J. Phys. G*, 29:2343–2363, 2003.

[186] M. Baak, G. J. Besjes, D. Côté, A. Koutsman, J. Lorenz, and D. Short. HistFitter software framework for statistical data analysis. *Eur. Phys. J. C*, 75:153, 2015.

[187] ATLAS Collaboration. Search for squarks and gluinos with the ATLAS detector in final states with jets and missing transverse momentum using 4.7 fb^{-1} of $\sqrt{s} = 7$ TeV proton-proton collision data. *Phys. Rev. D*, 87(1):012008, 2013.

[188] G. Choudalakis and D. Casadei. Plotting the differences between data and expectation. *Eur. Phys. J. Plus*, 127:25, Feb 2012.

[189] ATLAS Collaboration. Calibration of light-flavour b-jet mistagging rates using ATLAS proton–proton collision data at $\sqrt{s} = 13$ TeV. ATLAS-CONF-2018-006, 2018.

[190] ATLAS Collaboration. Measurement of b-tagging efficiency of c-jets in $t\bar{t}$ events using a likelihood approach with the ATLAS detector. ATLAS-CONF-2018-001, 2018.

[191] Stefano Frixione, Eric Laenen, Patrick Motylinski, Bryan R. Webber, and Chris D. White. Single-top hadroproduction in association with a W boson. *JHEP*, 07:029, 2008.

[192] Enrico Bothmann, Marek Schönherr, and Steffen Schumann. Reweighting QCD matrix-element and parton-shower calculations. *Eur. Phys. J. C*, 76(11):590, 2016.

[193] Wim Beenakker, Christoph Borschensky, Michael Krämer, Anna Kulesza, Eric Laenen, Vincent Theeuwes, and Silja Thewes. NNLL resummation for squarkg gluino production at the LHC. *JHEP*, 12:023, 2014.

[194] Wim Beenakker, Tim Janssen, Susanne Lepoeter, Michael Krämer, Anna Kulesza, Eric Laenen, Irene Niessen, Silja Thewes, and Tom Van Daal. Towards NNLL resummation: hard matching coefficients for squark and gluino hadroproduction. *JHEP*, 10:120, 2013.

[195] Wim Beenakker, Silja Brensing, Michael Krämer, Anna Kulesza, Eric Laenen, and Irene Niessen. NNLL resummation for squark-antisquark pair production at the LHC. *JHEP*, 01:076, 2012.

[196] Wim Beenakker, Silja Brensing, Michael Krämer, Anna Kulesza, Eric Laenen, and Irene Niessen. Soft-gluon resummation for squark and gluino hadroproduction. *JHEP*, 12:041, 2009.

[197] A. Kulesza and L. Motyka. Soft gluon resummation for the production of gluino-gluino and squark-antisquark pairs at the LHC. *Phys. Rev. D*, 80:095004, 2009.

[198] A. Kulesza and L. Motyka. Threshold Resummation for Squark-Antisquark and Gluino-Pair Production at the LHC. *Phys. Rev. Lett.*, 102:111802, 2009.

[199] W. Beenakker, R. Höpker, M. Spira, and P. M. Zerwas. Squark and gluino production at hadron colliders. *Nucl. Phys. B*, 492:51, 1997.

[200] Alexander L. Read. Presentation of search results: the CL_S technique. *J. Phys. G*, 28:2693, 2002.

[201] Glen Cowan, Kyle Cranmer, Eilam Gross, and Ofer Vitells. Asymptotic formulae for likelihood-based tests of new physics. *Eur. Phys. J. C*, 71:1554, 2011.

[202] Graham D. Kribs, Adam Martin, Bryan Ostdiek, and Tom Tong. Dark Mesons at the LHC. *JHEP*, 07:133, 2019.

[203] ATLAS Collaboration. Search for new high-mass phenomena in the dilepton final state using 36 fb^{-1} of proton–proton collision data at $\sqrt{s} = 13\,\text{TeV}$ with the ATLAS detector. *JHEP*, 10:182, 2017.

[204] CMS Collaboration. Search for high-mass resonances in dilepton final states in proton–proton collisions at $\sqrt{s} = 13\,\text{TeV}$. *JHEP*, 06:120, 2018.

[205] G. Avoni et al. The new lucid-2 detector for luminosity measurement and monitoring in atlas. *JINST*, 13(07):P07017, 2018.

[206] ATLAS Collaboration. Luminosity determination in *pp* collisions at $\sqrt{s} = 8\,\text{TeV}$ using the ATLAS detector at the LHC. *Eur. Phys. J. C*, 76:653, 2016.

[207] ATLAS Collaboration. `https://gitlab.cern.ch/atlas/athena/blob/master/PhysicsAnalysis/DerivationFramework/DerivationFrameworkTop/share/TOPQ4.py`. Online; accessed 24 October, 2022.

[208] ATLAS Collaboration. `https://gitlab.cern.ch/atlas/athena/blob/master/PhysicsAnalysis/DerivationFramework/DerivationFrameworkTop/share/TOPQ1.py`. Online; accessed 24 October, 2022.

[209] Torbjorn Sjostrand, Stephen Mrenna, and Peter Z. Skands. A Brief Introduction to PYTHIA 8.1. *Comput. Phys. Commun.*, 178:852–867, 2008.

[210] Richard D. Ball, Valerio Bertone, Stefano Carrazza, Christopher S. Deans, Luigi Del Debbio, Stefano Forte, Alberto Guffanti, Nathan P. Hartland, José I. Latorre, Juan Rojo, and Maria Ubiali. Parton distributions with LHC data. *Nuclear Physics B*, 867(2):244–289, feb 2013.

[211] M. Beneke, P. Falgari, S. Klein, and C. Schwinn. Hadronic top-quark pair production with NNLL threshold resummation. *Nucl. Phys.*, B855:695–741, 2012.

[212] Jon Butterworth et al. PDF4LHC recommendations for LHC Run II. *J. Phys. G*, 43:023001, 2016.

[213] A. D. Martin, W.J. Stirling, R. S. Thorne, and G. Watt. Parton distributions for the LHC. *Eur. Phys. J. C*, 63:189, 2009.

[214] A. D. Martin, W.J. Stirling, R.S. Thorne, and G. Watt. Uncertainties on α_S in global PDF analyses and implications for predicted hadronic cross sections. *Eur. Phys. J. C*, 64:653–680, 2009.

[215] H.-L. Lai et al. New parton distributions for collider physics. *Phys. Rev. D*, 82:074024, 2010.

[216] J. Gao et al. CT10 next-to-next-to-leading order global analysis of QCD. *Phys. Rev. D*, 89:033009, 2014.

[217] ATLAS Collaboration. Studies on top-quark Monte Carlo modelling with Sherpa and MG5_aMC@NLO. ATL-PHYS-PUB-2017-007, 2017.

[218] Sayipjamal Dulat, Tie-Jiun Hou, Jun Gao, Marco Guzzi, Joey Huston, Pavel Nadolsky, Jon Pumplin, Carl Schmidt, Daniel Stump, and C. P. Yuan. New parton distribution functions from a global analysis of quantum chromodynamics. *Phys. Rev. D*, 93(3):033006, 2016.

[219] L.A. Harland-Lang, A.D. Martin, P. Motylinski, and R.S. Thorne. Parton distributions in the LHC era: MMHT 2014 PDFs. *Eur. Phys. J. C*, 75(5):204, 2015.

[220] Tomáš Ježo, Jonas M. Lindert, Niccolo Moretti, and Stefano Pozzorini. New NLOPS predictions for $t\bar{t} + b$-jet production at the LHC. *Eur. Phys. J. C*, 78(6):502, 2018.

[221] Tomas Ježo. Powheg-box-res ttbb source code, 2019.

[222] Emanuele Re. Single-top Wt-channel production matched with parton showers using the POWHEG method. *Eur. Phys. J. C*, 71:1547, 2011.

[223] Rikkert Frederix, Emanuele Re, and Paolo Torrielli. Single-top t-channel hadroproduction in the four-flavour scheme with POWHEG and aMC@NLO. *JHEP*, 09:130, 2012.

[224] Simone Alioli, Paolo Nason, Carlo Oleari, and Emanuele Re. NLO single-top production matched with shower in POWHEG: s- and t-channel contributions. *JHEP*, 09:111, 2009.

[225] Rikkert Frederix, Davide Pagani, and Marco Zaro. Large NLO corrections in $t\bar{t}W^{\pm}$ and $t\bar{t}t\bar{t}$ hadroproduction from supposedly subleading EW contributions. *JHEP*, 02:031, 2018.

[226] Stefano Frixione, Eric Laenen, Patrick Motylinski, and Bryan R. Webber. Angular correlations of lepton pairs from vector boson and top quark decays in Monte Carlo simulations. *JHEP*, 04:081, 2007.

[227] Pierre Artoisenet, Rikkert Frederix, Olivier Mattelaer, and Robbert Rietkerk. Automatic spin-entangled decays of heavy resonances in Monte Carlo simulations. *JHEP*, 03:015, 2013.

[228] Heribertus B. Hartanto, Barbara Jäger, Laura Reina, and Doreen Wackeroth. Higgs boson production in association with top quarks in the POWHEG BOX. *Phys. Rev. D*, 91(9):094003, 2015.

[229] D. de Florian et al. Handbook of LHC Higgs Cross Sections: 4. Deciphering the Nature of the Higgs Sector. 2016.

[230] ATLAS Collaboration. Search for the Standard Model Higgs boson produced in association with top quarks and decaying into $b\bar{b}$ in pp collisions at $\sqrt{s} = 8\,\text{TeV}$ with the ATLAS detector. *Eur. Phys. J. C*, 75:349, 2015.

[231] ATLAS Collaboration. Electron efficiency measurements with the ATLAS detector using the 2012 LHC proton–proton collision data. ATLAS-CONF-2014-032, 2014.

[232] ATLAS Collaboration. `https://twiki.cern.ch/twiki/bin/view/AtlasProtected/EGammaIdentificationRun2#Menus_for_2015_2016_and_2017_dat`. Online; accessed 24 October, 2022.

[233] ATLAS Collaboration. `https://twiki.cern.ch/twiki/bin/view/AtlasProtected/RecommendedIsolationWPs?rev=10#Electron_calo_track_isolation_wo`. Online; accessed 24 October, 2022.

[234] ATLAS Collaboration. Muon reconstruction and identification efficiency in ATLAS using the full Run 2 pp collision data set at $\sqrt{s} = 13$ TeV. *Eur. Phys. J., C*, 81:578. 44 p, Dec 2020.

[235] Lukas Adamek, Jonathan David Bossio Sola, Daniel Camarero Munoz, Christophe Clement, Eric Edward Corrigan, Ana Rosario Cueto Gomez, Jeffrey Rogers Dandoy, Maria Florencia Daneri, Caterina Doglioni, Dag Ingemar Gillberg, Julia Lynne Gonski, Robert Hankache, Eva Hansen, Kevin Hildebrand, Tanja Holm, Benjamin Paul Jaeger, Teng Jian Khoo, Vincent Kitali, Matthew Edgar Leblanc, Fan Li, Xingguo Li, Bogdan Malaescu, Kayla Dawn McLean, David Miller, Fabrizio Napolitano, Josef Pacalt, Katherine Pachal, Tae Hyoun Park, Krisztian Peters, Rebecca Hayley Pickles, Trine Poulsen, Michaela Queitsch-maitland, Jacob Henry Rawling, Steven Schramm, Sundeep Singh, Maximilian J Swiatlowski, Michel Vetterli, Chaowaroj Wanotayaroj, Lewis Joseph Wilkins, and Christopher Young. Jet energy scale and resolution measured in proton-proton collisions at $\sqrt{s} = 13$ TeV with the ATLAS detector. Technical report, CERN, Geneva, Feb 2020.

[236] The ATLAS Collaboration. Identification and rejection of pile-up jets at high pseudorapidity with the ATLAS detector. *The European Physical Journal C*, 77(9), sep 2017.

[237] ATLAS Collaboration. `https://twiki.cern.ch/twiki/bin/viewauth/AtlasProtected/BTagTaggerRecommendationsRelease21`. Online; accessed 24 October, 2022.

[238] ATLAS Collaboration. `https://gitlab.cern.ch/atlas/athena/blob/21.2/PhysicsAnalysis/AnalysisCommon/AssociationUtils/README.rst`. Online; accessed 24 October, 2022.

[239] ATLAS Collaboration. `https://twiki.cern.ch/twiki/bin/viewauth/Atlas/DataPreparationCheckListForPhysicsAnalysis`. Online; accessed 24 October, 2022.

[240] ATLAS Collaboration. Measurements of $t\bar{t}$ differential cross-sections in the all-hadronic channel using highly boosted top quarks in pp collisions at $\sqrt{s} = 13$ TeV using the ATLAS detector: Analysis of the full 2015 and 2016 dataset. ATL-COM-PHYS-2016-1696, 2016.

[241] Gregor Kasieczka, Benjamin Nachman, Matthew Schwartz, and David Shih. Automating the abcd method with machine learning. *Physical Review D*, 103, 02 2021.

[242] ATLAS Collaboration. Electron and photon performance measurements with the ATLAS detector using the 2015–2017 LHC proton-proton collision data. *Journal of Instrumentation*, 14(12):P12006–P12006, dec 2019.

[243] ATLAS Collaboration. Jet Calibration and Systematic Uncertainties for Jets Reconstructed in the ATLAS Detector at $\sqrt{s} = 13$ TeV. Jul 2015.

[244] ATLAS Collaboration. `https://twiki.cern.ch/twiki/bin/view/AtlasProtected/JetUncertaintiesRel21Summer2018SmallR`. Online; accessed 24 October, 2022.

[245] Michiel Botje, Jon Butterworth, Amanda Cooper-Sarkar, Albert de Roeck, Joel Feltesse, Stefano Forte, Alexander Glazov, Joey Huston, Ronan McNulty, Torbjorn Sjostrand, and Robert Thorne. The pdf4lhc working group interim recommendations, 2011.

[246] ATLAS Collaboration. `https://twiki.cern.ch/twiki/bin/view/LHCPhysics/TtbarNNLO`. Online; accessed 24 October, 2022.

[247] Kyle Cranmer, George Lewis, Lorenzo Moneta, Akira Shibata, and Wouter Verkerke. HistFactory: A tool for creating statistical models for use with RooFit and RooStats. Jan 2012.

[248] Wouter Verkerke and David P. Kirkby. The RooFit toolkit for data modeling. *eConf*, C0303241:MOLT007, 2003.

[249] M. Hatlo, F. James, P. Mato, L. Moneta, M. Winkler, and A. Zsenei. Developments of mathematical software libraries for the lhc experiments. *IEEE Transactions on Nuclear Science*, 52(6):2818–2822, 2005.

[250] ATLAS sensitivity to top squark pair production at the HL-LHC. Technical report, CERN, Geneva, 2018. All figures including auxiliary figures are available at https://atlas.web.cern.ch/Atlas/GROUPS/PHYSICS/PUBNOTES/ATL-PHYS-PUB-2018-021.